MUSC Theses and Dissertations

Fall 12-12-2022

An Imaging Mass Spectrometry Investigation Into the N-linked Glycosylation Landscape of Pancreatic Ductal Adenocarcinoma and the Development of Associated Tools for Enhanced Glycan Separation and Characterization

Colin McDowell
Medical University of South Carolina

Follow this and additional works at: https://medica-musc.researchcommons.org/theses

Part of the Analytical Chemistry Commons, and the Neoplasms Commons

An Imaging Mass Spectrometry Investigation Into the N-linked Glycosylation Landscape of Pancreatic Ductal Adenocarcinoma and the Development of Associated Tools for Enhanced Glycan Separation and Characterization

Colin Thane McDowell

A dissertation submitted to the faculty of the Medical University of South Carolina in partial fulfillment of the requirements for the degree of Doctor of Philosophy in the College of Graduate Studies

Department of Cell and Molecular Pharmacology and Experimental Therapeutics

2022

Approved By:

Chairman, Advisory Committee

_____
Richard Drake

_____
Peggi Angel

_____
Anand Mehta

_____
Russell Norris

_____
Denis Guttridge

Table of Contents

ABSTRACT

COLIN THANE MCDOWELL. An Imaging Mass Spectrometry Investigation Into the N-linked Glycosylation Landscape of Pancreatic Ductal Adenocarcinoma and the Development of Associated Tools for Enhanced Glycan Separation and Characterization (Under the direction of RICHARD DRAKE)

The severity of pancreatic ductal adenocarcinoma (PDAC) is largely attributed to a failure to detect the disease before metastatic spread has occurred. CA19-9, a carbohydrate biomarker, is used clinically to surveille disease progression, but due to specificity challenges is not suitable for early discovery. As CA19-9 and other prospective markers are glycan epitopes, there is great clinical interest in understanding the glycobiology of pancreatic cancer. Unfortunately, few studies have been able to link glycosylation changes directly to pancreatic tumors and instead have focused on peripheral glycan alterations in the serum of PDAC patients. To address this gap in our understanding, we applied an imaging mass spectrometry (IMS) approach with complementary enzymatic and chemical isomer separation techniques to spatially assess the PDAC N-glycome in a cohort of pancreatic cancer patients. Orthogonally, we characterized the expression of CA19-9 and a new biomarker, sTRA, by multi-round immunofluorescence (IF) in the same cohort. These analyses revealed increased sialylation, fucosylation and branching amongst other structural themes in areas of PDAC tumor tissue. CA19-9 expressing tumors were defined by multiply branched, fucosylated bisecting N-glycans while sTRA expressing tumors favored tetraantennary N-glycans with

polylactosamine extensions. IMS and IF-derived glycan and biomarker features were used to build classification models that detected PDAC tissue with an AUC of 0.939, outperforming models using either dataset individually. While studying sialylation isomers in our PDAC cohort, we saw an opportunity to enhance the chemical derivatization protocol we were using to address its shortcomings and expand its functionality. Subsequently, we developed a set of novel amidation-amidation strategies to stabilize and differentially label α2,3 and α2,6-linked sialic acids. In our alkyne-based approach, the differential mass shifts induced by the reactions allow for isomeric discrimination in imaging mass spectrometry experiments. This scheme, termed AAXL, was further characterized in clinical tissue specimens, biofluids and cultured cells. Our azide-based approach, termed AAN$_3$, was more suitable for bioorthogonal applications, where the azide tag installed on α2,3 and α2,8-sialic acids could be reacted by click chemistry with a biotin-alkyne for subsequent streptavidin-peroxidase staining. Furthering the use of AAN$_3$, we developed two additional techniques to fluorescently label (SAFER) and preferentially enrich (SABER) α2,3 and α2,8-linked sialic acids for more advanced glycomic applications. Initial experiments with these novel approaches have shown successful fluorescent staining and the identification of over 100 sialylated glycoproteins by LC-MS/MS. These four bioorthogonal strategies provide a new glycomic tool set for the characterization of sialic acid isomers in pancreatic and other cancers. Overall, this work furthers our collective understanding of the glycobiology underpinning pancreatic cancer and potentiates the discovery of novel carbohydrate biomarkers for the early detection of PDAC.

LIST OF TABLES

LIST OF FIGURES

ACKNOWLEDGEMENTS

Denys, Harrison, Jaclyn, Jade, Stephen) and Mehta (Alyson, Andrew, Harmin, Jake D., Jake G. and Shaaron) labs are also deserving of thanks. Xiaowei (Vivian) Lu in particular fueled my organic chemistry development through an undeserving level of mentorship, for which I am grateful. To my friends Calvin and Andrew, who encouraged me to rotate in Dr. Drake's lab on the condition that I not be allowed to join, I'm glad that I ignored the both of you. Having close friends with which to share the ups and downs of a PhD turned out to be invaluable.

Besides my academic group here at MUSC, my friends and family have been a huge source of strength and support during this period of my life. I wouldn't be where I am today without the encouragement of my parents and siblings, who have supported my every academic and personal endeavor along the way. It is a debt I'm afraid I cannot repay. To Connor, Corey, Ellis, Hunter, John, Stephen S., Stephen U. and Tyler, who are listed *alphabetically* not in order of *importance*, thank you for your friendship along the way. I would also like to thank my Charleston friends who have made my so life enjoyable over the past four and a half years. You are too many to list here, but if you're reading this, know that I'm talking about you. Finally, my most sincere gratitude goes to my girlfriend Madeline, who has supported me in every way that a partner can during this process. I couldn't have made this final push without you; I love you and I'm excited for what's to come.

"Into the wild blue yonder" – Robert MacArthur Crawford, 1939

Chapter 1: Introduction

1.1 Pancreatic Ductal Adenocarcinoma

1.1.1 Development of the Pancreas and Normal Function

The human pancreas develops early in embryogenesis as two separate outpouchings, dorsal and ventral buds, from the endoderm of the foregut. These buds gradually rotate and fuse to become a single organ with head and tail sections by E14 in mice and by day 41 of gestation in humans[1]. Branching morphogenesis creates the primary ductal structures of the pancreas while pluripotent progenitor cell populations differentiate into the three main cell types of the pancreas: acinar exocrine cells, endocrine islet cells (islets of Langerhans) and ductal epithelium[2]. Acinar cells form clusters around the termini of intralobular ductal epithelium which conjoin into larger interlobular ducts finally coalescing into the main pancreatic duct which secretes digestive enzymes directly into the intestinal lumen. Endocrine cells form distinct puncta known as pancreatic islets which stud the organ and secrete hormones directly into a mesh of capillaries which vascularize the pancreas[3].

Pancreatic functions can generally be divided into two distinct categories: exocrine and endocrine. Acinar cells in clusters secrete zymogen granules of the digestive enzymes responsible for nutrient breakdown in the small intestine, namely the proteases trypsin and chymotrypsin, lipase for lipids and amylase for carbohydrates[4]. Pancreatic islets are composed mainly of five distinct cell types: α, β, δ, ε, and PP cells which secrete glucagon, insulin, somatostatin, ghrelin and pancreatic polypeptide, respectively[5]. Glucagon and insulin work in a counterbalanced fashion to promote the release of glucose stored as glycogen from the liver into the blood stream when levels are low, and to regulate the

removal of glucose from the blood into glycogen stores when levels are high[6]. Somatostatin released from δ cells functions as a master inhibitor of α and β cell secretions in response to blood glucose levels[7]. Pancreatic polypeptide (PP) inhibits pancreatic exocrine secretions and functions mainly as a satiety hormone while ghrelin stimulates the appetite and fat storage[8,9]. Together, these exocrine and endocrine cell types provide dynamic regulatory control of nutrient breakdown and hormonal nutrient signaling (Figure 1).

1.1.2 Pancreatic Cancer Progression, Etiology and Symptoms

Pancreatic ductal adenocarcinoma (PDAC) is a cancerous malignancy arising from the transformation of epithelial cells in pancreatic ducts which constitutes upwards of 90% of all pancreatic neoplasias[10]. In the United States in the year 2020 an estimated 58,000 new cases of pancreatic cancer were reported while 47,000 succumbed to the disease[11]. Worldwide, the prevalence of pancreatic cancers is on the rise, with 496,000 new cases and 466,000 deaths in 2020[12]. Proportionally, PDAC affects males more than females, black people more than other ethnicities and the elderly (60 years and older) over those younger[13–15]. Troublingly, the 5-year survival rate for pancreatic cancer remains low (9 – 11%) despite surgical and therapeutic advances in recent decades, making pancreatic ductal adenocarcinoma the deadliest amongst other cancers[16]. The severity of the disease is mainly attributed to the majority of cases being diagnosed at the advanced (metastatic, 52%) or locally advanced stage (30%)[17] as there are currently no effective biomarkers for early detection.
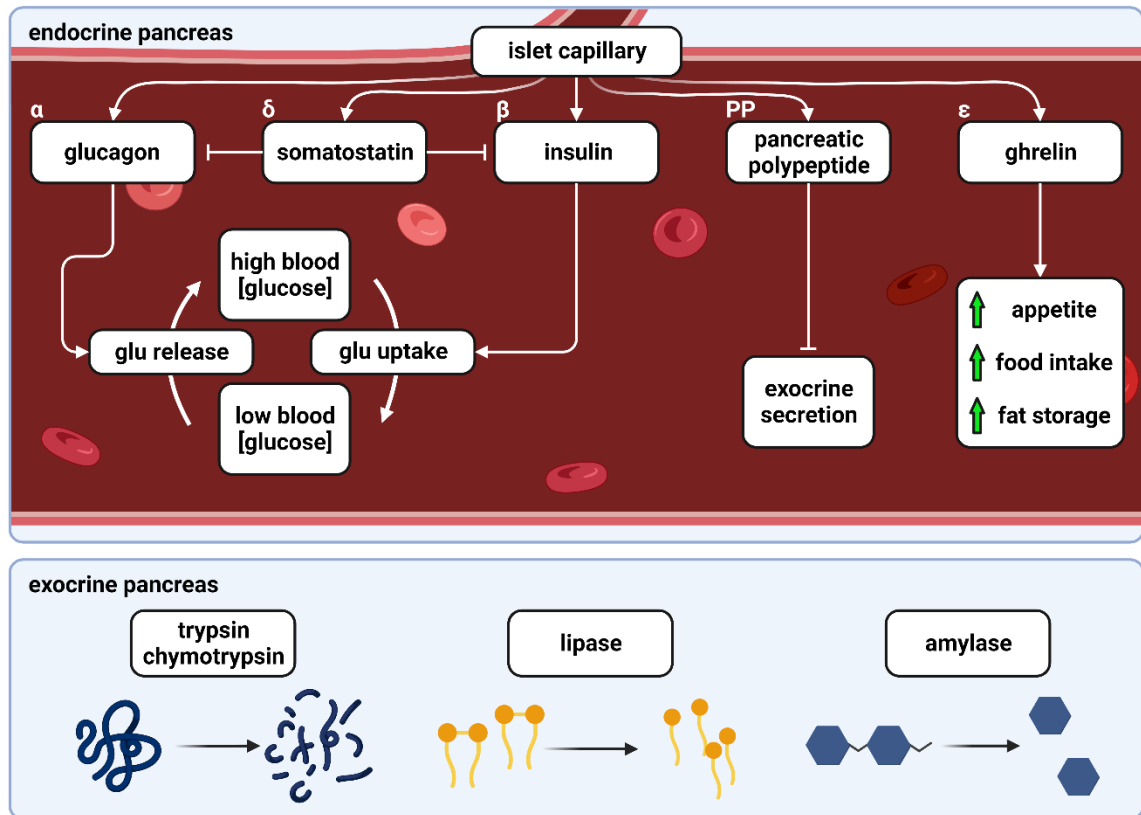
Figure 1: Endocrine and Exocrine Functions of the Pancreas. α, β, δ, PP and ε cells making up pancreatic islets secrete glucagon, insulin, somatostatin, pancreatic polypeptide and ghrelin, respectively to hormonally regulate blood glucose and nutrient metabolism. Exocrine acinar cell clusters secrete trypsin, chymotrypsin, lipase and amylase as part of the digestive system.

The majority of PDAC cases develop when ductal epithelia undergo neoplastic transformation to form precursor lesions termed pancreatic intraepithelial neoplasias (PanINs), although other less common mucinous lesions known as intraductal papillary mucinous neoplasias (IPMNs) and mucinous cystic neoplasias (MCNs) also give rise to the disease[18]. As PanIN lesions acquire more mutations they progress through histopathologically classified stages (PanIN-1 → PanIN-3) defined by nuclear and cytoplasmic atypia and increasingly distorted papillary architecture leading to invagination of the ductal epithelium and the eventual occlusion of the ductal lumen[19,20]. The transition from PanIN3 lesions to a ductal adenocarcinoma phenotype is fluid and relies on histopathological and genetic evaluation. PDAC tumors are typically small, solid, immunologically-cold, hypovascularized masses with dense stromal networks making up the majority of the mass by volume[21]. These carcinomas are staged using the TNM system which evaluates tumor size and arterial involvement (T), metastasis to lymph nodes (N) and metastasis to distant sites (M) with most cases diagnosed at T3N1M0 (stage IIB)[22,23]. The prognosis for patients diagnosed with PDAC is poor, with an average T1 → T4 time to progression of 14 months in which survival is negatively correlated with increased age and more advanced disease status at time of diagnosis[24]. Clinical consensus and meta-analyses list tobacco smoking, diabetes mellitus, obesity, hepatitis B viral infection and heavy alcohol consumption as serious risk factors for developing pancreatic cancer[25].

The above risk factors may in some cases induce acute or chronic inflammation of the pancreas leading to a condition known as pancreatitis, which

is strongly associated with the development of pancreatic ductal adenocarcinoma[26]. Pancreatitis is characterized by increased fibrosis and the loss of acinar and islet cell populations resulting in abdominal pain and both endocrine and exocrine deficiencies[27]. Acute pancreatitis (AP) stems from temporal acinar cell injury events often resulting in the premature activation of digestive enzymes which leads to autodigestion of pancreatic tissue, leukocyte recruitment and chemo/cytokine release as part of the acute phase response[28]. Recurrent pancreatic insult and the accumulation of acute events induces sustained recruitment of macrophages and neutrophils to the pancreas in chronic pancreatitis (CP)[29]. Cytokines released by this resident immune population, along with injured acinar cells, have been shown to activate quiescent pancreatic stellate cells to transform into myofibroblast-like cells which induce the mostly collagen and fibronectin-based fibrotic scarring typifying chronic disease[30]. The sustained immune-inflammatory response associated with pancreatitis results in DNA damage, accelerated mutagenesis and often acinar to ductal metaplasia events[31]. This in combination with prolonged and exacerbated secondary oxidative injury fosters a more favorable environment for the development of the precursor lesions that precede PDAC[32]. It is important to note that while pancreatitis is predictive of the development of pancreatic cancer, less than 10% of PDAC cases are thought to arise from CP[33].

A related causative factor with inflammatory ties is type two diabetes mellitus (T2DM), where those diagnosed have a relative risk factor or hazard ratio ranging from 1.5 – 2.0 for the development of pancreatic ductal adenocarcinoma[34].

6

T2DM is characterized by a resistance to the ability of insulin to suppress hepatic release of glucose, leading to initially elevated intrapancreatic insulin levels, high blood glucose concentrations and damage to various organ systems[35]. Sustained high insulin levels are associated with β-cell failure and activation of the unfolded protein response causing senescence and apoptotic events which increase the likelihood for the development of pancreatic cancer[36]. The proximity of acinar cells and ductal epithelium to islets with hyper-elevated insulin production in T2DM accelerates the proliferation of transformed cells within these populations by directly stimulating growth signaling through insulin and IGF-1 receptors in a process known as the proxicrine effect[37]. Additionally, prolonged inflammatory signaling in the pancreas in response to T2DM creates a pro-oncogenic environment similar to that described for pancreatitis[38]. Complicating etiological considerations for diabetes is the dual-causal nature of PDAC and diabetes, where T2DM is a considered a long-term risk for the development of pancreatic cancer while concomitantly PDAC is considered a long-term risk for diabetes[39]. Studies of pancreatic cancer patients have found diabetes to be prevalent in 47% of those profiled, as compared with only 7% of the normal population[40]. It is theorized that shared risk factors for pancreatic cancer and T2DM may in part explain to the complex overlap between both diseases[41]. Impairment of normal pancreatic function by the progression of PDAC may also play a causative role in the development of pancreatic cancer associated-diabetes[42].

Despite the well-established roles of pancreatitis and diabetes mellitus in the development of PDAC, 90% of pancreatic cancers are considered sporadic in

origin[43]. The accumulation of somatic mutations in pancreatic cells over a lifetime leads to increasing oncogenic potential through multiple prominent genetic pathways. Most well characterized amongst these are mutations to the KRAS gene in the RAS small GTPase family[44]. Oncogenic KRAS is associated with over 90% of pancreatic cancers and is known to be the primary driver of neoplastic transformation in the development of PDAC[45]. Amongst this family of mutations, G12D is the most common in pancreatic cancer followed by G12V and G12R, with less than 10% of KRAS mutations at other sites[46]. Aspartic acid, valine and arginine substitutions at the G12 residue hinders the interaction between KRAS and its associated GAP, preventing GTP hydrolysis and leading to constitutive activation[47]. Thus, the KRAS signaling axis drives both MAP/ERK and PI3K/PDK/AKT pathways resulting in cell survival, proliferation and Warburg metabolic effects[48,49]. Targeted therapeutics towards mutant KRAS have been largely ineffective, although a new wave of interest in KRAS inhibitors has yielded promising treatment strategies[50,51].

While oncogenic KRAS is the canonical progenitor mutation of early PanIN-1 lesions, the progression of these precursor lesions towards the more aggressive PanIN-3 and eventual PDAC phenotype is driven largely by the accumulation of further somatic mutations. Early PanIN lesions are characterized by mutant KRAS, telomere shortening and overexpression of HER2 while more advanced PanINs show aberrant TP53, BRCA2, SMAD4 and CDKN2A (p16) expression[52,53]. Overexpression of the heavily glycosylated mucin family proteins MUC1 and MUC5AC is also associated with PanIN progression[54]. Increasing oncogenic

burden and atypical protein expression drives a variety of signaling pathways which promote the proliferation, cell survival and metastatic escape associated with aggressive PDAC (Figure 2).

Although most genetic drivers for pancreatic ductal adenocarcinoma occur as sporadic mutations, a subset of cases arise through familial genetic variations. Pancreatic cancers with a genetic background can be further subdivided into those patients with one or more relatives diagnosed with pancreatic cancer (90%, termed familial pancreatic cancer or FPC) and those without pancreatic cancer in the family but with a familial genetic syndrome that predisposes them to a high risk for PDAC[55]. In FPC, risk for pancreatic cancer increases proportionally with the number of first degree relatives diagnosed in a patient's pedigree: 6.4% when two relatives are affected and 32% when three are affected[56]. The genetic causes for FPC are not well understood and seem to be as varied as in sporadic cases, although large pedigree studies have implicated hereditary BRCA2, PALB2 and CDKN2A as common mutations in a significant subset of hereditary pancreatic cancers[57,58]. The remaining 10% of inherited cases stem from hereditary genetic syndromes with increased pancreatic cancer risk, namely hereditary pancreatitis, Peutz-Jeghers syndrome, Lynch syndrome and familial breast cancer, ovarian cancer and melanoma syndromes[59–63]. A hereditary disposition towards pancreatic cancer warrants increased and earlier surveillance or preemptive partial to full pancreatectomy in some extremely high risk cases[64].
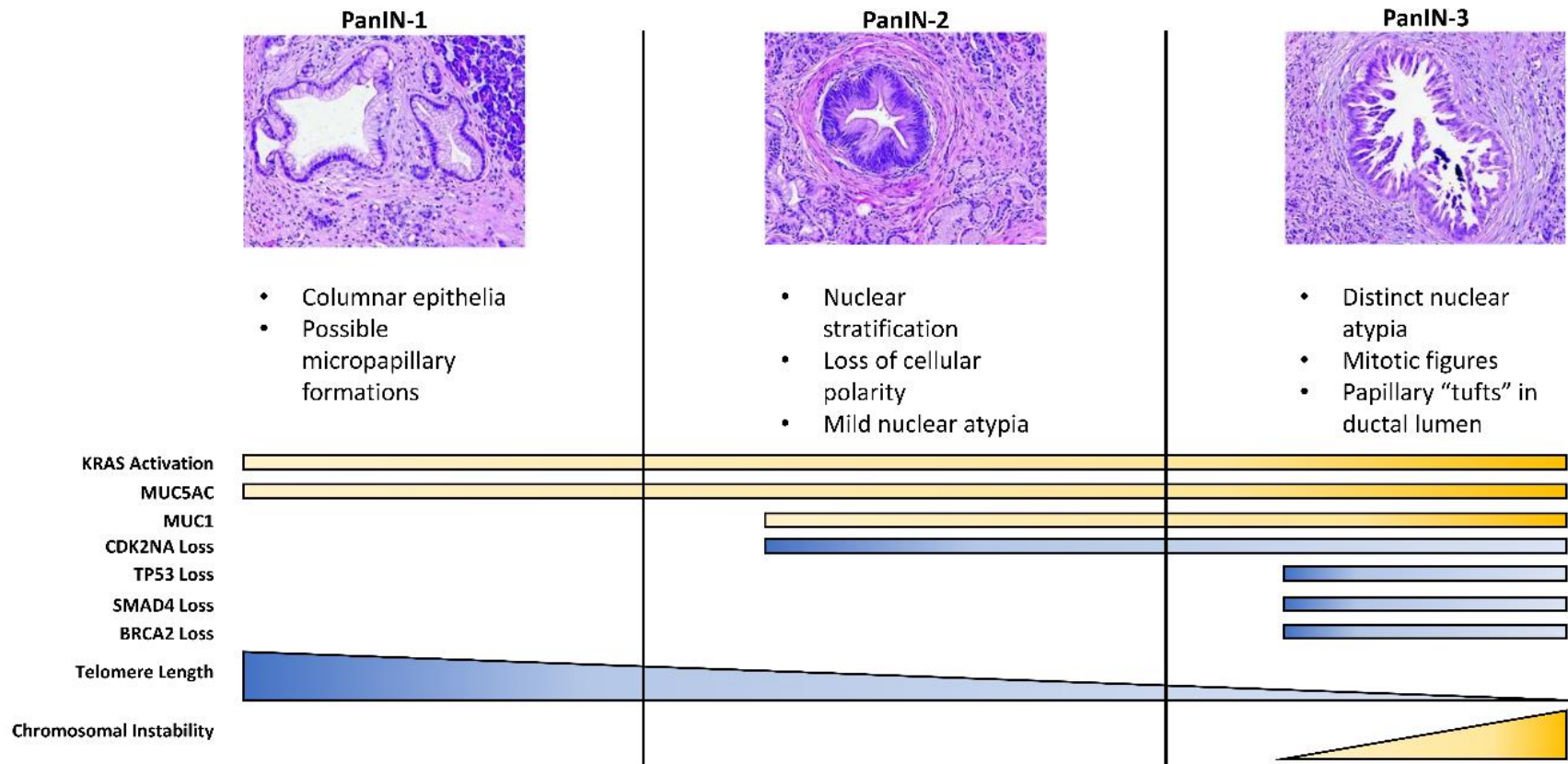
Figure 2: Genetic, Molecular and Morphological Hallmarks of PanIN Lesion Progression. The accumulation of somatic mutations, genetic superstructure alterations and increasingly distorted papillary architecture define the progression from PanIN-1 to PanIN-3 lesions and eventually pancreatic ductal adenocarcinoma.

Symptoms, like the genetic causes of pancreatic cancer, are heterogenous and show large patient-to-patient variability. Complicating early detection efforts, the disease initially causes few if any symptoms until it has progressed to an advanced stage[65]. Those patients who do present with early symptoms often describe non-specific complaints like bloating, nausea and back pain which are attributable to a number of more benign conditions[66]. Clinical manifestations presenting with the highest frequency at the time of pancreatic cancer diagnosis are jaundice, lower back pain, weight loss, new onset diabetes, abnormal liver function and nausea[67]. Jaundice-like symptoms are associated with PDAC tumors originating in the head or neck of the pancreas which are more likely to cause biliary duct occlusion and thus present as painless jaundice[68]. Abdominal or back pain are more frequently associated with tumors in the pancreas body, which tend to invade local vasculature and crowd the retroperitoneal space[69]. Particularly lethal are pancreatic tail tumors, which reside in a more sparsely populated anatomical neighborhood and thus cause fewer symptoms and tend to grow unimpeded leading to a more advanced stage at diagnosis[70]. Collectively, the variation in clinical presentation challenges early diagnosis and is one of the major causative factors in the lethality of PDAC.

1.1.3 Detection and Diagnosis

Following the presentation of symptoms and the clinical suspicion of disease, pancreatic cancer is typically diagnosed using one or multiple imaging modalities followed by an invasive tissue biopsy for confirmation of primary tumor development or of metastatic spread[71]. Multi-detector computed tomography

(MDCT), which maps the abdomen via differential X-ray penetrance between tissue types, is the most common and cheapest imaging option used for clinical diagnosis and staging but can result in nephrotoxicity from radiation exposure[72]. Magnetic resonance imaging (MRI) and positron emission tomography (PET) are also used to diagnose PDAC when CT is not suitable for the patient[73]. Confirmation of diagnosis is typically established by endoscopic ultrasound-guided fine-needle aspirate (EUS/FN) with on-site cytopathological evaluation[74]. EUS/FN can also be used to monitor disease status during the course of treatment. Standard CT, MRI and PET instruments are resolution-limited at 0.5 mm, 1.5 mm and 2.5 mm, respectively, which allows them to distinguish most pancreatic tumors (3 – 7 cm), however PDAC precursor lesions often escape detection due to their small size (< 0.5 mm) and failure to contrast in comparison to normal pancreatic tissue[75–79]. Additionally, the location of the pancreas in difficult to reach retroperitoneal space challenges clinical access, meaning that precise tissue biopsies are often difficult and uncomfortable to obtain repeatedly for surveillance[80]. Unfortunately for patient outcomes, the diagnostic utility of imaging is usually after the onset of symptoms, when metastatic spread of the disease has likely already occurred. Today, screening for new onset pancreatic cancer by imaging is clinically-recommended only for a very small subset of extreme risk patients[81].

As previously mentioned, pancreatic ductal adenocarcinoma is diagnosed and staged using the TNM system which considers tumor volume, level of arterial invasion and metastasis to lymph nodes and distant sites as agreed upon by the American Joint Commission on Cancer. TNM classifications are used to sort

patients into one of 5 stages ranging from I – IV, where stages I and IIA are considered resectable to borderline resectable (11%), stages IIB and III are considered borderline resectable to unresectable (37%) and stage IV is considered unresectable and metastatic (52%)[82]. Stage at diagnosis is a critical determinant of patient outcomes, where resectable pancreatic cancers have a 42% 5-year survival rate while unresectable, metastatic PDAC, which tends to metastasize to the liver, lymph nodes, lung, peritoneum and bone, has an abysmal 3% 5-year survival[83]. The current screening shortcomings and subsequently advanced stage of disease at detection for most PDAC patients – resulting in the poorest patient survival statistics amongst any cancer – highlight the critical need for novel early detection methods.

1.1.4 Pancreatic Cancer Biomarkers

CA19-9, also known as the sialyl-Lewis A (sLe^A) (NeuAc[α2,3]Hex[β1,3]HexNAc[α1,4]Fuc) motif, is to date the only FDA-approved biomarker for pancreatic cancer[84]. Elevated in ~70% of PDAC patients, this epitope realizes its utility as a prognostic indicator for judging a patient's response to therapy. In pancreatic ductal adenocarcinoma patients with abnormal CA19-9, serum CA19-9 levels correlate directly with tumor burden and thus changes in disease severity are reflected by the biomarker making it a useful surveillance tool[85]. However, because CA19-9 is associated with other cancers and non-cancer maladies like pancreatitis, cystic fibrosis and liver disease, it lacks the specificity for early detection or diagnosis[86]. The clinical CA19-9 immunoassay detects the sLe^A epitope on a variety of protein carriers, the most well-characterized of which

13

are the mucins MUC1, MUC5AC and MUC16, cluster of differentiation 44 (CD44), galectin 3 binding protein (LGALS3BP), bile globular membrane (BGM), apolipoprotein B-100, kininogen and apolipoprotein E[87–89]. CA19-9 is a sialylated member of the Lewis histo-blood group antigens, which are similar to the well-known ABO antigen group for their roles in immunity, infection, cardiobiology and metabolism[90,91]. Lewis blood antigens generally fall into two types, Lewis A and Lewis B, which are determined by an individual's Lewis (Fucosyltransferase 3, FUT3) and Secretor (Fucosyltransferase 2, FUT2) enzyme expression status, respectively[92]. The Lewis antigens, their associated synthesis enzymes and their defining linkages are shown in Figure 3. L^{A+B+} and L^{A+B-} individuals have overall higher expression of the CA19-9 epitope, whose biosynthesis is critically dependent on fucosylation by FUT3. Studies have shown that L^{A-B-} persons – around 5% of the population – often have more severe PDAC, although the association of total Lewis negative status with non-cancer-related pulmonary health abnormalities may explain their poorer outcomes[93–95]. Unfortunately for patients, CA19-9 is no longer considered solely a biomarker of pancreatic cancer but is now recognized as an active promotor of disease progression and severity. A 2019 study in mice which overexpressed CA19-9 through transduction of FUT3 and β1,3-galactosyltransferase 5 (B3GALT5) – the main two enzymes responsible for sLe^A biosynthesis – demonstrated rapid development and increased severity of pancreatitis[96]. Specifically, CA19-9 attached to fibulin 3 had increased interaction with the epidermal growth factor receptor (EGFR) which is both necessary and
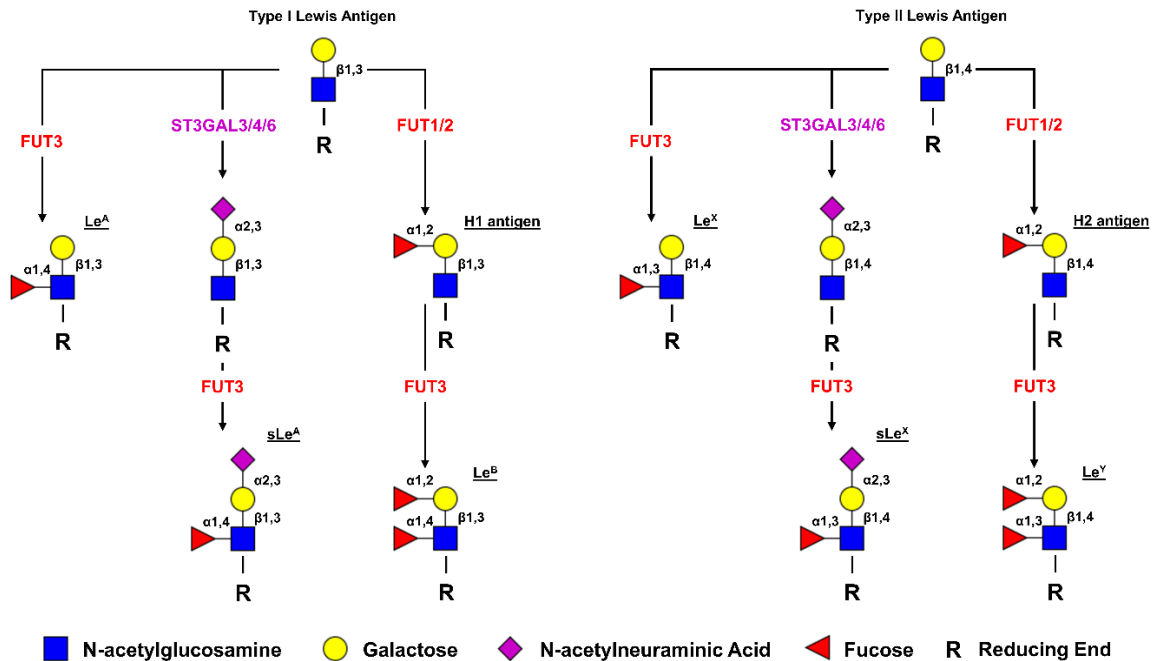
Figure 3. CA19-9 and the Lewis Antigens: Structure and Synthesis. The Lewis antigens, defined initially by the galactose – N-acetylglucosamine linkage into types I (β1,3) and II (β1,4), are further decorated by various fucosyl- and sialyltransferases to produce the full histo-blood group spectrum including CA19-9. Adapted[97].

sufficient to induce pancreatitis and can initiate neoplastic transformation to pancreatic cancer[98,99]. Additionally, expression of CA19-9 in KRAS-transgenic mice from the same study worked synergistically with the oncogene to accelerate the development of pancreatic cancer. Besides interaction with EGFR, the CA19-9 epitope has been shown to drive PDAC metastasis through E-selectin-mediated initiation and can promote tumor growth by increasing local microvessel density[100–102]. This shift in perspective towards CA19-9 as not just a marker of but an active participant in pancreatic cancer has sparked interest in therapies targeting the epitope itself[103–106]. Use of humanized monoclonal antibodies towards CA19-9 during surgical resection has recently shown success in decreasing recurrence rates for pancreatic cancer patients[107].

A more recently developed biomarker candidate, the sialylated Type 1 Type 2 LacNAc termed sTRA, occurs in a majority of pancreatic tumors where it often but not always overlaps with CA19-9 expression. This marker has demonstrated increased performance over CA19-9 in the detection of PDAC and together these antigens are in development for a new clinical surveillance panel[108–110]. Another marker, CA-125 (MUC16), is a heavily glycosylated mucin glycoprotein which is elevated in pancreatic cancer patients but faces the same challenges as CA19-9 due to a lack of specificity and association with other cancers[111,112]. The severity of pancreatic cancer and the dearth of adequate markers has made the search for new PDAC markers a popular field of research. A recent review summarized over 300 pancreatic ductal adenocarcinoma biomarker candidates and associated factors which include a variety of serum glycoproteins, glycolipids, growth factors

and chemokines, lncRNAs, miRNAs, exosomes and ctDNA as well as urinary, cystic, salivary, biliary, and fecal-associated molecules[113]. It is apparent to both clinicians and researchers that any sole biomarker will likely lack the sensitivity and specificity to detect PDAC amongst the general population, suggesting that a multi-marker panel, in conjunction with associated clinical data, may lead to better diagnostic efficacy. A 2020 study tested 2047 combinations of 11 cancer-associated markers with increased prevalence in pancreatic cancer which resulted in a 6-pannel marker consisting of Apolipoprotein A1, CA-125, CA19-9, carcinoembryonic antigen (CEA), Apolipoprotein A2, and transthyretin (TTR) that was able to diagnose PDAC with a sensitivity of 0.93 and a specificity of 0.96 for a total area under the curve (AUC) of 0.993[114]. As more and more sensitive biomarkers, panels and algorithms are discovered it is foreseeable that larger at-risk subsets of the general population may be able to be preemptively screened for the early development of PDAC.

1.1.5 Standard of Care

For patients diagnosed with pancreatic ductal adenocarcinoma, those who are able to undergo successful surgical resection have the best survival statistics by a wide margin. Despite this, surgical intervention is possible in less than 20% of PDAC cases as those patients with locally advanced or metastatic disease are typically not eligible for tumor resection[115]. In rare cases tumor extirpation from the pancreas can be performed, but the majority of surgical interventions in PDAC are pancreaticoduodenectomies (Whipple's Procedure) in which the head of the pancreas and parts of the stomach and gall bladder are removed and the

remaining stomach, bile duct and pancreas tail are fused directly to the small intestine[116,117]. Other interventions include distal and total pancreatectomies when the patient needs a large amount or all of the pancreas removed to achieve an R0 margin, but these procedures are likely to result in diabetes mellitus and are less commonly recommended[118]. In the past decade the definitions of resectability have been fluid, with many borderline resectable (BLR) PDACs evaluated on a case-by-case basis[119]. Resectability is typically defined as minimal to no tumor contact with major vessels, however BLR patients may have venous involvement and/or partial arterial involvement and still be considered eligible[120].

Because survival in pancreatic cancer is so heavily associated with eligibility for surgical resection, many clinical management strategies focus on using neoadjuvant chemotherapeutic and radiological treatments to shrink tumor volume to within surgically appropriate margins[121]. Gemcitabine in combination with other cytotoxic agents such as Paclitaxel, Tegafur and Erlotinib has long been considered the gold standard of care for advanced PDAC cases and thus has been used neoadjuvantly as well[122,123]. In recent years, a combination of drugs including Folinic acid, 5-fluorouracil, irinotecan and oxaliplatin (FOLFIRINOX) has shown improved efficacy in managing PDAC over Gemcitabine, although it was associated with increased toxicity[124,125]. The main chemotherapeutic agents in both FOLFIRINOX and Gemcitabine combinations act as both DNA damaging agents and as antimetabolites to target the susceptibility of cancer cells to growth phase or cellular division disruption[126]. A similar suite of therapies is also used in an adjuvant fashion to prevent recurrence in patients who have undergone surgical

resection and is associated with improved survival[127]. Interventional radiology by radiofrequency ablation (RFA) or irreversible electroporation (IRE) is also commonly used as an alternative to or in conjunction with chemotherapy in BLR cases[128]. Unfortunately for the majority of patients who are diagnosed at a locally advanced or metastatic stage, surgical resection is not an option. In these cases FOLFIRINOX, Gemcitabine and other chemotherapeutics are used in a palliative fashion to prolong patient survival and improve quality of life[129]. The importance of discovering PDAC at a resectable stage, in terms of positive clinical outcomes, highlights the need for novel early detection strategies. Figure 4 summarizes diagnoses and their associated treatment sequences, as well as survival statistics, in pancreatic ductal adenocarcinoma.

1.2 N-linked Glycosylation

1.2.1 N-glycan Biosynthesis

Glycosylation is the enzymatic addition of carbohydrate residues (or glycans) to a biomolecule, most commonly to a protein or lipid. These sugars can either be attached as monomers or can be linked together to form long, complex chains in a non-template driven synthetic manner. Individual sugar moieties used to produce glycans include, but are not limited to, glucose (Glc), mannose (Man), galactose (Gal), fucose (Fuc), N-acetylglucosamine (GlcNAc), N-acetylgalactosamine (GalNAc), and N-acetylneuraminic acid (Neu5Ac)[130]. Relevant to glycan synthesis, these carbohydrate monomers exist intercellularly
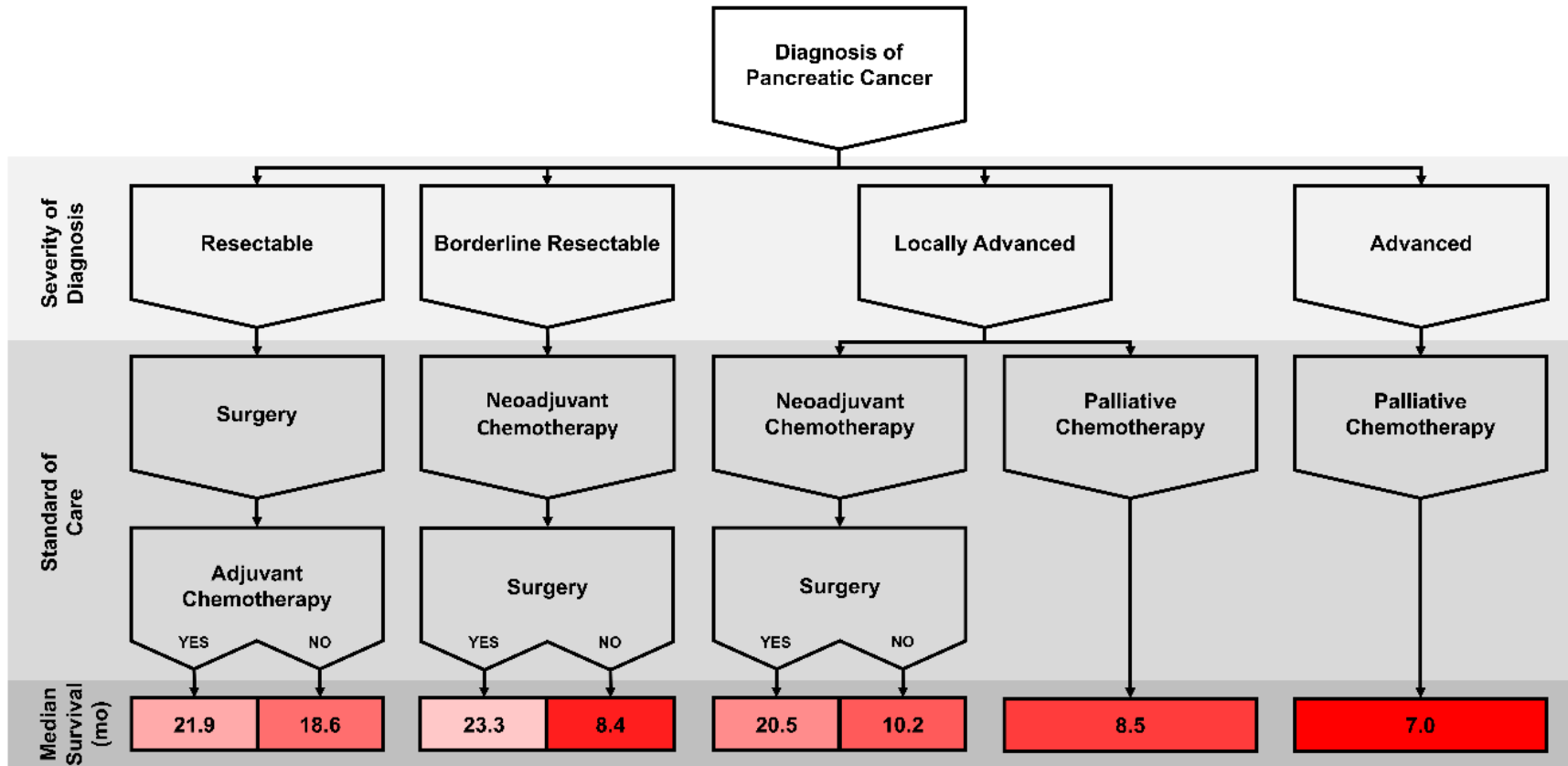
Figure 3. Treatment Sequence and Survival Outcomes as a Function of Diagnosis in PDAC. Diagram of the different treatment options for those diagnosed with pancreatic ductal adenocarcinoma. Survival is directly correlated with resectability at diagnosis. Adapted[131].

as nucleotide sugars, synthesized de novo from dietary monosaccharides or via recycling and salvage pathways[132]. Together chains of these sugars form a dense carbohydrate scaffold on the cell's outer membrane known as the glycocalyx[133]. This dynamic surface is comprised of multiple subclasses of glycosylated molecules, namely N- and O-linked glycoproteins, glycolipids, glycosaminoglycans (GAGs) and proteoglycans[134]. The glycocalyx governs interactions with the local microenvironment by acting as a barrier, filter, substrate and active chemical or enzymatic agent. Glycosylated proteins and lipids in this surface are implicated in cell–cell communication, signal transduction, secretion, interactions with the immune system, cellular migration and adherence, proliferation and regulation amongst other processes[135,136]. Critically, the glycocalyx is sensitive to the temporal physiological state of the cell and thus reflects internal cellular health[137]. Accordingly, it is well known that the composition and structure of the glycocalyx is regulated in response to a variety of diseases[138].

N-linked glycans, attached to asparagine residues as part of N-X-S/T motif sites on the glycoprotein backbone, are able to play diverse cellular roles due to their structural heterogeneity (Figure 5). The biosynthesis of N-linked glycans is dependent on a discrete number of glycosidases and glycosyltransferases, as well as their sugar monomer substrates, the local concentrations of which often determine which classes of N-glycans are expressed[139]. Initially, synthesis begins on the cytosolic face of the endoplasmic reticulum, where a dolichol phosphate anchor acts as the attachment point for the addition of successive GlcNAc,
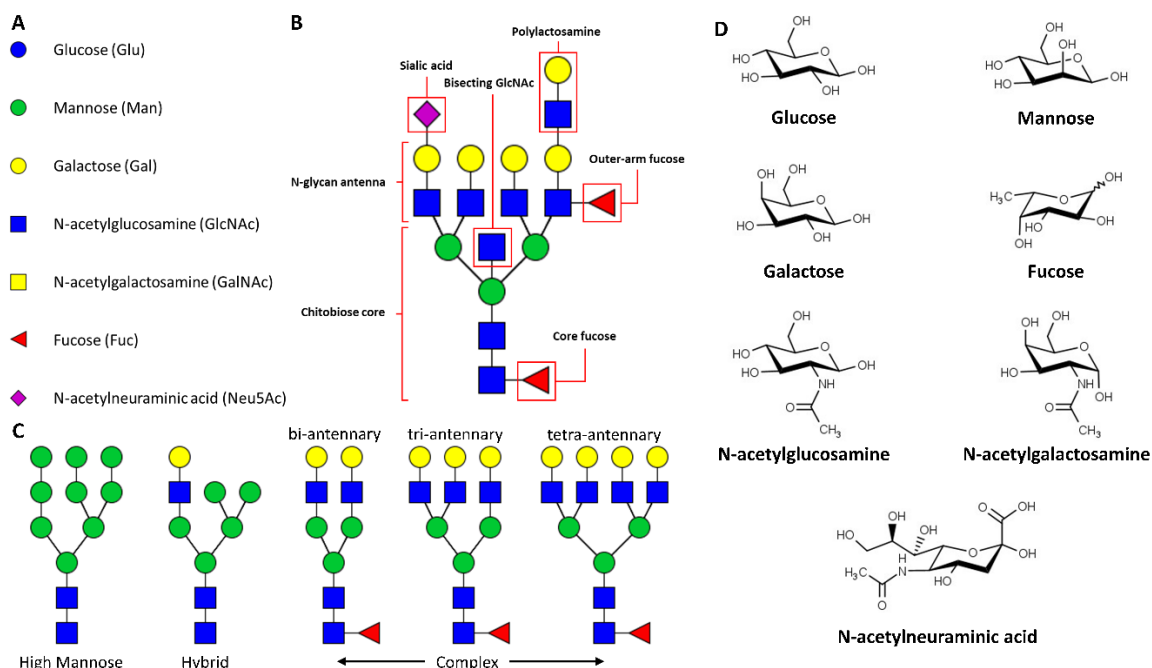
Figure 5. N-glycan Structural Classes, Motifs and Individual Sugar Monomers. A) cartoon representations of the various sugar monomers which N-glycans comprise. B) common N-glycan structural motifs referred to in this dissertation. C) N-glycan structural classes including high mannose, hybrid and bi-, tri- and tetra- antennary complex glycans. D) Precise chemical structures for the cartoonized sugar monomers in A.

mannose and glucose sugars catalyzed by a series of n-acetylglucosaminyltransferases, mannosyltransferases, and glucosyltransferases, respectively, to form an initial Glc3Man9GlcNAc2 chain[140]. During the formation of this precursor glycan, a flipase inverts the growing glycan into the ER interior for the addition of the final sugars[141]. Once formed, this proto-N-glycan is transferred by oligosaccharlyltransferase (OST) co-translationally onto a newly synthesized protein, linked to an asparagine residue which must be followed by an X-S/T sequence in which X cannot be proline[142].

The covalent modification of newly synthesized proteins with this glycan initiates one of the most important biological processes regulated by N-linked glycans – protein folding. Specifically, cells use the Glc3Man9GlcNAc2 glycan precursor as a molecular indicator of successful protein folding events[143]. Sequential trimming of the three terminal glucose monomers occurs concomitantly as the protein transitions from a nascent amino acid chain to its fully folded conformation, assisted by the lectin-like protein chaperones calnexin and calreticulin which bind the monoglucosylated, truncated form of the precursor glycan[144]. The final glucose on the partially trimmed Glc1Man9GlcNAc2 glycan is routinely cycled on and off until the protein is folded successfully, at which point a mannosidase removes a single terminal mannose and the fully folded protein is secreted to the Golgi via coated vesicle[145].

In the Golgi, the Man8GlcNAc2 glycan is further trimmed by a series of mannosidases before glycosyltransferases are able to synthesize a complete N-glycan (Figure 6). This process begins with the β1,2/4 addition of N-
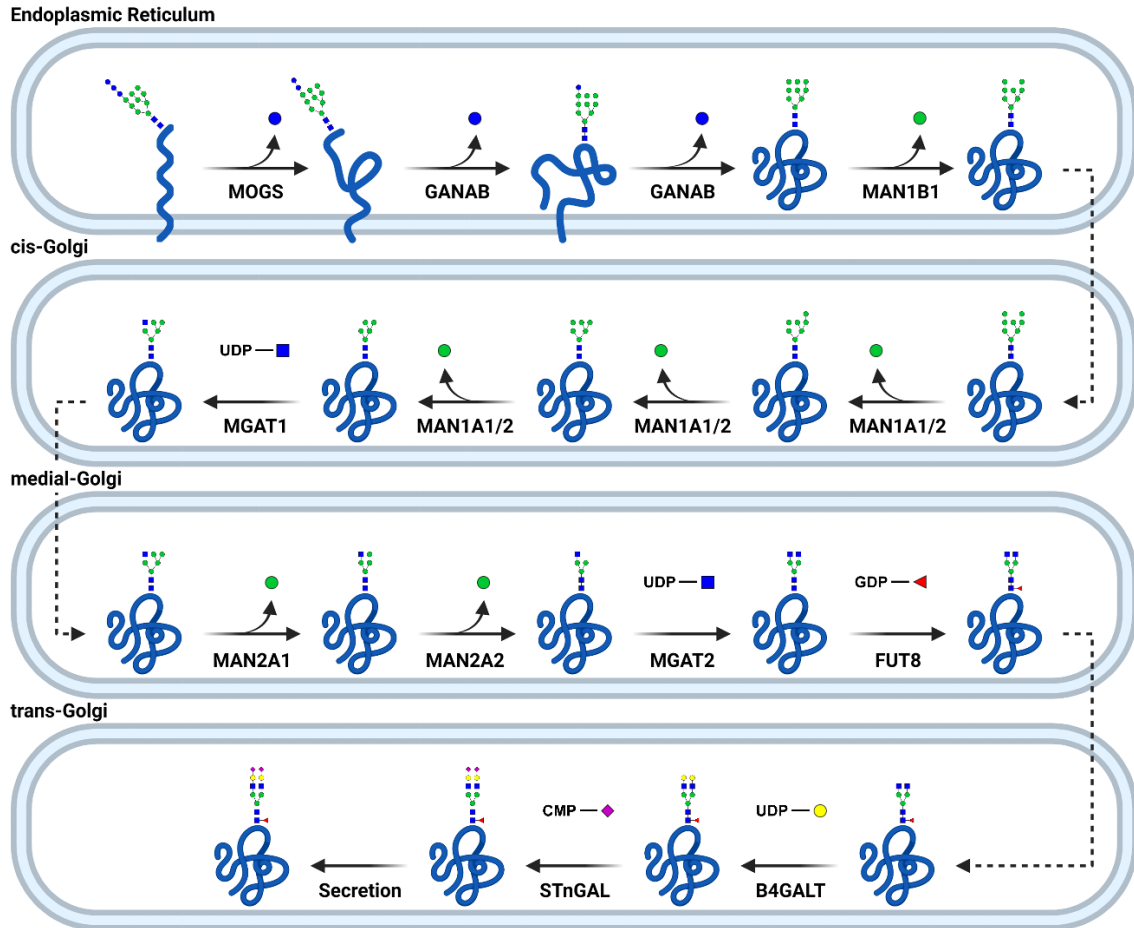
Figure 6. N-glycan Biosynthesis in the Endoplasmic Reticulum and Golgi. MOGS, α-glucosidase I; GANAB, α-glucosidase II; MAN1B1, ER α-mannosidase I; MAN1A1/2, α-mannosidase I; MGAT1, α-1,3-mannosyl-glycoprotein 2-β-N-acetylglucosaminyltransferase; UDP, uridine diphosphate; MAN2A1, α-mannosidase II; MGAT2, α-1,6-mannosyl-glycoprotein 2-β-N-acetylglucosaminyltransferase; FUT8, fucosyltransferase VIII; GDP, guanosine diphosphate; B4GALT, β-1,4-galactosyltransferase; STnGAL, β-galactoside α-2,3-sialyltransferase or β-galactoside α-2,6-sialyltransferase; CMP, cytidine monophosphate.

acetylglucosamine (GlcNAc) residues to the N-glycan chitobiose core by the MGAT enzyme family, which are then further substituted with a galactose (Gal) monomer by GALT family enzymes[146]. B1,4-linked Gal-GlcNAc units constitute N-glycan antennae, the number of which on an individual glycan define the biantennary (2), triantennary (3) and tetraantennary (4) subclasses of complex N-glycans[147]. N-acetylglucosamine residues are also in some cases added to the central mannose of the chitobiose core as bisecting GlcNAc by a specialized β-N-acetylglucosaminyltransferase, MGAT3[148]. Additional Gal-GlcNAc subunits can be added to one or more antennae of a tetraantennary N-glycan to form what are known as poly-N-acetyllactosamine (LacNAc) extensions[149]. Complex N-linked glycans may be decorated with fucose residues by a discrete set of enzymes with differing affinities for an N-glycan's antennae or core GlcNAc residue. FUT8 is the sole enzyme responsible for core fucosylation, where fucose is attached α1,6 to the 1st GlcNAc residue covalently linked to the amino acid backbone[150]. Outer arm fucose residues are α1,3 or α1,4 linked to GlcNAc monomers in N-glycan antennae by a large number of fucosyltransferases[151]. N-linked glycan branches are often capped with a terminal neuraminic acid (sialic acid) residue, which generally exist as either α2,3 or α2,6 linkage isomers installed by specialized sialyltransferases[152]. It is important to note that N-glycan biosynthesis does not occur via sequential installation of sugar monomers in a biologically pre-specified order, rather these reactions exist concomitantly with glycosyltransferases and glycosidases competing for substrates and access. The resulting N-glycan is thus dependent on the specific temporal cellular conditions under which it was synthesized, rather

than being encoded by the cell. A summary of complex N-glycan biosynthesis enzymes and their associated modifications is provided in Figure 7.

Although the consensus amino acid motif for N-linked glycans has been well characterized, there are outstanding questions in the field regarding N-X-S/T site occupancy and glycan heterogeneity at the same site. Site occupancy is often a function of position within the amino acid backbone in relation to a protein's secondary structure. As the nascent peptide chain beings to fold, N-X-S/T sites near turns in β-sheets or between secondary superstructural features are more accessible to glycation by OST and thus are more often N-glycosylated[153]. Additionally, the X amino acid in the N-glycosylation motif critically affects the ability of OST to modify the growing protein. Bulky, hydrophobic amino acid side chains at the X position sterically hinder enzyme access and can inhibit glycan transfer while negatively charged glutamate and aspartate actually increase the affinity of OST for the N-X-S/T site[154]. As previously mentioned, proline at the X position confines the amino acid sequence to unreceptive conformations and prevents the interaction between arginine and the proteoglycan entirely[155]. While secondary structure is more likely to affect N-glycan site occupancy, protein tertiary structure exerts outsized influence on the heterogeneity of the individual N-glycan occupying the site. The 3D conformation of the fully folded protein determines glycosyltransferase and exoglycosidase access to the precursor N-glycan, limiting the potential mature glycan structures at any one given site. More exposed N-X-S/T sites can accommodate larger, multiply branched, fucosylated and or sialylated N-glycans which cannot be synthesized at less accessible locations on

26
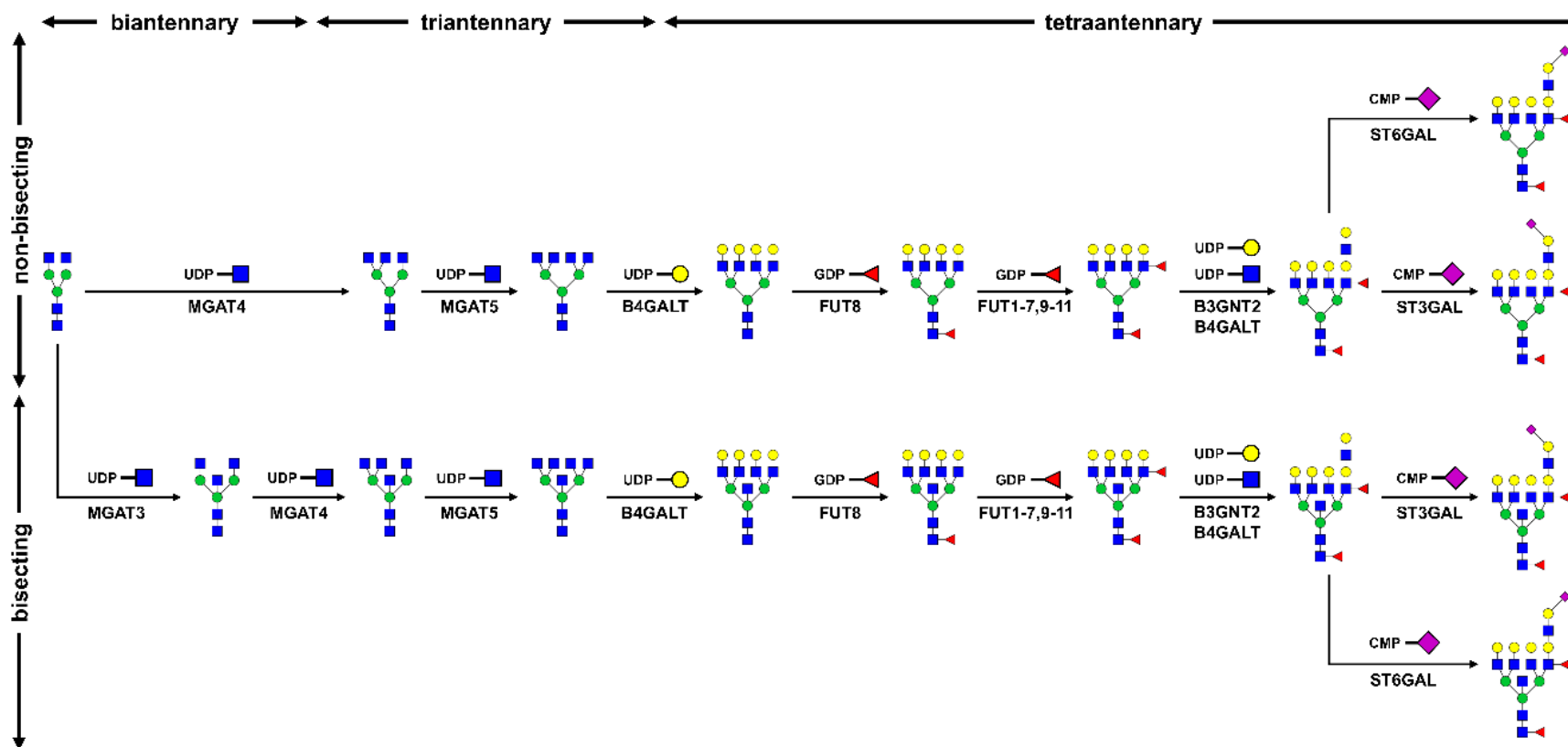
Figure 7. Glycosyltransferases Involved in the Synthesis of Complex N-glycans. MGAT3, β-1,4-mannosyl-glycoprotein 4-β-N-acetylglucosaminyltransferase; MGAT4, α1,3-mannosyl-glycoprotein 4-β-N-acetylglucosaminyltransferase; MGAT5, α1,6-mannosyl-glycoprotein 6-β-N-acetylglucosaminyltransferase; B4GALT, β-1,4-galactosyltransferase FUT8, fucosyltransferase VIII; ST3GAL, β-galactoside α-2,3-sialyltransferase; ST6GAL, β-galactoside α-2,6-sialyltransferase; UDP, uridine diphosphate; GDP, guanosine diphosphate CMP, cytidine monophosphate.

the protein[156]. Complicating analysis, most glycoproteins exhibit micro-heterogeneity at each individual N-glycan site, where otherwise identical copies of the same protein may have radically different glycoforms[157]. This is once again likely due to temporal changes in enzyme concentrations and substrate availability during N-glycan maturation.

1.2.2 The Biological Role of N-glycosylation

As a class of post-translational modifications, glycans have biological utilities which are less specific to individual subtypes but are more broadly a function of the physical and chemical properties of carbohydrates. The hydrophilicity of N-glycans and other bulky glycans modifications often contributes to the solubility of a protein and can be protective against proteolysis[158]. Additionally, N-glycans on the protein surface may intrinsically enhance the kinetic and thermal properties of proteins by stabilizing their underlying energy landscapes[159]. In the case of immunoglobulin G (IgG) and other dimerized proteins, favorable hydrophobic interactions between glycans on individual protein monomers enhance the overall stability of the quaternary structure[160,161].

N-glycans change the overall 3D protein conformation and are commonly a part of protein – protein interplay where they may serve as a partial to full epitope for recognition by interactors or otherwise indirectly stabilize the complex[162]. Lectins, a class of carbohydrate-binding proteins, can directly recognize whole or partial N-glycans as part of cell – cell self-recognition events, glycoprotein trafficking, ECM adhesion and signal transduction amongst other biological purposes[163]. Accordingly, changes in N-glycan structural elements by the action of

glycosyltransferases and exoglycosidases modify the N-glycan as a spatial epitope and consequently the types of lectins with which a glycoprotein may interact – thus altering its biological function. Rather than an in-depth discussion of lectins which is outside the scope of this dissertation, a summary table of N-glycan-associated lectins and their biological functions is provided in Table 1.

Related to their interaction with lectins and other carbohydrate-binding proteins, N-linked glycans play a crucial role in protein trafficking within the cell[164]. Studies have shown that the N-glycosylation of recombinant GFP in HeLa cells substantially reduces Golgi residence time, suggesting that N-glycans may act as a signal for exocytic trafficking at the *trans*-Golgi[165]. Intracellular translocation of sensitive lysosomal enzymes is governed by N-glycosylation, where 6'-phosphoyrlated oligomannose N-glycans are recognized by the mannose-6-phosphate receptor in the Golgi and subsequently trafficked to the lysosome[166,167]. N-glycosylation can even facilitate polarized sorting, where N-glycans are recognized by chaperone proteins to traffic membrane glycoproteins to the apical face of epithelial cells as opposed to the basolateral surface[168]. N-glycan associated congenital disorders of glycosylation (CDG) – a collection of hereditary N-glycan processing and modification diseases – in some cases result from dysregulated protein sorting, secretion or intracellular trafficking[169].

More often than an "on" or "off"-like switch, N-linked glycans exhibit a tuning effect on glycoprotein function, where the addition of different modifications like fucosylation, branching or bisecting GlcNAc modulates a protein's biological

Table 1. N-glycan-Binding Lectin Classes

Lectin Class	Glycan Epitope	Cellular Location	Functions
Calnexin	Glc1Man9	ER	ER protein sorting
C-type	Gal, GalNAc	Cell membrane, extracellular	Innate immunity (collectins), cell adhesion (selectins)
F-box Lectins	GlcNAc	Cytoplasm	Misfolded glycoprotein degradation
Ficolins	GlcNAc, GalNAc	Cell membrane, extracellular	Innate immunity
F-type	Fuc	Extracellular	Innate immunity
Galectins	B-galactoside	Cytoplasm, extracellular	ECM glycan crosslinking
Siglecs	Sialic acids	Cell membrane	Cell adhesion
Intelectins	Gal	Cell membrane, extracellular	Innate immunity, embryogenesis, fertilization
M-type	Man8	ER	Misfolded glycoprotein degradation
P-type	Man-6-P	Golgi	Lysosomal enzyme targeting, glycoprotein trafficking
R-type	Mannose	Golgi, cell membrane	Hormone turnover, glycoprotein trafficking

ER, endoplasmic reticulum; ECM, extracellular matrix; Man-6-P, mannose-6-phosphate; Adapted[170].

activity level, association with other proteins or stability within its microenvironment. These three functions intersect in the case of EGFR. Studies have shown that when N-glycans on EGFR are core fucosylated, the receptor is stabilized in the plasma membrane which allows it to form nanodomains with other EGFR receptors[171]. These nanodomains increase the signaling activity of EGFR and thus its downstream processes[172]. Inhibition of core fucosylation accordingly destabilizes the receptor, prevents its association with other EGFR and decreases signaling intensity[173]. The normal biological functions of N-linked glycans, with their capacity to regulate cellular processes, are often implicated in the development, maintenance and progression of disease.

1.2.3 N-glycans in Cancer and Other Diseases

It is now well understood that N-glycosylation changes are not only a hallmark of cancer but are active drivers of neoplastic transformation, growth, survival, immune evasion and metastatic escape[174]. N-glycan modifications like branching, fucosylation, sialylation, bisecting GlcNAc and poly LacNAc extensions have a diverse yet sometimes overlapping set of biological functions, which in cancer are frequently driven to extremes. Increased nucleotide sugar availability due to the Warburg metabolic effect and elevated glycosyltransferase expression driven by oncogenic signaling often results in the synthesis of large, multiply branched, fucosylated and sialylated N-glycans which typify malignant disease[175,176].

Branched N-glycans, specifically the tetraantennary class synthesized by β-1,6-N-acetylglucosaminyltransferase V (MGAT5), are associated with tumor

progression and metastasis[177]. Deletion of MGAT5 production in a *Mgat5*^{-/-} mouse model reduced N-glycan branching and subsequently suppressed mammary tumor growth and metastatic potential by decreasing focal adhesion signaling[178]. Many cancers share this phenotype, where MGAT5 overexpression positively modulates cell-cell adhesion events leading to an increased likelihood of metastasis[179,180]. Tetraantennary N-glycans resulting from increased MGAT5 expression also serve as the host glycan for polylactosamine (poly LacNAc) extensions, which are associated with breast and other cancers[181]. These LacNAc epitopes are known leukocyte suppressors and in cancer may facilitate aspects of immune evasion[182]. Aberrant fucosylation, both core and outer arm, similarly drives multiple aspects of cancer biology. As previously mentioned, core fucosylation directly stabilizes EGFR receptors and leads to increased proliferative signaling in liver and other cancers amongst other functions[183]. Outer arm fucosylation has been shown to be increased in patient sera from breast, lung and ovarian cancer patients, which may be a signature of Lewis-antigen driven pro-oncogenic affects as described for CA19-9[184]. Bisecting GlcNAc residues are also heavily implicated in cancer. Using glioma cells as a model, researchers in Osaka, Japan showed that overexpression of MGAT3 led to increased extracellular signal-regulated kinase (ERK) proliferative signaling[185]. Conversely, bisecting GlcNAc is more often recognized as an inhibitor of growth signaling, where the addition of bisecting GlcNAc residues to cell surface receptors can have protective effects. Bisecting GlcNAc has been shown to increase receptor endocytosis leading to decreased growth signaling and may decrease the affinity of MGAT5 for bisecting

glycans[186,187]. The role of sialic acids, in cancer and in health, will be explored in greater detail in later sections.

While the pro-oncogenic functions of N-glycans are often non-specific to a particular cancer, the molecular and genetic drivers of each individual cancer subtype result in unique glycosylation abnormalities. For the focus of this review, a special emphasis will be placed on mass spectrometry-analyzed N-glycosylation hallmarks. These investigations have revealed distinct N-glycosylation patterns across tissue subtypes, N-glycan structural motifs associated with particular cancers as well as N-glycan ions whose detection specifically delineates healthy versus diseased tissue or discriminates between cancer stages. A summary of these cancer-associated N-glycan phenotypes is provided in Table 2.

Perhaps no other disease has been more frequently associated with N-glycosylation changes than cancers of the liver, specifically hepatocellular carcinoma (HCC)[188–190]. Interest in liver cancer glycosylation stems from initial studies of alpha-fetoprotein (AFP), which revealed core fucosylation as a critical indicator of hepatic dysfunction in HCC[191,192]. Discovered later, fucosylated Golgi protein 73 (GP73) has been shown to be up to three times more sensitive than AFP for the detection of HCC[193–195]. Fucosylation, amongst other structural motifs, have since been associated with a number of other circulating glycoproteins from patients with liver cancer[196–199]. To this end multiple N-glycan imaging mass spectrometry (IMS) analyses have been directed toward HCC tissue cohorts in hopes of linking in situ expression of N-glycan species directly with those found in circulation. In 2018 West et al. surveyed the N-glycome of a large HCC cohort

Table 2. Cancer-Associated N-glycan Changes Revealed by Mass Spectrometry.

Cancer	Study	Disease-associated N-glycans
Breast	Scott 2019[181]	Polylactosamines ↑ (HER2, TN)
	Herrera 2019[201]	Tetraantennary LacNAc ↑ (poor survival)
	Scott 2019[202]	Sialylation ↑ Fucosylation ↓ (necrosis)
	Angel 2019[203]	Hex9HexNAc2 ↑
Colorectal	Holst 2016[204]	Sialylation ↑
	Heijs 2019[205]	High Mannose ↑
	Boyaval 2020[206]	High Mannose ↑, Sialylation ↑
Lung	Drake 2017[207]	High Mannose ↑, Hex6HexNAc2 ↑
	Carter 2020[208]	High Mannose ↑ (hyperplasia), Fucosylated Biantennary ↑ (hyperplasia)
Liver	Powers 2014[209]	Hex7HexNAc6 ↑, Hex8HexNAc2 ↑
	Powers 2015[210]	Hex7HexNAc6 ↑, Core Fucosylation ↑
	West 2018[200]	Hex7HexNAc6 ↑, Branching ↑, Fucosylation ↑ (poor survival)
	Angel 2019[203]	Afucosylated bi-/triantennary ↑, Hex9HexNAc2 ↑
	West 2020[211]	Core Fucosylation ↑ (poor survival)
	Black 2020[212]	Hex3dHex1HexNAc4 ↑ (cirrhosis), Hex5HexNAc4NeuAc2 ↑ (cirrhosis)
Ovarian	Everest-Dass 2016[213]	High Mannose ↑
	Briggs 2019[214]	Hex9HexNAc2 ↑ (stage III), Fucosylation ↑ (stage III), Bisecting GlcNAc ↑ (stage III), Sialylation ↑ (stage III)
Pancreatic	Powers 2014[209]	Biantennary ± Fucose ↑ (fibrosis), Undecorated ↑ (necrosis)
	Powers 2015[210]	Biantennary ↑ (fibrosis)
	McDowell 2020[215]	Fucosylation ↑, Branching ↑ Bisecting GlcNAc ↑, Sialylation ↑, Polylactosamines ↑ (tumor margin), Undecorated ↑ (necrosis), High mannose ↓
Renal	Drake 2019[216]	Polylactosamines ↑, Branching ↑, Outer-arm Fucosylation ↓, Hex5dHex1HexNAc4NeuAc1 ↑ (fibrillar capsule)

↑, increased expression relative to normal healthy tissue; ↓, decreased expression relative to normal healthy tissue; () association with a specific disease or tissue subtype.

along with cirrhotic and non-transformed tissue samples[200]. Highly branched N-glycans with one or more fucose modification were expressed abundantly in HCC samples while in cirrhotic and adjacent normal tissues their expression was detected minimally or not at all. A later orthogonal analysis confirmed that the majority of the detected N-glycans with at least one fucose residue in the HCC TMA, especially those associated with poor survival, are core-fucosylated[211].

The role of N-glycosylation in the development, maintenance and progression of breast cancer has been extensively studied, but there has been limited translation of results to clinical or diagnostic applications[217]. In 2018, in situ analyses of breast cancer tissue microarrays (TMAs) and whole tissue sections by matrix-assisted laser desorption ionization imaging mass spectrometry (MALDI-IMS) revealed increases in polylactosamine containing N-glycans specific to the aggressive human epidermal growth factor receptor 2 (HER2) and triple negative (TN) subtypes. This finding has been corroborated by an orthogonal study utilizing MALDI-IMS which implicated tetra-antennary N-glycans containing just a single N-acetyllactosamine branch with poor survival outcomes in breast cancer patients[201]. Interestingly, mass spectrometry has revealed patterns of N-glycosylation which are specific to regions of necrosis in breast cancer tissues[202]. N-glycans localizing to these areas of cellular remnants were uniquely sialylated and lacked fucose residues when compared to the high mannose and multiply branched structures of the tumor tissue. Similar patterns have been observed in other cancer types, suggesting a possible role for N-glycosylation in the pathways leading to cellular death[218].

High mannose N-glycans, shown to be increased in breast tumors, have also been detected in the sera of breast cancer patients using MALDI-MS[219]. In this context, the Man9GlcNAc2 structure is especially elevated, which posits the incomplete trimming of pre-Golgi N-glycan intermediates as a feature of breast cancer. Other analyses of N-glycosylation in breast cancer serum have detected N-glycan signatures which delineates recurrent versus non-recurrent cancer, stage 1 breast cancer from healthy controls and signatures specific to the lymph node invasive subtype[220,221].

In colorectal cancer (CRC), N-glycosylation plays a well-defined oncological role[222]. Studies utilizing MALDI-time of flight (TOF) MS have analyzed N-glycans from CRC tissue homogenate, various CRC cell lines and patient serum[223–225]. These studies detected a wide variety of N-glycan structural features specific to CRC tumor tissue, including high mannose, core fucosylation, sialylation, increased branching and even sulfation. These distinctions were born out between healthy and diseased samples but also across molecular subtypes and disease stage. Elevated levels of sialylated N-glycans have been shown in CRC tissue samples[204]. A proof-of-concept study, which demonstrated both N-glycan and peptide IMS from the same tissue sections, detected high mannose N-glycans localized to tumor regions in a representative CRC sample[226]. These initial findings were solidified in 2020 by a comprehensive survey of the N-glycome of stage II CRC by IMS, which confirmed expression of sialylated and high mannose structures in cancer cells[206]. This increased expression was shown to be propagated into the surrounding stroma, suggesting the modification of N-

glycosylation in the tumor microenvironment ahead of the tumor's invasive front in advanced stage CRC.

The role of glycosylation changes in lung cancer are well known and initial studies suggest the existence of disease-specific N-glycosylation[227]. An early study which demonstrated the applicability of MALDI-IMS to N-glycan analyses featured tissue microarrays (TMAs) with lung adenocarcinoma cores matched to normal lung tissue. In these cores, high mannose N-glycan structures, especially Hex6HexNAc2, were found to be elevated[207]. Although not a direct analysis of lung cancer, a recent study employed the use of radiation to recapitulate pre-neoplastic transformation which may lead to lung cancer in rhesus macaques[208]. Areas of irradiation-induced hyperplasia in these lung samples analyzed by N-glycan IMS exhibited elevations in high mannose structures consistent with the human lung TMA cores from the aforementioned study, as well as fucosylated bi-antennary structures with and without bisecting GlcNAc residues. This elevation in high mannose N-glycans has also been observed in a MALDI-TOF MS analysis of lung adenocarcinoma patient sera across stages, positing that a further IMS evaluation of the lung cancer N-glycome may discover additional N-glycan features which map to serum expression for possible use as biomarkers[228].

Glycosylation changes in ovarian cancer were first observed in the mid 1960s[229]. Of recent interest is the translation of N-glycosylation analytical applications to clinical strategies for ovarian cancer, as N-glycans are known to be heavily involved in the oncogenesis and maintenance of this disease[214,230] Consistent with other types of cancers, a 2016 study detected increased

expression of high mannose N-glycans in ovarian cancer tumor tissue as compared to normal tissue from the same samples[213]. This same analysis also detected increases in hybrid-type structures specific to areas of intervening stroma in this cohort. N-glycans extracted and purified from FFPE ovarian cancer tissue samples for MALDI-TOF analysis by the Li group supported the specificity of high mannose N-glycan expression in ovarian tumor tissue[231]. This analysis also found that a seven-glycan panel consisting of four high mannose and three fucosylated complex structures was able to delineate epithelial ovarian cancer from healthy controls, while a similar yet distinct N-glycan panel could distinguish specific ovarian cancer grades. N-glycan IMS analyses have also been able to differentiate early- versus late-stage ovarian cancer using specific N-glycosylation signatures[232]. The high mannose N-glycan Hex9HexNAc2 was detected abundantly in stage III ovarian cancer samples as compared to stage I tissues. Additionally specific to late-stage ovarian cancer were fucosylated, bisecting and sialylated complex species. These glycosylation changes were not only detected in the whole tissue cohort analyzed in this report, but in corresponding TMAs which lends additional statistical power to these findings. Taken together these early N-glycan IMS studies suggest glycosylation changes as a feature of ovarian cancer potentially exploitable for clinical detection and surveillance of this disease.

The first publication of a standardized N-glycan MALDI-IMS workflow was demonstrated on a normal kidney tissue section which contained both medulla and cortex tissue regions[233]. Although the technology was in its infancy, the few N-glycan analytes detected were localized to specific tissue subtypes. A subsequent

analysis of FFPE murine kidneys demonstrated similar results[234]. This initial work was furthered by a more comprehensive 2020 study of clear cell renal cell carcinoma (ccRCC), which spatially profiled N-glycosylation in a cohort of normal kidney and renal cell carcinoma tissues[216]. A defining feature of healthy kidney tissue from this study was broad structural diversity between tissue subtypes, with bisecting, high mannose and fucosylated structures localized to the cortex while bi- and tri-antennary N-glycans with core fucose residues localized to medullary tissue. Interestingly, the interface between cortex and medulla also had a distinct glycosylation signature, defined by multiply-fucosylated structures which lacked bisecting GlcNAc residues. A high spatial resolution analysis from this study detected tetra-antennary N-glycans with and without sialic acid modifications specific to kidney glomeruli. These normal-associated structural features were conspicuously absent from ccRCC tumor tissue, which exhibited increased expression of tetra-antennary N-glycans with polylactosamine extensions of varying length. The fibrillar capsule surrounding a Fuhrman grade 2 ccRCC tumor was characterized by a bi-antennary, monosialylated N-glycan. N-glycan IMS findings were mapped directly to transcriptomic profiling by RNA sequencing from a prior study, which revealed altered expression of outer arm fucosyltransferases FUT3 and FUT6[235,236]. The decreased expression of these glycosyltransferases in ccRCC tissue across all stages matches less abundant outer-arm fucosylation of tumor N-glycan structures observed by IMS. Taken together the findings from this multi-omic study comprise the most comprehensive analysis to-date of the healthy and diseased renal N-glycome.

1.2.3.1 The Glycobiology of Pancreatic Cancer

In the pancreas, a variety of glycan changes have been associated with PDAC including increases in sialyl-Lewis A (CA19-9) and sialyl-Lewis X, truncation of O-linked glycans, increased O-GlcNAcylation and increase N-glycan fucosylation and branching[237]. These glycosylation changes are observable directly in PDAC tumors and their microenvironments and in many cases can be linked to similar changes in patient sera and plasma[238]. Altered expression of the glycosyltransferases MGAT5, MGAT3, FUT8 ST6GAL1 and ST3GAL3 in pancreatic cancer have been linked to greater metastatic capacity, suggesting that N-linked glycosylation may play a particularly significant role in PDAC[239–242].

For patients with PDAC, integrins and other ECM adhesion proteins are N-glycosylated at elevated levels, with greater site occupancy and increased microheterogeneity[243]. Additionally, proteins associated with critical pancreatic cancer signaling pathways like nuclear factor-κB (NF-κB), tumor necrosis factor (TNF) and tumor growth factor β (TGF-β) are heavily N-glycosylated in PDAC which may increase their stability and resistance to proteolysis and thus sustain elevated signaling levels[244]. Inhibiting N-linked glycosylation synthesis in pancreatic cancer cell lines decreases expression of the receptor tyrosine kinases (RTKs) insulin-like growth factor-I receptor (IGF-IR) and EGFR by disrupting protein synthesis and trafficking to the cell surface in the Golgi[245]. In the serum of pancreatic cancer patients, glycoproteins have been shown to be heavily fucosylated and those with more aggressive disease exhibit increased N-glycan branching[246–248]. Considerable research effort has gone into identifying N-

glycosylation changes on serum glycoproteins in pancreatic ductal adenocarcinoma, summarized in a 2018 review on serum glycoprotein biomarkers for PDAC (Table 3)[249]. Although serum protein glycosylation is often a helpful indicator of disease progression or severity, the link between N-glycosylation changes on serum glycoproteins and aberrant N-glycosylation in pancreatic tumors is not well understood. The majority of serum glycoproteins are hepatic in origin, thus N-glycan modifications on these proteins are a function of liver biology rather than pancreatic cancer-derived[250]. Frequently, changes in serum N-glycosylation in cancer are reflective of acute phase immune and inflammatory responses in the liver stimulated by immune cell-mediated cytokine storms[251,252]. Consequently, there is interest in better understanding the glycosylation landscape of pancreatic tumors to establish a link between tumor-associated N-glycosylation and changes to the serum glycoproteome.

Unlike for other cancers, few spatial N-glycome analyses of pancreatic cancer tumors have been performed. Early experiments using N-glycan IMS demonstrated biantennary N-glycan structures with and without core fucose residues specific to areas of fibrosis in pancreatic cancer tissues[209]. A further exploration of PDAC N-glycosylation by the same group in 2015 corroborated the finding of biantennary N-glycans as features of fibrotic tissue regions in pancreatic cancer[210]. These proof-of-concept experiments established the utility of N-glycan imaging mass spectrometry for studying cancer glycosylation but were not specific

Table 3. Alterations to Serum Protein N-glycosylation in Pancreatic Cancer.

Serum Glycoprotein	Core Fucose	Outer Arm Fucose	α2,3 sialylation	α2,6 sialylation	Branching	sLe^x
β2-glycoprotein 1 (P02749)	+	+	+	+		
Hemopexin (P02790)†	+	+	+	+		
Haptoglobin-related protein (P00739)	+	+		+		
Serum amyloid P component (P02743)†	+	+	+	+		
Clusterin (P10909)	+	+		+		
Antithrombin III (P01008)	+	+	+	+		
Kininogen 1 (P01042)	+	+	+	+		
α-1B-glycoprotein (P04217)				+		
Haptoglobin (P00738)†	+	+		+		+
α-1-antitrypsin (P01009)†				+		
Transferrin (P02787)†	+			+		+
α-1-acid glycoprotein 1 (P02763)†	+	+			+	+
Fetuin-A (P02765)	+				+	
Ceruloplasmin (P00450)†						+
RNase 1 (P07998)	+					
α-1-antichymotrypsin (P01011)†	+	+				
Thrombospondin 1 (P07996)	+	+				
Leukemia inhibitory factor receptor (P42702)	+		+	+		
Centrosome-associated protein 350 (Q5VT06)	+			+		

+, increased compared to healthy controls; (), uniport accession number; †, acute phase response

to pancreatic cancer – warranting a more thorough investigation. The need to understand the spatial biology of N-glycosylation in pancreatic cancer and the potential clinical implications associated with tumor-derived N-glycan biomarkers was an original inspiration for the work presented in this dissertation.

1.2.4 Sialic Acids

Sialylation is the addition of N-acetylneuraminic acid (NeuAc) residues to the branches of N-glycans, O-linked glycans or glycolipids. This major class of glycan modifications occurs when a sialyltransferase covalently attaches one or more sialic acid monomers in the form of cytidine monophosphate-linked nucleotide sugars to a glycan substrate. Sialyltransferases relevant to N-glycans are generally categorized by which sugar substrates they act upon, either terminal galactose residues or other sialic acid residues. Sialic acid chains known as polysialic acids are formed via the sequential addition of α2,8-linked sialic acids by ST8 α-N-acetyl-neuraminide α-2,8-sialyltransferases II and IV (ST8SIA2, ST8SIA4)[253]. Sialyltransferases which decorate terminal galactose can be further subdivided into those which catalyze an α2,3 linkage (ST3 β-galactoside α-2,3-sialyltransferase III, IV and VI, ST3GAL3, ST3GAL4, ST3GAL6) and those which catalyze an α2,6 addition (ST6 β-galactoside α-2,6-sialyltransferase I and II, ST6GAL1, ST6GAL2)[254]. Sialic acids also occur naturally in a hydroxylated form, n-glycol neuraminic acid (NeuGc), and although these sugars are synthesized by most mammals, humans have lost that ability over evolutionary time[255]. Nevertheless, NeuGc-decorated glycans still occur sparingly in human tumors and

in some healthy tissues, likely as a result of dietary consumption of NeuGc-containing animal products[256,257].

The role of sialylation in both health and disease has been extensively characterized[258]. Sialic acids are unique amongst the N-glycan sugar monomers for their carboxylic acid group, which is negatively charged a physiological pH. As such, this sugar is able to engage with different sets of molecular interactors than are the other neutral sugars which constitute N-glycans[259]. In the plasma membrane, electrostatic charge repulsion between sialylated glycoproteins prevents their association and thus modulates their signaling activity[260]. Conversely, electrostatic adhesion between sialic acids and positively charged amino acids may reinforce protein – protein interactions[261]. In cancer, hypersialylation confers distinct advantages for tumor cells which can generally be subdivided into four biological processes: immune evasion, apoptotic resistance, decreased adhesion and increased extravasation. By engaging inhibitory siglecs on NK cells, T cells and macrophages, sialic acids on the tumor cell surface are able to counteract the effect of activating receptors and induce quiescent states in these immune cells[262]. Sialylation of tumor necrosis factor (TNF) and Fas receptors has been shown to prevent their internalization – even in the ligand bound state – thus disabling these apoptotic signaling pathways[263]. The addition of sialic acid residues to integrins reduces adhesion between cancer cells and their microenvironments, which decreases the stability of the tumor mass and increases shedding of tumor cells into the local vasculature[264]. These sialylated circulating

tumor cells can then engage endothelial selectins resulting in extravasation and colonization to form metastatic secondary sites[265].

The α2,3, α2,6 and α2,8 linkages of sialic acids determine their configuration as spatial isotopes and therefore each epitope's ability to rotate, bend and adopt various binding topologies[266]. Accordingly, sialic acid-binding proteins are often biased towards – or exclusive to – specific sialic acid linkages[267]. Syntheses presented later in this dissertation will capitalize on the topological differences between these isomers. The biological importance of sialic acid linkage isomers is exemplified by the case of influenza flu virus trophism: human influenza A virus selectively binds α2,6-linked sialic acids while the avian influenza A strain is specific to α2,3 isomers[268]. In cancer, sialic acids play distinct roles based on their topology. Increased expression of ST6GAL family sialyltransferases and the subsequent α2,6-sialylation of glycoproteins is associated with tumor progression, apoptotic resistance, immune suppression and poor survival in multiple carcinomas[269,270]. Antibody-targeted removal of sialic acid isomers from tumors reduces immunosuppressive phenotypes in cancer models by repolarizing tumor-associated macrophages[271]. As previously mentioned, α2,6-sialylation of the Fas death receptor by ST6GAL1 in colorectal carcinoma protects against Fas-mediated apoptosis[272]. ST3GAL enzymes are involved in the biosynthesis of the α2,3-sialylated pancreatic cancer-associated sLe^A and sLe^X epitopes, where increased detection of these markers is associated with advanced disease. In addition, expression of ST3 sialyltransferases increases tumor proliferation, differentiation and metastasis in cholangiocarcinoma as well as promotes tumor

cell adhesion and invasion in gastric cancers[273,274]. Accordingly, knockdown of ST3GAL6 prevents myeloma cell bone marrow homing in xenograft mouse models, prolonging survival[275]. The differential physiological functions of α2,3- and α2,6-sialylated proteins and their relation to cancer biology make them attractive targets for biomarker and molecular mechanistic studies. Challenges in the analysis of sialic acid isomers – and strategies to overcome them – will be described in later sections.

1.3 Analysis of N-glycosylation

Approaches to study N-glycans have varied as widely as N-glycans themselves as the field has advanced over the past 60 years (Figure 8)[276]. From the first characterization of asparagine-linked β1-GlcNAc on ovalbumin to modern day comprehensive analyses of hundreds of N-glycan analytes, the concept of the N-glycome has evolved substantially and has gained a reputation as one of the most important yet understudied aspects of cellular biology[277]. French enzymologist François Jacobs was both too early in the eyes of his colleagues and yet far too late when in 1975 he acknowledged, "Together with nucleic acids and proteins, carbohydrates represent the third dimension of molecular biology"[278]. Today we recognize glycomics – with its associated instrumentation, methodologies and data analysis challenges – as on par with the more well-known "omics" fields like metabolomics and proteomics. For the purposes of this dissertation, the following sections will cover increasingly advanced N-glycan analysis techniques, beginning with the use of lectins.
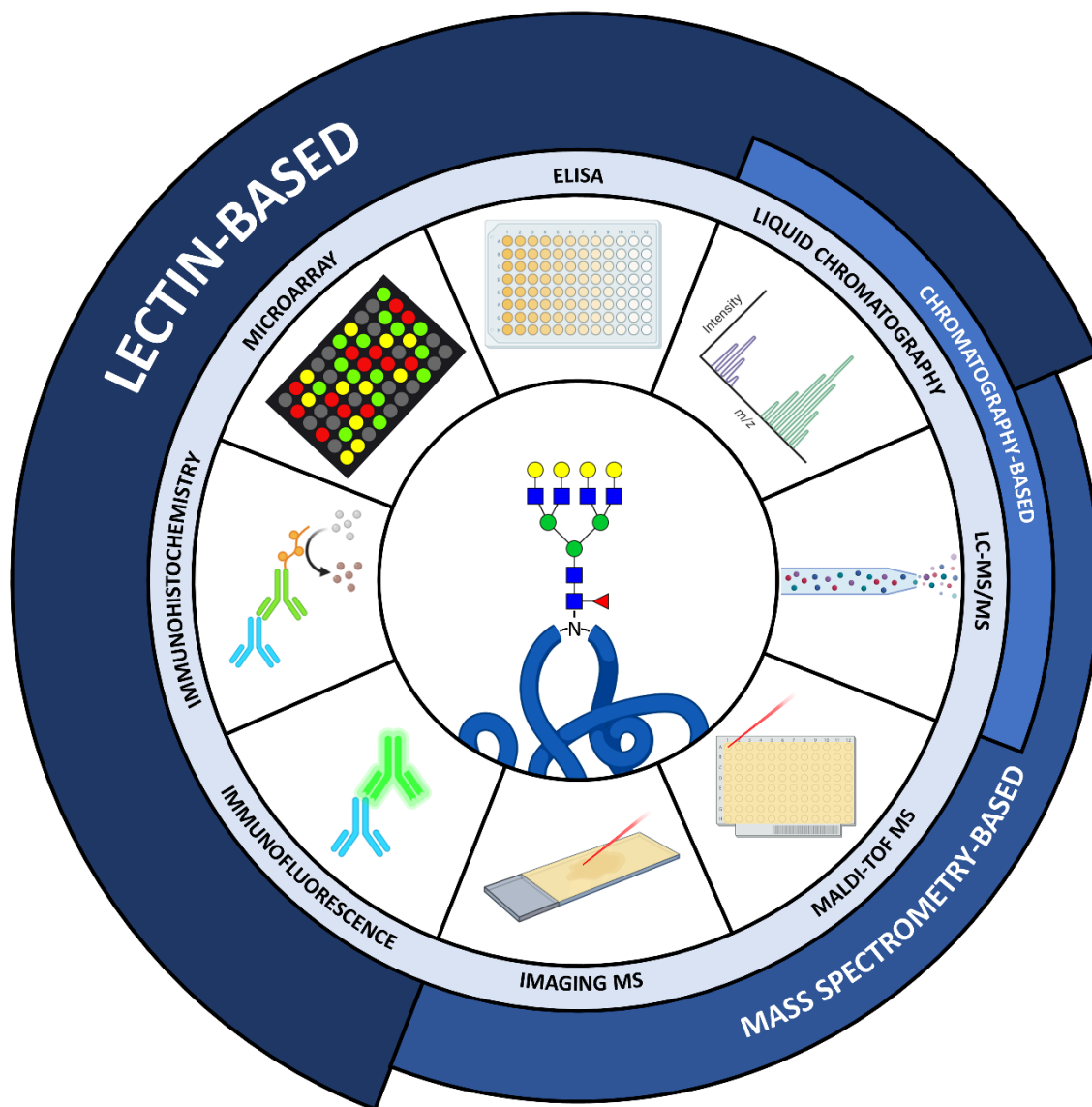
Figure 8. Techniques for the Analysis of N-linked glycans. Broadly, these analyses are either lectin-based, chromatography-based or mass spectrometry based, although significant overlap exists between these classes (e.g., liquid chromatography-coupled mass spectrometry or lectin affinity chromatography). LC-MS, liquid chromatography-coupled mass spectrometry; MALDI, matrix-assisted laser desorption/ionization; TOF, time-of-flight

1.3.1 Lectins

As previously described, lectins are carbohydrate-binding proteins which often exhibit antibody-like specificity for their glycan targets. Accordingly, lectins have long been utilized to detect, visualize and quantify N-glycans in a fashion analogous to immunolabeling. Lectins were used in some of the first glycomic experiments and have since been optimized and adapted into a wide variety of technologies, including microarray and chip formats where immunohistochemical (IHC), immunofluorescent (IF) or colorimetric readouts are often coupled to these configurations[279]. Most lectins commonly used as glycan tools today originated in plants, although some fungal and animal proteins have proven useful as well[280]. Typical lectins have specificities not for whole N-glycans themselves, but for particular structural motifs like branching (*Griffonia simplificolia* lectin-II, GSL-II; *Phaseolus vulgaris* L, PHA-L), bisecting GlcNAc (*Phaseolus vulgaris* E, PHA-E), sialylation (*Sambucus nigra*, SNA; *Maackia amurensis*, MAL), oligomannose (*Concanavalin* A, ConA) and fucosylation (*Aleuria aurantia* lectin, AAL; *Lens culinaris* hemagglutinin, LcH; *Pisum sativum* agglutinin, PSA)[281]. The specificity for broad architectural features only, however, limits their use for detailed structural analyses and thus lectin technologies are largely outdated for precise N-glycomic work. As a further complication, the affinity of lectins for their carbohydrate antigens is in the low micromolar range whereas antibodies routinely have nanomolar to picomolar affinities, therefore lectin binding is often assumed to be somewhat nonspecific[282,283]. Despite this, lectins regularly find utility as part of affinity chromatography columns where they facilitate preferential rather than

specific enrichment. Often, lectin affinity columns will combine multiple lectins with differing specificities to non-specifically enrich glycosylated molecules in bulk from a sample for analysis by liquid chromatography[284,285].

1.3.2 Liquid Chromatography

Liquid chromatography (LC) represents a major technological step forward for the analysis of N-glycans. Chromatographic separation of N-glycoproteins, chemically or enzymatically released N-glycans and glycan fragments by high- or ultra-performance liquid chromatography (HPLC, UPLC) can provide information about N-glycan site occupancy, microheterogeneity, composition and structure. LC separation is a function of how an analyte partitions between a liquid mobile phase and solid stationary phase as it passes through a chromatography column. Separated analytes are then passed by a detector coupled to the column outflow which typically measures ultraviolet absorbance, fluorescence or chemiluminescence amongst other readouts[286]. Common chromatography column materials for N-glycans and glycoproteins are C18 (reversed phase, RP), porous graphitized carbon (PGC) and unbonded silica (hydrophilic interaction liquid chromatography, HILIC) which separate glycan analytes by polarity and hydrophobicity[287]. When coupled with sequential exoglycosidase digestions prior to separation, liquid chromatography analyses can even provide precise N-glycan structural or linkage information[288].

The ability to separate released N-glycans on RP, PGC or HILIC columns often relies on derivatization of the N-glycan reducing end prior to injection into the LC system, where 2-aminobenzamide (2-AB), procainamide (ProA), aminoxyTMT,

rapifluor-MS (RFMS) and permethylation labels are commonly used[289]. While derivatization and labeling results in improved LC separation and detection, these reactions add substantial sample preparation time and require costly reagents[290]. In the context of potential high throughput diagnostic or clinical applications, such handicaps preclude the analysis of large sample cohorts in a feasible timeframe or cost-effective manner[291]..

1.3.3 Mass Spectrometry

To date, mass spectrometers are some of the most advanced tools applied to the analysis of N-glycosylation. As the name implies, mass spectrometers detect molecules of interest by their mass to charge ratio (m/z), which are then displayed as a spectrum of intensities corresponding to analyte abundance within the sample. Because these instruments measure a ratio of mass to charge, they necessarily must sample analytes as charged ions. Therefore, there are typically three main components of a mass spectrometer: an ionization source, a mass analyzer and a detector[292]. Ionization sources commonly impart electro- or photochemical energy into the analyte matrix to generate ions for detection[293]. Downstream of the ion source, mass analyzers use electrostatic or magnetic field potentials to characterize ion m/z values then gate, reject, select for, separate and steer analytes of interest through the instrument towards the detector[294]. In the detector, an ion's mass to charge ratio and abundance are then recorded, often as a function of charge induction[295]. The types and configurations of these components give birth to a wide variety of mass spectrometers with different speeds, sensitivities and analytical proclivities. Mass spectrometry instruments

and methodologies for the analysis of N-glycans – discussed further herein – are generally categorized by their ionization source (electrospray or matrix-assisted laser desorption) and their mass analyzers or detectors (time of flight or ion cyclotron).

1.3.3.1 LC-MS

Today, HPLC and UPLC instruments are increasingly coupled to mass spectrometers for detection of glycan analytes. Liquid chromatography-coupled mass spectrometry (LC-MS) relies on the ionization of chromatographically separated analytes before injection into the instrument for detection. Here, an electrospray ionization (ESI) source is commonly used that applies an electrostatic potential to an aerosolized spray of solvated molecules of interest, which undergo desolvation, a transition to the gas phase and ionization[296]. The principles of separation used in liquid chromatography applications are equally as relevant when coupled with mass spectrometry analysis. As previously discussed, N-glycans often must be labeled or derivatized to efficiently separate, ionize and fragment for LC-MS. Here too the increased sample preparation time impedes high throughput studies, which are already difficult due to the typically long on-column separation time required for LC-MS[297]. The ability for ESI sources to generate multiply charged ions, however, increases sensitivity of detection of low abundance analytes[298,299]. The decision whether to use LC-MS for N-glycan analysis is therefore largely dependent on the need for experimental sensitivity or for throughput. One immutable shortcoming of LC-MS for analyses of tissue-derived glycans is the loss of spatial context. Tissue sample preparation for LC-

MS and electrospray ionization necessarily involves homogenization of glycosylated tissue proteins for chromatographic separation[300]. Matrix-assisted laser desorption ionization imaging mass spectrometry (MALDI-IMS), which records an N-glycan's orientation relative to a tissue, is preferred for spatial characterizations. Accordingly, MALDI-IMS N-glycan analyses will be the focus of this dissertation. The mass analyzers and detectors for LC-MS are shared by those for MALDI-IMS and will be discussed in a further section.

1.3.3.2 MALDI-IMS

Imaging mass spectrometry (IMS) was first developed for the analysis of metal alloys and semiconductors in industrial applications[301]. Eventually termed SIMS (secondary ion mass spectrometry), this "ion microscope" technique, progenitor to all subsequent IMS strategies, involved sputtering a sample's surface with a high-energy gaseous ion beam. Collisions with this beam and the subsequent transfer of energy generated "secondary" ions from the sample which could then be analyzed in a mass spectrometer[302]. These initial demonstrations piqued interest in generating spatial analyte information from biological mediums. Caprioli and colleagues took advantage of prior research into the combined use of a high energy laser and a photoabsorbent organic acid matrix to generate ions for mass spectrometric analysis (collectively referred to as matrix-assisted laser-desorption ionization, MALDI) to generate the first molecular images of biological tissue specimens in 1997[303]. The group demonstrated that by rastering the laser beam across the sample surface in a gridded fashion, pseudo-colored heat maps could be generated to show the in-situ distributions and abundances of ions of

interest where each "pixel" represented a mass spectrum from where on the tissue the laser sampled. MALDI also proved capable of generating more massive ions than had previous ionization strategies, making it suitable for the analysis of a wide range of biologically relevant analytes[304].

Since these initial demonstrations, MALDI has come to dominate the field of imaging mass spectrometry. Workflows have been developed for a wide breadth of sample conditions and analytes of interest[305], however a general MALDI imaging mass spectrometry experiment proceeds as follows: 1. A sample is collected from the patient during a surgical procedure or posthumously. 2. The tissue specimen is preserved by snap-freezing in liquid nitrogen ("Fresh Frozen" tissues) or by fixation in formalin followed by embedment in paraffin wax ("Formalin-Fixed Paraffin-Embedded" tissues). 3. Embedded or frozen tissues are thinly sectioned (5 – 20 μm) and mounted on glass slides. 4. Samples are prepared for imaging dependent on the analyte of interest (this may include clearance of unwanted analytes, antigen retrieval or chemical/enzymatic release of molecules of interest, amongst other steps). 5. A crystalline organic acid or similar matrix is applied as a thin layer over the sample surface. 6. Analytes are ionized by laser desorption for detection by the mass spectrometer. 7. Collected spectra are spatially mapped for visualization of molecular distributions. 8. Data is processed by statistical analysis, image co-registration, peak identification or other software.

Imaging mass spectrometry holds distinct advantages over other imaging modalities. Imaging by light microscopy limits the number of identifiable analytes in a single experiment, whereas IMS platforms may detect hundreds of analytes at

the same time[306]. Unlike immunohistochemical or immunofluorescent staining, IMS experiments do not require lengthy incubations with molecular probes or extensive washing, fixation and mounting steps, making sample preparation simpler and quicker. The high-resolution mass analysis afforded by modern mass spectrometers allows for fine discrimination between analytes of very similar mass and high confidence in the specificity of molecular assignments, a feature especially useful in metabolomics and lipidomic investigations[307]. Advancements in laser, computational and instrumental technologies allow imaging mass spectrometry to vastly outperform other imaging strategies in terms of the speed of data acquisition[308]. IMS also boasts the broadest range of detectable analytes, facilitating label free imaging of proteins, lipids, nucleic acids, carbohydrates, metabolites and pharmaceuticals ranging from less than 100 to more than 100,000 Da[309]. Additionally, the sensitivity of imaging mass spectrometry platforms allows for the detection of molecules of interest at femtomolar levels directly from their biological milieu[310]. Most critically, the ability to analyze patient tissue specimens is core to the insights gained from today's IMS experiments, where disease-mediated molecular and morphological features are directly manifest. Linking histopathologically-defined tissue structures to the expression of specific biomolecules potentiates the discovery of disease markers and therapeutic targets. At its most reductive function, IMS acts as a "molecular microscope" to reveal the biological and chemical mechanisms underpinning pathophysiology, resulting in better understanding of the origins, maintenance and progression of disease.

Although multiple imaging mass spectrometry strategies have been developed since the theoretical groundwork for the field had been laid, by far the commonly utilized technology in the imaging space is MALDI-IMS. N-glycan imaging experiments utilizing a MALDI source rely heavily on three primary factors: enzymatic release of N-glycans from the tissue surface, the application of a light-absorbing organic matrix to the tissue sample and the use of a neodymium-doped yttrium aluminum garnet (Nd:YAG) or similar laser for ion generation[311,312]. Photoablation of the co-crystallized N-glycans and matrix by the laser results in the subsequent transfer of sample molecules to the vapor phase, analyte ionization and ejection into the mass spectrometer[313]. These characteristics make MALDI an ideal technology for the generation of N-glycan ions, which had been traditionally difficult to ionize due to their large size and complex structural properties[209,233,314]. The basic N-glycan MALDI IMS schematic is shown in Figure 9. A key component of the N-glycan IMS workflow is the use of a solvent sprayer to apply a thin molecular layer of peptide N-glycosidase F (PNGase F) enzyme onto tissue or cells to release only N-linked glycans from their carrier proteins. Diffusion of the released glycans is minimal allowing spatial colocalization to tissue regions and specific cell types. As MALDI is considered the gold standard for spatial N-glycan analyses, the following section will focus heavily on sample preparation and instrumentation for MALDI experiments.
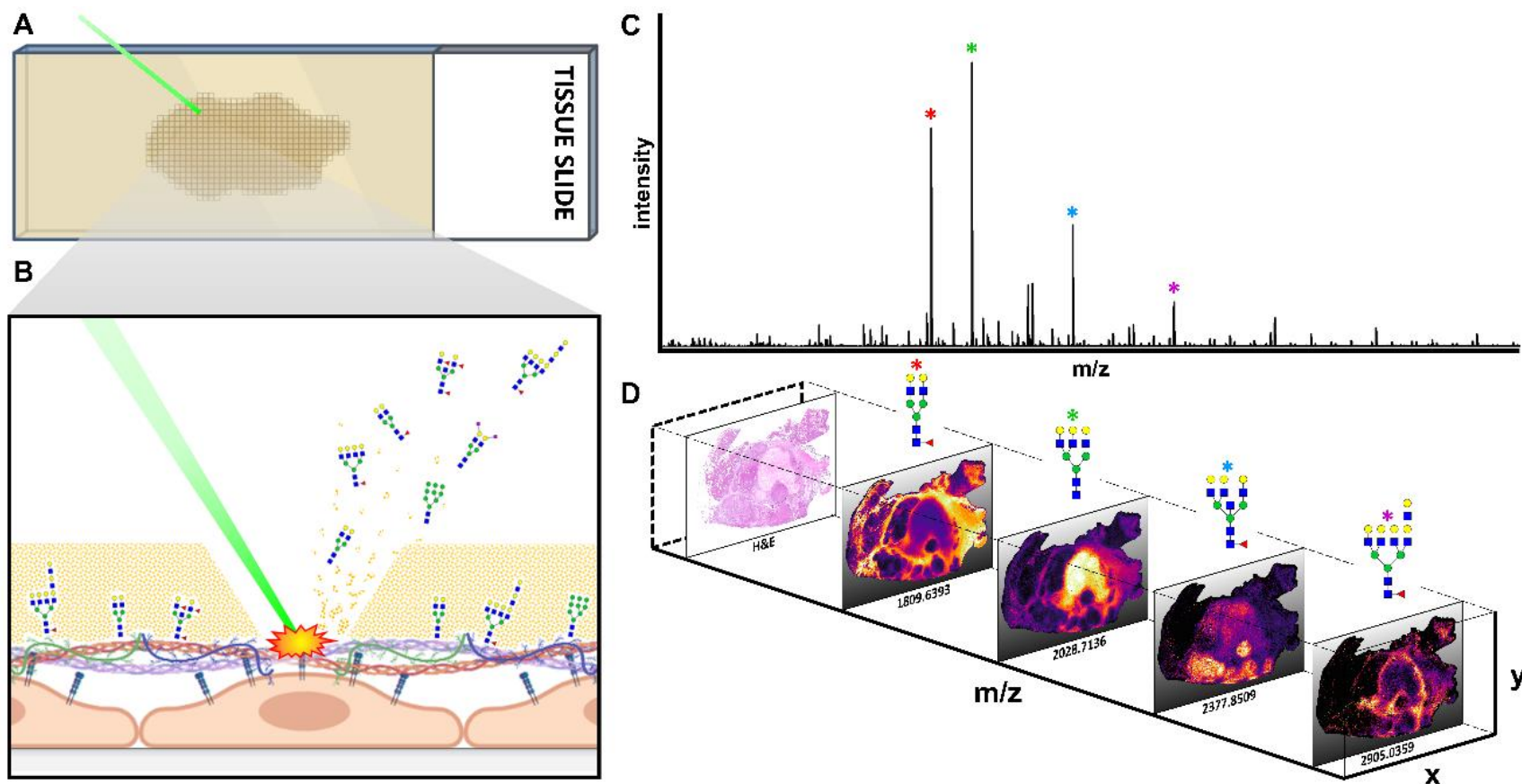
Figure 9. MALDI Imaging Mass Spectrometry for the Analysis of N-glycans. A) MALDI laser striking a grid pixel on an FFPE tissue section. B) Close up view of MALDI photoablation of the tissue surface and subsequent desorption/ionization and ejection of N-glycan ions into the mass spectrometer. C) Representative mass spectrum generated from a single MALDI pixel. D) Mapping of individual pixel spectra back to their original X,Y coordinates generates N-dimensional N-glycan heat maps.

1.3.3.2.1 Sample Preparation for MALDI IMS of N-glycans

A standardized N-glycan IMS sample preparation workflow is presented in Figure 10. Current MALDI-IMS workflows are able to accommodate both fresh-frozen (FF) and formalin-fixed paraffin-embedded (FFPE) tissue sources from clinical pathology labs or tissue biorepositories, granting access to a nearly unlimited supply of specimens for analysis. 5 μm FFPE tissue slices from pathology blocks or cores from tissue biopsies cut and affixed to glass slides (indium tin oxide (ITO) -coated for analyses in some TOF instruments) are dewaxed and rehydrated in a graded series of ethanol and water washes prior to heat induced epitope retrieval in a citraconic anhydride-based buffer. 8 μm cryosectioned fresh frozen tissues are rinsed in organic solvents to remove lipids, salts and other metabolites, thus increasing downstream N-glycan signal. FF tissues do not require antigen retrieval prior to enzymatic N-glycan release. In addition to whole-tissue imaging, both FFPE and fresh-frozen tissue samples are routinely homogenized for N-glycan extraction and purification as previously mentionied[223]. Doing so enables the analysis of multiple tissues on the same MALDI target plate but forgoes the retention of N-glycan spatial information. Alternatively, liquid-phase extraction of N-glycans from tissue homogenate is routinely used orthogonally to whole-tissue MALDI-IMS for precise structural identification via ESI-LC-MS[315].

N-glycans are released from their glycoprotein carriers via on-tissue incubation with peptide N-glycosidase F (PNGase F), which cleaves between
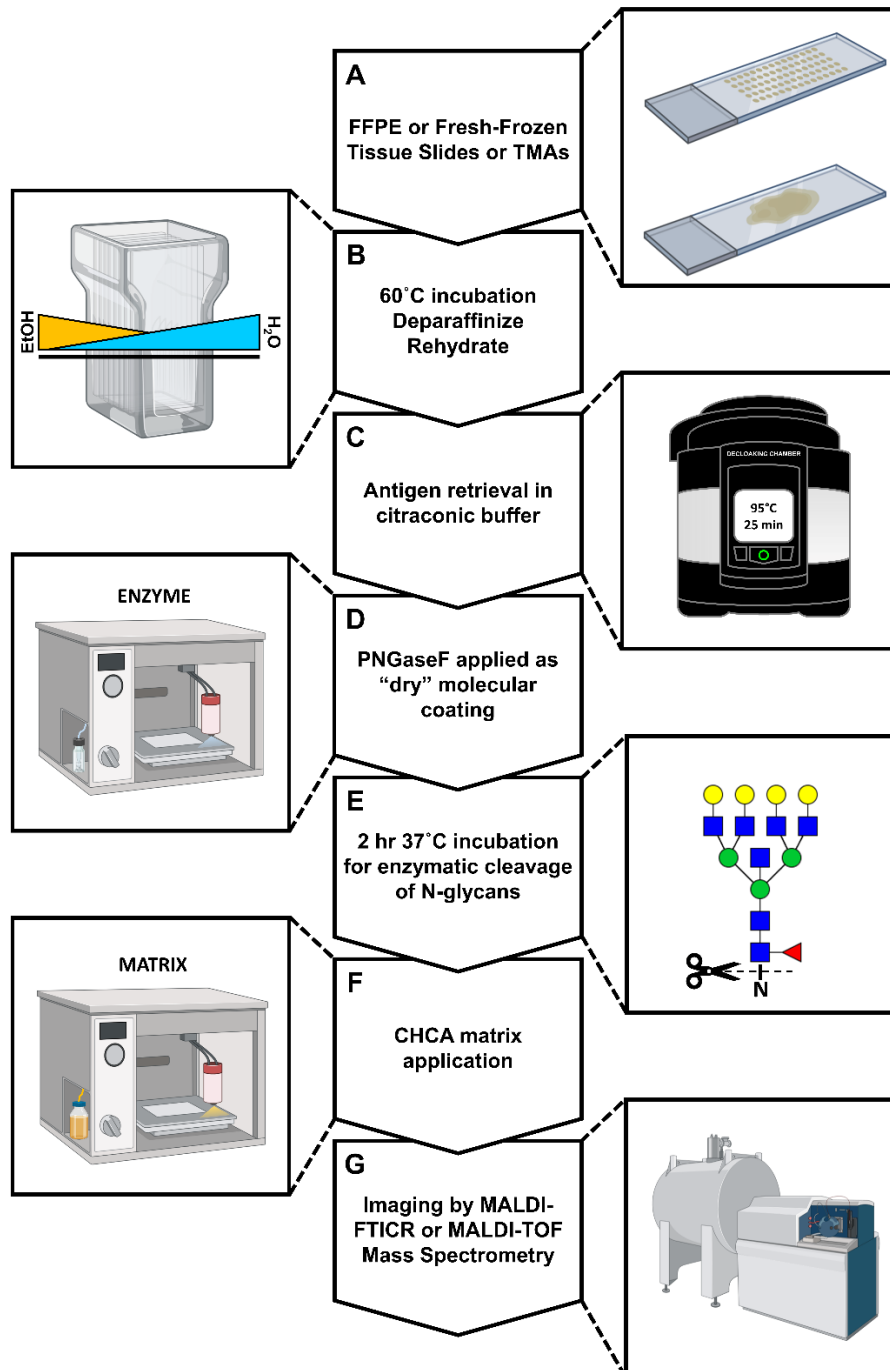
Figure 10. A Standardized Workflow for N-glycan MALDI-IMS. A) FFPE or FF tissue slides, B) dewaxing and rehydration, C) heat-induced epitope retrieval, D) application of peptide N-glycosidase F, E) enzymatic N-glycan release, F) application of matrix and G) spatial analysis by MALDI-FTICR or MALDI-TOF.

asparagine and the first GlcNAc residue on the chitobiose core of the N-glycan[316]. For N-glycan IMS, the retention of analyte spatial information is accomplished through a "dry" molecular coating of PNGase F that limits diffusion of released N-glycans across the tissue. Current protocols using an automated sprayer system to apply this coating are robust and highly reproducible[314]. Tissue slides sprayed with PNGase F are incubated in a pre-warmed (37°C) chamber at ≥80% relative humidity for a minimum of two hours to remove the N-glycan structures.

Desorption and ionization of analytes into a MALDI mass spectrometer for detection is dependent on the application of a crystalline chemical matrix, which absorbs laser energy and transfers it to the substrate below resulting in a transition to the vapor phase and the ionization of analytes[317–319]. The most common organic acids used for N-glycan IMS are α-cyano-4-hydroxycinnamic acid (CHCA) and 2,5-dihydroxybenzoic acid (DHB)[207]. Other matrix molecules like 1,5-diaminonaphthalene (DAN) and 2′,4′,6′-trihydroxyacetophenone monohydrate (THAP) have also been used[320,321]. Because matrix crystal size and consistency of matrix application are critical determinants of analyte signal intensity and reproducibility, most current approaches use an automated sprayer for N-glycan imaging experiments, although the use of sublimation platforms to transform vapor-phase matrix solution into a solid matrix coating is also widely used[322,323]. Ideally, the CHCA-coated tissue slides are analyzed within a few days after preparation but can be stored in a desiccator for several weeks.

1.3.3.2.2 MALDI Instrumentation

     N-glycan ions ejected for detection span a wide mass range, with the simplest sugar chains detected at ~700 *m/z* and multiply branched, fucosylated and sialylated structures detected upwards of 4,000 *m/z.* Complicating N-glycan mass-spectrometry analysis of these analytes are variable formation of sodium adducts, isotopic overlap between structures and the presence of sulfate or phosphate groups on some species. Interference from the chemical matrix lends additional obscurity. Aside from blunting analyte signal, the process of laser desorption fragments the matrix and matrix ions are ejected into the mass spectrometer, leading to potential overlap or obfuscation of N-glycan ions. N-glycans are typically detected in positive mode, however certain special applications are better suited to negative mode analysis thus demanding instrument versatility[324]. Critical to overcoming these challenges is instrument resolving power, which must be high for fine resolution of analytes close in mass. To meet these needs, two broad classes of MALDI-outfitted mass spectrometers, each with their own advantages and disadvantages, are typically used to detect released N-glycan ions from tissue, those being Fourier transform (FT) and time of flight (TOF) instruments.

1.3.3.2.2.1 MALDI-TOF

     Time of flight (TOF) mass spectrometry, although typically less sensitive, offers the advantages of higher spatial resolution and increased analysis speed. TOF instruments accelerate MALDI-ionized N-glycans through an electric field then maneuver them through a series of pulsers and reflectors to separate the ion

packets. The time at which these ions hit the detector is then converted to a measurement of accurate mass[303,325]. TOF mass spectrometers have a fixed resolving power across the mass range which is typically less than their FT counterparts, where resolving power is a measure of an instrument's ability to separate equally intense ions which differ only slightly in mass[326]. Despite this, the rapid time from the laser-ejection of N-glycan ions to detection increases the number of pixels which can be analyzed in a given time frame (up to 50X faster than FT-MS for some instruments), resulting in the practical feasibility of much higher spatial resolution analyses (< 5 μm)[327,328]. Because of this speed, TOF mass spectrometers are routinely used for assessment of N-glycans from tissue homogenate via spotting on multi-sample target plates in high throughput experiments. Advantageously for TOF instruments, there is no theoretical bound to their upper *m/z* detection limits. As *m/z* in these instruments is ultimately a function of flight time, increasing the length of the drift tube allows for detection of increasingly more massive analytes[329]. Much of the work presented in this dissertation was performed on a timsTOF flex (Bruker Daltonics) MALDI-Q-TOF mass spectrometer, where the Q represents a quadrupole mass analyzer between the MALDI ion source and detector and "tims" indicates a trapped ion mobility device upstream of the mass analyzer. Ion mobility separation will be discussed in later sections.

One difficulty common to all MALDI platforms is the detection of analytes of very low abundance or very high molecular weight. This complicates the analysis of mammalian N-glycans, which are synthesized to well past 10,000 *m/z* via the

addition of polylactosamine extensions[330]. Critical factors contributing to this shortcoming are ionization efficiency and analyte decomposition in the MALDI-source[331]. When compared to alternative ionization schema such as ESI, laser-induced ionization of analytes in a MALDI instrument is relatively inefficient (1 out of every ~10^5 molecules ionized). This is especially true for low-proton affinity substrates like carbohydrates, which ionize at an efficiency of 10^{-7} – 10^{-8} in MALDI experiments[332,333]. Recently, a novel MALDI-TOF instrumentation approach has been developed to overcome this obstacle. Inefficient primary MALDI-ionization is rectified by an additional, subsequent ionization of the analyte plume by a secondary laser oriented perpendicular to the axis of ion ejection in laser positronization-coupled MALDI-IMS (MALDI-2) platforms[334]. Thus, low abundance or difficult to ionize structures in the analyte cloud are more likely to be ionized and detected by the mass spectrometer. This new technology has already shown applicability for N-glycan analyses, where a MALDI-2 instrument operating in negative mode demonstrated an order of magnitude more sensitive detection of N-glycans from brain tissue samples than did a positive mode traditional MALDI platform[205]. Another possibility afforded by MALDI-2 outfitted mass spectrometers is tissue analysis at subcellular resolution. Coupling a secondary positronization laser with a transition-geometry MALDI mass spectrometer, which positions the primary laser behind the tissue sample, allows pixel sizes on the order of 600 nm and thus the analysis of single cells[335]. Secondary post-ionization is critical for generating acceptable signal at these low rasters, as the volume of sample ejected into the instrument decreases proportionally with reduced pixel size[336]. MALDI-2

sources could theoretically be coupled with FT instruments, but currently are only in use on Bruker Daltonic's timTOF flex MALDI-2 configuration.

1.3.3.2.2.2 MALDI-FT-ICR and Orbitrap

Both ion-cyclotron resonance (ICR) and Orbitrap mass spectrometers are categorized as Fourier transform (FT) instruments by the way they deconvolute ion signal in the detector. ICR mass spectrometers excite N-glycan ions using alternating radiofrequency pulses inside a powerful magnetic field (typically ranging from 1-21T), resulting in differential cyclotron resonance frequency of the ion packets within the detector proportional to their masses[337–339]. This amalgam of resonances is detected by opposed detection plates inside the ICR cell as a single image current which is then deconvoluted into its component frequencies and converted into a measurement of accurate N-glycan mass and intensity by Fourier transformation[340]. FT-ICR instruments achieve the highest resolving power (R) in the space (R > 1,600,000) which is proportional to the strength of the instrument's magnetic field, however this resolving power drops off for high-mass analytes (> ~2,000 m/z)[307]. The composition of N-glycans presented in this dissertation were confirmed by accurate mass measurements on a 7T solariX MALDI-FT-ICR-MS (Bruker Daltonics).

Demonstrated in 2000 and commercially released in 2005 to compete with FT-ICR instruments, Orbitrap mass spectrometers utilize two outer electrodes surrounding an inner spindle electrode to create a strong linearized electric field[341,342]. The shape of these electrodes causes ions injected into the volume between them to harmonically oscillate along the central spindle, with the

frequency of this oscillation once again proportional to the masses of the ions[343].

As in ICR cells, a total image current detected along the central spindle is broken

down into individual mass frequencies through Fourier transformation. Although

not as high as ICR instruments, Orbitrap mass spectrometers demonstrate

substantial resolving power (R > 1,000,000) for the fine resolution of N-glycans of

similar mass and outperform ICR detectors in the very high mass range[344]. Due to

the compact nature of these analyzers and the pulsed injection of ion packets into

the trap, orbitrap mass spectrometers are able to utilize a refined Fourier

transformation through the incorporation of ion phase information, resulting in

increased analysis speed as compared to ICR cells[345]. Not without their

drawbacks, the reduced analyzer internal volume causes orbitrap instruments to

suffer shape-charge interference from coalescing ion clouds, resulting in mass

shifts and slightly less accurate mass detection[346]. The unique geometry of

Orbitrap mass spectrometers (such as Thermo Scientific's Fusion Lumos Tribrid,

used in this dissertation for glycopeptide analysis) allows for the incorporation of

multiple quadrupoles and collision cells into the instrument, potentiating MS/MS

and MS^n measurements (discussed further in later sections)[347].

1.3.3.2.3 Data Processing for N-glycan MALDI-IMS

Whether generated by MALDI, SIMS or other imaging strategies, mass

spectra datasets from imaging mass spectrometry experiments are challenging to

analyze due to their complexity and sheer data footprint[348]. These challenges

require significant computational resources to overcome. For example, a typical

high spatial resolution MALDI-IMS experiment consists of hundreds of thousands

of individual pixels, where each pixel represents a spectrum comprising hundreds of thousands of small *m/z* bins. These spectra require thresholding and normalization amongst other processing steps and finally spatial mapping to create a composite dataset of pseudo-colored images for every possible *m/z* of interest. Adding to this complexity, most IMS instruments operate vendor-specific software for initial data processing, making cross-platform comparisons and data sharing traditionally difficult[349].

The recent emergence of vendor neutral IMS processing software eases these difficulties. Open-source packages like MSiReader, Cardinal, and msIQuant utilize MATLAB, R and C++ programming, respectively, to analyze imzML data, the common imaging mass spectrometry file format[350–353]. Even vendor specific software like Bruker Daltonic's SCiLS Lab and Waters' High Definition Imaging can accommodate this shared format which allows for the integration of multiple imaging mass spectrometry datasets from different platforms. The complex analyses performed by these software packages are critical for extracting the pathological relevancy of a particular N-glycan's spatial distribution. Overlaying high-resolution, annotated images of histological staining with N-glycan IMS data reveals colocalization of analytes of interest with distinct tissue morphologies[354]. These programs also allow for statistical considerations such as segmentation, classification and multivariate analyses[355,356]. New to the space are applications for the multiplexed integration of orthogonal imaging modalities including immunohistochemical and immunofluorescence microscopy, autofluorescence scans and magnetic resonance imaging with N-glycan IMS data to link

glycosylation differences to biomarkers of interest or specific pathological features[357,358].

Unlike peptide, lipid and small molecule imaging which have been around for longer and thus enjoy well-developed peak-picking applications, the relative novelty of N-glycan IMS means that limited software resources are available for peak assignment[359]. Currently, most laboratories manually assign N-glycan structures to mass spectra via the use of an in-house N-glycan database generated using software such as GlycoWorkbench or GlycoMod or rely on shared online databases like GlyConnect or GlyTouCan[360–363]. Software for automated peak picking of N-glycans from IMS-generated spectra is still in its infancy, but new applications such as Bruker Daltonic's Metaboscape have shown promise for alignment of mass spectra peaks to an extensive database of known N-glycan masses with matched structures.

1.3.3.3 Tandem Mass Spectrometry

Mass spectrometry approaches typically identify N-linked glycans by accurate mass alone, which allows for the precise identification of a particular N-glycan's carbohydrate composition. Lost in these analyses however is precise information on the linkages which define N-glycan structural features. A traditional approach to deconvoluting N-glycan structural heterogeneity is fragmentation by Tandem mass spectrometry (MS/MS or MS[n])[364]. The sequential dissolution of glycosidic linkages from the complete N-glycan is typically facilitated by collision induced dissociation (CID) fragmentation (Figure 11). Other tandem mass
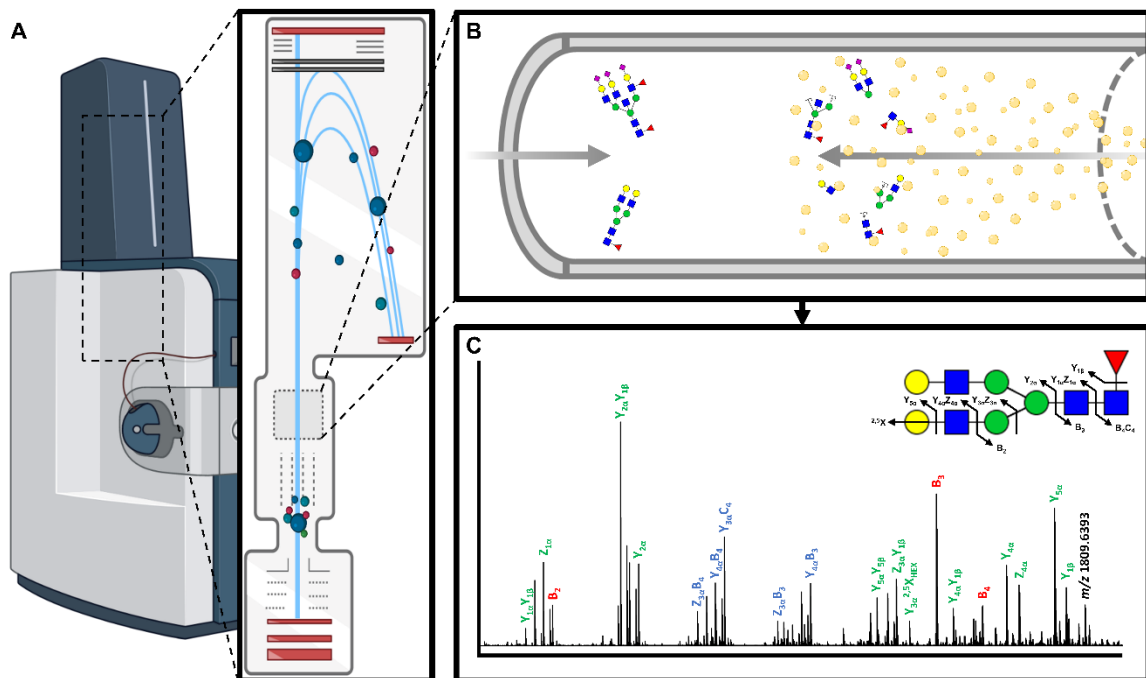
Figure 11. CID Fragmentation For N-glycan Structural Identification. A) timsTOF mass spectrometer with on-line CID collision cell. B) Accelerated precursor N-glycan ions collide with an inert gas (e.g., nitrogen) leading to gas-phase fragmentation. C) Analysis of the N-glycan fragment ions allows for reconstruction of the complete N-glycan structure. CID generates B/Y, C/Z and A/X fragment ions.

spectrometry strategies such as higher-energy collisional dissociation (HCD) and electron-transfer dissociation (ETD) are more commonly employed for glycopeptide identification[365]. Although ESI-based LC-MS/MS traditionally yields more rich fragmentation information, MALDI-MS/MS systems employing on-line CID collision cells now routinely provide fragmentation sufficient for structural identification in imaging experiments[366,367]. Briefly, tandem mass spectrometry by CID involves selective isolation of precursor masses of interest via a multi-pole ion guide followed by introduction of an inert collision gas. Acceleration of precursor ions through application of an electric potential results in gas-phase fragmentation upon collisions of N-glycan ions with the neutral gas molecules[368]. Fragment ions are then introduced into the mass analyzer for detection. Increasing the collision voltage yields a proportional increase in N-glycan fragments. CID fragmentation typically generates both B/Y and C/Z ions and at high energies may also yield A/X cross-ring fragments of individual sugar monomers[369]. By observing the sequential loss of sugar monomers from the complete N-glycan, an accurate understanding of the specific linkages composing the structure of interest may be inferred. These structural inferences are made more concrete by multiplexing CID-based experiments with orthogonal analyses on ion mobility instruments as will be discussed[370].

1.4 Isomer Separation for Mass Spectrometry

While mass spectrometry is widely recognized for its ability to deliver molecular specificity, individual spectral peaks often contain multiple analytes which are compositionally identical yet diverse in their configuration. Accordingly,

even mass spectrometers with ultra-resolution capabilities cannot resolve these isomers by mass alone. LC-MS too often fails to separate isomeric compounds, as their chromatographic retention properties are frequently identical[371].

Despite these challenges, interest in characterizing isomers by mass spectrometry continues to increase due to the biological importance of molecularly asymmetrical molecules[372]. This is particularly true for N-glycans, where non-linear, non-template driven biosynthesis results in a breadth of structural diversity. Within this heterogeneity are a variety of MS-detected masses that comprise multiple compositionally identical analytes which differ only with respect to the anomeric linkage of specific residues[373]. Terminal versus bisecting GlcNAc moieties, the specific attachments of sialic acids and core versus outer arm fucosylation, amongst other characteristics, are typically indistinguishable using conventional IMS analyses.

In order to separate isomers by mass spectrometry, scientist must design instruments or experiments which exploit the single largest differentiating factor between isomers: stereochemistry. Alternate stereochemistry means that differentially arranged isomers are able to engage in different chemical reactions and have different 3D orientations in space. The latter characteristic is typically exploited with instrumentation while derivatization approaches often target disparate reactivities between isomers. Special attention will be given to the separation of sialic acid isomers which are the focus of later chapters.

1.4.1 Instrumentation

Laser ionization of N-glycan ions directly from tissue in MALDI has not traditionally afforded incorporation of isomeric separation techniques. The recent introduction of ion mobility separated MS instruments into the MALDI space helps to deconvolute this complexity[374,375]. In trapped ion mobility separated (TIMS) instruments like the timsTOF flex used in this dissertation, N-glycan isomers within a single *m/z* ion packet migrate along with an inert drift gas against an oppositely opposed electric field, where their final equilibrium migratory distance is a function of their collisional cross sectional (CCS) areas[376]. Gradual reduction of the counter-acting electric field thus elutes these ions in a structural geometry-dependent manner from the mobility cell into the mass analyzer for detection. This technology has already demonstrated utility in parsing out N-glycan isomers[377].

Traveling wave separation via structures for lossless ion manipulation (TW-SLIM), high-field asymmetric waveform IMS (FAIMS) and cyclic IMS instruments have also recently been used to separate glycan isomers[378,379]. Both traveling wave and FAIMS ion mobility instruments are able to separate simple sialylated glycan isomers, however resolution is inversely proportional to increasing glycan molecular weight in these technologies[380,381]. As an N-glycan grows more complex, the impact of a single sialic acid monomer's orientation contributes less and less to the overall glycan topology, CCS and therefore its mobility in IMS. Consequently, TW and FAIMS technologies struggle to resolve bi-, tri- and tetraantennary sialylated N-glycan isomers.

It should be noted that adding a 4th dimension of data (ion mobility) to IMS experiments exponentially increases the data footprint acquired during a single run. The data handling challenges associated with this new field of analysis are complex and require the development of advanced software solutions before the routine implementation of ion mobility into the imaging space[382,383].

1.4.2 Derivatization

Despite the promise of ion mobility separating instruments, their relative novelty, high cost and functional limitations have restricted their widespread use for glycomics. Accordingly, glycan-focused research groups have pursued isomer-targeted chemical derivatization schemes as a cheaper and more useful alternative to instrumentation approaches. Differential stereochemistry between glycan isomers facilitates the selective introduction of disparate mass tags, where the resulting mass shifts enable resolution by conventional mass spectrometers. Because of their reactive carboxylate groups, sialic acids are particularly susceptible to these strategies.

Most sialic acid derivatization schemes focus around a common approach, where α2,6 isomers react with an external nucleophile while α2,3 isomers undergo internal lactonization, as summarized by a 2019 review[384]. Generally, these methylesterification, ethylesterification and amidation reactions embed a discrete mass shift in α2,6-linked species as determined by the particular combination of reactants, while introducing a -18 Da mass shift in α2,3-linked glycoconjugates via intramolecular dehydration[321,385–388]. The instability of the α2,3 lactone in these approaches is well characterized and limits downstream chemical or enzymatic

steps, thus multiple methods now include a second reaction to intentionally delactonize α2,3 isomers and introduce a stabilizing mass tag by aminolysis, permethylation, or amidation[389–391]. While most of the aforementioned reactions are typically used to prepare sialylated glycans for LC-MS/MS, Holst et al. designed a synthesis in 2016 which facilitates in-situ resolution by MALDI imaging of FFPE tissues (Figure 12)[204]. Although their scheme was a pioneering application of sialic acid derivatization technology, the -1 Da mass shift introduced to α2,3 isomers in the secondary reaction causes unfavorable spectral overlap between α2,3-sialylated structures and neighboring N-glycan analytes in N-glycan IMS experiments. Because the unstable α2,3 lactone in these syntheses is susceptible to various amine-containing uncoupling reagents, we theorized that a more useful mass tag for MALDI-IMS (and expanded approaches) might be incorporated – a hypothesis that inspired the developmental work later in this dissertation.

1.5 Broad Overview

To summarize, pancreatic ductal adenocarcinoma is an aggressive, highly lethal cancer affecting significant portions of the US and global population. The molecular origins of PDAC are predominantly somatic mutations, however diabetes and pancreatitis are associated with increased risk. These oncogenic drivers produce the heterogenous and non-specific symptoms of PDAC which challenge early discovery efforts. Accordingly, diagnosis is often confirmed by imaging or endoscopic biopsy well after metastatic progression. CA19-9, the sole
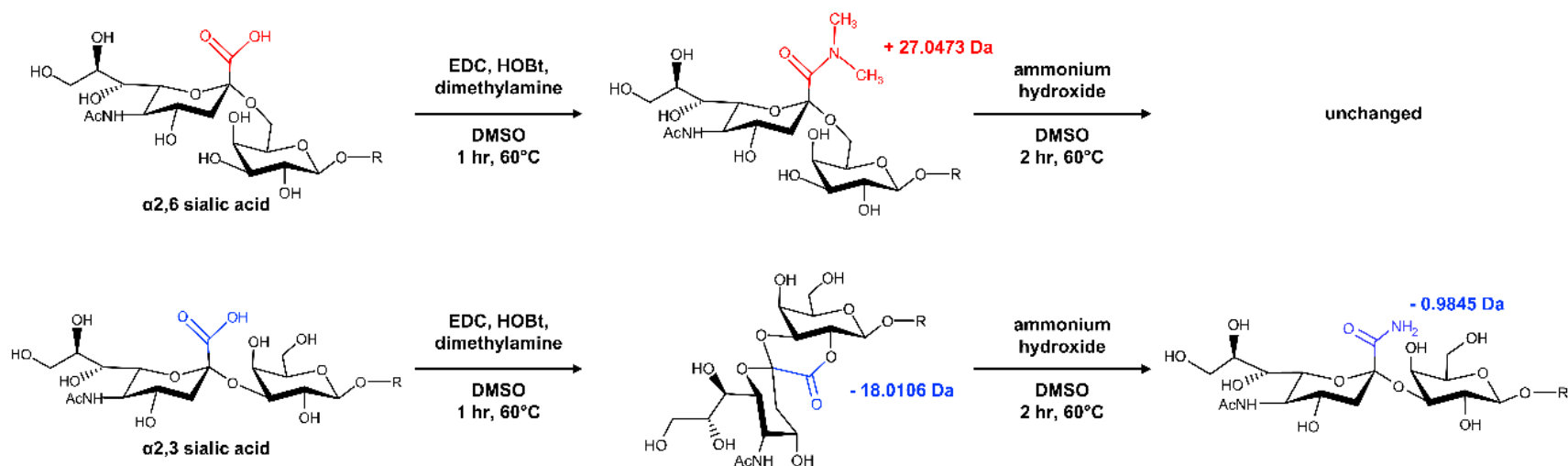
Figure 12. Sialic acid Stabilization and Derivatization by Amidation-Amidation. EDC, HOBt and dimethylamine catalyze the dimethylamidation of α2,6-linked sialic acids and the internal lactonization of α2,3-linked sialic acids. A secondary reaction with ammonium hydroxide decyclizes the α2,3-lactone to form a stable amide. Dimethylamidated α2,6 sialic acids are stable and unreactive.

PDAC biomarker, lacks the specificity for disease detection and thus is used in a surveillance capacity. Surgical resection in combination with adjuvant or neoadjuvant chemotherapy is the only curative treatment option for PDAC, where survival is inversely correlated to disease severity at time of detection and directly linked to tumor resectability. Put simply, the major causative factor in the lethality of PDAC is the failure to detect the disease early prior to metastasis.

As CA19-9 is a carbohydrate modification on serum glycoproteins, researchers have long speculated the existence of other, more sensitive glycan epitopes specific to pancreatic cancer. N-linked glycans – in particular amongst carbohydrates as a class – are sensitive to the temporal physiological health of the cell and for this reason are frequently direct manifestations of aberrant cellular processes in malignant disease. N-glycosylation alterations in PDAC have been previously characterized, where most studies analyze serum glycosylation. The link between N-glycan changes in serum and the N-glycobiology of PDAC tumors, however, has not been established. Better understanding the tumor N-glycome for correlation with that of serum is therefore an attractive area for biomarker discovery.

N-glycans are analyzed with a variety of approaches including the use of lectins, liquid chromatography and mass spectrometry. These techniques should be recognized for their contributions to our understanding of glycan synthesis, structure and function in biological systems, however lectins suffer from specificity issues while LC and LC-MS often require lengthy sample preparation and separation times. Mass spectrometry is often seen as an ideal platform to study N-

glycosylation for its ability to characterize hundreds of analytes at once while retaining high throughput functionality. N-glycan imaging by MALDI-IMS adds a spatial dimension to N-glycan analyses which provides insight into how N-glycans function as part of morphologically defined tissue structures.

In the intersection between aberrant PDAC glycosylation and N-glycan imaging mass spectrometry, we saw an opportunity for a first of its kind study to spatially characterize the pancreatic cancer N-glycome. This novel work applied N-glycan IMS to a histopathologically annotated cohort of pancreatic ductal adenocarcinoma patient tissues and was complimented by orthogonal analyses to characterize fucosylation, sialylation and biomarker expression. Our intention was to use PDAC-specific N-glycan features uncovered by these analyses to complement existing pancreatic cancer biomarkers to better discriminate between pancreatic tumors and benign tissue. Critically, this work may inform future studies that attempt to link tumor N-glycobiology to the PDAC serum glycome and ultimately establish novel carbohydrate biomarkers for the early detection of pancreatic cancer.

Our investigation into the PDAC N-glycome included an analysis of sialic acid isomers stabilized by amidation reactions. Shortcomings inherent to the labeling method used led us to think more deeply about strategies to characterize sialylation isomers. For studies of sialylation, imaging mass spectrometry – and mass spectrometry in general – suffers from the inability to deliver molecular specificity as defined by the capacity to resolve sialic acid isomers by mass alone. Instrumentation and chemical derivatization approaches have been developed to

discriminate between sialic acid isomers, however the field remains in its infancy. As such, we believed this space was wide open for the development of novel derivatization tools targeting sialylated N-glycan isomers. As a credit to the syntheses before it, our approach adapted a previously published chemical amidation reaction for the in situ IMS analysis of sialic acid-containing N-glycans from FFPE tissues[204]. Our goal was to retain the advantages of the previous approach while enhancing isomer separation properties in IMS and to potentiate future bioorthogonal functionalities. Collectively, an investigation into PDAC N-glycosylation and the glycan tools developed from its insights are presented in this dissertation.

Chapter 2: Hypothesis

2.1 Aim 1 Background

Pancreatic ductal adenocarcinoma (PDAC) presents a challenge for clinical management due to typically late detection of the disease, leading to the lowest five-year survival rate of any neoplasia at just 10%[16]. The sole FDA-approved biomarker for PDAC is carbohydrate antigen 19-9 (CA19-9), which is useful for the clinical surveillance of pancreatic cancer progression but because of its affiliation with other malignancies, it is not suitable for specific early detection of PDAC[71]. Another carbohydrate antigen, sialylated tumor-related antigen (sTRA), is under development to complement CA19-9, but the need for more specific biomarkers to delineate PDAC remains pressing[110]. Both CA19-9 and sTRA are carbohydrate motifs found as part of N- and O-linked glycans which decorate glycoproteins and glycolipids comprising the glycocalyx. Glycosylation governs complex interactions between cells and their local microenvironments, and has been implicated in cancer origination, maintenance, signaling and metastatic escape[237,392,393]. N-linked glycans have been shown to be especially sensitive to the development and progression of pancreatic cancer and therefore there is great clinical interest in evaluating N-glycans as PDAC biomarkers[174].

Although many studies have characterized N-glycan changes associated with pancreatic cancer, these works typically examine serum glycoprotein changes which occur concomitantly with the development and progression of the disease[249]. Unfortunately, the relationship between N-glycan changes in serum and those occurring in PDAC tumors is unclear which hinders clinical translation of these findings. Analyses of the PDAC tumor N-glycome often utilize tissue

homogenate and thus fail to capture the spatial component of an N-glycan's expression. No studies to date have comprehensively explored the relationship of N-glycans to malignant tissue structures directly from pancreatic cancer tumors, which may provide insight into glycan or glycoprotein changes associated with morphological hallmarks of disease development, progression or metastasis. Matrix-assisted laser desorption ionization imaging mass spectrometry (MALDI-IMS) is an ideal technology for this application, where the rastered sampling of N-glycan ions in an imaging format allows for the reconstruction of N-glycan heatmaps. These images can be overlaid onto histopathologically defined tissue regions to – for the first time – link pathological features to the expression of particular N-glycans or N-glycan motifs in pancreatic cancer.

To address this gap in our understanding of PDAC tumor N-glycosylation, we proposed a comprehensive investigation into the N-glycome of the pancreas and PDAC by utilizing a MALDI-IMS workflow developed by our lab. Our overall hypothesis was that there are specific changes in N-glycan structural features like sialylation, bisecting GlcNAc residues, branching and fucosylation that are distinct to PDAC and absent from non-diseased tissue. By better understanding the global glycosylation state of pancreatic cancer we hope to discover novel carbohydrate biomarkers to enhance the clinical identification of PDAC and its many subtypes. This hypothesis was examined by the following specific aim.

2.2 Specific Aim 1

Analysis of N-glycosylation patterns in a biomarker-defined FFPE PDAC tissue cohort by MALDI imaging mass spectrometry.

The goal of this aim, presented in Chapter 3, was to analyze N-glycan structural features and spatial localizations in clinically derived formalin-fixed paraffin-embedded PDAC tissues. We chose to apply our analyses to both PDAC tissue microarrays as well as tissue slices from their corresponding pathology blocks. In doing so, we took advantage of MALDI's high throughput capacity to assay a large number of patient samples for statistical significance, as well as its ability to generate spatially encoded information from whole tissue sections. Critical to this latter function was the use of an automated sprayer system for enzyme and matrix application, which prevented the lateral diffusion of released N-glycans away from their in-situ locations. By utilizing a combination of high spatial resolution (timsTOF flex, Bruker) and high mass resolving power (7T solariX, Bruker) instruments, we were able to correlate N-glycan analytes to specific tissue substructures while maintaining high confidence in our spectral assignments. Anomeric linkages of fucose and sialic acid residues for the N-glycans analyzed in this aim were determined via orthogonal enzymatic and chemical amidation approaches, respectively[204,211]. Our N-glycan IMS findings were further complemented by immunofluorescence (IF) assessment of CA19-9 and sTRA expression from the same tissues. To demonstrate the clinical biomarker potential for the glycans evaluated in our study, IMS and IF-derived features were used to build and test classification models for delineation between healthy and cancerous tissue. In the future, correlations between biomarker expression and N-glycan structural features may help reveal which glycans and glycoproteins carry these carbohydrate epitopes. Ultimately, extrapolation of these

findings may lead to discovery of novel N-glycan markers in PDAC serum or plasma samples, a critical first step in the development of a clinically relevant biomarker or biomarker panel for pancreatic cancer.

2.3 Aim 2 Background

The path of discovery in a dissertation is rarely linear. Rather, the evaluation of results, approaches and technologies during the course of research often reveals unanticipated opportunities for further exploration. Such is the case for our study of sialic acids in pancreatic cancer. Sialic acid isomers have biologically distinct functions in health and disease yet are difficult to study in that they only differ by their anomeric linkages[394]. Consequently, resolving these isomers by mass spectrometry is challenging. Ion mobility-coupled mass spectrometers are able to partially separate α2,3, α2,6 and α2,8 linkage isomers, however their ability to resolve sialylated species is inversely proportional to the overall mass of the sialylated glycan[395]. Therefore, multi-antennary sialylated N-glycans known to be overexpressed in pancreatic and other cancers cannot be fully characterized by conventional mass spectrometry approaches. Chemical derivatization strategies, which capitalize on differential stereochemistry between sialylated isomers, are frequently used as an alternative to ion mobility instruments. Through the installation of distinct mass tags on α2,3 and α2,6-linked sialic acid carboxylate groups, these reactions generate spectral distance between isomers in the *m/z* dimension. Permethylation, esterification and amidation reactions targeting sialic acid linkage isomers have shown utility in LC-MS, MALDI-TOF and even MALDI-

IMS experiments, however they often suffer from lengthy sample preparation times and unfavorable overlap between labeled isomers and other analytes of interest[384].

As part of our characterization of PDAC N-glycosylation in Aim 1, we utilized a previously published in-situ sialic acid derivatization approach to explore the spatial distribution of sialic acid linkage isomers in pancreatic cancer[204]. After the chemical amidation reactions in this method, α2,3 and α2,8-linked sialic acids are modified with a -0.9845 Da mass tag while α2,6 isomers are mass shifted by +27.0473 Da. For labeled α2,3 sialic acids, the ~ -1 Da mass shift causes spectral overlap with N-glycan analytes of similar molecular weight, complicating peak annotation and data analysis overall. To address this shortcoming, we proposed the development of our own derivatization reaction with enhanced mass spectrometry separation features. Our hypothesis was that by incorporating more functional mass tags into α2,3 isomers, we could 1) better separate isomeric sialic acid-containing N-glycans in imaging mass spectrometry experiments and 2) potentiate downstream bioorthogonal applications. The development of this novel labeling system is the focus of Specific Aim 2.

2.4 Specific Aim 2

Optimization of a novel sialic acid-targeted derivatization strategy for enhanced imaging mass spectrometry and bioorthogonal functionality.

The goal of this aim was to develop an improved sialic acid-targeted chemical labeling strategy for N-glycan imaging mass spectrometry applications. The amidation-amidation reaction for sialic acid isomer derivatization applied in Aim 1 was used as a starting point. Here, the initial step in this synthesis converts

α2,3 and α2,8 sialic acids into intramolecular lactones, while stably dimethylamidating α2,6 isomers. A second step then decyclizes the unstable lactone with the introduction of ammonium hydroxide, however in theory the lactone is susceptible to ring opening by any amine-containing reagent. Prior work in our lab had explored the use of alkyne and azide-coupled amines to hydrolyze the α2,3 lactone, which showed great promise on sialylated model compounds and proteins. Our theory was that by using alkyne- and azide-amine conjugates we could introduce an azide or alkyne mass tag to α2,3 and α2,8-linked sialic acids. This dual-purpose label introduces a favorable mass shift for IMS and, *critically*, acts as a bioorthogonal, click chemistry compatible handle for more advanced visualization and enrichment approaches. In the first part of this aim, presented in Chapter 4, both propargylamine and azido-PEG$_3$-amine secondary reagents were evaluated for their utility in imaging mass spectrometry experiments on FFPE tissues. Spectral overlap, detection intensity and derivatization efficiency performance metrics were defined for these labeling agents and compared to those for the parent synthesis. The alkyne-based synthesis was further tested on clinical biofluids and cultured cells. Conversely, our azide-based reaction was selected for further click chemistry development and immunohistochemical (IHC) functionality. The bioorthogonal functionality of the azide-introducing scheme was then tested for compatibility with advanced applications. Two developmental efforts, both presented in Chapter 5, were pursued 1) for fluorescent labeling and imaging of azide-tagged α2,3 and α2,8 sialic acids and 2) for solid phase enrichment of α2,3 and α2,8 sialic acid-containing glycoproteins for glycoproteomic

analysis. Through the development of this derivatization protocol, we hope to introduce a novel tool for the study of sialylation into the glycomic space. Current and future applications of our method will increase our collective understanding of the biological functions of sialic acids.

Chapter 3: Detection of Pancreatic Cancer Through N-glycan MALDI-IMS

Imaging Mass Spectrometry and Lectin Analysis of N-Linked Glycans in Carbohydrate Antigen–Defined Pancreatic Cancer Tissues

Colin T.McDowell[1], Zachary Klamer[2], Johnathan Hall[2], Connor A. West[1], Luke Wisniewski[2], Thomas W. Powers[1], Peggi M. Angel[1], Anand S. Mehta[1], David N. Lewin[3]; Brian B. Haab[2], Richard R.Drake[1]

[1]Department of Cell and Molecular Pharmacology and Experimental Therapeutics, Medical University of South Carolina, Charleston, South Carolina, USA

[2]Van Andel Research Institute, Grand Rapids, Michigan, USA

[3]Department of Pathology and Laboratory Medicine, Medical University of South Carolina, Charleston, South Carolina, USA

3.1 Abstract

The early detection of pancreatic ductal adenocarcinoma is a complex clinical obstacle yet is key to improving the overall likelihood of patient survival. Current and prospective carbohydrate biomarkers CA19-9 and sTRA are sufficient for surveilling disease progression yet are not approved for delineating PDAC from other abdominal cancers and non-cancerous pancreatic pathologies. To further understand these glycan epitopes, an imaging mass spectrometry approach was utilized to assess the N-glycome of the human pancreas and pancreatic cancer in a cohort of PDAC patients represented by tissue microarrays and whole tissue sections. Orthogonally, these same tissues were characterized by multi-round immunofluorescence which defined expression of CA19-9 and sTRA as well as other lectins towards carbohydrate epitopes with the potential to improve PDAC diagnosis. These analyses revealed distinct differences not only in N-glycan spatial localization across both healthy and diseased tissues but importantly between different biomarker-categorized tissue samples. Unique sulfated bi-antennary N-glycans were detected specifically in normal pancreatic islets. N-glycans from CA19-9 expressing tissues tended to be bi-, tri- and tetra-antennary structures with both core and terminal fucose residues and bisecting N-acetylglucosamines. These N-glycans were detected in less abundance in sTRA-expressing tumor tissues, which favored tri- and tetra-antennary structures with polylactosamine extensions. Increased sialylation of N-glycans was detected in all tumor tissues. A candidate new biomarker derived from IMS was further explored by fluorescence staining with selected lectins on the same tissues. The lectins confirmed the

expression of the epitopes in cancer cells and revealed different tumor-associated staining patterns between glycans with bisecting GlcNAc and those with terminal GlcNAc. Thus, the combination of lectin-IHC and IMS techniques produces more complete information for tumor classification than the individual analyses alone (Figure 13). These findings potentiate the development of early assessment technologies to rapidly and specifically identify PDAC in the clinic that may directly impact patient outcomes.
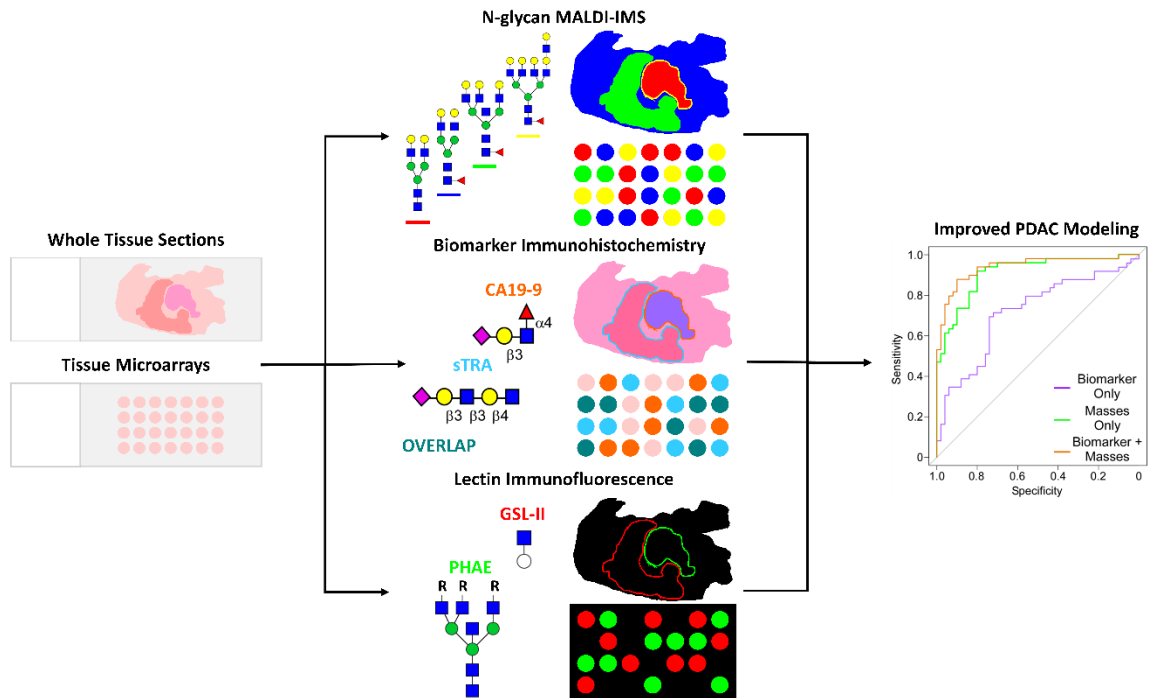
Figure 13. Combining N-glycan MALDI IMS, Biomarker IHC and Lectin IF. Graphical Abstract.

3.2 Introduction

As previously described, pancreatic ductal adenocarcinomas (PDAC) are aggressive neoplasia diagnosed in approximately 58,000 patients in the United States with nearly 47,000 recorded deaths during the year 2020, and both metrics are predicted to continue to increase. PDAC accounts for 7% of total cancer deaths and has the lowest 5-year survival rate of any cancer at just 9% for all stages combined[11,12]. The high mortality associated with pancreatic cancer is due to late detection of the disease as compared to other cancers, with 30% of patients diagnosed at the locally invasive stage, 13% at the locally advanced stage and 52% at the metastatic stage[17]. The typically late identification of PDAC owes to the heterogeneity of often-mild early-stage symptoms, the location of the pancreas deep within the abdominal cavity and the lack of reliable biomarkers for early identification. Currently, the sole FDA-approved biomarker for pancreatic cancer is carbohydrate antigen 19-9 (CA19-9), increased levels of which are associated with the majority of PDAC cases. Despite CA19-9's utility as a prognostic indicator for judging the effectiveness of a patient's treatment regiment, the antigen's association with other cancers and non-cancer malignancies such as cystic fibrosis, pancreatitis and liver disease make it unsuitable as a diagnostic predictor for pancreatic cancer[71]. The glycan epitope of the CA19-9 antibody appears on the surface of cancer cells in about 60% of PDACs. Another glycan marker called sTRA, recently discovered as a biomarker of pancreatic cancer, likewise appears in the majority of tumors but in a non-identical subgroup of tumors[110]. Some tumors have only one of the glycans, some have both and some have neither. Together,

these two antigens are in development for clinical use as a means of pancreatic cancer surveillance and differentiation between pancreatic cancer and other pancreatic diseases. Because CA19-9 and sTRA only recognize sialyl-Lewis A (sLeA) and a de-sialylated Type 1 Type 2 LacNAc carbohydrate motifs, respectively, an important aspect of better understanding their ability to recognize PDAC is the elucidation of specifically which glycans or glycoproteins these antibodies are binding to, and what role these molecules play in the biological processes underlying the development of pancreatic cancer.

An important and yet often under-studied aspect of cancer biology – and a major focus of this dissertation – is the glycocalyx, the dense layer of complex carbohydrates that plays a significant role in governing the interactions between cancer cells, immune cells and the local microenvironment. The glycocalyx is composed of N- and O- linked glycans attached to a wide variety of glycoproteins, glycosaminoglycans attached to proteoglycans and glycolipids. The majority of human proteins and lipids have glycan modifications, which play key roles in protein folding, cell-cell communication, intracellular trafficking and signal transduction amongst other functions[392]. Consequently, aberrations in glycosylation state often result in or are indicators of disease, and many glycoproteins or glycans are known biomarkers of cancer. Indeed, it has been well studied that changes in glycan structure and composition can alter the metastatic capacity and the invasive spread of cancer cells[393]. Of specific interest to pancreatic cancer is N-linked glycosylation (attached to the asparagine residue in Asn-X-Ser/Thr protein motifs) which is known to play a role in immune recognition,

cellular mobility and cell signaling. Increases in N-glycan branching, fucosylation and sialylation have also previously been associated with PDAC[237].

In an attempt to better define the N-linked glycome of pancreatic cancer directly in clinical tissues, we have used matrix assisted laser desorption ionization imaging mass spectrometry (MALDI-IMS) to identify peptide N-glycosidase released N-glycans linked spatially and histochemically to pathology features. This method has been used to map N-glycan distribution across multiple cancer types using formalin-fixed paraffin embedded (FFPE) tissue samples[181,200,202,207,210,211,213,216,233,393,396]. When complemented with histopathological identification, this combined analysis can map correlations between specific glycans or groups of glycans and different tissue regions and subtypes including tumor, necrotic and adjacent normal tissues[210]. The present study analyzes the N-glycome of the pancreas and of PDAC. A majority of previous studies on the role of glycosylation in pancreatic cancer have focused on serum profiling of N-glycans as well as the truncation of O-linked glycosylation and increased O-GlcNAcylation[237]. As outlined in Chapters 1 and 2, comprehensive spatial mapping of N-glycan distribution in normal and pancreatic cancer tissues is lacking, and correlative mapping of N-glycans to IHC staining of current and prospective pancreatic cancer biomarkers has only recently begun to be explored[109]. The current study addresses this using a MALDI-IMS approach to characterize the N-glycans present in healthy pancreatic tissue and a cohort of pancreatic cancer tissues represented by multiple tissue microarrays (TMAs) and a subset of the source whole-block tissue slices. Changes in tissue glycans

associated with PDAC were further correlated with antibody-based assessments for CA19-9, sTRA and other carbohydrate epitopes in the same tissues. The cumulative analyses revealed multiple subsets of N-glycans with increased branching, bisecting N-acetylglucosamine, fucosylation and sialylation in PDAC-specific regions of tissues, many of which could be correlated with each carbohydrate antigen biomarker.

3.3 Materials and Methods

3.3.1 Materials

HPLC-grade acetonitrile, ethanol, methanol, xylene and water as well as CitriSolv Hybrid were obtained from Fisher Scientific (Pittsburg, PA, USA). 28-30% Ammonia in H_2O, bovine serum albumin (BSA), dimethyl sulfoxide (DMSO), citraconic anhydride and 1X phosphate buffered saline (PBS) were obtained from Thermo Scientific (Bellefonte, PA, USA). Acetic acid, alpha-cyano-4-hydroxycinnamic acid (CHCA), chloroform, 4′,6-diamidino-2-phenylindole (DAPI), dimethylamine, hydrogen peroxide (H_2O_2), 1-hydroxybenzotriazole hydrate (HOBt), sodium bicarbonate, trifluoroacetic acid (TFA), Triton-X100 and Tween-20 were obtained from Sigma-Aldrich (St. Louis, MO, USA). 1-(3-Dimethylaminopropyl)-3-ethylcarbodiimide (EDC) was obtained from Alfa-Aesar (Ward Hill, MA, USA). Recombinant PNGase F PRIME^{TM} was obtained from N-Zyme Scientific (Doylestown, PA, USA) and recombinant Endoglycosidase F3 (Endo F3) was obtained from the laboratory of Dr. Anand Mehta (Charleston, SC, USA) as described[207,211]. Hematoxylin and eosin (H&E) stains were obtained from Cancer Diagnostics (Durham, NC, USA). Horseradish peroxidase-3,3′-

diaminobenzidine (HRP-DAB) staining kits were obtained from R&D Systems (Minneapolis, MN, USA). CA19-9 mAb was obtained from USBiologicals (Salem, MA, USA). TRA-1-60 mAb was obtained from Novus Biologicals (Littleton, CO, USA). Sulfo-cyanine3 NHS and sulfo-cyanine5 NHS esters were obtained from Lumiprobe (Hunt Valley, MD, USA). TRITC conjugated anti-PHA-E, biotinylated GSL-II and Cy5-conjugated streptavidin were obtained from EY Laboratories (San Mateo, CA, USA), Vector Laboratories (Burlingame, CA, USA) and Roche Applied Science (Penzberg, Germany) respectively. α2-3,6,8 Neuraminidase and 1X Glycobuffer were obtained from New England Biolabs (Ipswich, MA, USA).

3.3.2 Clinical Pancreatic Cancer FFPE Tissues

Four formalin-fixed paraffin-embedded pancreatic cancer TMAs (n = 53 patients) were provided by the Medical University of South Carolina's Hollings Cancer Center Biorepository and Tissue Analysis Shared Resource in accordance with the National Cancer Institute's Best Practices for Biospecimen Resources. 51/53 cases of the pancreatic cancer cohort were adenocarcinomas with the remaining 2/53 cholangiocarcinoma and adenosquamous carcinoma. Each case was represented by a minimum of 4 cores, 2 from adjacent tissue and 2 from tumor tissue. Furthermore, 23/53 cases also had representative pre-tumor tissue, 29/53 had metastatic tissue, 22/53 had lymph node tissue and 14/53 had lymph node tumor tissue. The staging of the cases ranged from T1NOMX (2 cm or smaller tumor localized to pancreas, absent from regional lymph nodes) to T4N1MX (4 cm or larger tumor extending into local major arteries, spread to 1-3 regional lymph nodes) with most cases staged at T3N1MX (4 cm or larger tumor extending beyond

pancreas, spread to 1-3 regional lymph nodes)[397]. The majority of the patients'

tumors were moderately to poorly differentiated. 13/53 patients experienced

recurrence, mostly at distant sites such as the lungs and liver. More detailed

information is contained in Table 4. Full tissue slices of thirteen PDAC pathology

blocks that were the original sources of the tumor cores in the TMAs mentioned

above were also analyzed. All cases were adenocarcinomas, the majority of which

were staged at T3N1MX. Normal human pancreas FFPE tissue slides were

obtained from Zyagen (San Diego, CA, USA).

3.3.3 N-glycan MALDI-IMS

3.3.3.1 Tissue Preparation for MALDI-IMS

A standardized protocol was used for tissue preparation, enzymatic

digestion and matrix application by solvent sprayer[396]. Tissue slides were dewaxed

in xylenes then rehydrated in a gradation of ethanol and water washes prior to

antigen retrieval with citraconic anhydride buffer (25 µL citraconic anhydride, 2 µL

12 M HCL, 50 mL HPLC-grade H_2O, pH 3.0 ± 0.5) for 30 minutes in a decloaking

chamber at 95ºC. 15 passes of PNGase F or 10% Endo F3/90% PNGase F at 0.1

µg/µL were then sprayed onto the slides at a rate of 25 µL/min with a 3 mm offset

and a velocity of 1200 at 45ºC and 10 psi using a M5 TMSprayer (HTX

Technologies LLC., Chapel Hill, NC). Tissue slides were then incubated at 37ºC

for 2 h in pre-warmed humidity chambers followed by desiccation prior to matrix

application. 10 passes of 7 mg/mL CHCA matrix in 50% acetonitrile/0.1% TFA was

applied to the desiccated slides at 0.1 mL/min with a 2.5 mm offset and a velocity

Table 4. Associated Clinical Data for the Pancreatic Cancer Patient Cohort.

TB#	Race	Sex	Age	Vital Status	Recurrence	Type of Recurrence	Days between Surgery and Recurrence	Days between Surgery and Date of last contact/Death	Histological Type	Histological Grade	Staging
2204	WHITE	M	75	Unknown	Unknown	N/A	N/A	272	Adenocarcinoma	moderately differentiated	T3NOMX
2278	WHITE	M	76	Unknown	Unknown	N/A	N/A	211	cholangiocarcinoma	moderately differentiated	T3N1MX
2279	WHITE	F	61	Unknown	YES	distant recurrence - GAST	2233	2486	Adenocarcinoma	well differentiated	T3NOMX
2381	WHITE	M	73	Unknown	YES	Distant recurrence - CNS	2499	2587	Mucinous Adenocarcinoma	Not Reported	
2417	WHITE	M	80	Unknown	Unknown	N/A	N/A	23	Adenocarcinoma	poorly differentiated	T3N1MX
2454	WHITE	F	69	Unknown	Unknown	N/A	N/A	Unknown	Adenocarcinoma	moderately differentiated	T3NOMX
2487	BLACK	M	73	Unknown	Unknown	N/A	N/A	106	Adenocarcinoma	well differentiated	T3N1MX
2464	BLACK	F	61	Unknown	YES	metasticized to liver and omentum	N/A	Unknown	Adenocarcinoma	poorly differentiated	T4N1Mx
1751	WHITE	M	65	Unknown	Unknown	N/A	N/A	101	Adenocarcinoma	well differentiated	T3N1MX
1800	BLACK	F	67	Unknown	Unknown	N/A	N/A	204	Adenocarcinoma	poorly differentiated	T3N1MX
1691	WHITE	M	69	Unknown	Unknown	N/A	N/A	92	Adenocarcinoma	Not Reported	T3N1MX
1848	WHITE	M	71	Unknown	NO	Never disease free	N/A	314	Adenocarcinoma	poorly differentiated	T3N1MX
1911	WHITE	M	83	Unknown	NO	Disease free	N/A	118	Adenocarcinoma	moderately differentiated	T3N1MX
1747	WHITE	F	63	Unknown	NO	Possible recurrence	N/A	138	Adenocarcinoma	poorly differentiated	T3N1MX
1673	WHITE	M	78	Unknown	NO	Disease free	N/A	440	Adenocarcinoma	moderately differentiated	T3N1
1685	BLACK	M	66	Unknown	NO	Never disease free	N/A	173	Adenocarcinoma	poorly differentiated	T3N1MX
1987	WHITE	F	58	Unknown	NO	Disease free	N/A	404	Adenocarcinoma	moderately differentiated	T3N1MX
2055	WHITE	M	69	Unknown	Unknown	N/A	N/A	808	Adenocarcinoma	poorly differentiated	T3NXMX
1955	BLACK	F	51	Unknown	Unknown	N/A	N/A	392	Adenocarcinoma	moderately differentiated	T3N1MX
1958	WHITE	M	42	Unknown	Unknown	N/A	N/A	429	Adenocarcinoma	poorly differentiated	T3N1MX
1982	WHITE	F	66	Unknown	Unknown	N/A	N/A	336	Adenocarcinoma	moderately differentiated	T2N1MX
2572	WHITE	F	87	Unknown	NO	Disease free	N/A	1387	Adenocarcinoma	moderately differentiated	T1NOMX
2091	WHITE	F	54	Unknown	YES	Local Recurrence	406	547	Adenocarcinoma	Not Reported	T2NOMX
2495	WHITE	M	56	Dead	NO	Never disease free	N/A	76	Adenocarcinoma	Not Reported	T3N1MX
2807	BLACK	F	62	Unknown	NO	Never disease free	N/A	126	Adenocarcinoma	poorly differentiated	T3NOMX
2815	WHITE	F	76	Unknown	Unknown	N/A	N/A	Unknown	Ductal adenocarcinoma	moderately differentiated	T3NOMX
2893	BLACK	F	68	Unknown	YES	Local recurrence	613	613	Adenocarcinoma	moderately differentiated	T3N1MX
2916	WHITE	F	37	Unknown	YES	Distant recurrence	165	236	Adenocarcinoma	moderately differentiated	T3N1MX
2790	WHITE	M	78	Unknown	NO	Never disease free	N/A	32	Adenocarcinoma	moderately differentiated	T2N1bMX
2695	WHITE	M	70	Unknown	NO	Never disease free	N/A	185	Adenocarcinoma	Not Reported	T2NOMX
3721	WHITE	F	66	Unknown	NO	Never diease free	N/A	50	Ductal adenocarcinoma	poorly differentiated	T3N0MX
3627	BLACK	F	84	Unknown	Unknown	N/A	N/A	Unknown	Adenocarcinoma	moderately differentiated	T2N1MX
3508	WHITE	M	49	Unknown	NO	Never disease free	N/A	221	Adenocarcinoma	moderately differentiated	T3N1MX
3727	WHITE	M	74	Unknown	YES	Distant recurrence	140	140	Adenosquamous carcinoma	moderately differentiated	T3NOMX
3499	WHITE	F	66	Unknown	NO	Disease free	N/A	125	Ductal adenocarcinoma	Not Reported	T1NOMX
3463	WHITE	F	64	Unknown	NO	Disease free	N/A	215	Ductal adenocarcinoma	moderately differentiated	T3N1MX
3832	WHITE	M	68	Unknown	YES	Distant recurrence - LUNG	332	353	Adenocarcinoma	moderately differentiated	T3N1MX
3978	WHITE	M	63	Unknown	NO	Disease free	N/A	25	Adenocarcinoma	Not Reported	T2N1bMX
3922	BLACK	M	72	Unknown	NO	Disease free	N/A	94	Ductal adenocarcinoma	moderately differentiated	T1NOMX
3986	WHITE	F	70	Unknown	NO	Disease free	N/A	27	Adenocarcinoma	poorly differentiated	T3N1MX
3406	WHITE	F	74	Unknown	NO	Disease free	N/A	62	Ductal adenocarcinoma	moderately differentiated	T3N1MX
4038	WHITE	M	71	Unknown	YES	Distant recurrence - LUNG	525	318	Adenocarcinoma	moderately differentiated	T3N1MX
3859	WHITE	F	50	Dead	YES	Distant recurrence - HEPT	196	202	Ductal adenocarcinoma	moderately differentiated	T3N1MX
3915	WHITE	F	53	Dead	YES	Distant recurrence - LUNG	1182	1213	Ductal adenocarcinoma	moderately differentiated	T2N0MX
3891	WHITE	F	62	Unknown	Unknown	N/A	N/A	1148	Ductal adenocarcinoma	moderately differentiated	T3N1bM
3886	WHITE	M	62	Unknown	YES	Distant recurrence - HEPT	337	604	Adenocarcinoma	moderately differentiated	T3N1bMX
4072	WHITE	F	71	Unknown	NO	Disease free	N/A	27	Ductal adenocarcinoma	moderately differentiated	T3N0MX
4524	WHITE	F	60	Unknown	NO	Disease Free	N/A	130	Ductal adenocarcinoma	moderately differentiated	T3N1MX
4071	BLACK	M	64	Unknown	NO	Disease Free	N/A	43	Ductal adenocarcinoma	moderately differentiated	T1N1bMX
4365	WHITE	F	78	Unknown	NO	Disease Free	N/A	90	Adenocarcinoma	moderately differentiated	T1NOMX
4180	WHITE	M	87	Unknown	NO	Disease Free	N/A	69	Adenocarcinoma	poorly differentiated	T3N1bMX
4374	BLACK	M	51	Unknown	YES	Distant recurrence - HEPT	735	736	Ductal adenocarcinoma	moderately differentiated	T3N1MX
4257	ASIAN	M	39	Dead	NO	Never disease free	N/A	9	Ductal adenocarcinoma	moderately differentiated	T3N1MX

of 1300 at 80ºC and 10 psi using the TMSprayer. After matrix application slides were desiccated until analysis by MALDI-FTICR MS or MALDI quadrupole time-of-flight mass spectrometry (MALDI-QTOF MS). Post-analysis whole tissue slides were H&E stained according to a standardized protocol and annotated for histological classification by an expert pathologist.

3.3.3.2 Amidation-Amidation Stabilization of Sialic Acids

Sialic acids were stabilized by chemical amidation directly on tissue using an established protocol, with some slight modifications as follows[204]. Tissue slides were dewaxed and rehydrated as described above then incubated with 200 µL of primary reaction solution (22 µL EDC, 42.2 mg HOBt, 15.8 µL dimethylamine, 0.5 mL DMSO) for 1 hour at 60ºC. After incubation tissues were washed with 200 µL DMSO 3X then incubated with 200 µL of secondary reaction solution (150 µL 28-30% Ammonia in H_2O, 350 µL DMSO) for 2 hours at 60ºC. Following the second incubation slides were rinsed sequentially in 100% EtOH for 2min 2X, Carnoy's Solution (30% chloroform, 60% EtOH, 10% acetic acid) for 10 min 2X, H_2O for 1 min, 100% EtOH for 2 min 2X and 0.1% TFA in EtOH for 30 seconds. Slides were then immediately processed for MALDI-IMS as described above starting with antigen retrieval.

3.3.3.3 MALDI IMS Analysis of N-glycosylation

A Solarix dual source 7T FTICR mass spectrometer (Bruker Daltonics, Bremen, Germany) (*m/z* 490-5000) equipped with a 2000 Hz SmartBeam II laser utilizing a laser spot size of 25 µm was used to detect PNGase F released N-glycans in positive ion mode. Using the Smartwalk feature set at a width of 30 µm

97

and one scan per pixel, 200 laser shots per pixel were collected for analysis with an ion accumulation time of 0.1 s. A 1.2059 s transient with a calculated resolving power of 160,000 at *m/z* 400 was used over a mass range of 500-5000 *m/z* and a time domain set to 512K word. A timsTOF Flex trapped ion mobility separated QTOF mass spectrometer (Bruker Daltonics, Bremen, Germany) (*m/z* 500 – 4000) operating in positive mode equipped with a 10 kHz Smartbeam 3D laser and a spot size of 20 µm was used to detect released N-glycans with high spatial resolution (20 – 40 µm raster). 300 laser shots per pixel were collected with an ion transfer time of 125 µs, a pre-pulse storage time of 25 µs, a collision RF of 4000 Vpp, a multipole RF of 500 Vpp and a collision cell energy of 15 eV. Instrument parameters for collision-induced dissociation (CID) are reported in Figure 14.

3.3.3.4 Data Processing

After MS data acquisition, spectra were imported to SCiLS Lab 2017a and 2020a imaging software for analysis of the mass range *m/z* 500-4000. SCiLS-generated N-glycan spectra were normalized to total ion count (ICR Noise Reduction Threshold = 0.95) which were then matched within ± 5 ppm against an in-house database of known N-glycans generated using GlycoWorkbench and GlycoMod for annotation[360,361]. N-glycan structures annotated in this paper are compositionally accurate as determined by accurate mass, CID and through prior structural characterizations by both MALDI-TOF-MS/MS and RP-LC-MS/MS[315]. A list of all N-glycans reported in this chapter along with mass error calculations and representative structures can be found in Tables 5 and 6.

timsTOF Flex MALDI-QTOF MS/MS Settings

Transfer
Funnel 1 RF: 425.0 Vpp
Funnel 2: RF: 500.0 Vpp
Multipole RF: 550.0 Vpp
Deflection Δ: 70.0 V
MALDI Plate Offset: 50.0 V

MS Settings
Scan Begin: 50 *m/z*
Scan End: 2500 *m/z*
Ion Polarity: Positive
Scan Mode: MS/MS
Laser Shots: 400
Laser Power: 36%
Frequency: 10000 Hz

Pre-TOF Focus
Transfer Time: 72.0 μs
Pre-Pulse Storage: 12.0 μs

Collision Cell
Collision Energy: 25.0 eV
Collison RF: 1500.0 Vpp

Quadrupole
Ion Energy: 4.0 eV
Low Mass: 150 *m/z*

CID Settings
Isolation Width: 10.00 *m/z*
Collision Energy: 150.00 eV

Notes on CID

CID fragmentation of 23 N-glycan base structures representing a mix of both core and terminally-fucosylated bi-, tri- and tetra-antennary configurations with and without bisecting GlcNAc residues. Where applicable EndoF3 was used to trim higher-mass core-fucosylated N-glycans to improve CID performance

CID Legend

X,Y,Z ions
B,C ions
Intermixed X,Y,Z/B,C ions
**Precursor ions**

Example MS/MS
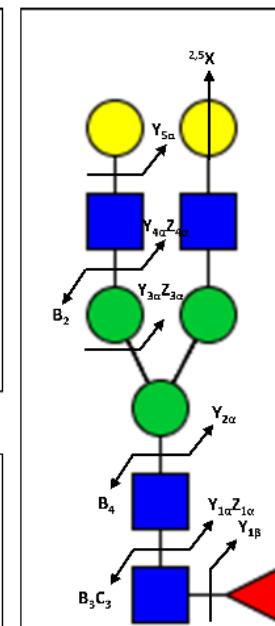
Figure 14. Structural Annotation of Reported N-glycans by CID Fragmentation. Relevant instrument settings for collision-induced dissociation are provided, along with example fragmentation patterns. Intended to be used as a key for CID spectra referenced further in this dissertation.

Table 5. Composition and Mass Accuracy of N-glycans in this Chapter.

Composition	Theoretical Mass	Observed Mass	Mass Error	Composition	Theoretical Mass	Observed Mass	Mass Error	Composition	Theoretical Mass	Observed Mass	Mass Error
Hex3dHex1HexNAc2 + Na	1079.3749	1079.3735	1.2961	Hex5HexNAc5(2,6)NeuAc1 + Na	2184.8035	2184.8077	1.9224	Hex6dHex4HexNAc5(2,3)NeuAc1 + Na	2903.0566	2903.0591	0.8612
Hex3HexNAc3 + Na	1136.3961	1136.3971	0.6169	Hex5dHex1HexNAc6 + Na	2215.7980	2215.7952	1.2637	Hex8dHex1HexNAc7 + Na	2906.0393	2906.0507	3.9229
Hex5HexNAc2 + Na	1257.4226	1257.4224	0.1583	Hex6HexNAc6 + Na	2232.7964	2232.7902	2.7589	Hex7dHex1HexNAc6 + Na	2979.0808	2979.0835	0.9063
Hex3dHex1HexNAc3 + Na	1282.4543	1282.4522	1.6367	Hex3dHex2HexNAc6 + Na + 2S	2242.6469	2242.6535	2.9430	Hex6dHex1HexNAc6(2,3)NeuAc1(2,6)NeuAc1 + Na	2986.1050	2986.1060	0.3349
Hex4HexNAc3 + Na	1298.4492	1298.4495	0.2318	Hex5HexNAc4(2,3)NeuAc2 + Na	2243.8042	2243.8000	1.8718	Hex6dHex2HexNAc7(2,3)NeuAc1 + Na	3017.0996	3017.1001	0.1657
Hex6HexNAc2 + Na	1419.4754	1419.4769	1.0574	Hex5dHex2HexNAc4(2,3)NeuAc1 + Na	2245.8086	2245.8094	0.3562	Hex7dHex3HexNAc7 + Na	3036.1023	3036.1050	0.8893
Hex4dHex1HexNAc3 + Na	1444.5071	1444.5063	0.5531	Hex5HexNAc4(2,3)NeuAc1(2,6)NeuAc1 + Na	2271.8355	2271.8445	3.9616	Hex6dHex2HexNAc7(2,6)NeuAc1 + Na	3045.1309	3045.1407	3.2183
Hex5HexNAc3 + Na	1460.5020	1460.5026	0.4115	Hex4dHex2HexNAc5(2,3)NeuAc1 + Na	2286.8352	2286.8368	0.6997	Hex6dHex3HexNAc5(2,3)NeuAc2 + Na	3047.1101	3047.0993	3.5443
Hex3dHex1HexNAc4 + Na	1485.5337	1485.5338	0.0680	Hex5dHex1HexNAc5(2,3)NeuAc1 + Na	2302.8301	2302.8257	1.9107	Hex8HexNAc7(2,3)NeuAc1 + Na	3049.0894	3049.0859	1.1479
Hex4HexNAc4 + Na	1501.5286	1501.5282	0.2657	Hex5dHex3HexNAc5 + Na	2304.8345	2304.8318	1.1710	Hex8dHex1HexNAc8 + Na	3109.1187	3109.1186	0.0322
Hex3HexNAc5 + Na	1542.5552	1542.5536	1.0366	Hex6dHex1HexNAc5(2,3)NeuAc1 + Na	2318.8250	2318.8205	1.9406	Hex7dHex3HexNAc6(2,3)NeuAc2 + Na	3120.1265	3120.1198	2.1473
Hex7HexNAc2 + Na	1581.5282	1581.5320	2.4034	Hex6dHex2HexNAc5 + Na	2320.8294	2320.8242	2.2401	Hex7dHex3HexNAc6(2,3)NeuAc1 + Na	3122.1309	3122.1277	1.0249
Hex4HexNAc3(2,3)NeuAc1 + Na	1588.5606	1588.5557	3.0846	Hex5dHex1HexNAc5(2,6)NeuAc1 + Na	2330.8614	2330.8532	3.5180	Hex9HexNAc8 + Na	3174.1353	3174.1252	3.2379
Hex5dHex1HexNAc3 + Na	1606.5599	1606.5528	4.4188	Hex6HexNAc5(2,6)NeuAc1 + Na	2346.8563	2346.8634	3.0253	Hex6HexNAc6(2,3)NeuAc2(2,6)NeuAc1 + Na	3130.1585	3130.1478	3.4184
Hex4dHex1HexNAc4 + Na	1647.5865	1647.5862	0.1815	Hex6dHex1HexNAc6 + Na	2377.8509	2377.8482	1.1351	Hex6dHex2HexNAc6(2,3)NeuAc2(2,6)NeuAc1 + Na	3132.1629	3132.1748	3.7993
Hex5HexNAc4 + Na	1663.5814	1663.5831	1.0225	Hex5HexNAc6(2,6)NeuAc1 + Na	2387.8828	2387.8879	2.1358	Hex7dHex2HexNAc7(2,3)NeuAc1 + Na	3179.1524	3179.1513	0.3460
Hex3dHex1HexNAc5 + Na	1688.6131	1688.6128	0.1771	Hex4dHex1HexNAc5(2,3)NeuAc2 + Na	2389.8621	2389.8575	1.9248	Hex8dHex2HexNAc8 + Na	3255.1766	3255.1788	0.6758
Hex4HexNAc5 + Na	1704.6080	1704.6083	0.1766	Hex5dHex3HexNAc4(2,3)NeuAc1 + Na	2391.8665	2391.8600	2.7175	Hex7HexNAc6(2,3)NeuAc3 + Na	3264.1800	3264.1855	1.6850
Hex4dHex1HexNAc3(2,3)NeuAc1 + Na	1734.6158	1734.6101	3.2860	Hex7HexNAc6 + Na	2393.8458	2393.8466	0.3346	Hex7dHex2HexNAc6(2,3)NeuAc2 + Na	3266.1844	3266.1844	0.0000
Hex8HexNAc2 + Na	1743.5810	1743.5814	0.2300	Hex5dHex1HexNAc4(2,3)NeuAc1(2,6)NeuAc1 + Na	2417.8934	2417.8946	0.4963	Hex7dHex4HexNAc6(2,3)NeuAc1 + Na	3268.1888	3268.1996	3.3046
Hex5HexNAc3(2,3)NeuAc1 + Na	1750.6134	1750.6177	2.4563	Hex5dHex3HexNAc4(2,6)NeuAc1 + Na	2419.8978	2419.9008	1.2397	Hex9dHex1HexNAc8 + Na	3270.1681	3270.1758	2.3549
Hex4HexNAc4(2,3)NeuAc1 + Na	1791.6189	1791.6489	0.0000	Hex5dHex2HexNAc5(2,3)NeuAc1 + Na	2448.8880	2448.8986	4.3285	Hex7dHex1HexNAc7(2,3)NeuAc2 + Na	3323.2059	3323.2070	0.3310
Hex5dHex1HexNAc4 + Na	1809.6393	1809.6394	0.0558	Hex6dHex1HexNAc5(2,3)NeuAc1 + Na	2464.8829	2464.8741	3.5701	Hex7dHex3HexNAc7(2,3)NeuAc1 + Na	3325.2103	3325.2053	1.5037
Hex4dHex1HexNAc5 + Na	1850.6659	1850.6646	0.7019	Hex6dHex3HexNAc5 + Na	2466.8873	2466.8915	1.7030	Hex7dHex5HexNAc7 + Na	3328.2181	3328.2107	2.2234
Hex5HexNAc5 + Na	1866.6608	1866.6627	1.0184	Hex5HexNAc5(2,3)NeuAc1(2,3)NeuAc1 + Na	2474.9149	2474.9121	1.1314	Hex6dHex1HexNAc6(2,6)NeuAc3 + Na	3332.2790	3332.2829	1.1704
Hex3dHex1HexNAc6 + Na	1891.6925	1891.6903	1.1625	Hex6dHex3HexNAc6 + Na	2507.9139	2507.9015	4.9443	Hex7dHex1HexNAc6(2,3)NeuAc3 + Na	3410.2379	3410.2364	0.4399
Hex9HexNAc2 + Na	1905.6338	1905.6345	0.3679	Hex6dHex2HexNAc6 + Na	2523.9088	2523.9113	0.9909	Hex7dHex2HexNAc7(2,3)NeuAc2 + Na	3469.2638	3469.2783	4.1796
Hex5dHex1HexNAc4 + 2Na + S	1911.5859	1911.5781	4.0636	Hex6dHex1HexNAc7 + Na	2581.9336	2581.9336	0.0155	Hex8dHex1HexNAc7(2,3)NeuAc2 + Na	3485.2587	3485.2551	1.0329
Hex6HexNAc3(2,3)NeuAc1 + Na	1912.6662	1912.6619	2.2482	Hex5dHex1HexNAc5(2,3)NeuAc2 + Na	2592.9415	2592.9445	1.1570	Hex8dHex3HexNAc7(2,3)NeuAc1 + Na	3487.2631	3487.2583	1.3764
Hex4dHex1HexNAc4(2,3)NeuAc1 + Na	1937.6979	1937.6928	2.6320	Hex5dHex3HexNAc5(2,3)NeuAc1 + Na	2594.9459	2594.9536	2.9673	Hex7dHex2HexNAc6(2,3)NeuAc3 + Na	3544.2846	3544.2935	2.5111
Hex4dHex1HexNAc5 + Na + S	1952.6175	1952.6059	3.3801	Hex7HexNAc7 + Na	2596.9752	2596.9769	0.6550	Hex7dHex2HexNAc6(2,3)NeuAc3 + Na	3556.3210	3556.3148	1.7434
Hex5HexNAc4(2,3)NeuAc1 + Na	1953.6978	1953.6978	0.0000	Hex6HexNAc5(2,3)NeuAc2 + Na	2608.9364	2608.9475	4.2546	Hex7dHex4HexNAc6(2,3)NeuAc2 + Na	3558.3002	3558.3117	3.2319
Hex5dHex2HexNAc4 + Na	1955.6972	1955.6959	0.6642	Hex6dHex2HexNAc5(2,3)NeuAc1 + Na	2610.9408	2610.9421	0.4979	Hex7dHex2HexNAc6(2,3)NeuAc2 + Na	3560.2795	3560.2885	2.5279
Hex3dHex1HexNAc6 + Na + S	1993.6390	1993.6337	2.6585	Hex6dHex4HexNAc5 + 1Na	2613.9486	2613.9419	2.5632	Hex9dHex1HexNAc8(2,6)NeuAc1 + Na	3588.3108	3588.3089	0.5295
Hex4HexNAc5(2,3)NeuAc1 + Na	1994.7193	1994.7098	4.7626	Hex6dHex1HexNAc6(2,3)NeuAc1 + Na	2667.9623	2667.9623	0.0000	Hex8dHex4HexNAc7(2,3)NeuAc1 + Na	3633.3210	3633.3287	2.1193
Hex4dHex2HexNAc5 + Na	1996.7238	1996.7235	0.1502	Hex6dHex3HexNAc6 + Na	2669.9667	2669.9796	4.8319	Hex10dHex1HexNAc9 + Na	3636.3037	3636.2973	1.7600
Hex5dHex1HexNAc6 + Na	2012.7187	2012.7180	0.3473	Hex7dHex2HexNAc6 + Na	2685.9616	2685.9595	0.7815	Hex8dHex1HexNAc8(2,3)NeuAc1 + Na	3674.3476	3674.3471	0.1361
Hex4HexNAc5(2,6)NeuAc1 + Na	2022.7506	2022.7546	1.9775	Hex7dHex1HexNAc7 + Na	2742.9831	2742.9857	0.9482	Hex7dHex3HexNAc6(2,3)NeuAc3 + Na	3702.3789	3702.3866	2.0797
Hex6HexNAc5 + 2Na + S	2028.7136	2028.7158	1.0849	Hex5dHex1HexNAc5(2,3)NeuAc2 + Na	2754.9943	2754.9948	0.1815	Hex8dHex4HexNAc8(2,3)NeuAc1 + Na	3704.3330	3704.3417	2.3486
Hex5dHex1HexNAc4 + 2Na + S	2057.6438	2057.6533	4.6325	Hex5dHex3HexNAc5(2,3)NeuAc1 + Na	2756.9987	2756.9994	0.2539	Hex9dHex1HexNAc8 + Na	3709.3452	3709.3412	1.0784
Hex6dHex1HexNAc3(2,3)NeuAc1 + Na	2058.7242	2058.7323	3.9345	Hex6dHex2HexNAc6(2,3)NeuAc1 + Na	2814.0202	2814.0335	4.7263	Hex8dHex2HexNAc8(2,6)NeuAc1 + Na	3734.3687	3734.3618	1.8477
Hex4dHex2HexNAc4(2,3)NeuAc1 + Na	2083.7558	2083.7473	4.0792	Hex7dHex1HexNAc6(2,3)NeuAc1 + Na	2830.0151	2830.0192	1.4488	Hex10HexNAc9(2,3)NeuAc1 + Na	3779.3888	3779.3858	0.7888
Hex3dHex1HexNAc6 + Na + 2S	2095.5856	2095.5805	2.4337	Hex7dHex3HexNAc6 + Na	2832.0195	2832.0124	2.5067	Hex8dHex4HexNAc8(2,3)NeuAc1 + Na	3836.4004	3836.4063	1.5379
Hex5dHex1HexNAc4(2,3)NeuAc1 + Na	2099.7507	2099.7501	0.2857	Hex6HexNAc6(2,3)NeuAc1(2,6)NeuAc1 + Na	2840.0471	2840.0494	0.8098	Hex9dHex1HexNAc8(2,3)NeuAc1 + Na	3850.3909	3850.3930	0.5454
Hex5dHex3HexNAc4 + Na	2101.7551	2101.7545	0.2850	Hex6dHex2HexNAc6(2,6)NeuAc1 + Na	2842.0515	2842.0592	2.7093	Hex9dHex3HexNAc8(2,3)NeuAc1 + Na	3852.3953	3852.4069	3.0111
Hex5dHex1HexNAc4(2,6)NeuAc1 + Na	2127.7820	2127.7791	1.3629	Hex7dHex1HexNAc6(2,6)NeuAc1 + Na	2858.0464	2858.0526	2.1693	Hex9dHex5HexNAc8 + Na	3855.4031	3855.3881	3.8906
Hex3dHex2HexNAc6 + Na + S	2139.6969	2139.6970	0.0467	Hex6dHex3HexNAc7 + Na	2873.0461	2873.0331	4.5245	Hex8dHex1HexNAc8(2,6)NeuAc1 + Na	3880.4266	3880.4128	3.5563
Hex4dHex1HexNAc5(2,3)NeuAc1 + Na	2140.7773	2140.7724	2.2889	Hex7dHex2HexNAc7 + Na	2890.0444	2890.0463	0.6574	Hex8dHex5HexNAc8(2,3)NeuAc1 + Na	3982.4583	3982.4489	2.3604
Hex5HexNAc5(2,3)NeuAc1 + Na	2156.7722	2156.7735	0.6028	Hex6dHex1HexNAc7(2,6)NeuAc1 + Na	2899.0729	2899.0739	0.3449				
Hex5dHex2HexNAc5 + Na	2158.7766	2158.7746	0.9760	Hex6dHex2HexNAc5(2,3)NeuAc2 + Na	2901.0522	2901.0474	1.6546				
Hex6dHex1HexNAc5 + Na	2174.7715	2174.7747	1.4719								

Table 6. N-glycan Structures in this Chapter.

m/z	Structure	m/z	Structure	m/z	Structure	m/z	Structure	m/z	Structure	m/z	Structure
1079.3745*		1905.6338		2215.7980*		2539.9037*		2979.0808*		3485.2587	
1136.3964		1911.5859*		2232.7964		2581.9336		2986.1050		3487.2631	
1257.4226		1912.6662		2242.6469*		2592.9415		3017.0996		3544.2846	
1282.4543*		1937.6979		2243.8042		2594.9459		3036.1023*		3556.3210	
1298.4492		1952.6125*		2245.8086		2596.9252		3045.1309		3558.3002	
1419.4754		1953.6928		2271.8355		2608.9364		3047.1101		3560.2795	
1444.5071*		1955.6972*		2286.8352		2610.9408		3049.0894		3588.3108	
1460.5020		1993.6390*		2302.8301		2613.9486		3109.1187*		3633.3210	
1485.5337*		1994.7193		2304.8345*		2667.9623		3120.1265		3636.3037	
1501.5286		1996.7238*		2318.8250		2669.9667*		3122.1309		3674.3476	
1542.5552		2012.7187*		2320.8294*		2685.9616*		3124.1353*		3702.3789	
1581.5282		2022.7506		2330.8614		2742.9831*		3130.1585		3704.3330	
1588.5606		2028.7136		2346.8563		2754.9943		3132.1629		3709.3452	
1606.5599*		2057.6438		2377.8509*		2756.9987		3179.1524		3734.3687	
1647.5865*		2058.7242		2387.8828		2814.0202		3198.1551*		3779.3888	
1663.5814		2083.7558		2389.8621		2830.0151		3255.1766*		3836.4004	
1688.6131*		2095.5856*		2391.8665		2832.0195*		3264.1800		3850.3909	
1704.6080		2099.7507		2393.8458		2840.0471		3266.1844		3852.3953	
1734.6158		2101.7551*		2417.8934		2842.0515		3268.1888		3855.4031	
1743.5810		2127.7820		2419.8978		2858.0464		3270.1681*		3880.4266	
1750.6134		2139.6969*		2448.8880		2873.0461*		3323.2059		3982.4583	
1791.6489		2140.7773		2464.8829		2890.0444*		3325.2103			● Galactose (Hex)
1809.6393*		2156.7722		2466.8873*		2899.0729		3328.2181*			● Mannose (Hex)
1850.6659*		2158.7766*		2474.9149		2901.0522		3332.2790			■ N-acetylglucosamine (HexNAc)
1866.6608		2174.7715*		2507.9139*		2903.0566		3410.2379			□ N-acetylgalactosamine (HexNAc)
1891.6925*		2184.8035		2523.9088*		2906.0393*		3469.2638			◄ Fucose (dHex)
											◆ 2,3-Sialic Acid (2,3NeuAc)
											◆ 2,6-Sialic Acid (2,6NeuAc)

*Presence of core fucose confirmed by EndoF3 analysis

101

3.3.4 DAB Immunohistochemical Staining for CA19-9

FFPE (5 µm) whole tissue block slides were dewaxed, rehydrated and antigen retrieved as described above in preparation for IHC-DAB staining. Samples were sequentially incubated with 100 µL each of peroxidase blocking reagent, serum blocking reagent, avidin blocking reagent and biotin blocking reagent for 5 min, 15 min, 15 min and 15 min respectively. CA19-9 primary antibody was diluted to 15 µg/mL in PBST (50 µL Triton-X100, 50 mL PBS pH 7.4) containing 0.025% serum blocking reagent and tissue samples were incubated with diluted antibody overnight at 4°C. After incubation samples were washed with PBS, incubated with 100 µL HSS-HRP secondary antibody at room temperature for 1 hour, then developed with DAB chromogen solution for 5 minutes with observation under a microscope. Stained samples were rinsed in H_2O, dehydrated in the reverse gradation of ethanol solutions and xylenes, then sealed and permanently mounted. Slides were subsequently imaged in a Nanozoomer 2.0RS high resolution slide scanner (Hamamatsu, Hamamatsu-city, Japan) at 40X magnification across the whole tissue. Scanned images were analyzed using Image Color summarizer, a freely available online k-means clustering based algorithm, to generate an unbiased clustering of pixels by color to delineate between blank slide background, low-intensity CA19-9 staining and high-intensity CA19-9 staining. Subsequently generated grouped pixel maps were then co-registered in FlexImaging software with the original slide scans used for MALDI-IMS analysis to draw regions of CA19-9 staining for import into SCiLS lab software for analysis.

3.3.5 Immunofluorescence Staining for CA19-9 and sTRA

Paraffin was removed from 5 µm thick FFPE sections using CitriSolv Hybrid and then tissue was rehydrated through an ethanol gradient. Following rehydration, antigen retrieval was achieved through incubating slides in citrate buffer at 100 °C for 20 minutes. Slides were then blocked in phosphate-buffered saline with 0.05% Tween-20 (PBST0.05) and 3% bovine serum albumin (BSA) for 1 hour at RT. Primary antibodies against CA19-9 and TRA-1-60 were labeled for immunofluorescent staining with Sulfo-Cyanine5 NHS ester and Sulfo-Cyanine3 NHS ester respectively. Dialysis was performed following labeling to remove unreacted conjugate and the primary antibodies were then diluted into the same solution of PBST0.05 with 3% BSA to a final concentration of 10 µg/mL. Slides were incubated overnight with this solution at 4 °C in a humidified chamber.

The following day antibody solution was decanted and the slides were washed twice in PBST0.05 and once in 1X PBS, each time for 3 minutes. The slides were dried via blotting then incubated with DAPI at 10 µg/mL in 1X PBS for 15 minutes at RT. Two five-minute washes were performed in 1X PBS, and then slides were cover-slipped and scanned using a fluorescent microscope. All TMA slides were scanned using Vectra (Perkin Elmer, Waltham, MA, USA), while the whole tissue sections were scanned using an Axio Scan.Z1 (Zeiss, Oberkochen, Germany). Each system collected data for each field of view at three different emission spectra. All image data were quantified using SignalFinder-IF.

Following scanning, slides were stored in a humidified chamber. Coverslips were removed for the subsequent rounds of staining by submerging the slide in

deionized water at 37 °C until the coverslip floated free (between 30-60 minutes). Fluorescence was quenched between rounds by incubating the slides with 6% H_2O_2 in 250 mM sodium bicarbonate (pH 9.5-10) twice for 20 minutes at RT. Subsequent rounds of staining were performed as described above using TRITC conjugated anti-PHA-E and biotinylated GSL-II as the primary detections. Cy5-conjugated streptavidin was used as a secondary to detect the biotinylated GSL-II for 1 hour at RT. This was done following washing after primary incubation.

To perform sialidase treatment, slides were incubated with a 1:200 dilution (from a 50,000 U/mL stock) of α2-3,6,8 Neuraminidase in 1X Glycobuffer (5 mM $CaCl_2$, 50mM pH 5.5 sodium acetate) overnight at 37 °C. Slides were washed as described above and then antibody detections were performed. Hematoxylin and eosin staining were performed following a standard protocol.

3.3.6 Statistical Analysis

A total of 327 tissue cores across 4 TMAs representing 53 patients were analyzed in this study, with each core consisting of 171 individual spectra on average. Individual spectra pixels in each core were averaged to generate a representative spectrum for the whole core which was subsequently used for statistical analysis. Each patient in the study was represented at minimum by n = 2 adjacent normal tissue cores and n = 2 tumor tissue cores. SCiLS Lab was used to generate area under the peak (AUP) values for TMAs after normalizing glycan intensity values to total ion current, which were subsequently exported to statistical software for analysis. Log_2 Fold Change (FC) was calculated by comparing individual glycan intensities between normal and tumor tissues on a patient-

matched basis. To determine statistically significant changes in glycan expression, AUP values were evaluated using a two-sample t-test assuming unequal variance. 13 whole tissue blocks from which some TMA cores were derived were also used to draw qualitative conclusions about spatial localization trends across different PDAC regions. An automated thresholding program, SignalFinder-IF, was used to identify real signals on fluorescently labeled tissues. The algorithm uses multi-round segmentation to separate non-tissue, tissue background, and signal levels of fluorescence[109,398,399]. The immunofluorescence data was overlaid onto MALDI mass and H&E images using the custom-built Overlay program and Canvas 14. LASSO-regularized logistic regression was performed using the R "glmnet" package setting the mixing parameter alpha to 1 and setting lambda through cross validation to 0.0582. The mass only model was similarly performed with a lambda set to 0.1017. Individual mass comparisons were performed using a paired t-test between tumor and adjacent normal cores from the same tissue and were plotted using the R "ggplot" package.

3.4 Results

3.4.1 N-glycan Imaging of Normal Pancreas Tissue

The goal of this chapter was to characterize N-glycan changes in normal pancreas and pancreatic cancer tissues, thus an initial step was to define the distribution of N-glycans present in normal pancreas, which comprises distinct endocrine, exocrine and ductal cell types. A normal human pancreas tissue was antigen retrieved, sprayed with a molecular coating of PNGase F and coated with CHCA matrix as described in the Experimental section. Some selected tissues

were also treated with endoglycosidase F3 to distinguish core fucosylated structures from outer arm fucosylated species. The enzymatically released N-glycans were detected first with a MALDI-FTICR mass spectrometer for accurate mass identification at a low spatial resolution (150 μm raster) then again at a higher spatial resolution (30 μm raster, offset) using a MALDI-QTOF mass spectrometer according to a standardized protocol[314]. Distinct differences in glycan patterning were observed between endocrine tissue, exocrine tissue and ductal tissue subtypes (Figure 15A). High-mannose N-glycan structures were primarily localized to pancreatic exocrine acinar tissue but were detected at lower levels in other tissue regions as well (Figure 15B). N-glycans associated with inter- and intralobular ductal tissue were primarily core-fucosylated bi- and tri-antennary structures (Figure 15C).

A more targeted N-glycan analysis of pancreatic islets (Islets of Langerhans) was performed for normal human pancreas tissue. Prior to preparation for MALDI-IMS, tissue was H&E stained and scanned at 40X magnification before proceeding to antigen retrieval. These high-resolution histopathological images were co-registered in FlexImaging software to direct targeted glycan IMS of only pancreatic islets. These same tissues were then re-analyzed at the whole-tissue level to generate a profile of non-islet pancreatic tissue for comparison. Comparing the N-glycan profiles between islet and non-islet regions, detection of the most common N-glycans were generally consistent in both regions, but with lower expression levels for most structures in the islets. (Figure 16A). There were however a distinct set of sulfated N-glycans which were
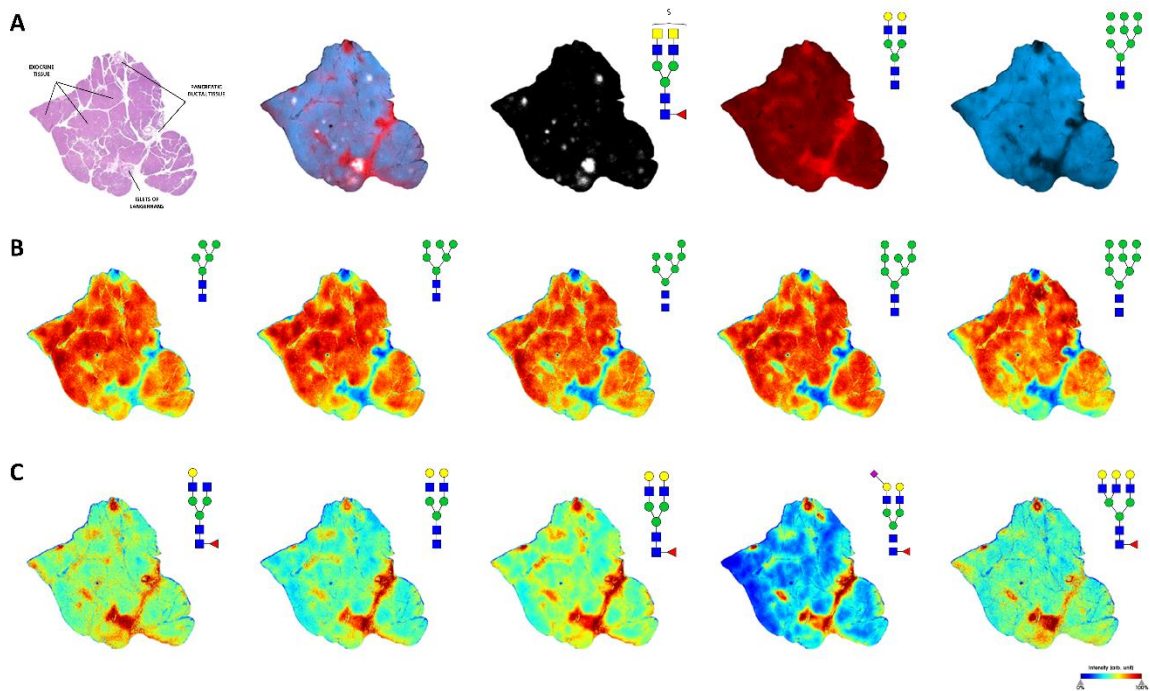
Figure 15. N-glycan imaging of a normal human pancreas. A) Overlay image of three representative N-glycans corresponding to acinar exocrine tissue (Blue, Hex9HexNAc2 *m/z* 1905.6338), ductal tissue (Red, Hex5HexNAc4 *m/z* 1663.5814) and Islets of Langerhans (White, Hex3dHex1HexNAc6SO$_4$2 *m/z* 1993.6390) along with accompanying annotated H&E stain. B) High-mannose N-glycans predominantly localized to acinar exocrine tissue. C) N-glycans expressed predominantly in pancreatic ductal tissue tend to be bi- and tri-antennary structures with core fucose residues lacking terminal fucosylation.
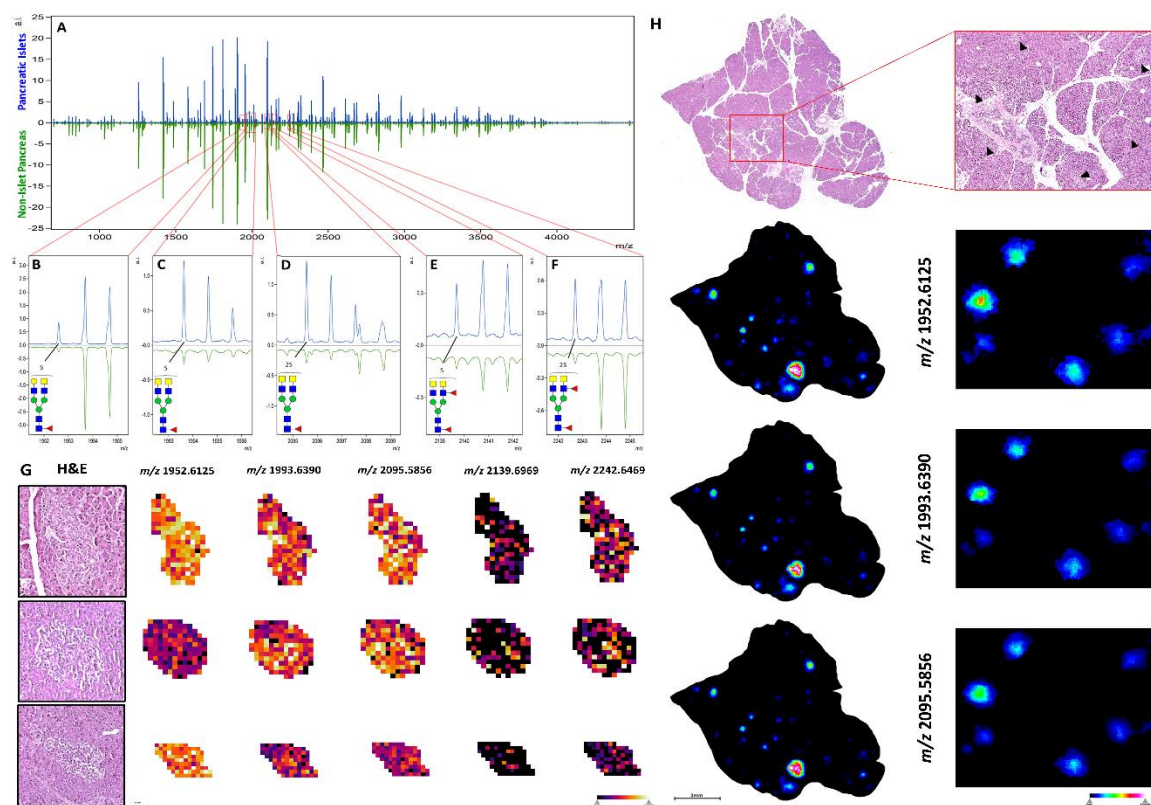
Figure 16. Sulfated Terminal GalNAc N-glycans Specific to Pancreatic Islets of Langerhans. A) Comparative mass spectra of pancreatic Islets of Langerhans (blue) and non-islet pancreatic tissue (green) from the same normal pancreas tissue section. Sulfated hybrid N-glycans B) Hex4dHex1HexNAc5SO$_4$, *m/z* 1952.6125, C) Hex3dHex1HexNAc6SO$_4$, *m/z* 1993.6390, D) Hex3dHex1HexNAc6SO$_4$2, *m/z* 2095.5856, E) Hex3dHex2HexNAc61SO$_4$, *m/z* 2139.6969, F) Hex3dHex2HexNAc6SO$_4$2, *m/z* 2242.6469 unique to endocrine islet tissue. G) Targeted imaging of unique islet N-glycans along with representative H&E staining. H) Non-targeted whole-tissue images of normal human pancreas showing specific localization of the 3 most abundant hybrid, sulfated N-glycan structures to Islets of Langerhans tissue (black carats), which are clearly absent from other pancreatic tissue regions.

108

Detected in islets that were either not present or expressed at much lower levels in non-islet regions. These 5 N-glycans were all sulfated, core fucosylated and had at least one terminal N-acetylgalactosamine (GalNAc) residue, with some structures having outer arm fucose (Figure 16B-F). The mass-based structural predictions for these novel islet glycans were orthogonally confirmed via fragmentation by on-tissue collision-induced dissociation (CID) (Figure 17). Sulfated N-glycan structures with terminal GalNAc have been previously reported to be detected in adult pig islet tissue[400]. Targeted analysis images of these 5 structures for individual islets are shown in Figure 16G. In addition, whole-tissue scans of the normal pancreas tissue exhibited specific localization of these unique sulfated N-glycans to pancreatic islets, which were clearly absent from other non-islet pancreatic tissue regions (Figure 16H).

A normal tissue section was digested with endoglycosidase F3 (Endo F3) to assess the anomeric linkages of fucose residues in reported structures. Endo F3 cleaves N-glycans above the first GlcNAc residue on the chitobiose core in the presence of a fucose residue attached to that primary GlcNAc[211]. Core fucosylated structures are thereby freed from their protein carriers with a distinct mass shift representing the loss of one GlcNAc residue and one fucose residue. By using a combination of Endo F3 and PNGase F in a 1:10 ratio both core and terminally fucosylated N-glycan isomers can be released for analysis (Figure 18A). Although some outer arm fucosylated isomers were detected (Figure 18B), N-glycan structures with at least 1 fucose residue were predominantly core fucosylated
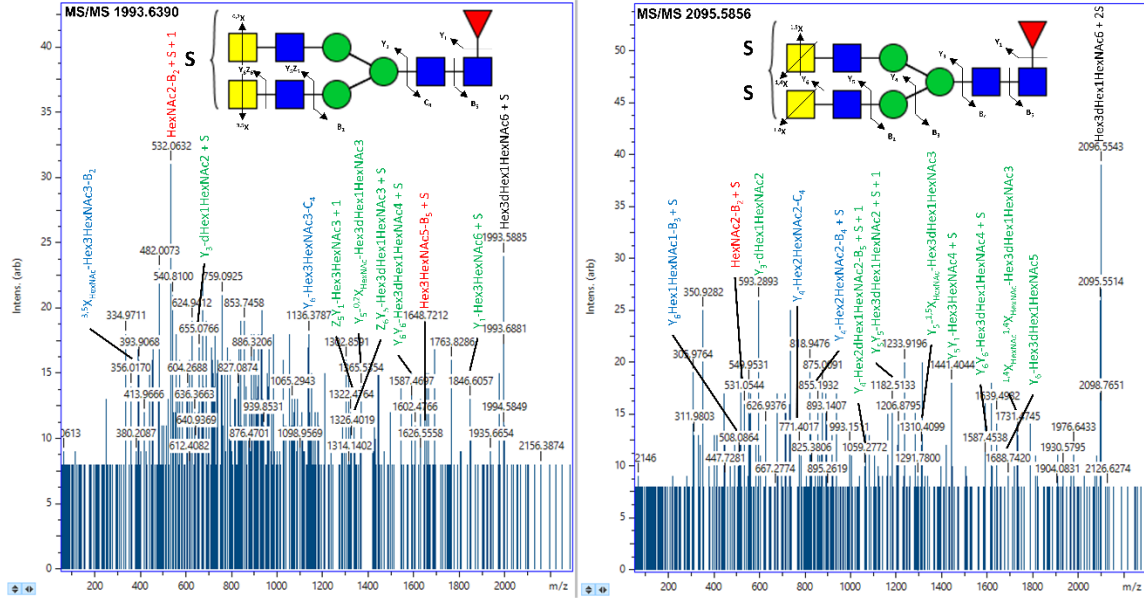
Figure 17. CID Fragmentation of Sulfated Terminal GalNAc Islet N-glycans.
Representative CID spectra for Hex3dHex1HexNAc6SO$_4$, *m/z* 1993.6390 and
Hex3dHex1HexNAc6(SO$_4$)$_2$, *m/z* 2095.5856.
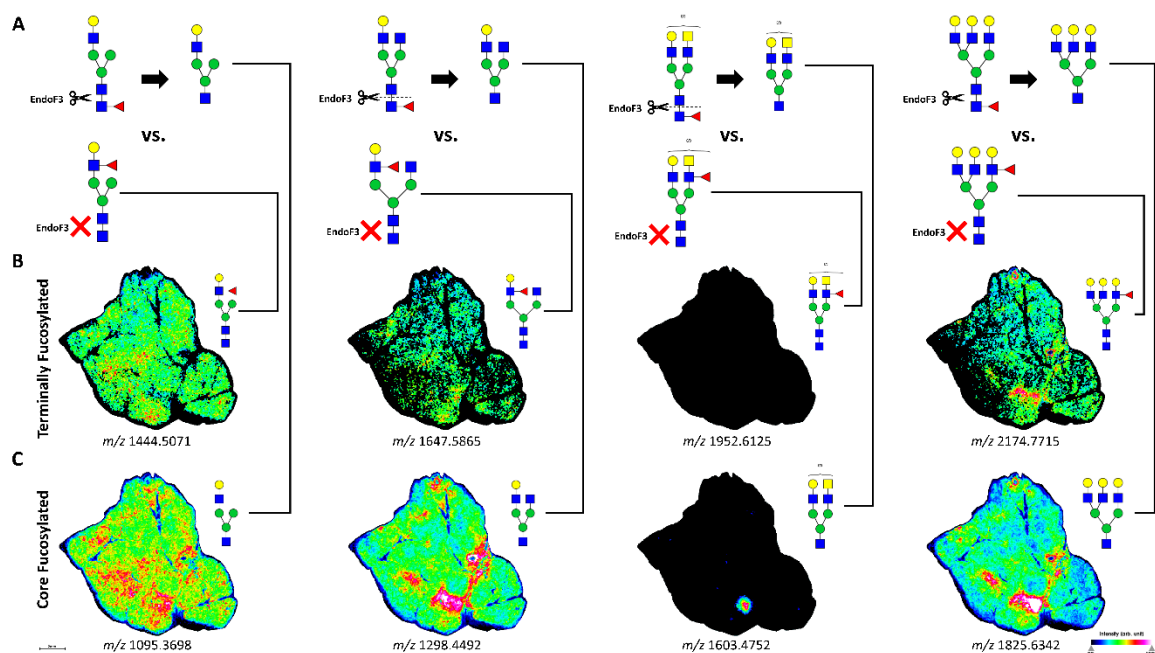
Figure 18. Endoglycosidase F3 Reveals Core Fucosylated N-glycans. A) Endo F3 cleaves N-glycans between GlcNAc residues on the chitobiose core only in the presence of a core fucose residue and is unable to cleave terminally fucosylated isomers. B) Terminally fucosylated isomers were detected minimally (Hex4dHex1HexNAc3 m/z 1444.5071, Hex4dHex1HexNAc4 m/z 1647.5865, Hex6dHex1HexNAc5 m/z 2174.7715) or not at all (Hex4dHex1HexNAc5SO41 m/z 1952.6125). C) Endo F3 cleavage products from core fucosylated isomers with a distinct -349.1373 mass shift were observed in much greater abundance for the four representative structures shown (Hex4HexNAc2 m/z 1095.3698, Hex4HexNAc3 m/z 1298.4492, Hex4HexNAc4SO41 m/z 1603.4752, Hex6HexNAc4 m/z 1825.6342) as well as for most structures with at least one fucose residue in this report

(Figure 18C), illustrated by the unique islet N-glycan *m/z* 1952.6125 for which no outer-arm fucosylated isomers were observed.

3.4.2 N-glycosylation Changes in Pancreatic Ductal Adenocarcinoma

To evaluate PDAC glycosylation by N-glycan MALDI-IMS, representative whole tissues were analyzed, and data compared with a series of carbohydrate antigen defined tissue microarray slides. These same samples were also evaluated for differences in isomeric sialic acid distributions. As an example. a PDAC tumor tissue staged at T3NXMX was analyzed for N-glycan composition differences by IMS (Figure 19). N-glycan spatial distributions could be linked with the histopathologically-annotated primary tumor tissue, necrotic tissue, tumor margin tissue and adjacent normal tissue regions as shown in the H&E stained tissue (Figure 19A) adjacent to four N-glycans detected in these regions (Figure 19B). N-glycan structures primarily localized to necrotic tissue tended to be bi-, tri- and tetra-antennary structures lacking any fucose or sialic acid residues (Figure 19C), which has previously been reported for tumor necrosis regions of other cancer tissues[202]. Core-fucosylated tri- and tetra-antennary N-glycan species with bisecting GlcNAc modifications and terminal GalNAc residues were primarily localized to adenocarcinoma regions (Figure 19D). The interface between tumor, necrosis and adjacent normal tissue was defined by tetra-antennary core-fucosylated structures with terminal poly LacNAc extensions of increasing length (Figure 19E), while N-glycans localized to adjacent normal tissue were typically bi- and tri-antennary structures with core fucose residues (Figure 19F). High
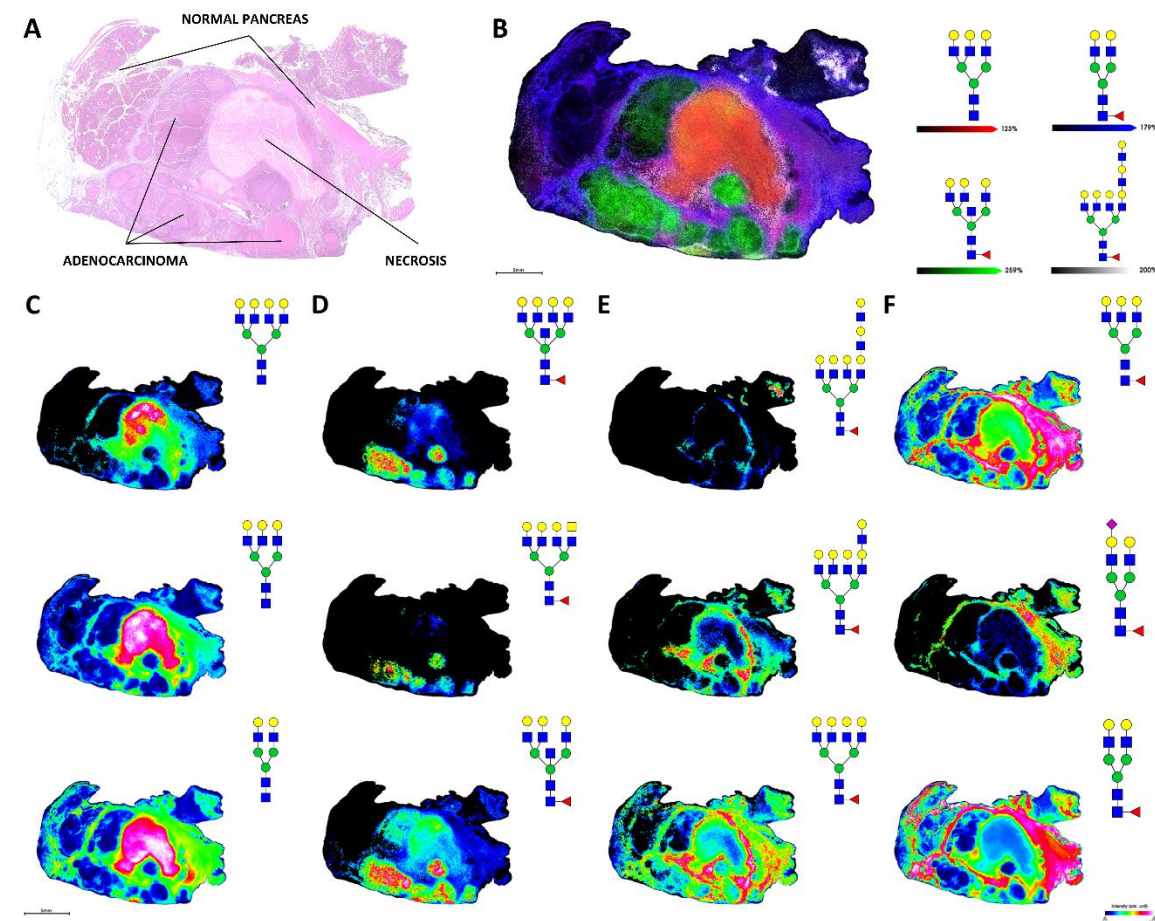
Figure 19. N-glycan Imaging of a Representative Stage 3 PDAC Tumor Tissue. A) H&E staining of T3NXMX PDAC tissue with annotations. B) Overlay of 4 representative N glycans corresponding to necrotic tissue (Red, Hex6HexNAc5 *m/z* 2028.7136), adenocarcinoma (Green, Hex6dHex1HexNAc6 *m/z* 2377.8509), tumor margin (White, Hex9dHex1HexNAc8 *m/z* 3270.1681) and adjacent non-tumor tissue (Blue, Hex5dHex1HexNAc4 *m/z* 1809.6393). C) N-glycan structures localized to necrotic tissue (top to bottom) Hex7HexNAc6 *m/z* 2393.8458, Hex6HexNAc5 *m/z* 2028.7136 and Hex5HexNAc4 *m/z* 1663.5814. D) N-glycan structures localized to adenocarcinoma tumor (top to bottom) Hex7dHex1HexNAc7 *m/z* 2742.9831, Hex6dHex1HexNAc7 *m/z* 2580.9302 and Hex6dHex1HexNAc6 *m/z* 2377.8509. E) N-glycan structures localized to tumor margin (top to bottom) Hex9dHex1HexNAc8 *m/z* 3270.1681, Hex8dHex1HexNAc7 *m/z* 2905.0359 and Hex7dHex1HexNAc6 *m/z* 2539.9037. F) N-glycan structures localized to adjacent non-tumor tissue (top to bottom) Hex6dHex1HexNAc5 *m/z* 2174.7715, Hex5dHex1HexNAc4NeuAc1 *m/z* 2100.7347 and Hex5dHex1HexNAc4 *m/z* 1809.6393.

mannose glycans were predominantly localized in normal tissue regions (data not shown). Structural confirmation for many of these reported N-glycans were assessed by CID (Figure 20).

An on-tissue sialic acid derivatization reaction was performed on a different PDAC tumor tissue to assess differential patterns of sialylation. The amidation-amidation (AA) chemistry derivatizes the sialic acid 1' carboxyl group differentially for α2,3- and α2,6-linked residues, introducing a mass shift which allows for the delineation of these isomers[204]. This pancreatic cancer tissue, shown in Figure 21, contained late stage adenocarcinoma (T3N1MX) tissue surrounded by a network of tumor stroma as well as Pan-IN lesions and adjacent normal tissue (Figure 21A). An overlay image of three representative N-glycan structures corresponding to these regions is shown in Figure 21B. Adjacent normal tissue in this PDAC sample contained the same abundance of high-mannose structures seen in other tissues analyzed in this report (Figure 21C), and few sialylated N-glycans were localized to this region. In contrast, most structures detected in regions of primary tumor or tumor stroma tissue contained one or more sialic acid residues. The N-glycans from tumor stroma regions were typically α2,3 sialylated (Figure 21D). This differed from areas of primary adenocarcinoma, which were a mixture of α2,3 and α2,6 sialylation slightly favoring α2,6 sialylated species (Figure 21E). Interestingly, differential α2,3 versus α2,6 sialylations of the same base N-glycan structures indicated distinct spatial localizations of these structures within the same tissue and even within the same tissue region, suggesting possible compartmentalization
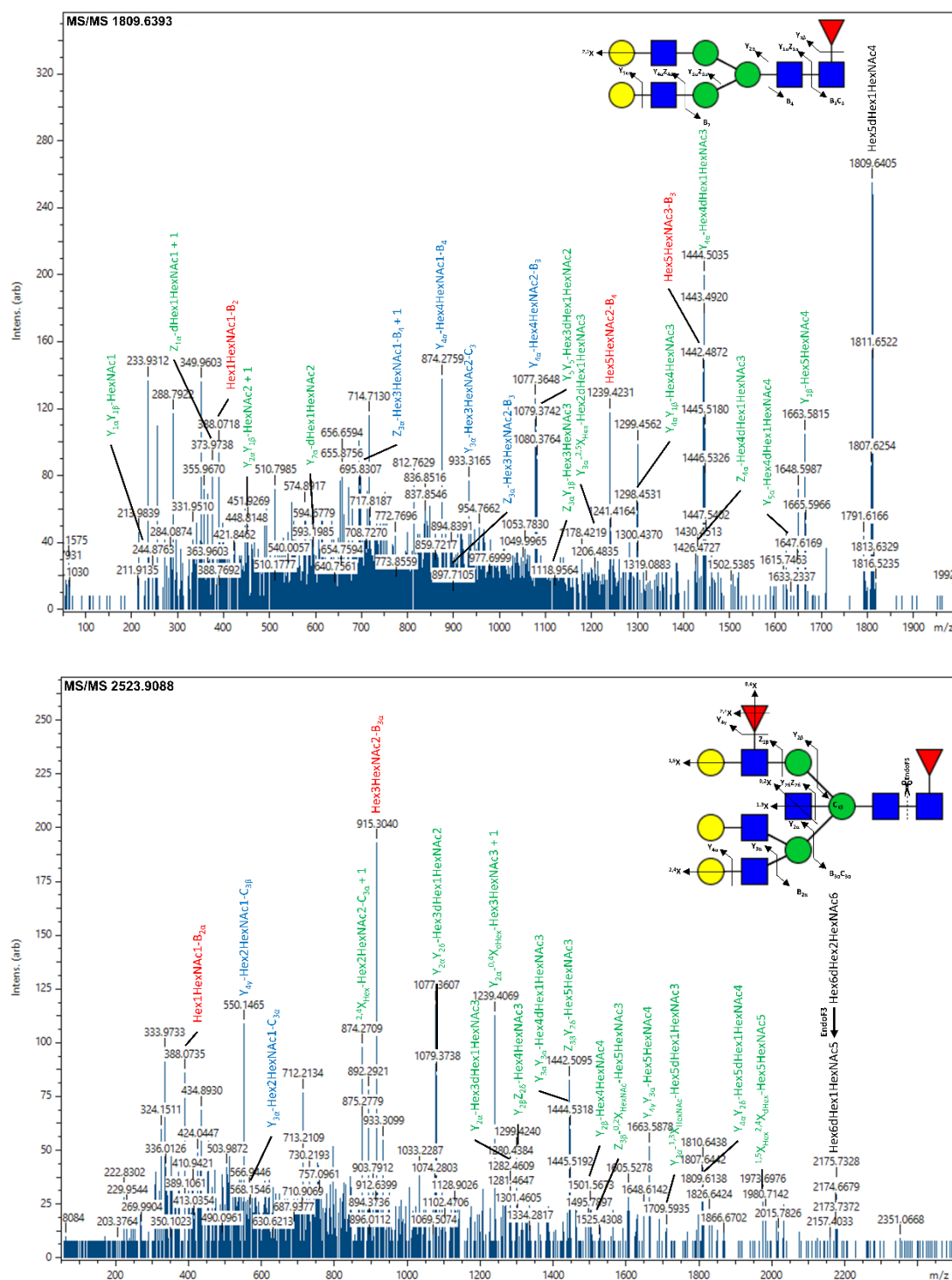
Figure 20. CID Fragmentation of Representative Base N-glycans. Example fragmentation of the commonly expressed *m/z* 1809.6393 and *m/z* 2523.9088 glycans. 21 additional structures were analyzed by CID (data not shown).

115
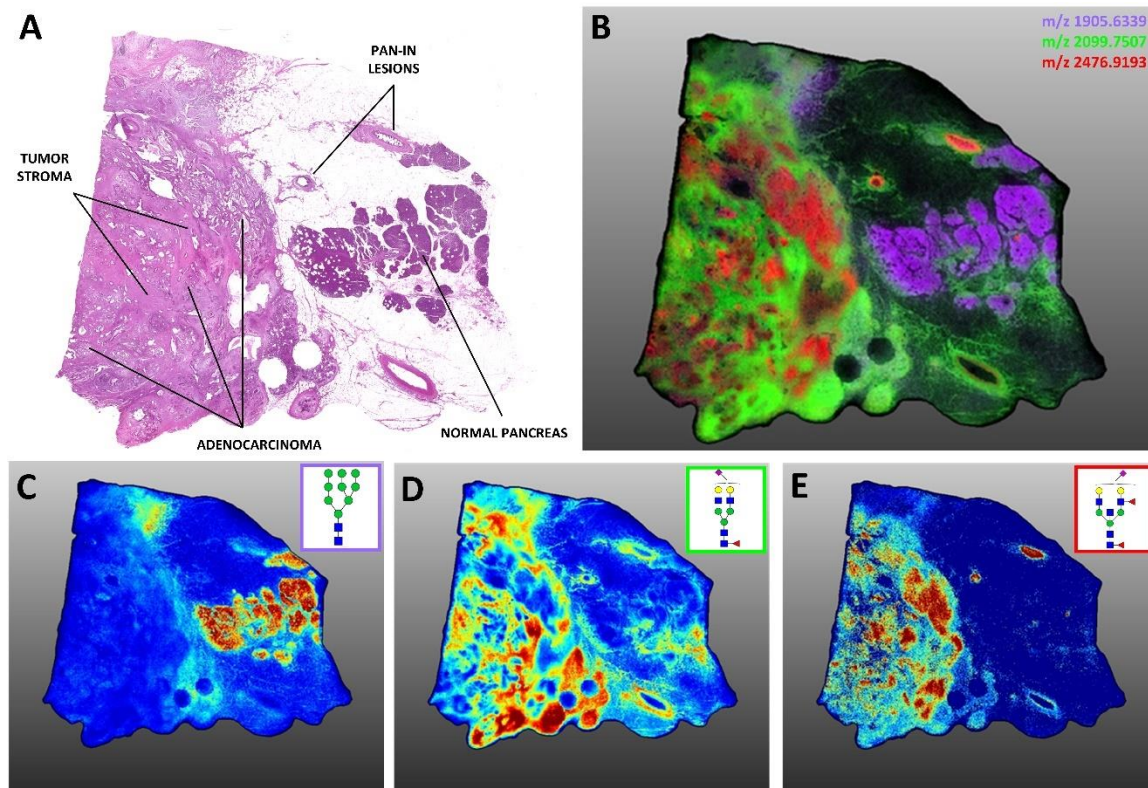
Figure 21. Sialic Acid Linkage Isomer Expression in an Advanced Stage PDAC Tissue. 40 µm MALDI-IMS of AA-stabilized sialylated N-glycans. A) Annotated H&E staining. B) Overlay of three N-glycan structures localized to adjacent normal tissue (purple, Hex9HexNAc2 *m/z* 1905.6339), tumor stroma (green, Hex5dHex1HexNAc4NeuAc1(2,3) *m/z* 2099.7507) and adenocarcinoma (red, Hex5dHex2HexNAc5NeuAc1(2,6) *m/z* 2476.9193). C) High mannose glycan structures tended to associate with normal adjacent tissue. D) α2,3 oriented sialic acid-decorated N-glycan structures localized to tumor stroma regions. E) Adenocarcinoma-associated N-glycans were predominantly α2,6 sialylated although α2,3 vs. α2,6 sialylation of the same base structures drove different intra-tumor localization. These same α2,6 sialylated structures were also present within Pan-IN lesions.

Of specific sialyltransferases to distinct tissue regions and subtypes in pancreatic cancer.

3.4.3 Correlation of PDAC Biomarkers and N-glycan Expression

A more comprehensive assessment of the pancreatic ductal adenocarcinoma N-glycome was performed using four tissue microarrays representing 53 individual patients including matched adjacent normal tissue, tumor tissue and metastatic tissues as well as some patients with samples of pre-tumor lesions, normal lymph node tissue and cancerous lymph node tissue. N-glycans were released from these tissue arrays as described above and N-glycan intensities across the tissue cores were analyzed via MALDI-FTICR-MS. In conjunction to analysis by imaging mass spectrometry, serial TMA sections were analyzed via multi-round immunofluorescence for the CA19-9 and sTRA biomarkers (Figure 22A) followed by H&E staining as previously described[109]. This system allows for high-resolution and high-sensitivity quantification of multiple markers on one tissue section, while also preserving the ability to acquire brightfield imaging of the cellular histology using H&E staining. An in-house image processing program called SignalFinder was used to automatically locate and quantify the signals from each marker. The maps of identified signal can be overlaid onto the brightfield images to gain information about the types of cells that produce each marker as well as overlaps in marker expression (Figure 22B). These analyses drove classification of tumor cores as "Both" (significant CA19-9 expression and significant sTRA expression), "CA19-9 Only" (significant CA19-9
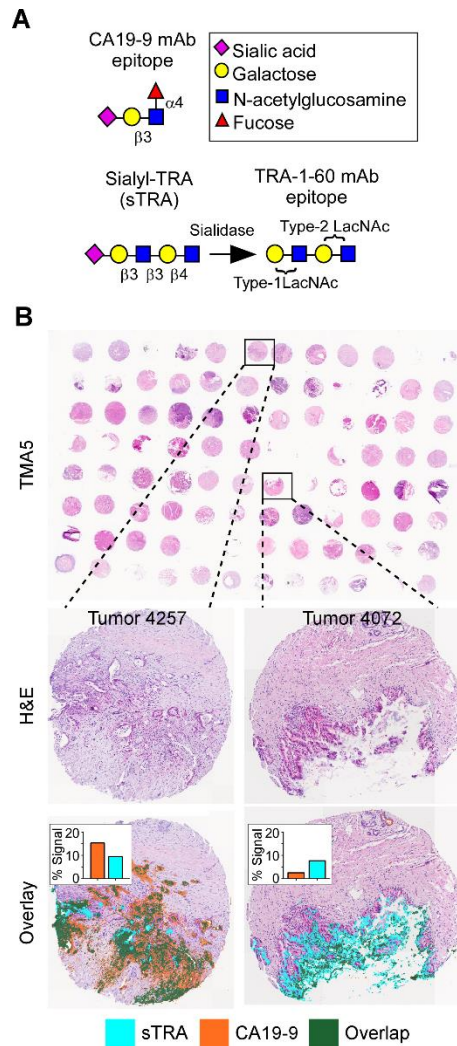
Figure 22. Quantifying Biomarker Epitopes in Tissue Samples Using Immunofluorescence. A) Treatment of the sTRA epitope with sialidase exposes the TRA-1-60 epitope, allowing for detection with anti-TRA-1-60 mAb. B) Tissue microarrays were used to obtain marker data on primary PDAC and related tissues from multiple patients. TMAs were stained using multi-round immunofluorescence with subsequent H&E staining and imaging. Each core was quantified to determine the percentage of tissue pixels above background.

expression with low sTRA expression), "sTRA Only" (low CA19-9 expression with significant sTRA expression) or "Neither" (low in CA19-9 expression and low in sTRA expression). These designations subsequently informed statistical analyses of differential N-glycan patterns between varying levels of TMA biomarker expression.

Tumor cores and their matching non-tumor tissue cores were analyzed in SCiLS Lab to elucidate differential N-glycan expression between the groups. Heat map images of specific N-glycan structure distributions, normalized to total ion count, were generated and then cores were then grouped according to their biomarker-classified designations for visualization (Figure 23A). N-glycans significantly associated with CA19-9 expression tended to be core-fucosylated bi-, tri- and tetra-antennary structures with bisecting N-acetylglucosamine residues and multiple outer arm fucoses. These structures were detected less frequently in tumor cores with high sTRA expression, which instead tended to be tri- and tetra-antennary structures lacking outer arm fucosylation. Average Log_2 fold change between patient matched tumor and normal cores is shown in Figure 23B. These data as well as average intensity data across the four biomarker classified groupings are provided in Table 7 and were used in further evaluations in the next section. The same TMAs were also treated by the sialic acid amidation-amidation stabilization reactions prior to the standard imaging workflow and analyzed by MALDI-IMS (Figure 23C). Like that shown for the whole tissue, the abundance
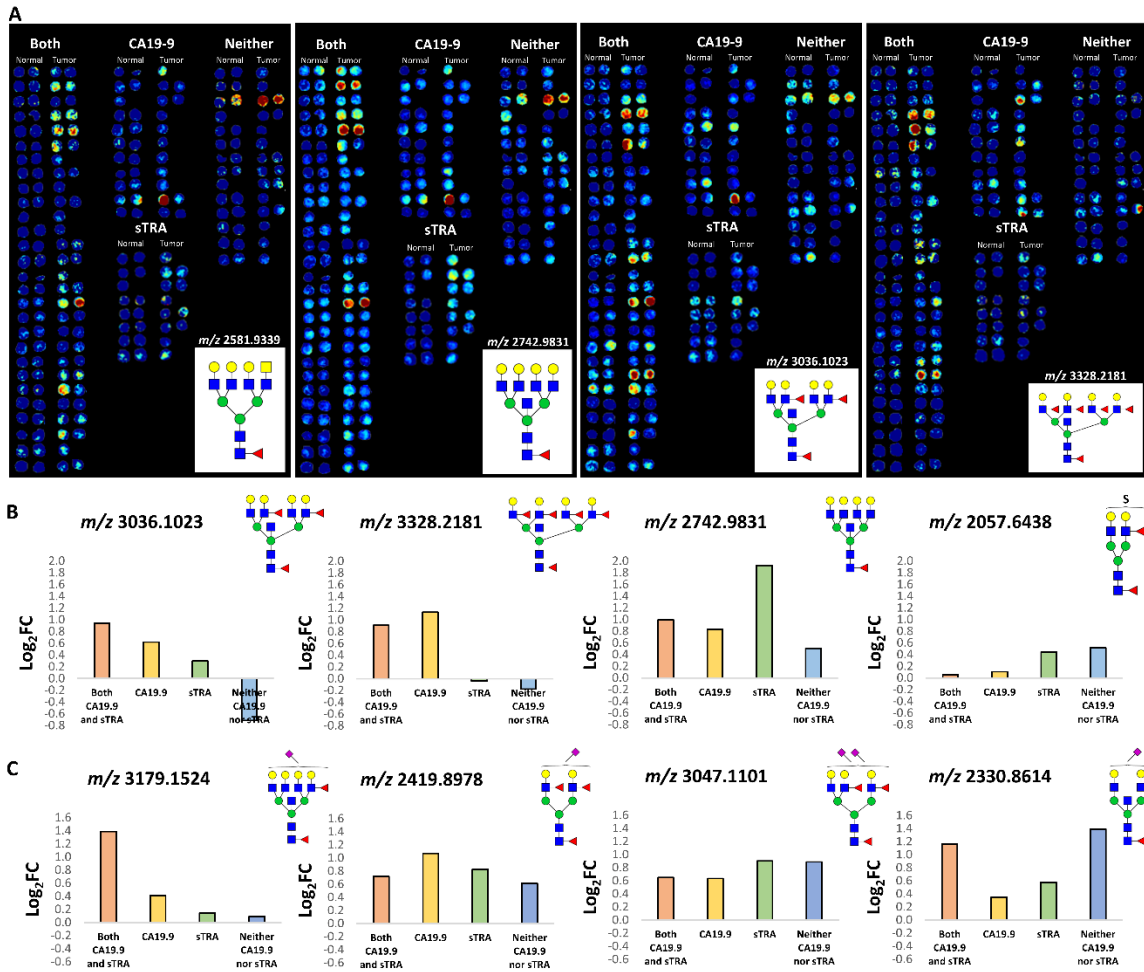
Figure 23. TMA Cores Grouped by CA19-9 and sTRA Expression. A) Individual patient core pairs analyzed by SCiLS Lab were extracted from each of the 4 TMAs and grouped in one of four designations based on biomarker expression. Four representative sorted TMA heatmaps for N-glycans *m/z* 2581.9339, *m/z* 2742.9831, *m/z* 3036.1023 and *m/z* 3328.2181 are shown. Average Log$_2$ fold change between patient matched tumor and normal cores across the four groupings for B) non-sialylated N-glycans and for C) amidation-amidation stabilized sialic acid containing N-glycans. Positive values represent enrichment in tumor tissue.

Table 7. Log₂-FC and AUP Intensity Data for Biomarker-Classified TMA Cores.

Centroid [m/z]	Both CA19.9 and sTRA		CA19.9		sTRA		Neither CA19-9 nor sTRA	
	Fold Change	Intensity	Fold Change	Intensity	Fold Change	Intensity	Fold Change	Intensity
1079.3749	0.5580	1030.2615	0.5620	1013.5629	0.7529	799.8649	0.0691	681.6336
1136.3964	0.6459	676.5595	0.3493	637.1259	0.7473	578.7372	0.7534	556.2163
1257.4226	0.1402	2654.0624	-0.0147	2351.0033	0.3208	2490.4892	0.0796	2039.8801
1282.4543	0.3096	2313.2134	0.3698	2365.8460	0.6335	2372.4875	0.3087	1953.0532
1298.4492	0.2279	3618.3780	0.0596	3606.5293	0.4242	3475.8308	0.5033	3542.7250
1419.4754	-0.0708	4435.2276	0.0448	4359.8460	-0.0115	4282.9775	-0.0462	4038.3505
1444.5071	0.2024	6781.2728	0.2931	7440.2953	0.6529	7254.8175	0.4100	6397.8605
1460.5020	0.4495	1261.6067	0.2437	1421.0725	0.8493	1163.6526	0.5832	1078.5609
1485.5337	0.3397	4496.9126	0.1656	4925.8533	0.7496	4141.5008	0.5373	3847.4355
1501.5286	0.4488	3504.0746	0.1823	3252.7713	0.5833	3217.3858	0.6136	3322.8205
1542.5552	0.6699	631.8115	0.0037	479.5078	0.5234	704.8998	0.2051	472.3477
1581.5282	0.2772	3565.8188	0.2526	3591.4847	0.3927	2961.3900	0.1304	2688.9080
1606.5599	0.3671	940.9854	0.4849	1080.3293	0.9305	1025.6925	0.6006	931.9258
1647.5865	0.2576	10790.2408	0.2137	11085.4327	0.4937	11279.3008	0.3803	11031.1855
1663.5814	0.2230	47111.1360	0.0303	48719.1733	0.4207	45885.2833	0.5582	48841.2200
1688.6131	0.0528	2952.7942	-0.2663	2889.9897	0.5822	3677.0442	0.0743	2442.0707
1704.6080	0.9186	2452.2669	0.3307	2116.1872	1.1304	1949.8679	0.8319	1476.5198
1743.5810	-0.0583	8841.7870	0.0148	8836.4647	-0.0550	7861.5800	-0.1055	7811.1225
1791.6489	0.4449	3437.4208	0.5246	4130.0147	1.1472	2999.8529	0.5074	2359.7695
1809.6393	0.2343	126072.3760	0.3589	145564.3267	0.7564	141867.2083	0.5121	119715.5000
1850.6659	0.4498	13157.5664	0.1981	13928.0233	0.8493	14265.8200	0.5151	11948.0795
1866.6608	0.6915	5408.9500	0.3092	4009.2933	0.8292	4745.9275	0.6856	5016.9438
1891.6925	0.0593	771.5054	0.2295	1007.8143	-0.1452	546.2488	-0.7741	468.9750
1905.6338	-0.3614	4891.3512	-0.1989	5941.8553	-0.0484	4008.0575	-0.1055	4541.7310
1911.5859	0.0774	9652.6898	-0.2242	10247.3253	0.2193	9037.3833	0.6677	11668.2585
1955.6972	-0.2590	7289.5402	-0.0843	7869.6207	-0.0750	6896.1758	-0.3268	6893.2070
1996.7238	0.8381	4608.1824	0.6761	3736.5147	0.5950	3428.9295	-0.2268	2940.5792
2012.7187	0.4143	43498.1460	0.3009	45450.9400	0.9035	51220.2250	0.4612	38769.4650
2028.7136	0.4012	9839.5872	0.2221	10008.1940	0.7816	9078.7983	0.8338	9383.0765
2057.6438	0.0535	18426.9780	0.1073	21937.0833	0.4448	20046.7167	0.5167	21521.1305
2101.7551	-0.0692	7501.7748	0.0102	8503.1773	0.6562	7969.7775	0.2302	7388.0085
2158.7766	0.4011	11363.7478	0.3342	9282.0100	-0.0345	7989.2683	-0.5551	7531.1735
2174.7715	0.2815	53484.7100	0.4252	57246.1800	0.7232	64477.1917	0.5321	59652.0200
2215.7980	0.9590	4382.5464	0.5851	4778.4880	1.2673	3955.2642	0.4642	3491.0819
2232.7964	0.9598	4320.7963	0.8038	3384.2840	1.4892	2737.8392	0.8888	2981.5574
2304.8345	0.8943	6529.6180	0.9264	6704.9727	0.5532	3284.2436	-0.2947	3249.5261
2320.8294	-0.1965	6459.7967	-0.1060	6053.7300	0.1800	5034.5917	-0.4141	5075.9610
2377.8509	0.4545	16636.5238	0.2718	14331.7167	0.9078	18517.2333	0.2226	17797.5590
2393.8458	0.5722	4319.5450	0.4443	4369.4367	1.2084	3761.7533	1.2048	3747.1576
2466.8873	-0.2042	8261.3122	-0.1177	8194.9387	0.2008	8662.9767	-0.3248	8401.9900
2507.9139	0.6044	2482.9564	0.8787	2573.6232	-0.4874	1244.8233	-0.7505	1571.1613
2523.9088	0.6238	8240.1160	0.4511	6913.1740	0.5957	5074.2350	-0.5965	4028.8324
2539.9037	0.0839	34950.5440	0.2730	34169.4800	0.5440	47457.7000	0.3586	46961.3775
2581.9336	0.9281	3156.8733	0.4690	3384.8950	0.8477	2477.0816	0.2002	3008.1229
2613.9486	-0.5574	1040.7924	-0.1643	1097.4909	-1.0460	1052.5307	-1.6169	1427.1412
2669.9667	1.2122	3157.0727	0.8713	3087.5575	0.5335	865.8589	-0.6530	927.7440
2685.9616	-0.3670	6207.3348	-0.2400	5973.3425	-0.0170	5614.4558	-0.6943	5776.5140
2742.9831	0.9924	11120.2304	0.8345	10064.4913	1.9265	8673.5875	0.5077	5522.0960
2832.0195	-0.3598	7215.8054	-0.3907	6264.5160	-0.0894	7355.2933	-0.6649	7728.5317
2890.0444	1.1449	5095.1726	0.4796	4355.5224	1.0930	1939.7393	-0.6336	1792.3854
2906.0393	0.3592	13588.1608	0.5779	16725.3580	1.1644	16365.6783	1.0149	14296.7880
2979.0808	-0.7050	2110.1836	-0.8280	3538.4809	-0.7391	1756.5904	-1.4827	2281.3808
3036.1023	0.9367	12185.8834	0.6211	7251.7120	0.2973	6190.2181	-0.7168	5473.1566
3109.1187	0.7600	3619.1301	0.8687	3715.9760	0.6550	3580.1689	0.4216	3847.6254
3124.1102	-0.0703	1367.6939	-0.2554	1744.9258	-0.2194	1498.8243	-0.9417	1624.6381
3198.1551	-0.5800	4070.1716	-0.4382	4077.9780	-0.6499	5322.4083	-0.9959	4366.8126
3255.1766	0.4646	4019.1874	0.3279	3363.3185	0.2530	2510.7031	-0.5447	2158.0608
3270.1681	0.3299	2498.8385	0.7281	3600.9105	1.3078	3232.0292	0.7372	2983.1392
3328.2181	0.9078	6558.7212	1.1305	6332.3680	-0.0396	3531.0183	-0.1763	3367.1860
3636.3037	0.0741	7494.0596	0.4479	8220.9520	0.4143	10278.0333	0.2161	10434.0220
3709.3452	-0.6620	2239.3698	-0.7074	2430.1141	-0.7433	3195.2648	-1.0279	2632.6308
3855.4031	-0.4590	2145.1399	-0.5476	1865.9784	-0.7010	3220.6986	-0.9423	3064.2660

of α2,3 sialylated glycans was higher relative to α2,6 sialylated glycans (Figure 24), but there was more specificity of the α2,6 glycans to distinguish biomarker antigen sub-types. In general, levels of sialylation were significantly elevated in all tumor tissues relative to normal controls (Table 8).

The extensive glycan data generated in the TMAs was further analyzed in combination with carbohydrate antigen data available for the same tissue cores. There exists a number of N-glycan differences between adjacent normal and tumor cores which suggests a potential for expansion of the biomarker repertoire. Hierarchical clustering of mass data resulted in clusters with distinct glycan properties and patterns for adjacent normal and cancer cores (Figure 25A). For example, the masses of clusters 1 and 5, which are more abundant in the tumor cores relative to adjacent normal, generally have an unbalanced HexNAc, meaning a terminal GlcNAc or GalNAc. In contrast, the normal-associated glycans of cluster 3 are mainly high-mass, balanced glycans with more than one fucose, and the tumor-associated glycans of cluster 2 are mainly non-extended, hybrid N-glycans. This result suggests that specific features may be present on glycans of different masses which are expressed in the same tissues.

Using LASSO-regularized logistic regression, masses which offered predictive value complementary to the CA19-9 and sTRA biomarkers were identified, 9 masses in total with 7 masses being associated with tumor cores (Figure 25B). The LASSO regression selects a subset of predictors with minimal collinearity and identifies the most informative masses from the tumor and normal

122
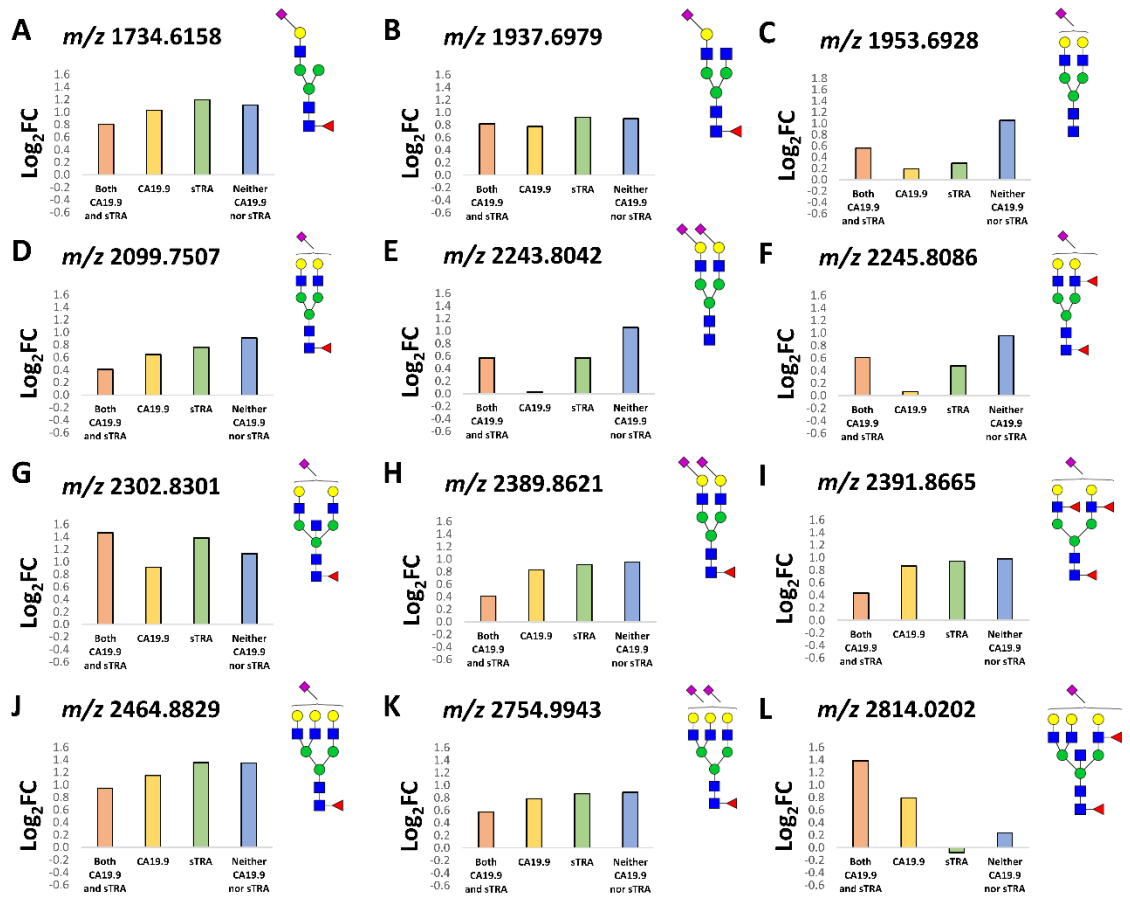
Figure 24. Sialic Acid Stabilization of TMA Cores. A-L) Representative α2,3-sialylated N-glycan structures enriched in tumor tissue cores as compared to patient matched normal tissue cores. Log$_2$-FC between patient matched tumor and normal cores, where positive values represent enrichment in tumor tissue.

123

Table 8. Log₂-FC and AUP Intensity Data for AA-Stabilized TMA Cores.

Table 8. Log$_2$-FC and AUP Intensity Data for AA-Stabilized TMA Cores.

Centroid [m/z]	Both CA19.9 and sTRA		CA19.9		sTRA		Neither CA19.9 nor sTRA	
	Fold Change	Intensity	Fold Change	Intensity	Fold Change	Intensity	Fold Change	Intensity
1588.5557	0.7300	878.9225	0.2582	698.8101	0.6013	914.8836	1.0571	900.6399
2099.7507	0.4085	46658.9906	0.6431	45193.2667	0.7600	67360.1333	0.9116	51497.8833
2391.8665	0.4367	34321.2866	0.8654	37454.7827	0.9439	53369.4667	0.9800	36108.7595
2389.8621	0.4071	33339.7756	0.8272	38784.7980	0.9122	49766.4667	0.9518	34549.3119
3045.1309	0.6408	13394.7468	0.6678	12234.5000	0.9185	20410.6367	0.7377	13590.6520
3047.1101	0.6488	12995.0706	0.6338	11794.2727	0.9016	19478.3375	0.8882	13156.2914
2245.8086	0.6080	11617.8172	0.0660	8465.1040	0.4763	12004.9650	0.9556	11237.0686
2754.9943	0.5707	11507.1192	0.7844	11127.6347	0.8623	16962.4208	0.8884	12515.7129
2243.8042	0.5690	11289.2776	0.0248	8271.0900	0.5687	12303.3358	1.0540	11417.7861
2756.9987	0.6774	10354.7216	0.6550	8177.2100	0.8206	14632.9867	0.7978	10887.5210
1953.6928	0.5610	5341.5294	0.1919	4483.8242	0.2918	5800.5642	1.0531	5745.1135
3122.1309	0.5321	5251.0380	0.3164	3755.3627	0.4770	6739.2292	0.5712	5701.2346
3120.1265	0.2387	4072.2387	0.2652	3178.2790	0.5609	5881.9900	0.6059	4716.3866
2302.8301	1.4655	3847.4997	0.9116	3172.0937	1.3803	4229.3554	1.1299	2820.8969
2464.8829	0.9450	3460.7556	1.1502	3142.9455	1.3584	5208.6625	1.3483	3688.6793
1937.6979	0.8157	2947.7337	0.7730	2664.7448	0.9204	3516.7792	0.8982	2645.7965
2330.8614	1.1615	2824.5832	0.3524	2297.8135	0.5762	2525.8255	1.3915	2862.6964
2899.0729	0.5971	2181.1156	-0.4711	1199.2390	0.6073	2430.2258	1.0099	2032.7094
2901.0522	0.7902	2170.4498	-0.2949	1141.1947	0.4682	2071.1514	0.7954	1771.5648
2814.0202	1.3854	1855.9642	0.7914	1118.1365	-0.0829	401.2256	0.2334	549.3123
3179.1524	1.3878	1669.0263	0.4102	1522.2567	0.1445	357.5152	0.0920	512.8538
1734.6158	0.8024	1607.1447	1.0297	1632.8729	1.1968	2150.3284	1.1124	1489.2360
3049.0894	0.5562	1284.9651	0.3277	1123.7731	1.1540	2015.6976	0.9335	1379.2139
2592.9415	1.2570	1263.7443	0.7126	1020.7995	1.1694	1692.1517	0.3048	835.1244
2184.8035	0.9618	1045.4470	1.3543	1027.8778	1.3159	1145.7591	1.4707	1051.8391
1791.6489	0.9779	1043.3444	0.4214	775.6399	0.8273	997.3373	1.0619	842.1190
3325.2103	1.1212	1008.8287	0.2911	1179.1920	-0.1319	256.9930	0.4174	438.9953
2594.9459	1.4722	953.4439	1.0805	656.8822	1.2411	867.6010	0.5377	449.5816
3266.1844	0.3052	952.2453	0.1311	720.6593	-0.0221	715.1896	0.3677	831.5409
2140.7773	1.5996	898.3702	0.9094	820.8087	1.6031	778.4248	1.1731	544.4596
2417.8934	0.7703	885.0449	0.5632	781.6632	0.8685	1023.3772	0.8630	778.8700
2667.9623	1.1839	881.8418	0.6622	906.5518	0.9665	597.8705	0.5209	557.4260
3588.3108	-0.1586	870.4476	-0.0132	771.8786	-0.2820	557.7137	-0.1153	561.1179
3633.3210	0.0963	846.9732	0.1725	731.8269	0.2039	761.6313	0.0689	719.0854
3556.3210	0.0232	801.2463	-0.0855	655.2075	-0.0248	673.1899	-0.0190	668.3081
3702.3789	0.0218	801.0947	-0.1589	584.6486	0.2690	1368.1991	0.1782	749.8388
3734.3687	0.3393	780.6715	0.2635	402.7431	0.1676	307.3056	0.3022	358.2584
3852.3953	0.2559	763.1563	0.6593	675.2545	1.1005	1101.8338	0.3252	928.5617
3880.4266	0.1475	737.3105	0.1582	250.2074	0.3917	243.8357	-0.0014	289.7402
2474.9149	0.8946	686.1145	0.9829	656.6366	1.1113	800.4861	0.9617	629.4493
2083.7558	1.0305	683.1610	0.9682	688.7409	1.0032	819.3805	0.7386	580.6011
3264.1800	0.1508	681.4168	0.1624	586.8056	-0.2936	466.6913	0.0243	587.8730
3558.3002	0.0887	650.5435	0.3413	448.1070	-0.1998	377.3892	-0.2380	445.9021
3017.0996	0.5944	628.9637	0.2463	897.2575	-0.1218	355.5194	0.2646	483.1616
3268.1888	0.3009	619.2407	0.0105	370.1782	-0.2830	310.6225	-0.0844	513.8394
3779.3888	0.0072	618.9588	-0.0012	491.1958	0.0765	590.6224	0.0306	592.2058
2271.8355	0.6132	595.1615	0.0929	578.5817	0.3732	457.5226	1.5522	689.6138
3544.2846	0.2542	594.1858	0.1111	567.3241	-0.4338	305.4741	-0.0415	332.0953
2986.1050	0.2106	585.3374	-0.5972	292.6053	0.0032	404.1517	0.2094	431.8489
2318.8250	0.6538	584.3362	0.3338	398.4857	0.5436	533.5258	0.9121	536.5304
3982.4489	0.4478	580.6259	-0.2800	425.2241	0.1226	352.2969	-0.3154	303.5218
3560.2795	0.3271	507.9753	0.1348	440.5444	0.1861	399.4267	0.0528	425.8965
2903.0591	0.4282	501.0887	0.0034	292.1498	0.0105	344.4316	-0.0149	318.7844
2830.0151	0.3095	497.6539	0.0635	333.8733	0.5711	682.2370	0.3720	670.9259
3836.4004	0.4564	485.8277	-0.2249	372.0839	0.0272	213.7607	-0.0277	227.1791
2858.0464	0.3286	471.1037	0.1159	399.8335	0.2109	351.9727	0.4582	408.8395
3332.2790	-0.2879	467.4517	-0.1936	555.6265	-0.3919	420.6194	-0.2819	452.3097
2156.7722	1.1207	463.3966	0.3849	198.9112	0.3225	211.8881	0.4691	176.1748
3674.3476	-0.0949	461.6950	0.4208	617.0365	0.0559	382.7484	0.0033	377.7417
3469.2638	0.3234	451.8388	0.2901	557.1624	0.1247	307.3554	-0.3367	235.0908
2419.8978	0.7187	438.1490	1.0715	691.8955	0.8272	399.9938	0.6140	341.8993
2840.0471	0.1858	435.9853	-0.1140	342.0754	-0.0157	372.8133	0.1023	411.9397
3132.1629	0.5202	414.1247	-0.2280	291.2164	0.2698	349.5046	0.4708	379.7658
2286.8352	1.2124	387.2843	0.7412	321.8799	0.6546	207.9919	0.0488	172.4521
3850.3909	0.0671	381.4620	-0.2276	292.1214	0.3974	414.4407	0.4601	430.5678
3485.2587	-0.0369	355.2222	0.3044	390.2540	0.6817	502.0180	0.2904	398.1496
2387.8828	0.4619	353.3201	0.6471	476.2327	1.1563	356.8234	0.4037	255.9164
3487.2631	0.0582	348.7592	-0.2127	280.0704	0.3030	414.5090	0.5492	425.8026
2448.8880	1.2145	346.3911	1.2166	203.4291	0.6341	124.8313	0.1787	104.3229
1912.6662	0.6200	338.5660	0.2897	223.6775	0.0208	266.9027	0.5936	271.3491
3704.3330	0.3689	334.1641	-0.0561	254.6241	0.0847	368.9007	0.1781	370.4934
3323.2059	0.3631	331.7865	0.3741	598.2298	-0.2183	262.0051	0.0551	305.2166
2022.7506	0.5885	283.7597	0.5043	262.4727	0.7844	332.7603	0.7320	276.5223
3410.2379	0.0387	278.9485	0.3709	243.1178	0.4703	363.7577	0.0509	260.5690
3130.1585	0.2613	277.6546	0.3256	240.1254	0.1284	210.9380	0.0178	239.1858
2610.9408	0.0568	217.1047	0.1058	147.2209	-0.4102	126.9894	-0.1188	148.4337
2842.0515	0.0351	204.7200	-0.0433	159.2148	-0.1203	190.2229	0.0270	191.5226
1994.7193	0.8127	197.2779	0.5334	157.6480	0.0055	119.7286	0.3797	115.8698
2346.8563	0.3056	190.8673	0.5525	219.4622	0.5506	168.0192	0.5498	194.9802
2058.7242	0.5841	187.8892	0.6469	125.5378	-0.2552	90.8619	0.3214	111.9037
2608.9364	0.1552	186.2921	-0.1916	110.5371	0.1005	178.4843	0.2861	184.8986
1750.6134	0.4084	172.3391	0.0769	142.8973	0.0794	146.7574	0.4893	159.4521
2101.7551	0.3837	126.9926	0.7124	143.5501	0.0491	130.0193	0.6879	128.6026
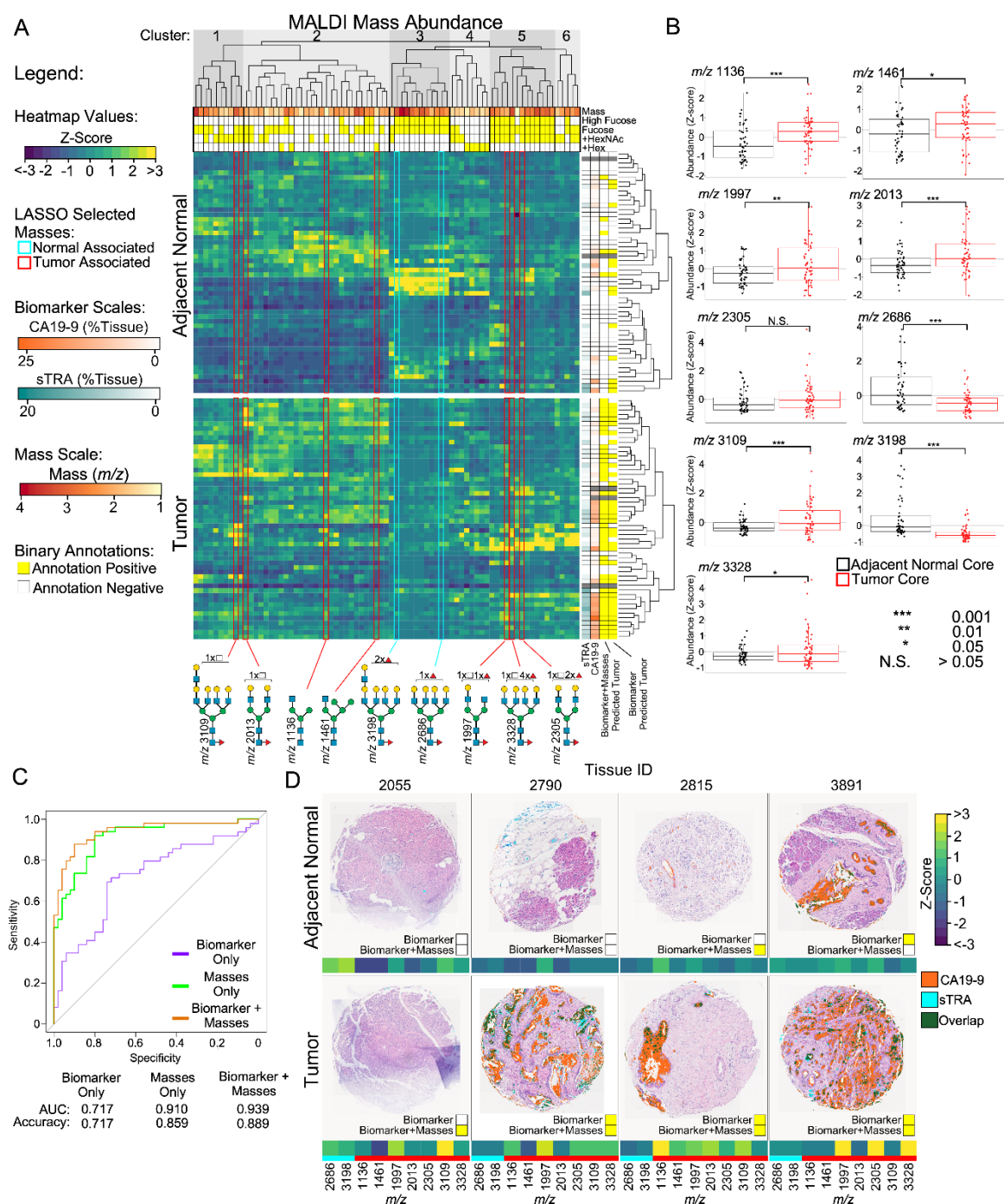
Figure 25. Glycan Structures with Potential Complementary Value to Current Biomarkers. A) Hierarchical clustering and LASSO-regularized logistic regression identified families of masses with potential complementary value to known PDAC biomarkers. Masses selected by LASSO-regularization are highlighted and color coded for tumor-core associated or normal-core associated. Cores predicted to be tumor are indicated by a yellow box on the right. B) Individually, the masses selected by LASSO regularization have significantly different abundances between

adjacent-normal and tumor cores. C) Receiver operator curves of the use of the models to distinguish the tumor cores from the adjacent-normal cores indicate an improved accuracy using the combination of masses and biomarkers. D) Example cores illustrate the complementary value the masses and the biomarkers. A yellow box indicates prediction as a tumor core. The addition of the masses correctly identified a tumor core missed by the biomarkers (2055) and correctly identified a normal core falsely called tumor by the biomarkers (3891). In other instances, the combination produced no change (2790) and falsely predicted a normal core to be a tumor core (2815).

associated clusters. Each of the selected masses had an abundance that was significantly different between the tumor and the adjacent-normal cores. When used in a predictive model in combination with the glycan biomarkers, overall predictive value was increased relative to using the biomarkers or the masses alone (Figure 25C). The area-under-the-curve (AUC) in receiver-operator characteristic (ROC) analysis was 0.939 using the combination, greatly improved over the value of 0.717 using the biomarkers alone and moderately improved over the value of 0.910 using the masses alone.

We further examined cores for which the immunostaining and glycan imaging were complementary to each other. Figure 25D shows cores from 4 tumors and their corresponding, adjacent-normal areas. In the adjacent normal cores, tissues 2055 and 2790 are examples that were correctly predicted to be normal by both the biomarker and the combination, while 2815 and 3891 were incorrectly predicted to be tumor cores by the combination and the biomarker, respectively. In each of the tumor sections, either the biomarker or the glycans provided a positive signal. Tissue 2790 represents a strongly predicted tissue by biomarker alone, while tissue 2815 was predicted more strongly through the high expression of the lower mass, hybrid and immature N-glycan structures.

In order to obtain more information about interesting glycans identified in the TMA, whole tissue sections corresponding to the cores highlighted in Figure 25D were analyzed by immunofluorescence. The TMA analysis showed that glycans with a terminal GlcNAc or GalNAc could be higher in certain tumors. Lectin immunofluorescence staining provides an additional layer of detail to mass

127

abundances, as it allows for distinguishing between mass isomers as well as binding a range of masses which share glycan motifs. We chose the lectin *Phaseolus Vulgaris* Erythroagglutinin (PHA-E) to detect bisecting GlcNAc and the *Griffonia (Bandeiraea) Simplicifolia* Lectin II (GSL-II) to detect terminal GlcNAc.

We first co-registered the imaging mass-spectrometry data from the relevant glycans with stains for CA19-9 expression obtained via HRP-DAB immunohistochemistry on serial sections (Figure 26A,B). Bi-, tri- and tetra-antennary N-glycans with both core and terminal fucosylation were specifically colocalized with areas of CA19-9 staining as determined by co-registration analysis in SCiLS Lab (Figure 26C). Segmentation analyses of 72 detected N-glycan structures revealed distinct glycoprofiles between those areas of high CA19-9 expression and those with little to no expression (Figure 26D,E).

H&E stains on the whole tissue sections revealed diverse tissue morphologies (Figure 27A). The immunofluorescence stains and MALDI-IMS analysis showed similar patterns as the selected TMA cores in Figure 25D, with tissue 2055 featuring low levels of biomarker expression, while the remaining tissues have regions of high and low expression. By overlaying the biomarker data on the mass abundances (Figure 27B) one can observe a complex relationship between the glycans identified by MS and the biomarkers. Tissues 2815 and 3891 have significant diversity, featuring regions with all combinations of high and low mass abundance and biomarker expression.

The lectins PHA-E and GSL-II had very distinct, largely non-overlapping staining (Figure 27C), indicating that these two epitopes are characteristic of

128
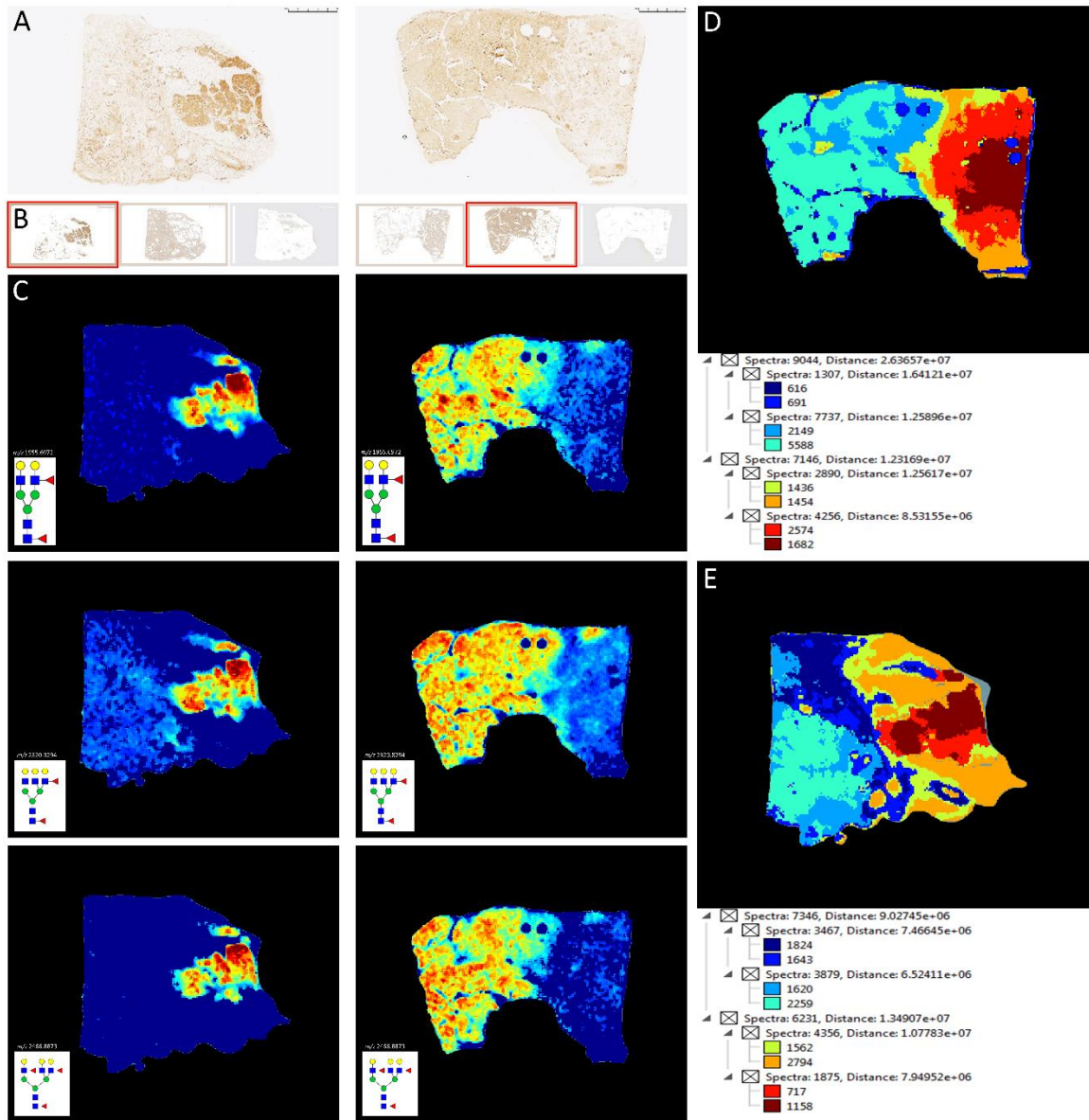
Figure 26. N-glycan Co-localization with CA19-9. A) Representative whole tissue block sections from which TMA cores were derived were IHC stained for CA19-9 expression. B) A color-based k-means clustering algorithm was applied to high-resolution staining images to generate unbiased staining classifications, the most intense of which (outlined in red) were co-registered with original scans in Fleximaging and used to draw regions of interest around stained tissue. C) SCiLS lab software was used to identify and create images of N-glycans colocalized to areas of CA19-9 staining. Shown are three representative N-glycans (Hex5dHex2HexNAc4 *m/z* 1955.6975, Hex6dHex2HexNAc5 *m/z* 2320.8294, Hex6dHex3HexNAc5 *m/z* 2466.8873). D, E) Segmentation analysis across eight nodes of 72 N-glycan structures showing differential associations of glycans between CA19-9-staining and non-CA19-9-staining tissue.
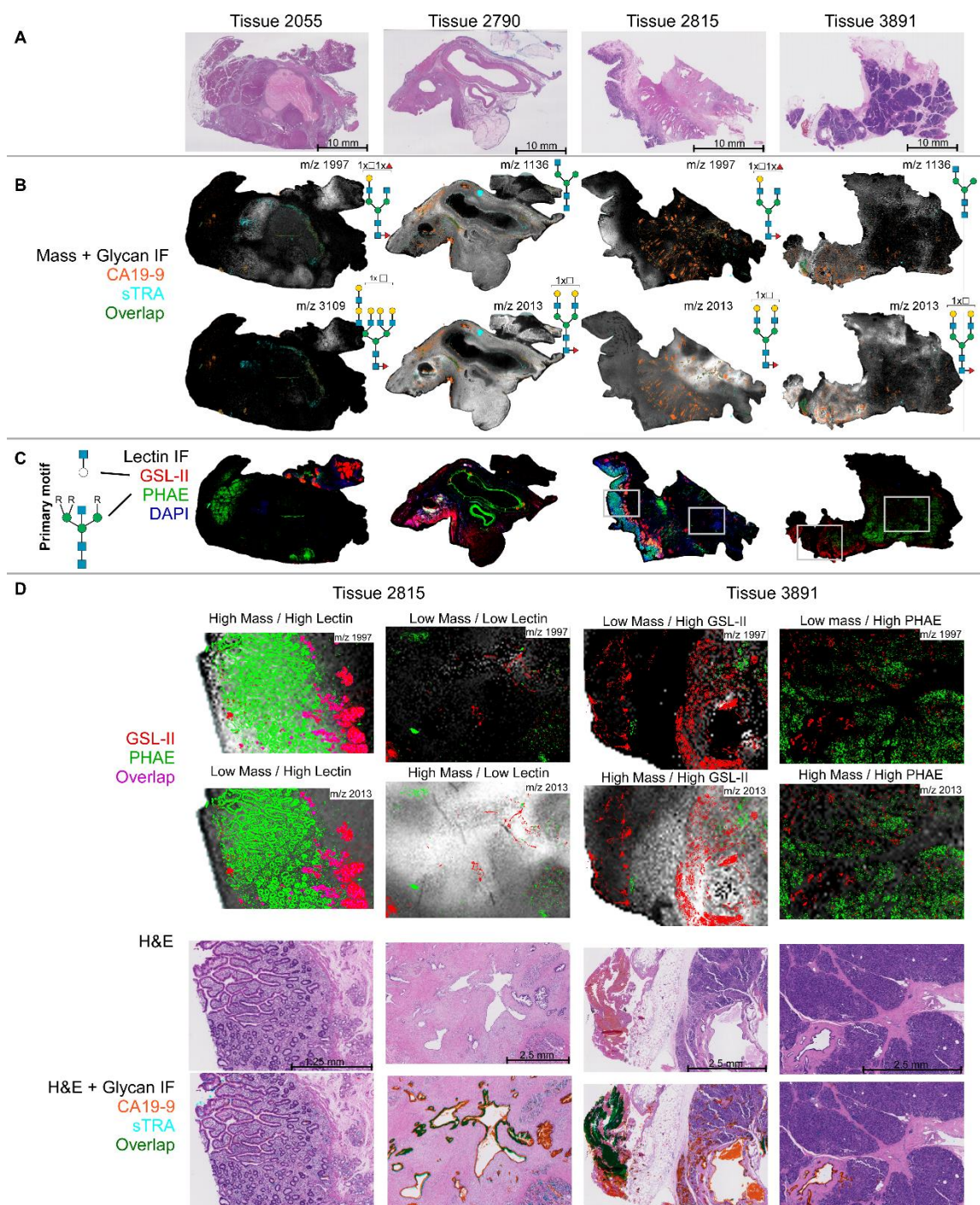
Figure 27. Immunofluorescence Stains Reveal Complex Relationships Between Biomarkers. Whole tissue sections for patients which contain both cancer and adjacent normal regions were investigated. A) Hematoxylin and eosin (H&E) stained tissue sections. B) Immunofluorescence (IF) signal above threshold for biomarkers CA19-9 and sTRA overlaid on select complementary mass abundance. C) Lectin stained IF images above threshold. The primary motif for PHAE (green) is a bisecting GlcNAc with two or three antennae while the primary

130

motif for GSL-II (red) is a terminal GlcNAc presented on an unbranched monosaccharide. D) Selected regions of interest in tissues 2815 and 3891 indicate mixed relationship between lectin binding, mass abundance, and biomarker presence. Regions low and high in biomarker (CA19-9 and sTRA) expression are given for each.

different types of cells. Regions of interest highlighted in Figure 27D show the diversity in mass abundance, lectin staining, and biomarker expression. Notably tissue 2815 shows regions high in *m/z* 1996.7238 and lectin staining as well as regions high in *m/z* 2012.7187 and biomarker expression with little lectin staining. While tissue 3891 shows regions with high *m/z* 2012.7187, biomarker expression, and GSL-II staining as well as regions which are low in the highlighted masses but show strong PHAE staining. Despite the combined binding specificity for PHAE and GSL-II for many +HexNAc containing structures, regions exist in all 4 highlighted tissues which have high mass abundance but low lectin binding. While this may be due to limited sensitivity of the lectins, it could also indicate that these regions feature mass isomers that do not have the primary binding motifs of these lectins. Such glycans could include tetra-antennary bisecting GlcNAc glycans, glycans with terminal GlcNAc presented on a branched chain, blood group A presenting glycans, and alpha-GalNAc terminated glycans. In sum, the combination of lectin staining with IMS data gives more information on the glycans containing the lectin epitopes, and it serves to shed light on the isomeric variants that are present for particular masses identified.

3.5 Discussion

This chapter describes a novel effort to determine the tissue N-glycome of the human pancreas and pancreatic cancer using formalin-fixed clinical specimens. Unique to the pancreas is the finding that high-mannose N-glycan structures are expressed abundantly in non-diseased organ tissue as well as normal tissue adjacent to cancerous regions (Figure 15 and Figure 21) but are not

detected with high abundance in the tumor regions. This is in contrast to other cancer tissues that all exhibit tumor-localized abundant detection of high-mannose structures, including prostate, ovarian, bile duct, breast, and colorectal cancers[209,213,219,401]. It is suspected that the abundance of high-mannose structures in these cancers is due to incomplete N-glycan processing[402]. This does not appear to be the case for pancreas, but rather a feature of healthy tissue whose functions have yet to be determined.

The analysis of normal pancreas detected multiple sulfated, terminally GalNAcylated bi-antennary N-glycan structures in islets (Figure 16). As mentioned previously sulfated N-glycans of the same composition were reported in adult pig islet (API) transplant studies. Sulfation is already known to play a role in pancreatic islets, where in that glycolipid sulfatides are involved in normal insulin secretion and sulfation of heparin sulfate has been implicated in islet amyloid polypeptide (IAPP) aggregation in Type 2 Diabetes Mellitus[403,404]. Sulfated N-glycans on immunoglobulin G have also been extensively characterized, where these acidic modifications can lead to fine-tuned immune responses[405]. Sulfated N-glycan structures, especially those with sulfo-sLeX motifs, are known to enhance lymphocyte homing and are implicated in interactions with other immune cell populations[406]. Terminal sulfo-GalNAc residues found on N-glycans specific to pituitary hormones lutropin and thyrotropin are known to govern immune interactions with macrophages via the C-type mannose receptor MCR1[407]. Because the pancreas is a highly dynamic site of immune regulation, it is possible

that these unique sulfated, terminally-galactosylated islet structures play a role in normal immune recognition and homeostasis.

Key N-glycan structural themes associated with PDAC compared to non-tumor tissues were increased sialylation, poly-LacNAc extensions, branching and extensive fucosylation of high mass N-glycans. Also observed were structures with bisecting GlcNAc residues and terminal GalNAc (di-LacNAc) modifications. Low levels of sialylation were seen in normal tissue whereas α2,3 sialylated N-glycans were expressed abundantly in TMA tumor cores. α2,6-sialylated structures were detected at lower levels compared to their α2,3 counterparts but were typically more specific to primary adenocarcinoma clusters. This is in accordance with studies of pancreatic cell lines which showed increased but varied α2,3 and α2,6 content across different models as compared to normal pancreatic cells, with α2,3 sialylation implicated in a more metastatic phenotype[315]. In addition, analyses of pancreatic cancer in mouse models have detected β-galactoside α2,6-sialyltransferase 1 (ST6GAL1) overexpression and subsequent increases in α2,6 sialic acid linked to aggressive metastasis[239,240]. A lack of fucose and sialic acid residues characterized N-glycans in necrotic PDAC tissue in this study, which is consistent with findings from previous glycan MALDI imaging analyses of breast cancer tissues and other tumor tissue types that detected similar necrosis-associated glycans[202]. Increases in N-glycan branching is attributable to increased alpha-1,6-mannosylglycoprotein 6-beta-N-acetylglucosaminyltransferase V (MGAT5) expression which extends tri-antennary structures into tetra-antennary N-glycans. MGAT5 has been shown to be upregulated in PDAC in response to

KRAS-mediated oncogenesis[177]. Similarly, prior studies have demonstrated increased amounts of α1,3-linked fucose present in certain subsets of pancreatic cancer cell lines[408]. A different study reported expression of α-(1,3/1,4)-Fucosyltransferase (FUT3), which is one of the FUT enzymes responsible for adding fucose residues to N-glycan antennae, is upregulated in pancreatic cancers and is involved in the development of a more metastatic phenotype[409].

Another goal of this aim was to better link N-glycan structures associated with biomarker expression by integrating mass spectrometry and immunohistochemistry data. Consistently, N-glycan structures that colocalized with CA19-9 immunostaining in tissues (Figure 26) did not contain a sialyl Lewis A (sLeA) motif (Hex[β1,3](Fuc[α1,4])HexNAc) as assessed by IMS. CA19-9 epitopes have been detected specifically on mucin glycoproteins MUC5AC and MUC16 in PDAC patient populations, detection of which bolsters the performance of cancer identification when combined with clinically utilized CA19-9 panels[410]. These mucin glycoproteins are predominantly O-glycosylated, and it may be more likely that the CA19-9 epitope is present in these O-glycans. Studies of commonly-used pancreatic cancer cell lines have demonstrated variable levels of CA19-9 and sTRA expression between cell lines[110]. Other analyses of normal pancreas and PDAC cell lines have shown a complex relationship between the expression of Lewis antigens B, Y, sLeA and sLeX which in some lines correlated with increased metastatic capacity while in others showed little to no correlation[315]. These heterogeneous results demonstrate the challenges of using one or few PDAC cell lines to accurately study the common pancreatic cancer biomarkers. Linking

specific N-glycans to CA19-9 and sTRA biomarker expression levels is currently inconclusive due to the enormous complexity of the N-glycan structures detected in the CA19-9 and CA19-9/sTRA tissues. The N-glycans detected represent every major feature of complex N-glycans including bisecting GlcNAc, LacNAc extensions, di-LacNAc and multi-fucosylation and sialylation modifications. While an extensive number of N-glycans were detected in the tumor regions, there are an unknown number of higher mass glycans of m/z > 5000 that cannot be effectively detected by MALDI-FTICR directly from tissue without extensive instrument, method and sample preparation optimization. Stability of sialic acids in the MALDI process is an additional factor, which is mitigated by softer ionization environments in the MALDI-FTICR[233,364]. Stabilization by amidation is a useful tool for preventing sialic acid loss during ionization can further aid in the differentiation of isomeric sialic acid linkages[204,384]. Shortcomings of the amidation-amidation reaction used in this chapter led us to speculate that additional methods, explored in Chapter 4, may be created to better characterize sialyation in N-glycan IMS experiments.

The cumulative data generated from the IMS glycan tissue analyses also allowed integration of the detection of individual N-glycans with results from existing antibody-based linear regression models for the classification of PDAC tumor vs. normal tissue samples[110]. Improvements in receiver operator curve (ROC) accuracy and AUC were observed when both IMS glycan masses and biomarker data were combined to build linear regression models as compared to models based off those analyses individually. These results demonstrate a

complex relationship between mass spectrometry and antibody-biomarker characterization of these tissues which can be exploited to bolster classification algorithms. Complementary IMS and biomarker staining data enhances the confidence of tumor vs. non-tumor tissue calls in our modeling. Additionally, cases where biomarker data is lacking or insufficient can be rescued and correctly classified by the incorporation of imaging mass spectrometry data into these models. The ability of these separate techniques to inform one another as well as compensate for the limitations of either model is demonstrated herein and suggests future utility for combining cross-disciplinary analyses such as these into existing PDAC classification assays. The N-glycan distribution maps can also be used to select other lectins not previously evaluated for staining for more targeted screening of glycan motifs. The PNGase F-based IMS methods is specific for N-glycan species and combined use with multi-lectin stains can address O-linked antigens, which are well known in PDAC[411]. Lectin staining provides the opportunity to parse out further structural characterizations in our mass spectrometry data via the ability of specific lectins to recognize specific carbohydrate motifs. These data layered into analysis by mass spectrometry offers the possibility of identifying specific N-glycan isomers which are typically indistinguishable by most imaging mass spectrometry systems.

In summary, our N-glycome analysis of biomarker-defined PDAC tissues using N-glycan MALDI IMS approaches illustrates the potential to inform more targeted probing of specific N-glycans and N-glycan structural classes that correlate with current and prospective carbohydrate biomarkers of PDAC. The

glycan maps generated can be used in the future to target regions of interest to identify potential glycoprotein carriers. Combining imaging mass spectrometry with antibody immunostaining improves detection and classification of PDAC and informs on expanded directions for each method. Advancements in imaging mass spectrometry techniques and instrumentation and the use of new enzymes and chemistries to reveal a broader repertoire of structures, isomers, modifications and molecules will expand these approaches beyond the N-glycome. The continued search for new lectins which recognize carbohydrate structures associated with PDAC, as well as improvements to multi-round immunofluorescence technologies and advancements in statistical image analysis software, potentiates the discovery of further, novel subclasses of pancreatic cancer. Observations about PDAC biomarkers and N-glycan structures from this dissertation and ongoing work may provide leads to impactful new diagnostic and surveillance strategies critically needed in the clinic, as well as continued insights into the evolving role of the glycome in this disease. Critically for this body of work, limitations inherent to the sialic acid stabilization method used inspired the further glycomic developmental effort described in Chapters 4 and 5.

Chapter 4: Isomeric Characterization of Sialic Acids by Amidation-Amidation Reactions

Bioorthogonal chemical labeling probes targeting sialic acid isomers for N-glycan MALDI imaging mass spectrometry of tissues, cells and biofluids

Colin T. McDowell[1][†], Xiaowei Lu[1][†], Calvin R.K. Blaschke[1], Liping Liu[1], Grace Grimsley[1], Luke Wisniewski[2], ChongFeng Gao[2], Anand S. Mehta[1], Brian B. Haab[2], Peggi M. Angel[1], Richard R. Drake[1]*

[†]Both authors contributed equally to this work

[1]Medical University of South Carolina, Department of Cellular and Molecular Pharmacology and Experimental Therapeutics, Charleston, SC

[2]Van Andel Institute, Department of Cell Biology, Grand Rapids, MI

4.1 Abstract

Sialic acid isomers attached in either α2,3 or α2,6 linkages to glycan termini confer distinct chemical, biological and pathological properties, but they cannot be distinguished by mass differences in traditional mass spectrometry experiments. Multiple derivatization strategies have been developed to stabilize and facilitate the analysis of sialic acid isomers and their glycoconjugate carriers by high performance liquid chromatography, capillary electrophoresis and mass spectrometry workflows. Herein, a set of novel derivatization schemes are described that result in the introduction of bioorthogonal click chemistry alkyne or azide groups into α2,3 and α2,8-linked sialic acids. These chemical modifications were validated and structurally characterized using model isomeric sialic acid conjugates and model protein carriers. Use of an alkyne-amine, propargylamine, as the second amidation reagent effectively introduces an alkyne functional group into α2,3-linked sialic acid glycoproteins. In tissues, serum and cultured cells, this allows for detection and visualization of N-linked glycan sialic acid isomers by imaging mass spectrometry approaches. Formalin-fixed paraffin-embedded prostate cancer tissues and pancreatic cancer cell lines were used to characterize the numbers and distribution of alkyne-modified α2,3-linked sialic acid N-glycans. An azide amine compound with a poly-ethylene glycol linker was evaluated for use in histochemical staining. Formalin-fixed pancreatic cancer tissues were amidated with the azide amine, reacted with biotin-alkyne and copper catalyst, and sialic acid isomers detected by streptavidin-peroxidase staining. The direct chemical introduction of bioorthogonal click chemistry reagents into sialic acid-containing

glycans and glycoproteins provides a new glycomic tool set to expand approaches for their detection, labeling, visualization and enrichment.
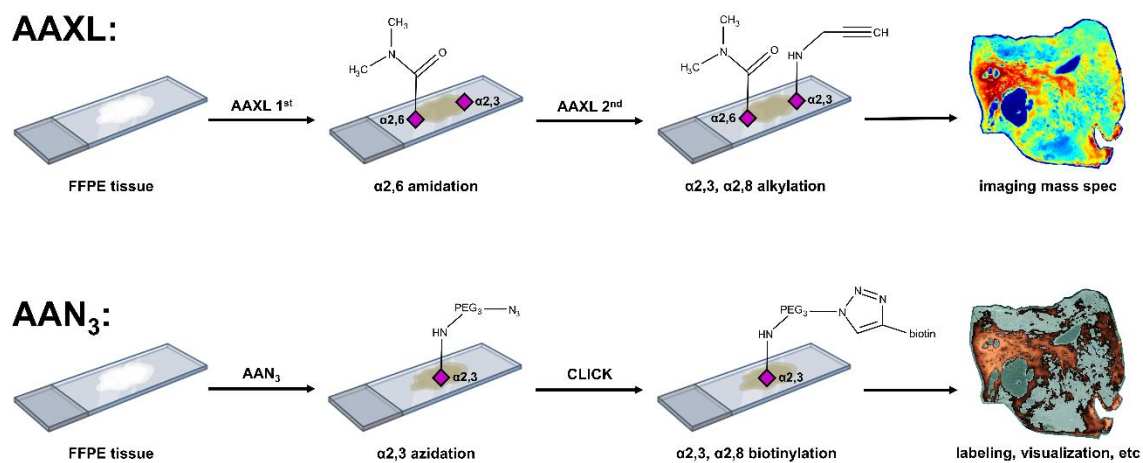
Figure 28. Bioorthogonal Probes for Sialic Acid Isomers. Graphical Abstract

4.2 Introduction

As outlined in the introduction, sialic acid (SA) sugar modifications on glycoproteins and glycolipids is a hallmark of the glycocalyx, the dense glycoconjugate network present in extracellular matrix and on the surface of the cell. Sialic acids act as receptors for the influenza virus and other infectious pathogens, are constituents of well characterized carbohydrate tumor antigens and are binding motifs for selectins and siglec family proteins amongst other biological functions[412–419]. Sialic acid sugars exist in nature as a variety of chemical compositions, where N-acetylneuraminic acid (NeuAc) is the predominant species in humans while N-acetylglycoylneuraminic acid (NeuGc), a hydroxylated variant, is more abundant in all other mammalian species[412,420,421]. These residues are attached as monomers to their protein and lipid carriers in α2,3 and α2,6 anomeric linkages or as polysialic acid chains in α2,8 and α2,9 isoforms[421]. α2,3-linked sialic acid occur in cancer as part of the carbohydrate tumor antigens sTRA, sialyl-Lewis X and sialyl-Lewis A (CA19-9)[110,422]. Multiple studies have demonstrated the association between increased α2,6 sialylation and various cancers[423,424]. Additionally, α2,3 and α2,6 sialic acids have well documented roles in influenza virus infections[414,425].

Due to their biological and pathophysiological importance, sialic acids have long been the target of chemical derivatization approaches to enhance functional studies by mass spectrometry analyses[384,421]. Historically, the lability of sialic acids in MS experiments has been a major concern for both laser desorption and electrospray sources, where the residue is often lost during ionization[384,385,426].

Sialic acids can be chemically stabilized through amidation or esterification of the anomeric carboxylate group as demonstrated by multiple groups[384,421]. In these reactions, α2,3, α2,8 and α2,9 linked sialic acids preferentially undergo intramolecular esterification due to the proximity of neighboring hydroxyl groups and the SA carboxylate, forming 6 member lactone rings[421,427]. This unstable lactone can be subsequently decyclized through reaction with primary amine-containing compounds[204,391,428]. α2,6-linked sialic acids do not form intramolecular lactones under these conditions and instead are stably amidated or esterified depending on the combination of reactants[384,421].

Bioorthogonal strategies incorporate chemical groups into living systems that are normally not present under natural conditions. In the past two decades, chemoenzymatic, metabolic and chemical labeling approaches have been used to introduce azide and alkyne bioorthogonal functional groups into sialic acids and other sugars, as well as to win Nobel Prizes[429–431]. Small and biologically inert azide and alkyne groups then lie dormant within the living system until they are reacted with their reciprocal chemical group, creating stable cycloaddition products. As an example, azido-labeled sugars can be reacted with bead or surface-bound alkynes, biotin-alkyne conjugates or alkyne fluorophores. Accordingly, this approach has relevant applications in microscopy, flow cytometry and mass spectrometry analyses[432]. The commercially availability of glycan precursor analogues has led to an increasing number of studies which capitalize on this technology to detect both N- and O-glycan alterations[433–439].

In 2016, Holst et al. reported a chemical amidation workflow for in-situ, linkage-specific sialic acid derivatization directly from FFPE tissues with applications towards N-glycan MALDI-IMS analyses[204]. As N-glycan IMS workflows have evolved, sialic acids stabilization strategies to differentiate α2,3 from α2,6 sialylated N-glycan isomers in spatial profiling experiments have proven very effective[204,206,209,215,233,440,441]. The goal of this chapter was to enhance Holst's original amidation-amidation workflow (AA), used in Chapter 3, to generate bioorthogonal α2,3 and α2,8 sialic acids variants. This aim was accomplished through the use of azide-and alkyne-amine compounds as ring-opening primary amine reagents towards α2,3 and α2,8 lactone intermediates after initial amidation. Thus, alkyne or azide functionality is specifically incorporated in α2,3 and α2,8-linked sialic acids. α2,6 sialic acid isomers are amidated as in the original synthesis and are unreactive to the secondary amidation reagents. Isomeric model sialic acid analogues and sialylated protein conjugates were previously used to optimize the reactions and confirm their products. The new amidation reactions were evaluated for use in FFPE tissues, serum and cultured cells, where the click chemistry tag and associated mass shift introduced to sialylated glycans potentiates multiple characterization strategies. By the direct chemical modification of specific sialic acid isomers with click chemistry-compatible bioorthogonal reagents we introduce a new glycomic tool set with applications for labeling, visualization and enrichment of sialylated glycoconjugates.

4.3 Preliminary Development

The experiments presented in this chapter can be divided into two parts. The initial in-vitro development of these theoretical syntheses was performed by a former member of our laboratory, Xiaowei (Vivian) Lu, to who much credit is given. As such, her work served as the basis for extensive further development to assess the compatibility of the reactions with clinical tissues, immobilized biofluids and cultured cells for imaging mass spectrometry, immunohistochemical and advanced labeling applications. Here a synopsis of the initial development work is included, as preface to the subsequent application effort which is the focus of this chapter.

To introduce alkyne and azide amines into α2,3 sialic acids, the previously reported amidation-amidation (AA) reaction[204] was used as the starting point for derivatization of commercially available α2,3 and α2,6 isomeric sialyllactose analogs as model compounds. As summarized in Figure 29, the first step was to incorporate a 2-aminobenzoate (2-AB) group into both compounds to facilitate detection and purification. The first amidation step of this reaction was not changed, in that both compounds were treated with dimethylamine, a 1-hydroxybenzotriazole (HOBt) catalyst and a 1-ethyl-3-(3-dimethylaminopropyl)carbodiimide (EDC) carboxylic acid activator. This reaction results in dimethylamidation of the α2,6-linked sialic acid carboxyl group, while generating a lactone in the α2,3 sialyllactose[388,442]. The original method used ammonium hydroxide amidation as a second step to stabilize the lactone. In contrast, propargylamine, a simple alkyne-amine, or a larger PEG-azide amine (11-azido-3,6,9-trioxaundecan-1-mine, or azido-PEG₃-amine), were used in place

of ammonium hydroxide as the lactone stabilizing second amidation reagent (Figure 29). The resulting products were purified and assessed by 1D and 2D NMRs analysis (data not shown). Both alternate amidation reactions were efficient (quantitative conversion yield, 80% isolation recovery), with confirmed products of an alkyne-amino-3'siallylactose-2AB (Compound 8) or azido-PEG$_3$-3'sialyllactose-2AB (Compound 9). The specific reagents for both derivatization reactions are listed in Table 9. In the rest of this dissertation, the propargylamine reaction will be abbreviated to AAXL (Alkyne-Amidation Expanded Linker for alkyne), and the azide-PEG$_3$-amine reaction as AAN$_3$ (Azide-Amidation N$_3$ for azide).

Additionally, as it is known that sialic acids in α2,8 isomeric linkages undergo a similar lactone cyclization reaction as α2,3, an α2,8-polysialic acid model compound, colominic acid (Compound 12) was reacted with the propargylamine workflow to generate a multiply alkyne-modified neurominic acid chain, Compound 14 (Figure 30). The resulting products were purified and assessed by 1D and 2D NMRs analysis (data not shown).

To investigate lactone formation by the first amidation reaction in AAXL and AAN$_3$, 2AB-labeled 3'sialyllactose (Compound 4) was reacted with the first dimethylamine solution for 1 hr at 60°C as described. The crude reaction mixture was then dissolved in DMSO-d$_6$ for NMR acquisition. A downfield shifted H-2^{II} in the lactone when compared to the amide indicated the formation of the 2,2 lactone (Compound 6) instead of the 2,4 lactone (Compound 7). The 2,2 lactone decomposed in aqueous solvent therefore no further purification was attempted. ^{1}H NMR indicated a quantitative conversion from Compound 4 to Compound 6.
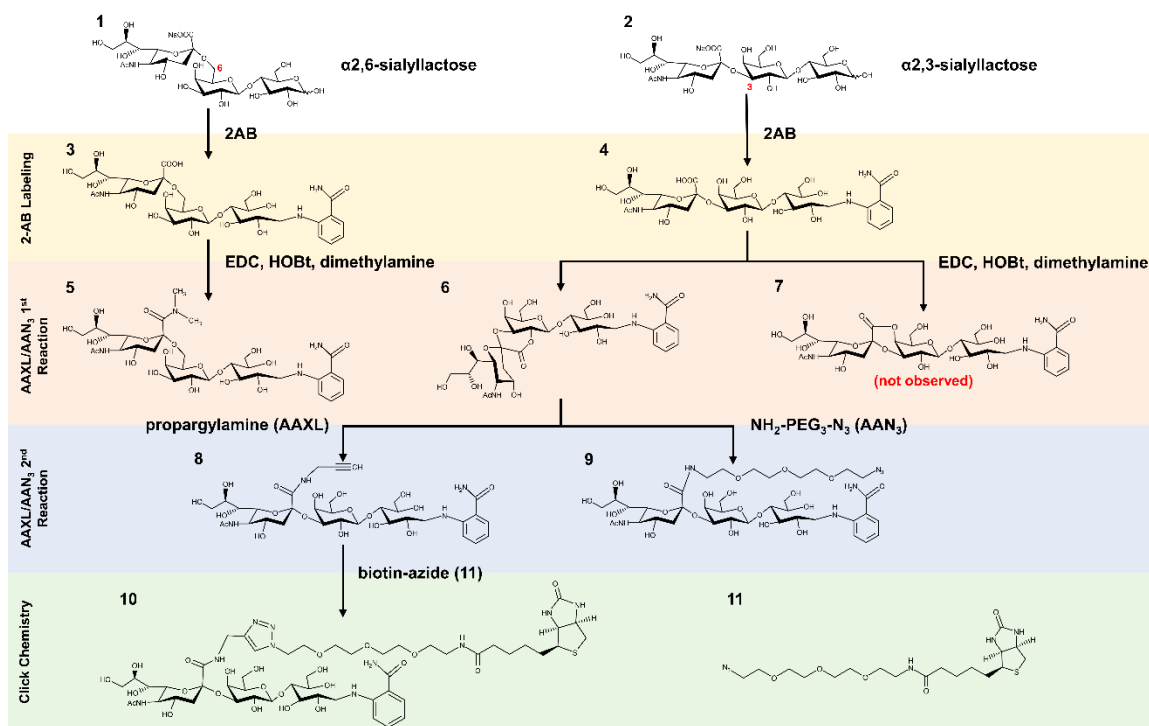
Figure 29. Reaction scheme for AAXL, AAN₃ and AAXL-click on model compounds. α2,6-linked and α2,3-linked sialyllactose model compounds were reductively labeled with 2-aminobenzamide (2-AB) then derivatized by either AAXL (dimethylamine, propargylamine) or AAN₃ (dimethylamine, azido-PEG3-amine). The AAXL-labeled sialyllactose analog was further modified by click chemistry with a biotin-azide conjugate. For simplicity, each structure was assigned a compound number (upper left corner).

Table 9. AAXL and AAN$_3$ Reactions.

AAXL			
	Weight or Volume	*Mole (mmol)*	*Concentration*
1st AAXL Reaction Solution			
EDC	22.0 µL	0.125	0.25
HOBt	42.2 mg	0.250	0.50
Dimethylamine	15.8 µL	0.125	0.25
DMSO	0.5 mL		
2nd AAXL Reaction Solution			
Propargylamine	300 µL		
DMSO	700 µL		

AAN$_3$			
	Weight or Volume	*Mole (mmol)*	*Concentration*
1st AAN$_3$ Reaction Solution			
EDC	22.0 µL	0.125	0.25
HOBt	42.2 mg	0.250	0.50
Dimethylamine	15.8 µL	0.125	0.25
DMSO	0.5 mL		
2nd AAN$_3$ Reaction Solution			
NH$_2$-PEG$_3$-N$_3$	300 µL		
DMSO	700 µL		
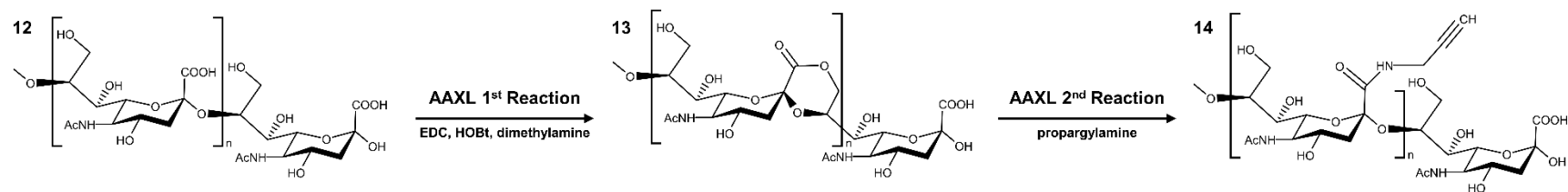
Figure 30. Derivatization of a polysialic acid analog by AAXL. Colominic acid as an analog for α2,8-linked polysialic acid was reacted by AAXL to produce an alkylated polysialic acid chain.

The α2,8 polysialic acid analog (Compound 12) underwent a similar lactone interconversion through the 2,9 lactone intermediate (Compound 13) (Figure 30). Dimethylamidated 6'sialyllactose-2AB was unreactive to the addition of propargylamine or azido-PEG$_3$-amine. To test the stability of the converted α2,6 amide, isolated pure dimethylamidated 6'sialyllactose-2AB was incubated in propargylamine-DMSO (v/v 2/5) at 60°C for 5 hr. After incubation no change was observed as assessed by NMR, indicating the stability of the amidation product.

To confirm that the incorporated alkyne group could be used for click chemistry conjugation, purified alkyne-amine-3'sialyllactose-2AB was further reacted with a biotin-PEG3-azide conjugate through a Cu(I)-catalyzed azide-alkyne cycloaddition to yield a 1,4-disubstituted 1,2,3-triazole link between the sialic acid and the biotin[443,444]. The structure of the resulting successfully biotinylated 3'sialyllacotse-2AB (Compound 10) was then confirmed by NMR (data not shown). The specific reagents and reaction conditions for the CuAAC reaction on AAXL-modified α2,3-sialic acids are listed in Table 10.

To assess derivatization by AAXL and subsequent click modification in a more biologically relevant context, commercially available 6' and 3'sialyllactose-conjugated bovine serum albumin (BSA) (Compound 15, Compound 16) were treated with the dimethylamine and propargylamine amidation reactions. The resulting dimethylamidated 6'sialyllactose-BSA (Compound 17) and alkylated 3'sialyllactose-BSA (Compound 18) were then further modified by CuAAC as previously described for the model compounds. An overall reaction schematic is shown in Figure 31A. To probe for biotinylation of the α2,3 isomer-containing

Table 10. CuAAC Reaction Mixture for AAXL.

		MW (g/mol)	Reagent Stock Prep (per 1 mL H₂O)	[Reagent Stock]	Volume Stock Solution	[Reag
A	Biotin-PEG$_3$-azide	356.16	17.8 mg	50 mM	10.0 µL	1.0 mI
B	CuSO$_4$	159.61	3.2 mg	20 mM	2.5 µL	0.1 mI
C	Sodium ascorbate	198.11	20.0 mg	100 mM	25.0 µL	5.0 mI
D	THPTA	434.50	21.7 mg	50 mM	5.0 µL	0.5 mI
E	Aminoguanidine HCl	110.55	11.0 mg	100 mM	25.0 µL	5.0 mI
F	10X PBS				432.5 µL	
	Overall Volume				500.0 µL	

Mix B and D, A and F in separate Eppendorf tubes. Sequentially add B&D mixture, E and C to A mixture. Reagents A, B, D, E and F may be prepared ahead of time. 100 mM sodium ascorbate must be prepared day of.
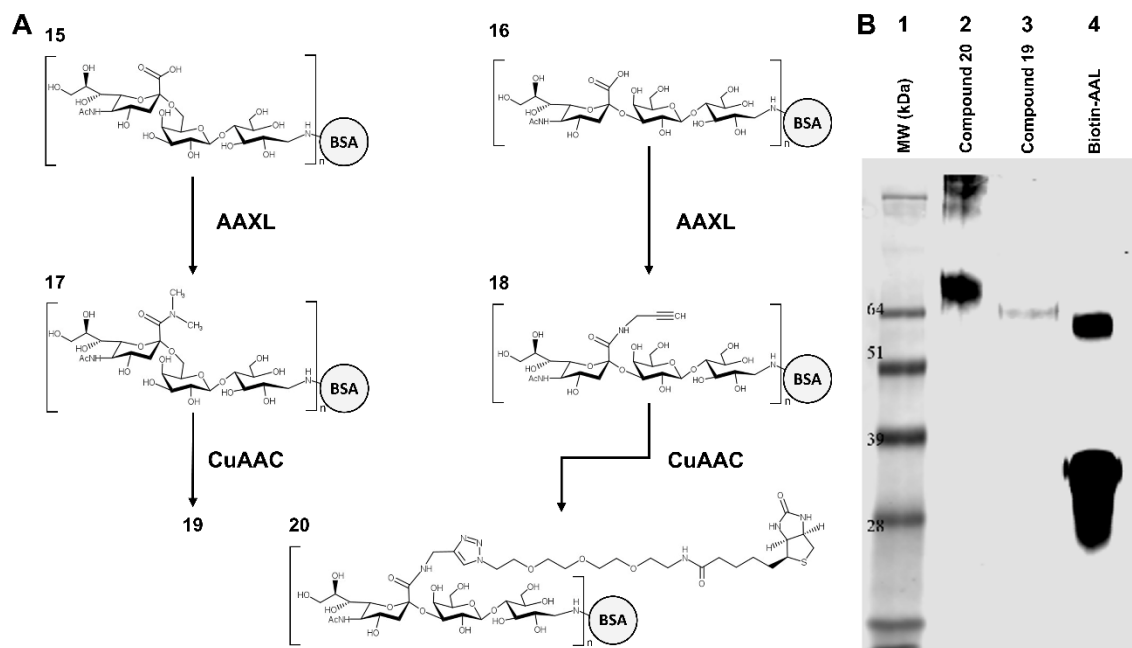
Figure 31. AAXL-Derivatization and Click-Biotinylation of Sialylated Model Proteins. 6' and 3'-sialyllactose-BSA (bovine serum albumin) were derivatized to test the specificity of AAXL-click biotinylation for α2,3-linked sialoproteins. A) reaction schematic for AAXL and subsequent copper-catalyzed azide-alkyne cycloaddition (CuAAC) with biotin-azide. B) western blot of crude reaction lysates for Compounds 19 and 20 probed with streptavidin-IR dye confirms biotinylation specificity for α2,3-sialylated BSA . Biotinylated *Aleuria Aurantia* lectin as a control for biotin installation.

model protein, the resulting crude mixtures from the click reaction were purified by filtration and analyzed by SDS-polyacrylamide gel electrophoresis and subsequent western blot (Figure 31B). As a positive control for detection of biotinylation, both product mixtures were run alongside a commercially available biotinylated *Aleuria Aurantia* lectin (b-AAL). Incorporation of a biotin was confirmed for 3'sialyllactose-BSA (Compound 20) using a streptavidin-conjugated IR dye incubated with the blot (Figure 31B). No specific biotinylation was observed for the CuAAC-reacted dimethylamidated 6'sialyllactose-BSA (Compound 19), confirming the specificity of CuAAC for only the alkyne-derivatized α2,3-sialic acid isomers. At this point AAXL and AAN_3 were developed to a point at which they warranted evaluation in N-glycan IMS and other platforms, presented in the bulk of this chapter.

4.4 Materials and Methods

4.4.1 Materials

1-hydroxybenzotriazole hydrate (HOBt, ≥20 wt. % in H_2O), 5-fluorouracil (99%), α-cyano-4-hydroxycinnamic acid (CHCA), aminoguanidine hydrochloride (98%), copper (II) sulfate ($CuSO_4$, 99%), dimethyl sulfoxide (DMSO), hydrochloric acid (37% in H_2O), Mayer's hematoxylin solution, N-(3-dimethylaminopropyl)-N'-ethylcarbodiimide (EDC, ≥97%), penicillin-streptomycin (P/S), propargylamine (98%), sodium ascorbate (99%), sodium bicarbonate (99%), sodium cyanoborohydride ($NaCNBH_3$, 95%), trifluoroacetic acid (TFA) and tris(3-hydroxypropyltriazolylmethy)amine (THPTA, 95%) were obtained from Sigma-Aldrich (St. Louis, MO). Acetic acid, acetonitrile (ACN, HPLC grade), ammonia (28-30 wt. % in H_2O), chloroform (HPLC grade), citraconic anhydride, H_2O (HPLC

grade), Cytoseal, fetal bovine serum (FBS, qualified), phosphate-buffered saline (PBS), RPMI 1640 media +/- L-glutamine, Slip-Rite cover glass, triethylamine (TEA, 99%) and xylenes (histological grade) were obtained from ThermoFisher Scientific (Waltham, MA). Ethanol (EtOH, 200 proof) was obtained from Decon Labs (King of Prussia, PA). 11-azido-3,6,9-trioxaundecan-1-mine (NH_2-PEG_3-N_3, 95%) and D-biotin (98%) were obtained from AK Scientific (Union City, CA). Biotin-alkyne (98%) was obtained from Synthonix (Wake Forest, NC). Horseradish peroxidase-3,3'-diaminobenzidine (HRP-DAB) staining kits were obtained from R&D Systems (Minneapolis, MN). Recombinant peptide N-glycosidase F (PNGase F PRIME) and sialidase were obtained by N-zyme Scientific (Doylestown, PA). Incubation chambers (200 µL) and Lab-Tek II CC2 8-chamber slides were obtained from Electron Microscopy Sciences (Hatfield, PA). Sialidase (SialEXO) was obtained from Genovis (Cambridge, MA). Gemcitabine hydrochloride (98%), Irinotecan hydrochloride hydrate (98%) and Oxaliplatin (98%) were obtained from Cayman Chemical Company (Ann Arbor, MI). AsPC-1 human pancreatic cancer cells (CRL-1682), HPAC human pancreatic carcinoma cells (CRL-2119), PANC-1 human pancreatic carcinoma cells (CRL-1469), PL45 human pancreatic carcinoma cells (CRL-2558) and Trypsin-EDTA solution were obtained from ATCC (Manassas, VA). 0.4% Trypan Blue was obtained from Lonza (Basel, Switzerland). L-glutamine (Amide-^{15}N, 98%) was obtained from Cambridge Isotope Laboratories (Tewksbury, MA). Nexterion Slide H amine-reactive microscope slides were obtained from applied microarrays (Tempe, AZ).

4.4.2 AA, AAXL and AAN$_3$ on FFPE Tissue Slides

FFPE tissue slides were heated at 60°C for 1 hr, dewaxed with xylenes and rehydrated in a series of graded ethanol and water washes, then dried in a vacuum desiccator for 30 min. The AAXL first reaction solution (200 μL, Table 9) was applied directly to the dewaxed and rehydrated tissue, then a glass coverslip was placed on top of the tissue to ensure even distribution of the reagents. Theses slides were then placed in a sealed container and incubated at 60°C for 1 hr. After incubation, the cover glass was removed, and the reaction solution was aspirated from the surface of the slide. Three 400 μL DMSO washes removed any residual solution, with vacuum aspiration after each. The AAXL second reaction solution, 200 μL of a 300 μL propargylamine/700 μL DMSO stock, was then applied to the tissue surface and once more a coverslip was placed on top. This secondary reaction was placed into a sealed container and further incubated for 2 hr at 60°C. After the second incubation, the coverslip was removed and residual 2nd reaction solution was aspirated away. The amidated slides were washed in EtOH for 2 min twice, Carnoy's Solution (60% EtOH, 30% chloroform, 10% acetic acid) for 10 min twice, EtOH for 2 min twice, 0.1% TFA in EtOH for 30 sec and H$_2$O for 3 min twice. The amidated slides could then be immediately incorporated into a MALDI-IMS workflow or stored in a desiccator for future use. Similar to AAN$_3$ on the model compounds, AAN$_3$ on FFPE tissues shares its first step with AAXL but substitutes an equivalent volume of azido-PEG$_3$-amine (NH$_2$-PEG$_3$-N$_3$) for propargylamine in the second step. The sole remaining difference between AAXL and AAN$_3$ for FFPE tissue preparation is the washing steps following the second amidation reaction,

where a 10 min DMSO wash is included in between the two 10 min washes in Carnoy's solution. This extra wash step is necessary to remove any residual azido-PEG$_3$-amine. A previously reported sialic acid amidation strategy upon which ours were adapted, termed AA, was also performed for comparison[204]. This reaction, like AAN$_3$, differed from AAXL only in its second reaction solution, which utilized an equivalent volume of 28-30% ammonia in H$_2$O instead of propargylamine.

4.4.3 Tissue Preparation for MALDI-IMS

A standardized tissue preparation workflow was followed, which has been previously published[314]. Briefly, derivatized tissue slides underwent heat-induced epitope retrieval (HIER) in citraconic anhydride buffer, pH 3 for 30 min in a decloaking chamber at 95°C. After buffer exchanging away the citraconic anhydride and subsequent drying in a desiccator, 15 passes of PNGaseF PRIME enzyme at 0.1 µg/µL in HPLC H$_2$O was applied to the tissue slides at a rate 25 µL/min with a velocity of 1200 mm/min and a 3 mm offset at 10 psi and 45°C using an M5 Sprayer (HTX Technologies, Chapel Hill, NC). Enzyme-sprayed slides were then incubated in prewarmed humidity chambers for 2 hr at 37°C for deglycosylation. After incubation, 7 mg/mL CHCA matrix in 50% ACN/0.1% TFA was applied to the deglycosylated slides at a rate of 100 µL/min with a velocity of 1300 mm/min and a 2.5 mm offset at 10 psi and 79°C using the sprayer. After matrix application slides were desiccated until analysis.

4.4.4 MALDI-QTOF IMS of Derivatized N-glycans

A timsTOF fleX trapped ion mobility separated QTOF mass spectrometer

(Bruker Daltonics, Bremen, Germany) equipped with a 10 kHz SmartBeam 3D laser operating in positive mode with a spot size of 20 µm was used to detect derivatized, released N-glycans at a high resolution (20 to 40 µm raster). 300 laser shots per pixel over a mass range of 500 to 4000 *m/z* were collected for analysis, with an ion transfer time of 125 µs, a prepulse storage time of 25 µs, a collision frequency of 4000 Vpp, a multipole frequency of 500 Vpp and a collision cell energy of 15 eV. For MS/MS analysis by CID, a 10 Da window was used for precursor isolation and precursors were fragmented with individually optimized collision energies ranging from 80 to 140 eV.

4.4.5 MS Data Processing and Analysis

Post-acquisition, spectra were imported to SCiLS Lab 2022b Pro (Bruker Daltonics, Bremen, Germany) for processing mass spectrometry imaging experiments. The generated N-glycan spectra were then normalized to the total ion count. Spectra were annotated by matching peaks against an in-house N-glycan database generated using GlycoMod and GlycoWorkbench, which was modified to include AAXL, AA and AAN_3-induced mass shifts in sialic acid isomers[360,361]. Structures annotated in this research article are compositionally accurate as determined by accurate mass. Structural assignments were based off of CID analyses and prior characterizations by reversed-phase liquid chromatography-coupled tandem mass spectrometry, MALDI-TOF-MS/MS and alternate enzymatic release experiments[215,315]. A list of the most abundantly detected sialylated N-glycans reported in this analysis, along with calculated mass errors, can be found in Table 11.

Table 11. Composition and Mass Accuracy of Sialylated N-glycans in this Chapter.

Composition	Theoretical	Observed	Error ppm	Composition	Theoretical	Observed	Error ppm
Hex4HexNAc3	1298.4492	1298.4476	1.2322	Hex6HexNAc5(α2,6)NeuAc2	2664.9990	2664.9964	0.9756
Hex4dHex1HexNAc3	1444.5071	1444.5089	1.2461	Hex5dHex1HexNAc5(α2,3)NeuAc2	2668.9727	2668.9747	0.7494
Hex4HexNAc3NeuAc1	1589.5446	1589.5528	5.1587	Hex6HexNAc5(α2,6)NeuAc1(α2,3)NeuAc1	2674.9833	2674.9866	1.2337
Hex4HexNAc3(α2,6)NeuAc1	1616.5919	1616.5907	0.7423	Hex7HexNAc6NeuAc1	2684.9412	2684.9472	2.2347
Hex4HexNAc3(α2,3)NeuAc1	1626.5762	1626.5769	0.4304	Hex6HexNAc5(α2,3)NeuAc2	2684.9676	2684.9695	0.7076
Hex5HexNAc4	1663.5814	1663.5759	3.3061	Hex7HexNAc6(α2,6)NeuAc1	2711.9885	2711.9765	4.4248
Hex4dHex1HexNAc3NeuAc1	1735.6025	1735.5996	1.6536	Hex7HexNAc6(α2,3)NeuAc1	2721.9728	2721.9841	4.1514
Hex4dHex1HexNAc3(α2,6)NeuAc1	1762.6498	1762.6519	1.1914	Hex6dHex1HexNAc5(α2,6)NeuAc2	2811.0569	2811.0583	0.4980
Hex4dHex1HexNAc3(α2,3)NeuAc1	1772.6341	1772.6390	2.7642	Hex6dHex1HexNAc5(α2,6)NeuAc1(α2,3)NeuAc1	2821.0412	2821.0318	3.3321
Hex5dHex1HexNAc4	1809.6393	1809.6397	0.2210	Hex7dHex1HexNAc6NeuAc1	2830.9991	2831.0171	6.3582
Hex5HexNAc5	1866.6608	1866.6610	0.1071	Hex6dHex1HexNAc5(α2,3)NeuAc2	2831.0255	2831.0171	2.9671
Hex5HexNAc4NeuAc1	1954.6768	1954.6824	2.8649	Hex7dHex1HexNAc6(α2,6)NeuAc1	2858.0464	2858.0399	2.2743
Hex5HexNAc4(α2,6)NeuAc1	1981.7241	1981.7284	2.1698	Hex7dHex1HexNAc6(α2,3)NeuAc1	2868.0307	2868.0367	2.0920
Hex5HexNAc4(α2,3)NeuAc1	1991.7084	1991.7117	1.6569	Hex6HexNAc5NeuAc3	2901.9998	2901.9832	5.7202
Hex5dHex1HexNAc5	2012.7187	2012.7180	0.3478	Hex6HexNAc5(α2,6)NeuAc3	2983.1417	2983.1438	0.7040
Hex6HexNAc5	2028.7136	2028.7153	0.8380	Hex6HexNAc5(α2,6)NeuAc2(α2,3)NeuAc1	2993.1260	2993.1291	1.0357
Hex5dHex1HexNAc4NeuAc1	2100.7347	2100.7324	1.0949	Hex6HexNAc5(α2,6)NeuAc1(α2,3)NeuAc2	3003.1103	3003.0979	4.1291
Hex5dHex1HexNAc4(α2,6)NeuAc1	2127.7820	2127.7769	2.3969	Hex6HexNAc5(α2,3)NeuAc3	3013.0946	3013.0747	6.6045
Hex5dHex1HexNAc4(α2,3)NeuAc1	2137.7663	2137.7654	0.4210	Hex7HexNAc6(α2,6)NeuAc2	3030.1312	3030.1215	3.2012
Hex5HexNAc5NeuAc1	2157.7562	2157.7573	0.5098	Hex7HexNAc6(α2,6)NeuAc1(α2,3)NeuAc1	3040.1155	3040.1121	1.1184
Hex6dHex1HexNAc5	2174.7715	2174.7719	0.1839	Hex7HexNAc6(α2,3)NeuAc2	3050.0998	3050.0848	4.9179
Hex5HexNAc5(α2,6)NeuAc1	2184.8035	2184.8157	5.5840	Hex6dHex1HexNAc5(α2,6)NeuAc3	3129.1996	3129.2010	0.4474
Hex5HexNAc5(α2,3)NeuAc1	2194.7878	2194.7710	7.6545	Hex6dHex1HexNAc5(α2,6)NeuAc2(α2,3)NeuAc1	3139.1839	3139.1782	1.8158
Hex5HexNAc4(α2,6)NeuAc2	2299.8668	2299.8703	1.5218	Hex6dHex1HexNAc5(α2,6)NeuAc1(α2,3)NeuAc2	3149.1682	3149.1609	2.3181
Hex5dHex1HexNAc5NeuAc1	2303.8141	2303.8026	4.9917	Hex6dHex1HexNAc5(α2,3)NeuAc3	3159.1525	3159.1491	1.0762
Hex5HexNAc4(α2,6)NeuAc1(α2,3)NeuAc1	2309.8511	2309.8388	5.3250	Hex7dHex1HexNAc6(α2,6)NeuAc2	3176.1891	3176.1752	4.3763
Hex6HexNAc5NeuAc1	2319.8090	2319.8118	1.2070	Hex7dHex1HexNAc6(α2,6)NeuAc1(α2,3)NeuAc1	3186.1734	3186.1694	1.2554
Hex5HexNAc4(α2,3)NeuAc2	2319.8354	2319.8311	1.8536	Hex7dHex1HexNAc6(α2,3)NeuAc2	3196.1577	3196.1417	5.0060
Hex5dHex1HexNAc5(α2,6)NeuAc1	2330.8614	2330.8571	1.8448	Hex7HexNAc6(α2,6)NeuAc3	3348.2739	3348.1882	25.5953
Hex5dHex1HexNAc5(α2,3)NeuAc1	2340.8457	2340.8429	1.1961	Hex7HexNAc6(α2,6)NeuAc2(α2,3)NeuAc1	3358.2582	3358.2479	3.0671
Hex6HexNAc5(α2,6)NeuAc1	2346.8563	2346.8587	1.0226	Hex7HexNAc6(α2,6)NeuAc1(α2,3)NeuAc2	3368.2425	3368.2255	5.0471
Hex6HexNAc5(α2,3)NeuAc1	2356.8406	2356.8345	2.5882	Hex7HexNAc6(α2,3)NeuAc3	3378.2268	3378.2327	1.7465
Hex7HexNAc6	2393.8458	2393.8495	1.5456	Hex7dHex1HexNAc6(α2,6)NeuAc3	3494.3318	3494.3108	6.0097
Hex5dHex1HexNAc4(α2,6)NeuAc2	2445.9247	2445.9153	3.8431	Hex7dHex1HexNAc6(α2,6)NeuAc2(α2,3)NeuAc1	3504.3161	3504.3126	0.9988
Hex5dHex1HexNAc4(α2,6)NeuAc1(α2,3)NeuAc1	2455.9090	2455.9027	2.5652	Hex7dHex1HexNAc6(α2,6)NeuAc1(α2,3)NeuAc2	3514.3004	3514.2848	4.4390
Hex6dHex1HexNAc5NeuAc1	2465.8668	2465.8693	0.9733	Hex7dHex1HexNAc6(α2,3)NeuAc3	3524.2847	3524.2854	0.1986
Hex5dHex1HexNAc4(α2,3)NeuAc2	2465.8933	2465.8898	1.4194	Hex7HexNAc6(α2,6)NeuAc4	3666.4166	3666.4334	4.5821
Hex6dHex1HexNAc5(α2,6)NeuAc1	2492.9142	2492.9150	0.3209	Hex7HexNAc6(α2,6)NeuAc3(α2,3)NeuAc1	3676.4009	3676.3462	14.8787
Hex6dHex1HexNAc5(α2,3)NeuAc1	2502.8985	2502.9067	3.2762	Hex7HexNAc6(α2,6)NeuAc2(α2,3)NeuAc2	3686.3852	3686.3779	1.9803
Hex5HexNAc5(α2,6)NeuAc2	2502.9462	2502.9692	9.1892	Hex7HexNAc6(α2,6)NeuAc1(α2,3)NeuAc3	3696.3695	3696.3753	1.5691
Hex5HexNAc5(α2,6)NeuAc1(α2,3)NeuAc1	2512.9305	2512.9593	11.4607	Hex7HexNAc6(α2,3)NeuAc4	3706.3538	3706.3381	4.2360
Hex5HexNAc5(α2,3)NeuAc2	2522.9148	2522.8841	12.1685	Hex7dHex1HexNAc6(α2,6)NeuAc4	3812.4745	3812.5034	7.5804
Hex7dHex1HexNAc6	2539.9037	2539.9076	1.5355	Hex7dHex1HexNAc6(α2,6)NeuAc3(α2,3)NeuAc1	3822.4588	3822.4288	7.8484
Hex6HexNAc5NeuAc2	2610.9044	2610.9202	6.0515	Hex7dHex1HexNAc6(α2,6)NeuAc2(α2,3)NeuAc2	3832.4431	3832.4439	0.2087
Hex5dHex1HexNAc5(α2,6)NeuAc2	2649.0041	2648.9881	6.0400	Hex7dHex1HexNAc6(α2,6)NeuAc1(α2,3)NeuAc3	3842.4274	3842.4212	1.6136
Hex5dHex1HexNAc5(α2,6)NeuAc1(α2,3)NeuAc1	2658.9884	2658.9626	9.7029	Hex7dHex1HexNAc6(α2,3)NeuAc4	3852.4117	3852.3924	5.0098

4.4.6 Biofluid N-glycan Profiling

Serum samples were processed as described previously[445]. Briefly, samples were diluted 2:1 in 100mM sodium bicarbonate then 1 μL diluted serum was spotted onto an amine-reactive slide. After immobilizing for 1 hr in a humidity chamber at RT, the samples were dried in a desiccator, washed with Carnoy's solution (60% EtOH, 30% chloroform, 10% acetic acid) for 3 min 3X and rinsed in HPLC H_2O. Slides were desiccated for 30 min until dry, then derivatized by AAXL using the same protocol as described for FFPE tissues. AAXL-labeled serum slides were then incorporated into the aforementioned N-glycan IMS workflow at the point of deglycosylation.

4.4.7 N-glycan IMS of Cultured Cells

N-glycan imaging mass spectrometry experiments on PANC1, ASPC1, HPAC and PL45 pancreatic cancer cell lines were performed according to a previously published protocol[203]. Briefly, 10,000 cells per well were plated into six of eight wells in an eight-chamber array (with 2 wells reserved for media blanks) on glass microscope slides and cultured in RPMI 1640 (5% FBS, 1% P/S, +L-glutamine) media under normal conditions. After overnight adherence the media was removed from the array, the cells were washed in cold PBS and then fixed in 10% neutral-buffered formalin (NBF) for 30 min at RT. After fixation, the arrays were removed from the slides, cells were briefly washed in PBS then derivatized by AAXL as described for FFPE tissues. Derivatized, fixed cell slides were then prepared for N-glycan IMS by the aforementioned protocol. An additional spraying step incorporated after matrix deposition applied 2 passes of 5 mM ammonium

phosphate monobasic at 70 μL/min with a velocity of 1300 mm/s at an offset of 3 mm at 10 psi and 60°C to reduce signal-suppressing matrix cluster formation. After MS data acquisition, media blanks were subtracted as background for each detected N-glycan analyte. Significant differences in the expression of sialylated glycans between the cell lines were assessed by one-way ANOVA using multiple comparisons in GraphPad Prism 9.3.1 (San Diego, CA). Principal component analyses (PCA) were performed in SCiLS Lab utilizing six components scaled by unit variance.

4.4.8 IDAWG Labeling for Cell Turnover

For IDAWG labeling experiments[446], all four pancreatic cancer cell lines were cultured in chambered arrays as previously described. After the cells had adhered to the slide, RPMI 1640 media containing L-glutamine was replaced with an L-glutamine-free RPMI 1640 media into which amide-^{15}N L-glutamine was spiked to a concentration of 2 mM. At the same time, four different chemotherapeutic agents (4.15 μM 5-fluorouracil, 1.08 μM Gemcitabine, 0.91 μM Irinotecan, 7.44 μM Oxaliplatin) were individually administered to separate chambered arrays for each of the four cell lines. The appropriate concentrations for each drug were assessed prior to the experiment by IC$_{50}$ measurements based on a trypan blue exclusion assay for cell viability. At 24-, 48- and 72-hour time points slides for each of the four cell lines were fixed, derivatized by AAXL, and prepared for N-glycan MALDI IMS as described above. Spectra were acquired by MALDI-IMS similarly to that for FFPE tissues but at a raster of 150 μm for a more high-throughput measurement approach. Again, media blanks were subtracted

from the cell-containing wells during post-acquisition processing. Heavy-labeled glycans were annotated from our glycan database modified to include a +0.9937 Da mass shift for every N-acetylglucosamine, N-acetylgalactosamine or N-acetylneuraminic acid in the glycan structure. $\%^{15}N$ incorporation was determined by the percentage of the total light- and heavy-labeled peak intensities which corresponded to the heavy labeled peak, which was controlled for interference from the light-labeled isotope peaks with the mass-shifted ^{15}N-labeled peak.

4.4.9 CuAAC on AAXL and AAN$_3$ FFPE Tissue Slides

AAXL and AAN$_3$ labeled tissue slides were rehydrated with 200 µL H$_2$O applied directly to the tissue surface for 1 min, which was then discarded. The AAXL-CuAAC reaction mixture was prepared as previously described (Table 10). A humidity chamber was prepared with a 200 µL incubation chamber placed well-side up. The incubation well was then filled with 200 µL click reaction mixture for AAXL and the rehydrated tissue slide was pressed tissue-side down onto the incubation well, sealing the silicone gasket of the incubation well around the tissue. The humidity chamber was then filled with nitrogen gas, sealed and incubated at RT overnight in the dark. After incubation, the slides were washed by gentle shaking in H$_2$O for 3 min 3 times, EtOH for 2 min, Carnoy's Solution for 10 min twice, EtOH for 2 min and H$_2$O for 3 min 3 times. The biotinylated slides could then be immediately stained by histochemistry or stored in a desiccator for future use. The CuAAC workflow for AAN$_3$ labeled tissue slides proceeded similarly but utilized 1.0mM biotin-alkyne prepared in DMSO/H$_2$O v/v 1:1 in place of biotin-PEG$_3$-azide.

4.4.10 Sialidase Treatment of FFPE Tissues

FFPE tissue slides were dewaxed, rehydrated and subjected to HIER as described above. A humidity chamber was prepared as mentioned for CuAAC. The incubation well was then filled with 200 µL of 1U/µL sialidase in 20 mM TRIS (pH 6.8) and the antigen retrieved tissue slide was placed on top. The humidity chambers were then sealed and incubated at 37°C overnight. Following incubation, residual sialidase solution was discarded and the slides were washed with H2O for 3 min 3 times. In an attempt to remove any residual sialic acid residues, the tissues were then subjected to two more rounds of sialidase incubation as described above in 0.5U/µL sialidase for 8 hr at 37°C each time. Following the final incubation, tissue slides were washed with H_2O for 3 min 3 times and then stored in a desiccator until labeling.

4.4.11 Histochemical Staining

Histochemical staining was performed with HRP-DAB Kit (R&D Systems, Minneapolis, MN). After the click reaction, HIER was performed with a decloaker at 95°C for 15 min in 10 mM sodium citrate (pH 6.0). Tissue slides were then placed face up in humidity chambers as described above. Samples were incubated at RT with 200 µL peroxidase blocking solution (spread across the tissue surface using a glass coverslip) for 30 min then washed with PBS for 5 min 3X. Slides were then incubated with 200 µL Odyssey PBS Blocking buffer for 30 min which was then aspirated away. Blocked slides were incubated with 200 µL HSS-conjugated HRP for 30 min, then washed thoroughly with PBS for 5 min 4X. For detection, slides were then incubated in DAB chromogen solution for 15 min followed by two 5 min

164

H2O washes. A nuclear counterstain was applied using Mayer's hematoxylin and then the slides were washed sequentially with H_2O for 3 min, 70% EtOH for 1 min, EtOH for 15 s, 2% ammonia in water (for bluing) for 10 s, 70% EtOH for 1 min, 95% EtOH for 1 min, EtOH for 1 min 2X and xylenes for 3 min 2X. DAB-labeled slides were air-dried for 10 min then sealed and permanently mounted. After overnight drying slides were imaged on a NanoZoomer 2.0-RS high-resolution slide scanner (Hamamatsu, Hamamatsu-city, Japan) at 40X magnification across the whole tissue.

4.5 Results

4.5.1 Comparison of AA, AAXL and AAN_3 for Tissue N-glycan IMS
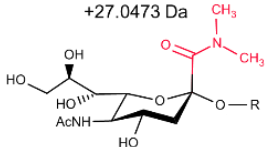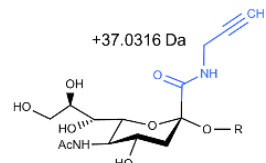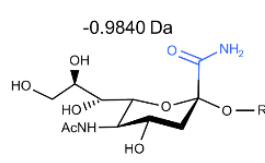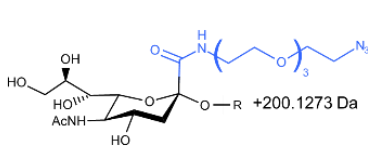
After the initial development of AAXL and AAN_3, we assessed the applicability of these syntheses to target sialic-acid containing N-glycans in tissues, as measured by N-glycan IMS in FFPE tissue sections[314]. A series of sequentially cut prostate cancer tissue slides were used for initial characterizations. For IMS, both the first and second reactions of AAXL and AAN_3 occur directly on the surface of the dewaxed and rehydrated FFPE tissue, where a glass cover slip placed on top is used to ensure sufficient contact of the derivatization reagents with the tissue. A standard antigen retrieval protocol was performed next, followed by spraying of peptide N-glycosidase F, digestion and CHCA matrix application as previously described[314]. For comparison, an adjacent slide treated with the original amidation-amidation (AA) derivatization strategy[204] and an underivatized tissue were similarly prepped for N-glycan IMS. The specific derivatization schemes and

reagents, as well as the resulting mass shifts for α2,3 and α2,6 sialic acid isomers, are shown in Table 12.

Initial comparisons for each condition focused on the detection and distribution of a singly sialylated, biantennary N-glycan (Hex5HexNAc4NeuAc1) that is abundant and easily detectable in prostate cancer tissues[447]. In the underivatized sample, the glycan appears at *m/z* 1954.6768 (1663.5814 Da for the Hex5HexNAc4 base + 291.0954 Da for the sialic acid residue) which represents the unresolved population both α2,3 and α2,6 isomers (Figure 32A). The tissue treated with the original AA reaction exhibits a peak at *m/z* 1953.6948 representing the amidated α2,3-linked isomer and expected -0.9840 Da mass shift, and a peak at *m/z* 1981.7241 corresponding to the dimethylamidated α2,6-linked species (Figure 32B). Unlike the underivatized, AAXL and AAN₃ spectra, the derivatized α2,3-sialylated peak exhibited what appears to be a non-standard isotopic distribution pattern, with increased signal at the +1 and +2 isotopes relative to the original mass. This is likely due to overlap between the derivatized isotopes, any residual underivatized peak at *m/z* 1954.6768 as well as the doubly fucosylated version of the base Hex5HexNAc4 glycan at *m/z* 1955.6972 (Hex5dHex2HexNAc4). The relative intensities of the underivatized and derivatized peaks for AA, AAXL and AAN₃ are shown in Figure 33.

In the AAXL-treated tissue, *m/z* 1991.7104 corresponds to the alkyne-amine α2,3 isomer while, *m/z* 1981.7241, like in AA, represents the dimethylamidated α2,6 isomer (Figure 32C). Use of AAXL avoids the isotopic

Table 12. Mass Shifts for AAXL, AA and AAN₃.

		AAXL	AA	AAN₃
Reaction Mixture	1st Step	← EDC, HOBt, dimethylamine/DMSO →		
	2nd Step	Propargylamine/DMSO (v/v 3:7)	Ammonia in H₂O (28%)/DMSO (v/v 3:7)	NH₂-PEG₃-N₃/DMSO (v/v 3:7)
Products	α2,6 sialic acid			
	α2,3 sialic acid			
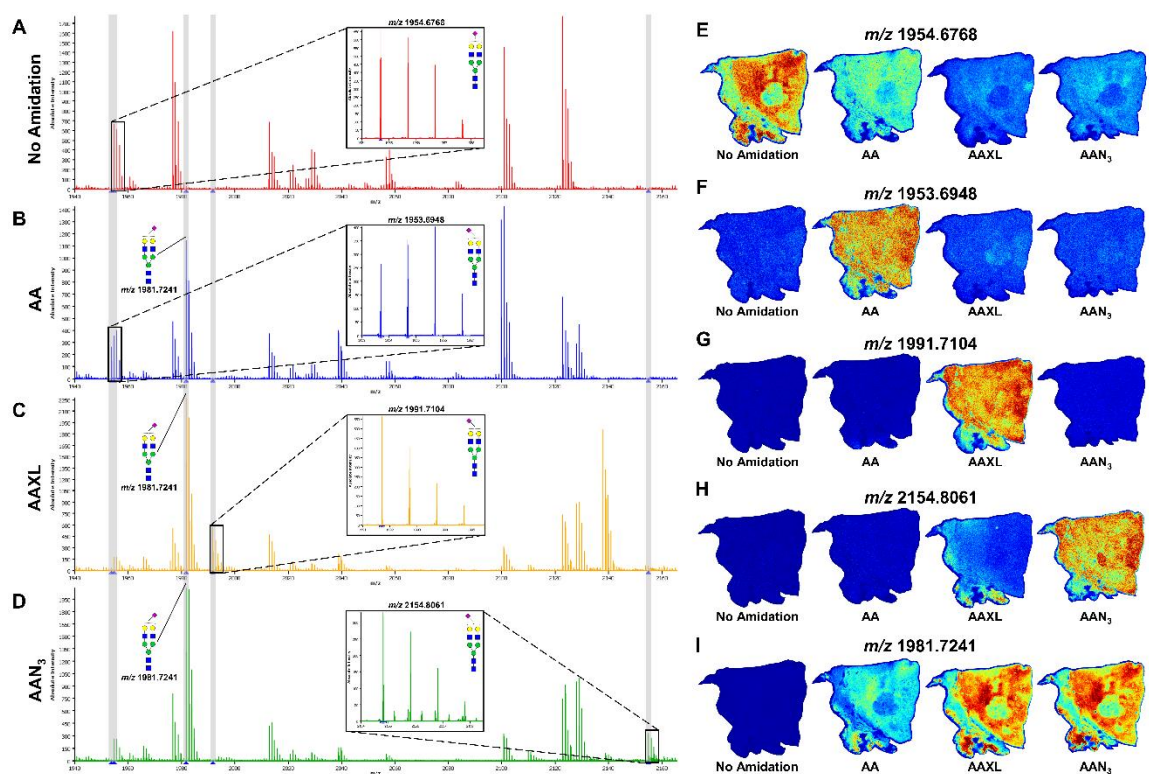
Figure 32. Determining the suitability of AAXL, AAN₃ and AA for N-glycan IMS applications. Three prostate cancer FFPE tissue serial sections were derivatized by AAXL, AAN3 and AA alongside a fourth unlabeled section. A) the undifferentiated Hex5HexNAc4NeuAc1 peak at *m/z* 1954.6768 (inset) in the non-derivatized tissue (red). B) Hex5HexNAc4(α2,3)NeuAc1 (*m/z* 1953.6948, inset) and Hex5HexNAc4(α2,6)NeuAc1 (*m/z* 1981.7241) in the AA-derivatized tissue (blue). C) Hex5HexNAc4(α2,3)NeuAc1 (*m/z* 1991.7104, inset) and Hex5HexNAc4(α2,6)NeuAc1 (*m/z* 1981.7241) in the AAXL-derivatized tissue (yellow). D) Hex5HexNAc4(α2,3)NeuAc1 (*m/z* 2154.8061, inset) and Hex5HexNAc4(α2,6)NeuAc1 (*m/z* 1981.7241) in the AAN₃-derivatized tissue (green). Mass spectrometry images of derivatized, sialylated N-glycans E), *m/z* 1954.6768; F) *m/z* 1953.6948; G) *m/z* 1991.7104; H) *m/z* 2154.8061; I) *m/z* 1981.7241 across the unlabeled, AA, AAXL and AAN₃ tissues.
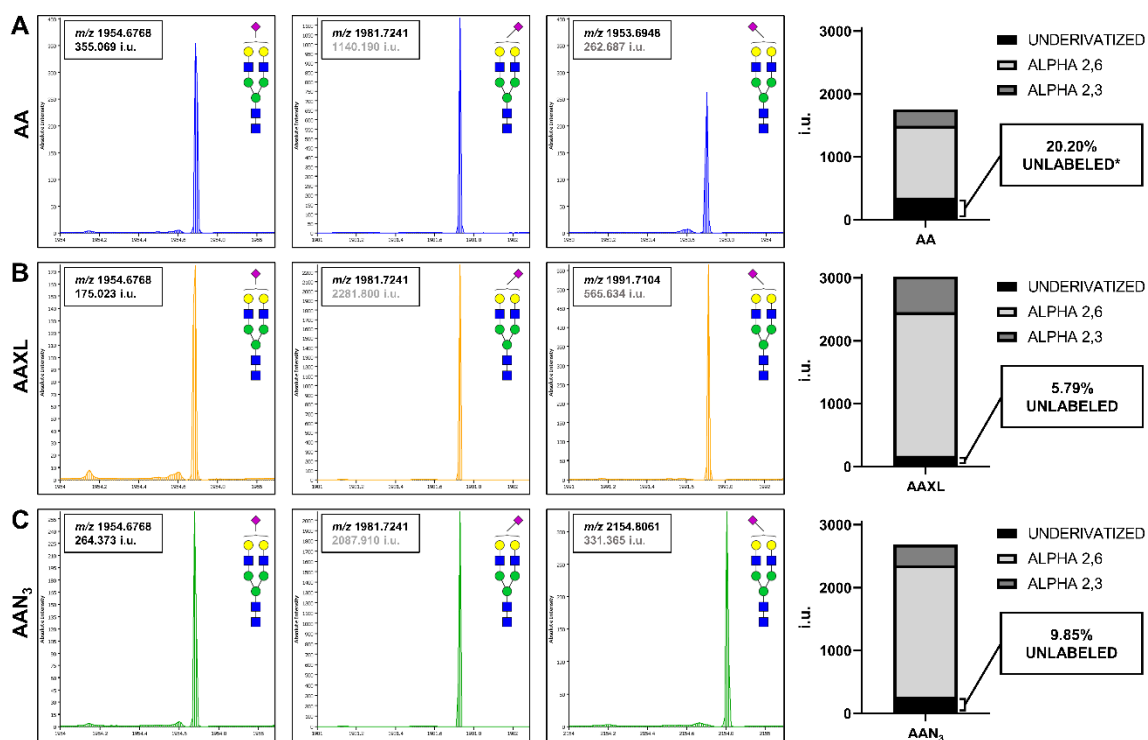
Figure 33. Derivatization Efficiency for AAXL, AA and AAN₃. Relative peak intensities were compared for the derivatized α2,3-sialylated, derivatized α2,6-sialylated and remaining underivatized Hex5HexNAc4NeuAc1 species in AA, AAXL and AAN₃. A) 20.20% of the total peak area for Hex5HexNAc4NeuAc1 represented the unlabeled peak at *m/z* 1954.6768 in the AA-treated sample. B) AAXL derivatized 94.21% of the Hex5HexNAc4NeuAc1 glycan while C) AAN₃ had a 90.15% efficiency.

overlap challenges described for AA, as no known glycan analytes appear within its isotopic distribution at that mass range. The AAN$_3$-derivatized sample also averts isotopic overlap, with the azide-labeled α2,3-linked species appearing at *m/z* 2154.8061 (+200.1273 Da mass shift) (Figure 32D). As in AA and AAXL, the dimethylamidated α2,6 isomer appears at *m/z* 1981.7241. Precise structural confirmations for these and other derivatized N-glycans were assessed by CID directly from the tissue slides (Figure 34). Relative to AAXL, the α2,3-derivatized isomer showed lower overall signal intensity in AAN$_3$. For imaging MS applications the +200.1273 Da mass shift associated with AAN$_3$ could limit detection of larger mass, multi-sialylated N-glycans[448]. Other applications of AAN$_3$ will be described, but for routine mass shifts in IMS applications, the +37.0316 Da AAXL derivatization is more effective.

Figure 32E-I shows the corresponding glycan intensity maps for the underivatized, AA, AAXL and AAN$_3$ sialylated isomers. The residual unlabeled peak at *m/z* 1954.6768 in the AA, AAXL and AAN$_3$ derivatization scheme is easily visualized (Figure 32E). Interestingly, although the dimethylamidated α2,6-linked isomer peak at *m/z* 1981.7241 appears in all three derivatized data sets, its expression is markedly lower in the AA-treated tissue when compared to either the AAXL or AAN$_3$-treated cases (Figure 32I). Ammonium hydroxide has been demonstrated to release N-linked glycans by β-elimination in previous studies[449]. We hypothesize that the use of ammonia hydroxide to decyclize the α2,3-lactone in AA eliminates a portion of the tissue's total N-glycans and thus suppresses overall signal when compared to AAXL and AAN$_3$. This assertion is bolstered by
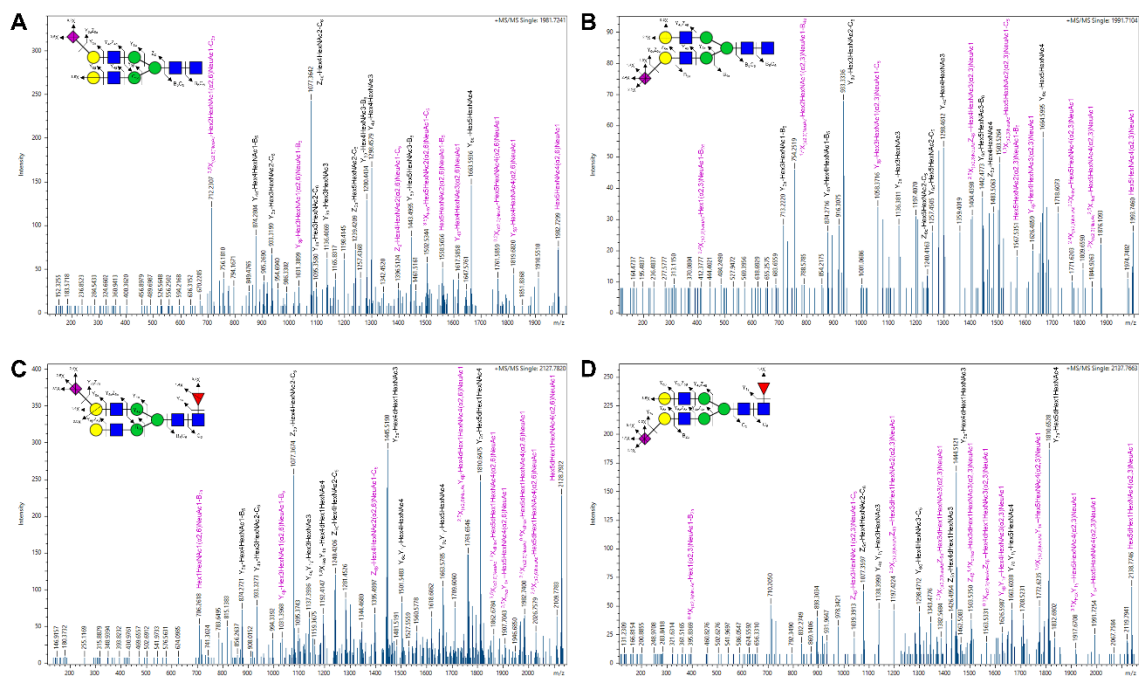
Figure 34. Structural Determinations and Labeling Confirmation by CID. Collision-induced dissociation MS/MS spectra for 4 representative N-glycans derivatized by AAXL. Glycan fragments containing a derivatized sialic acid are labeled in purple. A) Hex5HexNAc4(α2,6)NeuAc1, *m/z* 1981.7241. B) Hex5HexNAc4(α2,3)NeuAc1, *m/z* 1991.7104. C) Hex5dHex1HexNAc4(α2,6)NeuAc1, *m/z* 2127.7820. D) Hex5dHex1HexNAc4(α2,3)NeuAc1, *m/z* 2137.7663.

the suppression of non-sialylated glycan signals in the AA-treated tissue as well. Ultimately, the data suggests that AAXL presents an optimal derivatization strategy for resolving sialic acid isomers by IMS.

4.5.2 Detection of Multiply-Sialylated, High Mass N-glycans by AAXL

A prostate tumor tissue with larger mass multi-sialylated N-glycans localized to tumor regions was assessed for how effective AAXL modification was for stabilizing sialic acids (Figure 35). The tumor regions are highlighted in Figure 35A and 35B, and this tissue was derivatized with AAXL and prepared for N-glycan IMS. All isomeric combinations of the doubly sialylated, tri-antennary N-glycan Hex6dHex1HexNAc5NeuAc2 are shown in Figure 35C-E and are overlaid in Figure 35F. Figure 35G-K shows the triply-sialylated version of the same base glycan, with distinct detection of the full spectrum of sialylated isomers. Similar but non-overlapping distribution patterns for these glycans were observed, possibly indicating the compartmentalization of α2,3 and α2,6 sialyltransferases to different tissue regions. Taken together, these experiments demonstrate the potential of AAXL for the analysis of multiply-sialylated glycans which are normally difficult to detect and differentiate by traditional IMS approaches.

4.5.3 AAXL Derivatization of Serum Glycoproteins

A slide-based serum N-glycan analysis workflow was evaluated for AAXL derivatization of serum glycoproteins (Figure 36A)[445]. AAXL-labeled spotted serum slides were prepared as described in Materials and Methods and compared to non-derivatized controls and blank wells for background subtraction. Expected mass shifts of +27.0473 Da and +37.0316 Da for the α2,6- and α2,3 sialic acid isomers,
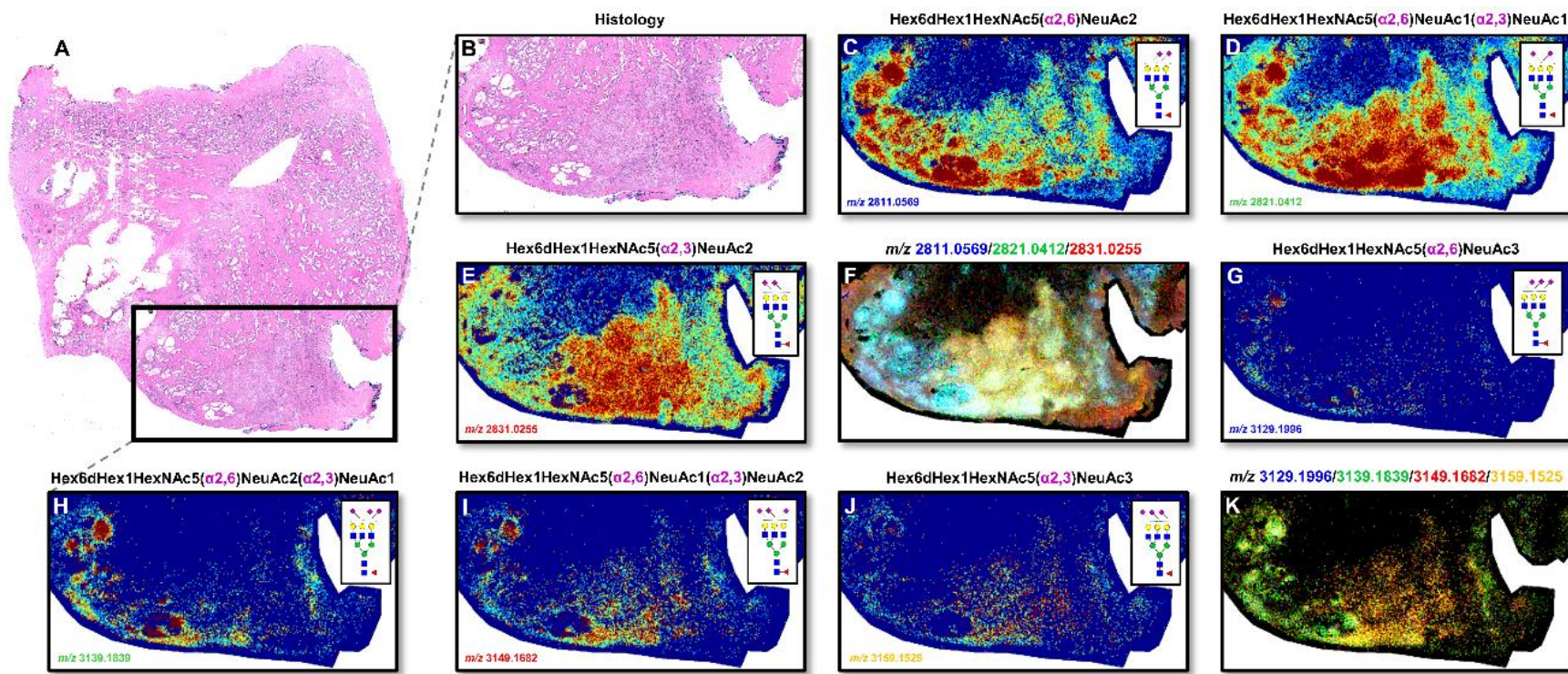
Figure 35. Detection of Multiply-Sialylated N-glycans After Derivatization by AAXL. A prostate cancer FFPE tissue section was labeled with AAXL then analyzed by N-glycan IMS. A) post-acquisition H&E staining image. B) enlarged region of mucinous tumor tissue. Intensity heatmaps for three di-sialylated isomers C) Hex6dHex1HexNAc5(α2,6)NeuAc2 (m/z 2811.0569), D) Hex6dHex1HexNAc5(α2,6)NeuAc1(α2,3)NeuAc1 (m/z 2821.0412) and E) Hex6dHex1HexNAc5(α2,3)NeuAc2 (m/z 2831.0255) overlaid in blue, green and red, respectively, in F). Intensity heatmaps for four tri-sialylated isomers G) Hex6dHex1HexNAc5(α2,6)NeuAc3 (m/z 3129.1996), H) Hex6dHex1HexNAc5(α2,6)NeuAc2(α2,3)NeuAc1 (m/z 3139.1839), I) Hex6dHex1HexNAc5(α2,6)NeuAc1(α2,3)NeuAc2 (m/z 3149.1682) and J) Hex6dHex1HexNAc5(α2,3)NeuAc3 (m/z 3159.1525) overlaid in blue, green, red and yellow, respectively, in K).

173
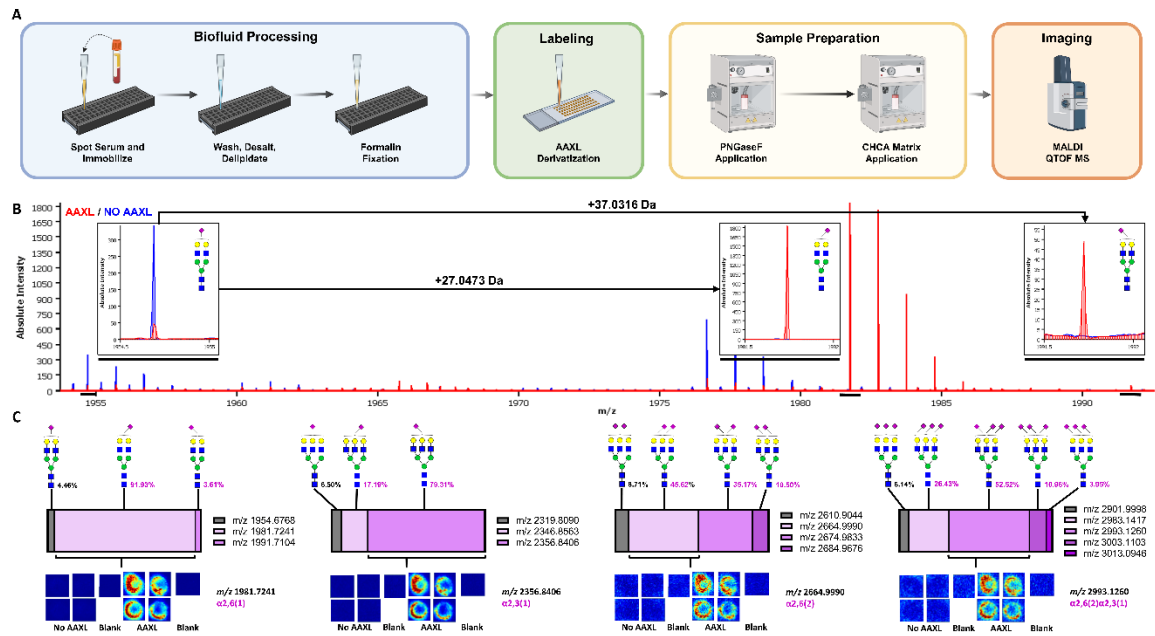
Figure 36. Analysis of Sialylation Patterns in Human Serum Enabled by AAXL. Human serum samples were analyzed by N-glycan IMS after derivatization by AAXL. A) incorporation of AAXL into a standard biofluid N-glycan analysis workflow between immobilization and deglycosylation. B) mass-shifted α2,6- (m/z 1981.7241) and α2,3- (m/z 1991.7104) sialylated isomers of Hex5HexNAc4NeuAc1 detected in AAXL-labeled serum samples. C) Relative intensities of the unlabeled (m/z 1954.6768, NeuAc1) and mono-sialylated (m/z 1981.7241, α2,6NeuAc1; m/z 1991.7104, α2,3NeuAc1) isomers of Hex5HexNAc4NeuAc1 as well as the unlabeled (m/z 2319.8090, NeuAc1; m/z 2610.9044, NeuAc2; m/z 2901.9998, NeuAc3) and mono- (m/z 2346.8563, α2,6NeuAc1; m/z 2356.8406, α2,3NeuAc1), di- (m/z 2664.9990, α2,6NeuAc2; m/z 2674.9833, α2,6NeuAc1α2,3NeuAc1; m/z 2684.9676, α2,3NeuAc2) and tri-sialylated (m/z 2983.1417, α2,6NeuAc3; m/z 2993.1260, α2,6NeuAc2α2,3NeuAc1; m/z 3003.1103, α2,6NeuAc1α2,3NeuAc2; m/z 3013.0946, α2,3NeuAc3) isomers of Hex6HexNAc5NeuAc1,2,3 with accompanying representative images of the most abundant sialylated isomer.

174

respectively, were observed in the AAXL-treated serum and absent from the unlabeled control serum (Figure 36B). Figure 36C shows the relative intensities of the derivatized and underivatized peaks for the mono-sialylated glycan Hex5HexNAc4NeuAc1 as well as the mono-, di- and tri-sialylated Hex6HexNAc5NeuAc1,2,3 with a representative image of the predominantly detected isomer for each set appended below. In serum, labeling efficiency remained comparable to that of FFPE tissues, ranging from 91 – 96%. A lack of signal in the unlabeled serum samples confirmed the specificity of the AAXL-shifted peaks to only the derivatized serum samples. These experiments establish the utility of AAXL for analyzing sialylation from serum and suggest expanded applicability of the approach to clinical biofluids.

4.5.4 Applications of AAXL for Studying Sialylation in Cultured Cells

A previously published workflow for N-glycan IMS of fixed cells on glass microscope slides was adapted for AAXL derivatization[203]. Briefly, four pancreatic cancer cell lines (PANC1, ASPC1, HPAC, PL45) were cultured under normal conditions in chambered array glass slides with MALDI source target frame compatible dimensions. Ten thousand cells per well were allowed to adhere overnight followed by fixation in neutral buffered formalin. Fixed cells were then briefly washed in PBS before undergoing derivatization by AAXL in a protocol identical to that for FFPE tissues. The overall workflow for culturing, fixing and derivatizing the cells is outlined in Figure 37A. Representative N-glycan IMS data of an α2,6- (*m/z* 2127.7820) and an α2,3- (*m/z* 2137.7663) sialylated glycan is shown in Figure 37B and 37C, respectively. AAXL demonstrated quantifiable
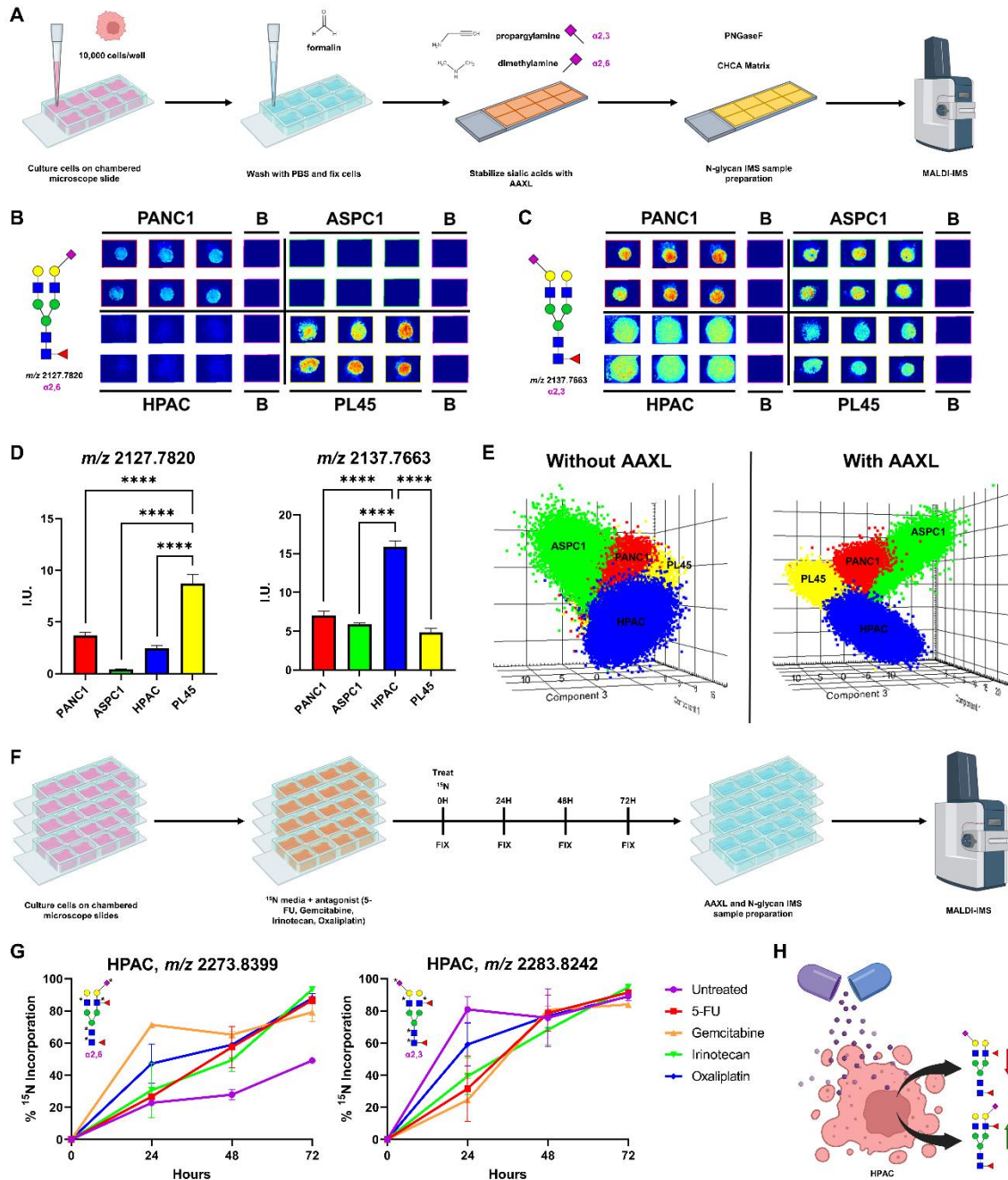
Figure 37. AAXL and IDAWG Analysis Reveals the Glycobiology of Cultured Cells. Applications of AAXL for studying sialylation in PANC1, ASPC1, HPAC and PL45 pancreatic cancer cell lines. A) incorporation of AAXL into a standard workflow for N-glycan IMS of cultured cells. B) a representative α2,6-sialylated N-glycan Hex5dHex1HexNac4(α2,6)NeuAc1 (*m/z* 2127.7820) with differential expression patterns between the four profiled cell lines. C) the α2,3-sialylated isomer Hex5dHex1HexNAc4(α2,3)NeuAc1 (*m/z* 2137.7663) exhibiting alternate patterns distinct from its α2,6-counterpart. D) relative quantification of the α2,6- (*m/z* 2127.7820) and α2,3- (*m/z* 2137.7663) isomers showing significant differences between the lines profiled. E) AAXL drives more distinct clustering of

the cell lines in PCA plots. F) isotopic detection of aminosugars with glutamine (IDAWG) approach followed by AAXL derivatization and N-glycan IMS. G) HPAC biosynthesis curves assessed by incorporation of 15N isotope into Hex5dHex2HexNAc4NeuAc1 α2,6- (*m/z* 2273.8399) and α2,3- (*m/z* 2283.8242) isomers. H) AAXL suggests alternative regulation of an isomer-separated N-glycan in HPAC cells treated with chemotherapeutics.

expression differences for these isomeric glycans between the cell lines profiled (Figure 37D). The differences and similarities between the N-glycomes of the four cell lines were assessed by principal component analysis (PCA) (Figure 37E), with and without AAXL derivatization. Inclusion of AAXL-derivatized N-glycans in the PCA result in discrete clusters specific to each cell line. For non-AAXL derivatized N-glycan PCA analysis, the cell lines aggregate into less-defined clusters with more overlap. Thus, the inclusion of specific sialic acid isomer linkages helps distinguish the cell line glycomes from each other in the PCA analysis.

Further, AAXL derivatization was combined with an established stable isotope labeling by amino acids in cell culture (SILAC)[450] using an isotopic detection of aminosugars with glutamine (IDAWG) labeling experiment[446]. As glutamine is a precursor nitrogen donor for the biosynthesis of N-acetylglucosamine, N-acetylgalactosamine and N-acetylneuraminic acid (sialic acid), a glycan metabolically synthesized in ^{15}N-glutamine media would gain a ~1 Da mass shift per incorporated aminosugar. As an example, synthesis of the common glycan Hex5dHex1HexNAc4 (*m/z* 1809.6393) in ^{15}N media would incorporate four heavy-labeled N-acetylglucosamine monomers that would shift its mass to 1813.6140 Da, which allows it to be discriminated from a nominal mass glycan synthesized prior to introduction of the labeled media. The overall experimental design is outlined in Figure 37F. Briefly, cells were again cultured in chambered slides with media containing ^{14}N glutamine and allowed to adhere overnight. At time zero (T0), the light-labeled media was substituted for media with heavy-labeled ^{15}N-glutamine and a previously determined amount of a common

pancreatic cancer chemotherapeutic agents (5-fluorouracil, Gemcitabine, Irinotecan or Oxaliplatin) were added (Figure 38). Cells were monitored over a three-day time period where slides were fixed at 24, 48 and 72 hours, derivatized with AAXL and then prepared for N-glycan IMS. Untreated replicates were prepared alongside the treated cells as a control for normal N-glycan metabolic turnover.

Figure 37G shows representative growth curves from the HPAC cell line for two sialylated N-glycans which differ only in which sialic acid isomer they contain. Here, %[15]N incorporation was measured by the intensity of the heavy labeled peak as a percentage of the total light-labeled and heavy-labeled peak intensities over time, which was controlled for overlap between the +5 isotope of the ^{14}N glycan and the +5 Da mass-shifted ^{15}N-labeled glycan. The α2,6-sialylated Hex5dHex2HexNAc4(α2,6)NeuAc1 ([14]N *m/z* 2273.8399, ^{15}N-labeled *m/z* 2278.8083) exhibited relatively linear biosynthesis in the untreated condition over the 72H period resulting in 49% labeled out of the total population at the end of the experimental duration. Treatment with the chemotherapeutics seemed to increase the relative production of this α2,6-sialylated glycan as compared to the control cells, where at 72H all treated conditions were between 79 – 93% labeled. The α2,3-linked Hex5dHex2HexNAc4(α2,3)NeuAc1 ([14]N *m/z* 2283.8242, ^{15}N-labeled *m/z* 2288.7926) exhibited an opposite effect, where treatment with any of the therapeutics decreased the initial synthesis rate as compared to the untreated control, yet both untreated and treated cells had synthesized similar amounts of the α2,3-sialylated isomer after 72H (84 – 95% incorporation). These data suggest
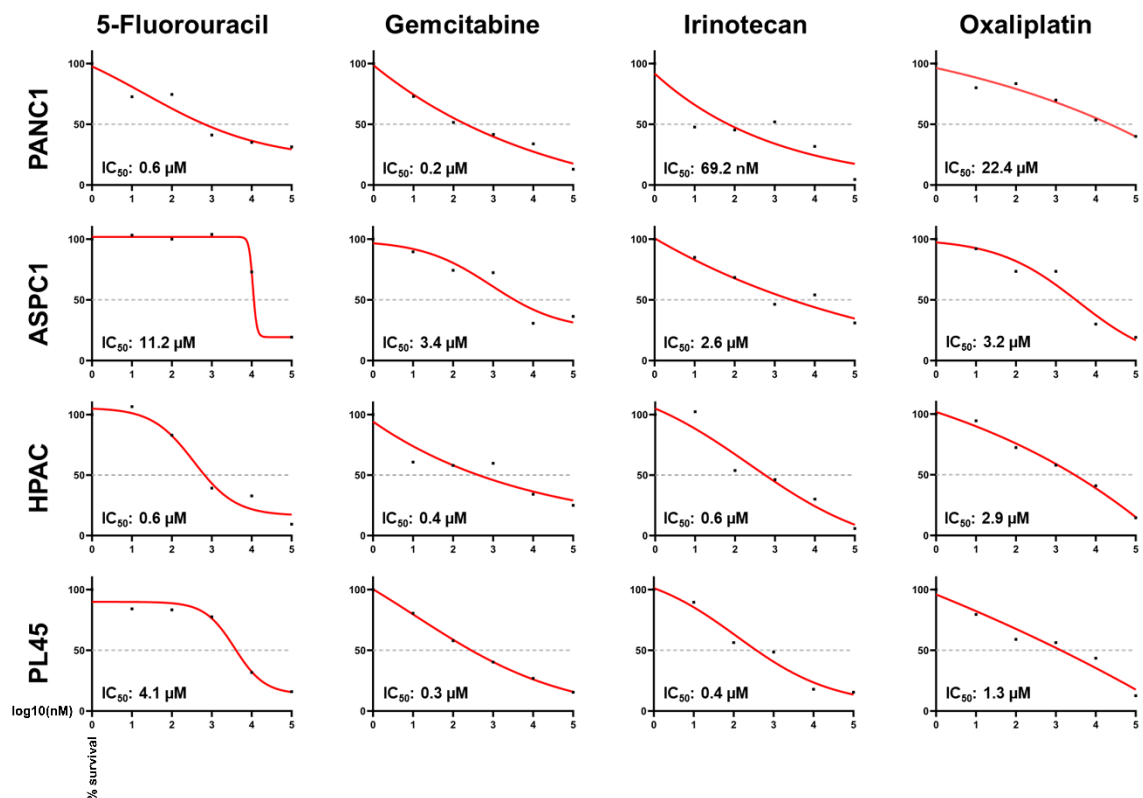
Figure 38. Dose Response Curves to Establish Chemotherapeutic IC$_{50}$. PANC1, ASPC1, HPAC and PL45 cell lines were treated with 1 nM, 10 nM, 100 nM, 1 µM, 10 µM and 100 µM 5-fluorouracil, Gemcitabine, Irinotecan or Oxaliplatin and cell viability was assessed at 72H by trypan blue exclusion assay. Curve fitting for IC$_{50}$ determination using 4-parameter variable slope non-linear regression analysis of log$_{10}$-transformed concentrations versus percent survival.

the specific, differential regulation of two N-glycans distinguished exclusively by their sialic acid isomers in response to chemotherapeutic antagonists (Figure 37H). Overall, we demonstrate the potential for AAXL to augment established cell culture experiments to provide mechanistic insights into the fundamental regulation of sialylation.

4.5.5. Comparison of AAXL and AAN$_3$ for Click-enabled IHC

As the AAXL and AAN$_3$ derivatizations are effective in FFPE tissues, the ability to biotinylate the derivatized α2,3-linked sialic acids was evaluated for use with established streptavidin-based staining methods[451]. In initial experiments, AAXL-treated FFPE pancreatic cancer tissue sections were further reacted with a biotin-azide conjugate in the presence of a CuSO$_4$ catalyst as described for the model sialylated compounds and proteins. Similarly, adjacent tissue slides were treated with AAN$_3$ and reacted with biotin-alkyne. The resulting biotinylated α2,3-linked sialic acids were then used to capture a streptavidin-fused HRP for staining with DAB chromogen (Figure 38). As shown in Figure 39A, the AAXL-biotinylated tissue had minimal DAB staining, while the AAN$_3$-biotinylated tissue had robust staining (Figure 39B). The reaction condition summary for AAN$_3$ and the biotin-alkyne conjugate are provided in Table 13. As a control, a serial tissue section was treated with both AAN$_3$ and the biotin-alkyne, omitting the copper catalyst (Figure 39C). Without CuSO$_4$ the azide-alkyne cycloaddition does not occur, and accordingly, no DAB staining was observed in this control tissue. An additional control was done on a different tissue section pre-treated with pan-sialidase to
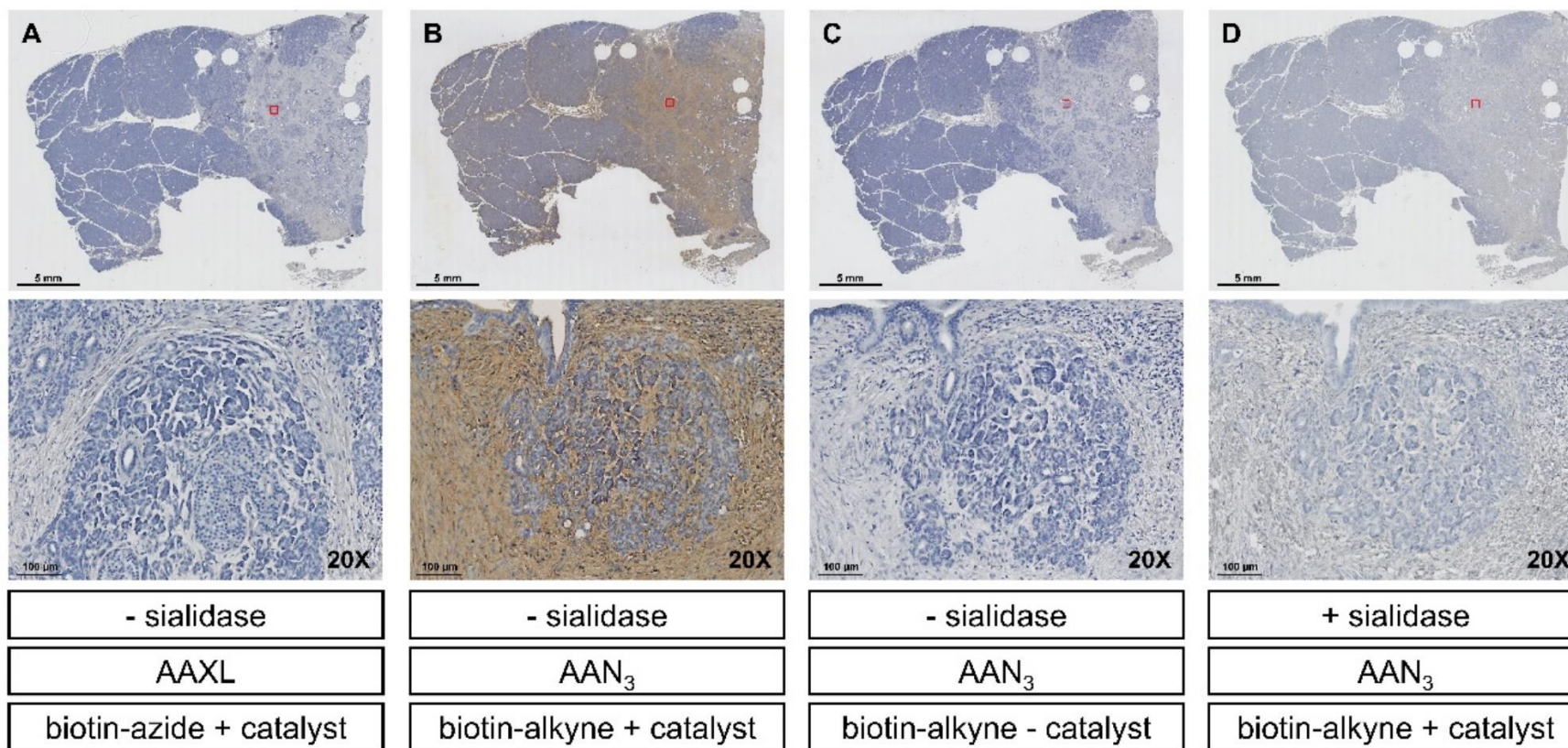
Figure 39. Comparing AAXL and AAN₃ for Histochemistry Applications. Pancreatic cancer FFPE tissue serial sections were derivatized by AAXL or AAN₃ then biotinylated by click chemistry for streptavidin-based histochemical staining alongside technical controls. A) the AAXL-treated tissue showed little to no DAB staining after click and probing with streptavidin-HRP. B) intense DAB chromogen staining after click-enabled HC in the AAN₃-derivatized tissue. C) omission of the CuSO₄ click-catalyst prevented biotinylation and subsequent DAB staining. D) exoglycosidase removal of sialic acids by neuraminidase attenuates AAN₃ staining.

Table 13. CuAAC Mixture for AAN$_3$.

		MW (g/mol)	Reagent Stock Prep (per 1 mL H$_2$O)	[Reagent Stock]	Volume Stock Solution	[Reag
A	Biotin-alkyne	281.12	7.0 mg†	25 mM	20.0 µL	1.0 m
B	CuSO$_4$	159.61	3.2 mg	20 mM	2.5 µL	0.1 m
C	Sodium ascorbate	198.11	20.0 mg	100 mM	25.0 µL	5.0 m
D	THPTA	434.50	21.7 mg	50 mM	5.0 µL	0.5 m
E	Aminoguanidine HCl	110.55	11.0 mg	100 mM	25.0 µL	5.0 m
F	10X PBS				422.5 µL	
	Overall Volume				500.0 µL	

† in DMSO/H$_2$O, v/v 1:1

Mix B and D and A and F in separate Eppendorf tubes. Sequentially add B&D mixture, E and C A&F mixture. Reagents A, B, D, E and F may be prepared ahead of time. 100 mM sodium ascorbate must be prepared day of.

remove sialic acids prior to AAN$_3$ derivatization and biotinylation. As shown in Figure 39D, the sialidase treated tissue showed minimal to no DAB staining after click-enabled histochemistry, Thus, the data suggests that AAN$_3$ and biotin alkyne treatments have little to no reactivity to non-sialylated targets.

4.6 Discussion

In the present study, we have developed a multi-functional isomer-targeted sialic acid derivatization strategy compatible with clinical tissues, biofluids and cultured cells. The AAXL and AAN$_3$ approach synergizes the established workflows for amidation of the lactone intermediate in α2,3-linked sialic acids[421,427], bioorthogonal sugar azides and alkynes[432], and N-glycan imaging mass spectrometry[204,206,441] resulting in new tools with unique features. First, it can be used to specifically introduce bioorthogonal groups into α2,3 and α2,8 sialic acids attached to proteins, and likely lipids, but not α2,6 sialic acids and other carboxylate containing moieties. Second, the AAXL and AAN$_3$ reactions will incorporate an alkyne or azide onto sialic acids without the need for a living system with active metabolic machinery or externally added glycosyltransferases and substrates. As demonstrated, the method can be applied to tissues preserved as formalin-fixed paraffin embedded blocks, the standard used worldwide for storing surgical specimens. Thus, there are potentially millions of clinical and experimental tissue samples available as targets for the approach. Fixed cells (Figure 37), biofluids (Figure 36) and tissues prepared by other methods than FFPE fixation are additional targets. Third, the reagents used for the direct AAXL and AAN$_3$ chemical reactions are affordable, readily available and components of established

184

chemical labeling workflows. Incorporation of AAXL/AAN$_3$ into a standard N-glycan IMS workflow adds only 4 hours of sample preparation with routine labeling efficiencies of 95% in clinical tissues and biofluids (Figure 33, Figure 36).

Currently, AAXL uses a propargylamine handle which is small and ionizes well, making it ideal for IMS applications (Figure 32). We anticipate that applications of AAXL to tissues and biofluids could lead to clinically useful tools to characterize sialylated cancer biomarkers more accurately by increasing the specificity with which isomeric configurations are detected, particularly in MALDI mass spectrometry-based assays. In solution, like that done for the standards and model glycoproteins, AAXL is very effective at introducing an alkyne for further reactions (Figure 29, Figure 31). For other applications that require click chemistry conjugation directly on the tissue slide, the short alkyne chemical handle installed by AAXL may not provide enough distance from the hydrophobic tissue surface to facilitate efficient reaction with the aqueous click chemistry reagents. Overall, DAB staining with AAXL on tissues has been variable and inconsistent (Figure 39A). In contrast for AAN$_3$, which contains a PEG linker extending the azide further away from the tissue, it may be more ideally suited for further click chemistry conjugation of imaging reporters. The AAN$_3$ treated pancreatic tissue showed intense DAB chromogen staining indicating a successful HRP capture and thus a highly effective biotinylation of α2,3-sialic acids (Figure 39B) with specificity (Figure 39C and 39D). Another possibility for these types of applications is use of amine-azides (or amine-alkynes) separated by a cleavable linker[452,453]. A theoretical system employing a cleavable label could allow for efficient biotinylation and subsequent

histochemical staining, then, once chemically or enzymatically cleaved, act as a small, IMS-compatible mass tag to generate multiplexed data from the same tissue section.

In summary, we have developed a novel set of sialic acid derivatization approaches which can be tuned for IMS or bioorthogonal click labeling applications depending on the secondary labeling agent used. AAXL is applicable to multiple sample types and has demonstrated utility in differentiating between sialic acid isomer in imaging mass spectrometry experiments. AAXL compliments biofluid N-glycan imaging workflows developed in our lab which are already being explored for their clinical utility. We envision a role for AAXL in detecting sialylated disease biomarkers as part of a clinical diagnostic evaluation of plasma or serum N-glycosylation. AAN_3 enables the visualization of α2,3-and α2,8-sialylated glycans by histochemical staining and is better suited for on- tissue click chemistry reactions than is AAXL. Currently, distinguishing whether an AAXL or AAN_3-labeled sialic acid observed by IMS or histochemistry is in the α2,3 or α2,8 configuration is a work in progress. Differential treatment with isomer-specific sialidases to clear the tissue of one or more isomeric linkage prior to labeling and staining is being evaluated. Introduction of the bioorthogonal click chemistry reagents by AAXL and AAN_3 affords many new research strategies for sialic acid isomer targeted visualization and glycoproteomic workflows, discussed further in Chapter 5.

Chapter 5: Advanced Bioorthogonal Applications of

Azide Amidation

5.1 Introduction

The development of a click chemistry amenable azide amidation protocol (AAN$_3$) in Chapter 4 and its successful implementation in a biotin-avidin-based histochemical staining approach led us to further speculate on more advanced click chemistry applications. The simplicity of click chemistry is key to its widespread applicability: an alkyne-cargo links to a biomolecule-azide (or an azide-cargo with biomolecule-alkyne in the reversed sense) in a selective reaction which is generally indifferent to the conjugates. Thus, the introduction of bioorthogonal azide or alkyne handles into living systems serves as a starting point for further modifications with various labeling agents, probes and reporters. This also allows for specific conjugation of tagged molecules on beads, chromatography columns or surfaces, all facilitated by copper- or otherwise-catalyzed azide alkyne cycloaddition reactions (CuAAC)[429,431,432,443,454]. Many sialic acid-targeted bioorthogonal applications have been developed, some of which use azido sugar analogues like azidoacetylmannosamine (Ac$_4$ManNAz)[436,437,455]. Glycoengineered cell libraries with 60+ click-modified Ac$_4$ManNAz sialic acid variants dramatically increased epitope affinity in siglec binding screens[456]. Modification of sialic acids with azido-sugars introduces a searchable mass tag onto sialylated peptides and may serve as the attachment point for further derivatization agents to boost ionization efficiency in glycoproteomic experiments[457]. Novel drug delivery approaches have also capitalized on this technology, where azido-sugar glycoengineered viral envelopes are modified with cancer-targeting motifs to home oncolytic viral vectors to the tumor[458,459]. A limitation inherent to all of these

techniques, however, is that they require living systems to provide metabolic machinery to uptake and metabolize the derivatives for incorporation into cellular glycoconjugates. As demonstrated in Chapter 4, our derivatization scheme does not require such biological machinery and thus is applicable to clinical tissue and biofluid samples which are typically not targeted by bioorthogonal sugar analog approaches.

Direct detection of sialic acids by fluorescence imaging is historically challenging. The ability of individual sialic acid sugar monomers to rotate around the axes of their bonds as part of a larger structure, combined with the complexity of multiply branched linkages in N-glycans, results in an epitope topology that is constantly in flux. Accordingly, carbohydrate-binding fluorescent probes designed to target sialic acids often lack the specificity or affinity conferred by antibodies in immunofluorescence experiments. These shortcomings notwithstanding, lectin, antibody and recombinant protein bioaffinity probes are frequently used to profile sialylation in cells and tissues or are fluorescent tags for flow cytometry and other separation techniques[460]. Recombinant sialyltransferases offer an alternate labeling approach for imaging through the direct attachment fluorophore-conjugated sialic acid analogues to N- and O-linked glycans[461]. Whether or not these recombinant enzymes and their xenobiotic substrates have an impact on the natural glycobiological functions of the cell, however, is an open question. An obvious application of azido-sugar-based bioorthogonal strategies is labeling sialic acids with click chemistry fluorescent probes, which has been successfully demonstrated by multiple groups[462–465]. Common to all of these approaches is the

189

loss of sialic acid linkage information and subsequently insights into isomer-specific biological functions.

Enrichment of sialylated glycoproteins has been traditionally done using affinity chromatography techniques coupled to LC-MS/MS. Titanium dioxide, hydrazine chemistry, strong cation exchange, silica dioxide and other liquid chromatography (LC) column formats take advantage of the charged sialic acid carboxylate group to retain sialylated glycoconjugates, however any sufficiently charged molecule will co-elute with analytes of interest, complicating downstream analysis[466,467]. Lectin affinity chromatography using a wheat germ agglutinin-conjugated (WGA) stationary phase often can enrich sialylated species from a general matrix of released glycans, although the affinity of WGA for GlcNAc-containing carbohydrates precludes specific capture[468]. Bead formats offer an alternate to chromatography for solid phase enrichment and allow for expanded purification, desalting or derivatization treatments prior to mass spectrometry analysis. Early enrichment approaches with hydrazide beads used harsh reaction conditions which limited the number of identifiable glycans and glycopeptides[469]. More recently, Lingjun Li and colleagues demonstrated the use of azide-beads to oxidize, alkylate and covalently enrich sialylated glycopeptides through click chemistry for analysis by LC-MS/MS[439]. Regrettably, the aforementioned approaches forgo the ability to be isomer selective in favor of bulk capture of sialylated glycoconjugates.

Chapter 5 details the development of two new protocols, one for fluorescent labeling of sialic acid-containing molecules and the other for selective enrichment

and proteomic analysis of sialylated glycoproteins, both of which are further click chemistry applications of the azide amidation (AAN$_3$) derivatization strategy presented in Chapter 4. Accordingly, both strategies are isomer specific to α2,3 and α2,8 sialic acid linkages. The first approach, Sialic Acid Fluorescent Enhancement Reaction (SAFER), biotinylates AAN$_3$-derivatized α2,3 and α2,8 sialic acids with a biotin-alkyne conjugate which is used to further capture a streptavidin fluorescent dye. SAFER was initially tested in both FFPE tissue sections and fixed, cultured cells. After the click reaction SAFER follows a standard immunostaining protocol, therefore we envision that this technique may one day be used in conjunction with other fluorescent probes to link the expression of sialic acids to specific molecules or tissue features of interest. The second approach stemming from AAN$_3$, Sialic Acid Bead Enrichment Reaction (SABER) uses a streptavidin-resin to enrich click-biotinylated α2,3- and α2,8-sialylated glycopeptides from the tissue milieu followed by on-bead digestion, purification and proteomic analysis by LC-MS/MS. An initial comparison was made between a SABER-enriched, AAN$_3$-derivatized prostate cancer FFPE tissue and a non-enriched serial tissue section to test SABER's ability to select for α2,3 and α2,8 sialylated species from the total glycoprotein matrix. Although still in development, SABER has the potential to not only gain information on the α2,3 and α2,8-sialylated proteins in a sample, but to gain site and N-glycan specific detail through expanded functionality. Together, these two extended applications broaden the reach of AAN$_3$ beyond imaging mass spectrometry to provide a cross-disciplinary tool set to study sialylation in biological systems.

5.2 Materials and Methods

5.2.1 Materials

1X phosphate-buffered saline (PBS), 12M HCl, 1M tris HCl pH 8, 16% formaldehyde, acetone, acetonitrile (ACN), citraconic anhydride, formic acid, HPLC H_2O, methanol, Pierce Microplate BCA Protein Assay Kit, sodium chloride, StageTips (C18), streptavidin-Cy5, trifluoroacetic acid (TFA), trypsin protease (MS-grade), Tween-20 and xylenes were obtained from ThermoFisher Scientific (Waltham, MA). 1,2-cyclohexanedione, 10M sodium hydroxide (NaOH), 2-2-2-trifluoroethanol (TFE), ammonium bicarbonate, bovine serum albumin (BSA), calcium chloride, DL-dithiothreitol (DTT), iodoacetamide (IAA), tris(2-carboxyethyl)phosphine hydrochloride (TCEP), sodium cyanoborohydride, sodium phosphate monobasic monohydrate and ZipTips (μ-C18) were obtained from Sigma (St. Louis, MO). Ethanol (EtOH) was obtained from Decon Labs (King of Prussia, PA). Streptavidin Sepharose high-performance affinity resin was obtained from Cytiva (Marlborough, MA). VectaShield Hardset with DAPI was obtained from Vector Laboratories (Newark, CA). Triton-X 100 was obtained from MP Biomedicals (Irvine, CA). AsPC-1 human pancreatic cancer cells (CRL-1682), HPAC human pancreatic carcinoma cells (CRL-2119), PANC-1 human pancreatic carcinoma cells (CRL-1469), PL45 human pancreatic carcinoma cells (CRL-2558) and Trypsin-EDTA solution were obtained from ATCC (Manassas, VA).

5.2.2 SAFER

5.2.2.1 SAFER Sample Preparation

Prior to SAFER staining, prostate cancer FFPE tissue slides were derivatized with AAN_3 and biotinylated via click chemistry as described in Chapter 4, sections 4.4.2 and 4.4.9. Alongside the FFPE tissues, PANC1, ASPC1, HPAC and PL45 pancreatic cancer cells were cultured and fixed as described in section 4.4.7[203], then derivatized and biotinylated as were the tissues. Desiccated AAN_3-biotinylated tissue and cell slides were rehydrated in 1X phosphate-buffered saline (PBS) for 2 min twice, antigen retrieved in citraconic anhydride buffer (25 µL citraconic anhydride, 2 µL 12 M HCL, 50 mL HPLC-grade H_2O, pH 3.0 ± 0.5) for 20 min in a preheated vegetable steamer then cooled at RT on the benchtop for 30 min. Once cooled, slides were washed in 1X PBS for 5 min twice, then the tissues were outlined with a hydrophobic barrier pen. The slides were then blocked in 200 – 500 µL PBST (0.05% Triton-X 100 in 1X PBS) with 3% bovine serum albumin (BSA) added for 1 hr at RT. Blocked slides were then placed in a humidity chamber and incubated in 10 µg/mL streptavidin-Cy5 in PBST for 2 hr at RT in the dark. After incubation, slides were washed with PBST for 3 min twice then in 1X PBS for 3 min. Finally, slides were dried with a kimwipe, sealed with a DAPI-containing mounting medium and allowed to dry overnight before imaging.

5.2.2.2 Fluorescence Microscopy

SAFER-labeled FFPE tissue slides were imaged the next day after overnight drying on an AMG EVOS cell imaging system (ThermoFisher Scientific, Waltham, MA) which captured both DAPI (357 nm) and Cy5 (635 nm)-stimulated

emission spectra. 16-bit monochromatic raw images were background subtracted using a rolling ball radius of 50 px in Image J then transferred to Adobe Photoshop for brightness adjustment and overlay in separate RGB channels to prepare figures. All images presented as comparisons were captured with uniform imaging parameters and manipulated equally post-acquisition.

5.2.3 SABER

5.2.3.1 Sample Preparation

Prior to SABER enrichment, prostate cancer FFPE tissue slides were AAN$_3$ derivatized followed by click chemistry biotinylation as described in Chapter 4, sections 4.4.2 and 4.4.9. Derivatized, biotinylated tissue slides were antigen retrieved in citraconic anhydride buffer (25 µL citraconic anhydride, 2 µL 12 M HCL, 50 mL HPLC-grade H$_2$O, pH 3.0 ± 0.5) for 30 min in a decloaker then buffer exchanged at room temperature and dried in a desiccator for 15 min. After drying, antigen-retrieved tissues were scraped from the glass slide into low-bind Eppendorf tubes using a clean razor blade. 50 µL 25 mM ammonium bicarbonate (AMBIC) and 50 µL 2-2-2-trifluoroethanol (TFE) were added to each scraped tissue and the samples were sonicated 20 sec on and 30 sec off three times while on ice. Sonicated tissue samples were briefly spun down then incubated at 60°C for 1 hr on a thermomixer at 300 rpm. Following incubation, the tissue samples were sonicated a second time as described above.

Sonicated tissue homogenates were cooled on ice for 5 min then reduced with 1 µL 1M tris(2-carboxyethyl)phosphine hydrochloride (TCEP) in AMBIC and 5 µL 500 mM DL-dithiothreitol (DTT) in AMBIC for 30 min at 60°C. After incubation,

the reduced homogenate was alkylated with 11 μL 500 mM iodoacetamide (IAA) in AMBIC at RT for 40 min in the dark. Following alkylation, 383 μL AMBIC was added to each sample to reduce the overall TFE concentration, samples were centrifuged at 4°C for 5 min at 15,000 rpm and the protein-containing supernatant was transferred to a new low-bind Eppendorf tube.

5.2.3.2 SABER Enrichment

Prior to enrichment, streptavidin resin was treated for protease resistance according to a previously published protocol[470]. Briefly, streptavidin beads were resuspended by inversion then 5 mL resin slurry was centrifuged at 1000 g for 5 min, after which the supernatant suspension buffer was discarded leaving only the resin pellet. Pelleted resin was washed in 10 mL PBST (100 μL Tween-20 in 100 mL 1X PBS), centrifuged at 1000 g for 5 min and the supernatant was discarded. Washed resin was resuspended in 14 mL CHD (120 mg 1,2-cyclohexanedione in 14 mL PBST, pH 13) then incubated rotating end-over-end for 4 hr at RT. After incubation, the resin was centrifuged at 1000 g for 5 min and the CHD was disposed of. Next, the resin was washed in 10 mL PBS, centrifuged at 1000 g for 5 min and the wash supernatant was discarded. Washed resin was resuspended in 7 mL reagent A (2 mL 16% formaldehyde in 6 mL PBST), 7 mL reagent B (0.101 g sodium cyanoborohydride in 8 mL PBST) was added and the resin was incubated at RT for 2 hr rotating end-over-end. After incubation in reagents A and B, the resin was centrifuged at 1000 g for 5 min and the supernatant was discarded. The resin pellet was then washed in 10 mL 0.1 M tris-HCl, pH 8 followed by washing in 10 mL PBST with centrifuging and supernatant disposal in between

as described. The washed resin was then finally resuspended in 5 mL PBST prior to use.

The protease-resistant streptavidin resin was inverted to homogenize then 200 µL of the resulting slurry was transferred to a low-bind Eppendorf tub using a wide-aperture pipette tip. 1800 µL binding buffer (20 mM sodium phosphate monobasic monohydrate, 0.15 M NaCl) was added to the resin which was then vortexed gently to wash and centrifuged at 1000 g for 5 min at which point the supernatant was discarded. This wash procedure was repeated an additional four times. Alkylated and reduced proteins were diluted with 1 mL binding buffer then applied to the washed streptavidin resin and rotated end-over-end in the dark for 1 hr at RT to bind. Following binding, the resin was centrifuged at 1000 g for 5 min and the supernatant was discarded without disturbing the resin pellet. The resin-bound proteins were resuspended in 1800 µL binding buffer to wash away unbound proteins, centrifuged at 1000 g for 5 min and the wash was discarded. This washing step was repeated an additional nine times with binding buffer followed by two washes in HPLC H_2O and two washes in AMBIC to remove binding buffer salts. The washed resin pellet was then stored on ice in preparation for tryptic digestion.

Trypsin protease was diluted to 0.1 µg/µL in digestion buffer (100 mM tris-HCl, 2 mM $CaCl_2$, pH 8). The washed protein-resin complex was resuspended in 500 µL digestion buffer, 20 µL 0.1 µg/µL trypsin (2 µg) was added and the samples were digested overnight at 37°C rotating end-over-end. After incubation, the resin was centrifuged at 1000 g for 5 min then the digest supernatant was transferred to

a new low-bind Eppendorf tube. The remaining resin pellet was gently resuspended in 500 µL HPLC H2O, centrifuged at 1000 g for 5 min and the wash supernatant transferred to the new Eppendorf tube. The resulting peptide digest was then acidified with 2 µL trifluoroacetic acid (TFA), dried under vacuum centrifugation and stored at -20°C prior to sample clean up.

5.2.3.3 Peptide Cleanup

Peptides were desalted with stop and go extraction (STAGE) tips according to the manufacturer's supplied protocol. Briefly, STAGE tips were retained by a plastic adapter in low-bind Eppendorf tubes then initialized with 50 µL initialization solution (5 mL formic acid and 15 mL HPLC H_2O in 80 mL acetonitrile) by centrifugation at 2000 g for 3 min. Following initialization, the tips were re-equilibrated with 50 µL equilibration solution (5 mL formic acid in 95 mL HPLC H_2O) by centrifugation at 2000 g for 3 min. The STAGE tip and adapter were then transferred to a new tube and the peptide digest – resuspended in 100 µL equilibration solution – was applied to the tip. The samples were then centrifuged at 2000 g for 15 min, the flowthrough was re-applied to the tip and residual peptides were bound to the tip by centrifugation again at 2000 g for 15 min. The sample-bound tips were then washed with 50 µL wash solution (5 mL formic acid in 95 mL HPLC H_2O) by centrifugation at 2000 g for 3 min three times. After washing, the STAGE tip and adapter were transferred to a new Eppendorf tube and the peptides were eluted from the column material with 50 µL elution solution (5 mL formic acid and 15 mL HPLC H_2O in 80 mL acetonitrile) by centrifugation at 2000 g for 3 min 3 times. 30 µL eluate was transferred to a separate tube for protein content

197

analysis by BCA then the remaining peptides were dried under vacuum centrifugation and stored at -20°C.

Following STAGE tip desalting, protein concentration in the samples was assessed by BCA protein assay using a Pierce Microplate kit (ThermoFisher Scientific, Waltham, MA). This was necessary to ensure that ≥ 2 µg peptides were retained after STAGE tip cleanup to ensure a saturating amount of material for the Zip Tip clean up step. The kit-provided protocol was followed and the results were measured at 562 nm on a SpectraMax M3 microplate reader (Molecular Devices, San Jose, CA). The resulting BSA standard absorbance values were plotted in excel and used to construct a standard curve from which sample protein concentrations were calculated. After the concentrations were determined to be ≥ 2 µg, the samples were cleaned up by Zip Tip.

STAGE tip cleaned samples were applied µ-C18 ZipTips capable of binding a total of 2 µg to desalt the digest and standardize the amount of peptide across the samples. The C18 microcolumn tips were attached to the pipette for cleanup, where solutions and samples were drawn into and expelled out of the tip. ZipTips were hydrated with 10 µL acetonitrile (ACN) in triplicate which was disposed to waste each time. Rehydrated tips were equilibrated with 10 µL equilibration solution (1 µL TFA in 1 mL HPLC H_2O) 3X which also was dispensed to waste each time. Dried, STAGE tip-desalted peptide samples were reconstituted in 30 µL equilibration solution then bound to the microcolumn through aspiration and dispensing of 30 10 µL volumes of reconstituted sample into and out of the ZipTip. Bound samples were then washed with 10 µL washing solution (1 µL TFA and 5

μL methanol in 994 μL HPLC H_2O) 10 times, with the wash dispensed to waste each time. Peptides were eluted from the tips through aspiration of 10 μL elution solution (1 μL TFA in 500 μL ACN and 500 μL HPLC H_2O) into the tip which was then dispensed into a new collection tube. This elution step was repeated three more times for a total elution volume of 40 μL, then the cleaned and desalted peptides were dried under vacuum centrifugation and stored at -20°C until LC-MS/MS analysis.

5.2.3.4 Glycoproteomic Analysis

Peptides were analyzed by LC-MS/MS on an EASY 1200 nanoLC in-line with an Orbitrap Lumos Tribrid mass spectrometer (ThermoFisher) running instrument control software version 4.2.28.14. A maximum of 2 μg of tryptic peptides were pressure loaded at 1,180 bar on to a reversed phase C18 column (Acclaim PepMap RSLC, 75 μm x 50 cm (C18, 2μm, 100 Å), ThermoFisher). Peptides were separated by a 5 – 40% B gradient over 180 minutes at flow rate of 300nL/min at 50°C, where solvent A was 5% acetonitrile, 0.1% formic acid, in LC-MS grade H_2O and solvent B was 80% acetonitrile, 0.1% formic acid in H_2O. Mass spectra were acquired in data-dependent mode with a high resolution (60,000) FTMS survey scan (mass range of 375-1575 *m/z*) followed by tandem mass spectra (MS/MS) of the most intense precursors with a 3 second cycle time and a 4.0e[5] automatic gain control target value for the survey MS scan. Higher energy collisional dissociation (HCD) fragmentation was performed using a precursor isolation window of 1.6 m/z, a maximum injection time of 22 ms, and a collision energy of 35%. Monoisotopic-precursor selection was set to "peptide" and apex

detection was not enabled. Precursors were dynamically excluded from resequencing for 30 seconds with a mass tolerance of 10 ppm. Precursor ions with charge states that were undetermined or > 5 were excluded.

To identify the peptides and infer the proteins present, Proteome Discoverer version 1.4.0.288 (ThermoFisher) was used to search the tandem mass spectrometric data against a human protein database (Uniprot). Briefly, the raw data were run through two major processing nodes: Spectrum Selector and Sequest HT. For the Spectrum Selector, a 15 minute retention time and precursor mass of 350 Da defined the lower limits while the upper limits were bounded at 200 minutes with a precursor mass of 5000 Da. A 1.5 signal-to-noise (S/N) ratio was set for the fourier-transform and MS2 activation was set at higher-energy collision-dissociation. For the Sequest HT node, trypsin-digested peptides were searched against a human protein database with a max missed cleavage site of 2, minimum peptide length of 7 and maximum peptide length of 144 parameters specified. 20 ppm and 0.02 Da mass tolerances were set for the precursors and fragments, respectively. Finally, dynamic deamidation of asparagine or glutamine (+0.984) and oxidation of methionine (+15.995 Da) modifications were included in the search along with static modification of carbamidomethylation of cysteine (+57.021 Da).   A false discovery rate threshold determined by searching against a reversed, human database was set at 0.01. An XCorr to charge state filter was used to filter out low scoring peptides. A total of 9156 peptides were detected corresponding to 782 protein groups, where at least 2 tryptic peptides were used to identify a protein.

5.3 Results

5.3.1 SAFER in FFPE Tissues and Cultured Cells

Following successful histochemical staining facilitated by AAN$_3$ and click biotinylation, we experimented with an alternate streptavidin-conjugated probe for fluorescent visualization of α2,3 and α2,8-linked sialic acids. We initially demonstrated this new staining system, <u>s</u>ialic <u>a</u>cid <u>f</u>luorescence <u>e</u>nhancement <u>r</u>eaction (SAFER), in two pancreatic cancer FFPE tissues which were morphologically separated by their stromal content. In 2018 Koay and colleagues developed a stromal scoring system which categorized pancreatic ductal adenocarcinoma tissues into "high delta" and "low delta" biophysical subtypes based on stromal patterning, computed tomography (CT) volumetric contouring and other characteristics[471]. A high Δ score – typified by lower levels of tumor stroma – was associated with earlier metastasis and poorer overall survival. Although these classifiers were absent from the clinical data associated with our PDAC cohort, the stromal phenotypes of many of the tissues visually corresponded to the classifications. Therefore, we considered these samples an ideal test bed to characterize α2,3 and α2,8 sialic acid expression between morphologically distinct tissues. Figure 40A shows H&E staining of the tumor stroma in a PDAC FFPE tissue that phenotypically corresponds to a low delta score, with visually apparent increases in extracellular matrix (ECM) and cells in the interstitium. In contrast, the pancreatic cancer tissue in Figure 40B has a lower ECM volume and a more homogenous mix of tumor and stromal cells which aligns with the high Δ stromal phenotype. In accordance with Δ classification-associated survival trends, the
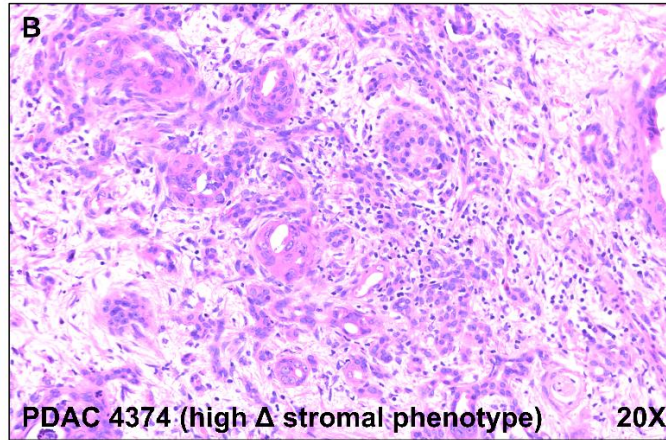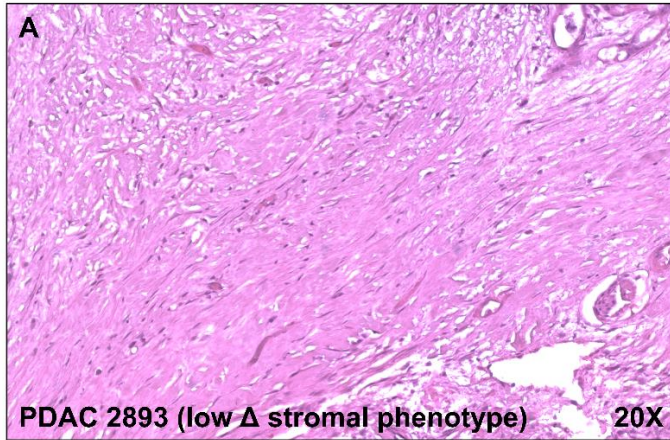
Figure 40. Stromal Morphology Variations in Pancreatic Cancer Tissues. H&E staining of two pancreatic cancer tissue samples. A) a low Δ stromal phenotype with increased ECM volume compared to B) a high Δ phenotype with decreased ECM volume and C) their associated clinical outcome data.

patient with the high Δ stroma phenotype presented later with distant recurrence following resection while the low Δ-like patient recurred only locally (Figure 40C).

The workflow for α2,3 and α2,8 sialic acid visualization by SAFER is outlined in Figure 41. Briefly, FFPE serial tissue sections were derivatized with azide handles through AAN_3 and biotinylated by an overnight click chemistry reaction with a biotin alkyne. The installed biotin on α2,3 and α2,8 sialic acid isomers was then used to capture a commercially available fluorochrome-conjugated streptavidin via a blocking and staining format adapted from a previously published immunofluorescence protocol[109]. Figure 42 shows the first SAFER staining analysis of pancreatic cancer tissues. Common to both tissues was vivid fluorescence staining in neoplastic PDAC lesions, with polarized α2,3 and α2,8-sialic acid expression on the luminal face. Tissue 2893, which had a low Δ stromal phenotype, exhibited decreased sialic acid staining in the stroma surrounding primary tumor and lesion tissues as compared to the cancerous and neoplastic cells in the sample (Figure 42 A-D). Conversely, stroma in the high Δ phenotype tissue 4374 stained intensely for α2,3- and α2,8-linked sialic acids. Increased ECM sialylation is linked to heightened metastatic potential in pancreatic and other cancers and may in part explain why patient 4374 from our cohort experienced distant recurrence post-resection[472]. Overall, these experiments demonstrate the potential of SAFER to highlight sialylation differences between disparate tissue morphologies.
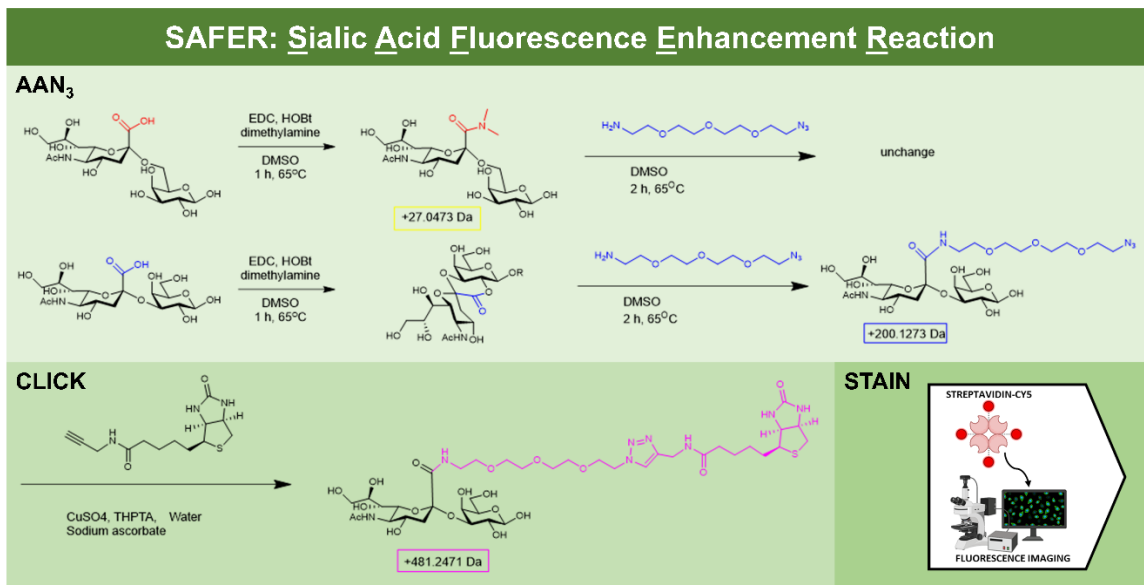
Figure 41. SAFER Schematic Workflow. Divided into 3 main parts, the SAFER method entails 1) AAN$_3$-derivatization of α2,3- and α2,8-linked sialic acids with a polyethylene glycol (PEG)-extended azide handle followed by 2) biotinylation by click reaction and 3) biotin-avidin affinity capture of a streptavidin-conjugated fluorochrome (Cy5) and imaging by fluorescence microscopy.

PDAC 2893 (low Δ stromal phenotype)

PDAC 4374 (high Δ stromal phenotype)
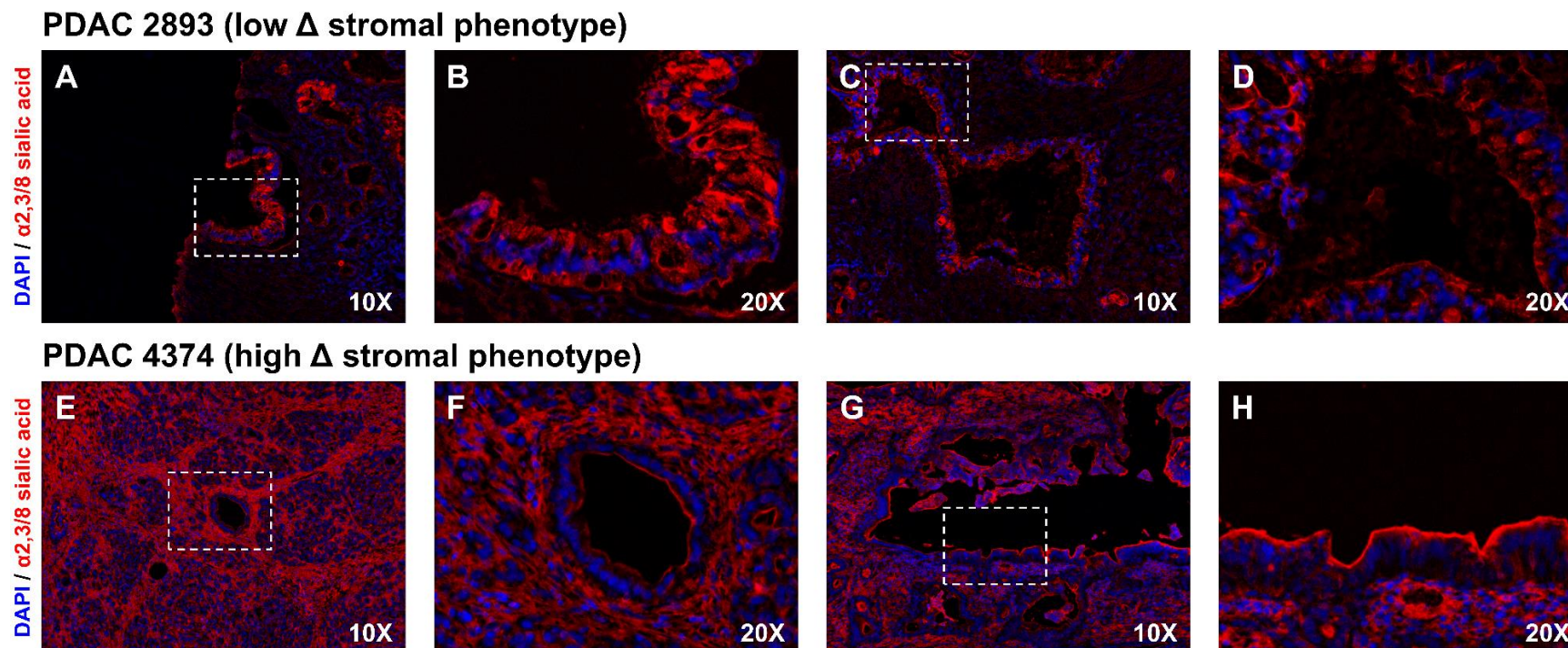
Figure 42. α2,3 and α2,8 Sialic Acid Staining with SAFER in PDAC FFPE Tissues. SAFER staining of morphologically distinct pancreatic cancer tissues. A-D) 10X and 20X optical fluorescence images of two lesions within a low Δ stromal phenotype PDAC tumor. Intense α2,3/α2,8 sialic acid staining (red, Cy5) was observed in the lesion cells as opposed to the surrounding stroma. E-H) 10X and 20X optical fluorescence images of two lesions within a high Δ stromal phenotype PDAC tumor. Intense α2,3/α2,8 sialic acid staining (red, Cy5) in both the lesions and surrounding stroma. Nuclei: blue, DAPI.

The next focus in the development of SAFER was to use this staining technique to characterize sialylation patterns in healthy versus diseased tissue. For this end, we applied SAFER to a normal kidney FFPE tissue section and to a clear-cell renal cell carcinoma (ccRCC) sample (Figure 43). Here we focused on the glomeruli, dense networks of blood vessels at the intersection of nephrons and the renal tubules which are critical to the kidneys' blood filtration function[473]. As these structures are known to be affected by the development and progression of ccRCC, we questioned whether there would be observable sialylation differences between healthy and afflicted glomeruli[474]. Figure 43A shows SAFER fluorescent staining of glomeruli from the non-diseased tissue while cancerous glomeruli are shown in Figure 43B. Although not significant, healthy glomeruli tended to be larger in size and contained more nuclei, while diseased structures had fewer nuclei and were smaller overall (Figure 43C). Visually, diseased glomeruli appeared deformed while healthy glomeruli were more circular. We quantified the intensity of SAFER staining in each glomeruli, normalized to both glomerular area and nuclear content, and demonstrated significantly increased α2,3 and α2,8 sialic acid content in glomeruli from the ccRCC tissue (Figure 43D). The ability to reliably quantitate SAFER fluorescence is a developmental benchmark and will be key to its successful integration into more advanced fluorescent imaging experiments.

We further evaluated SAFER's capacity to complement other staining techniques in post-mortem SARS-CoV-2 (COVID-19) infected lung tissue
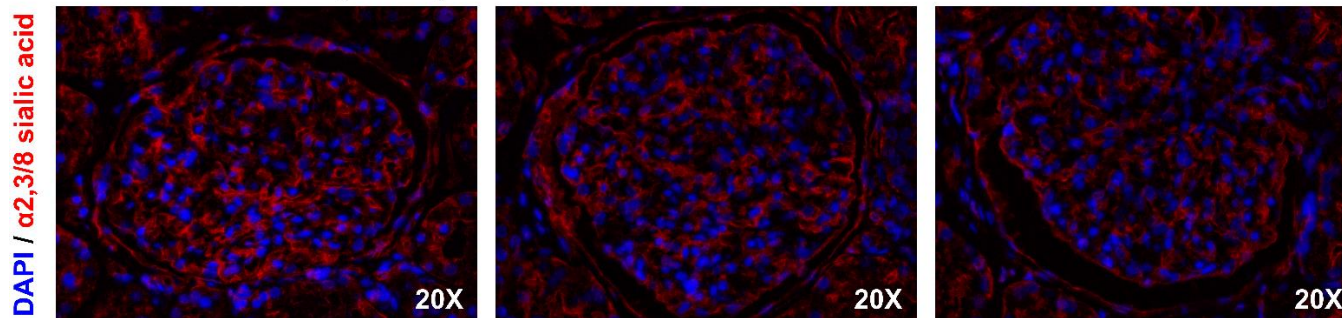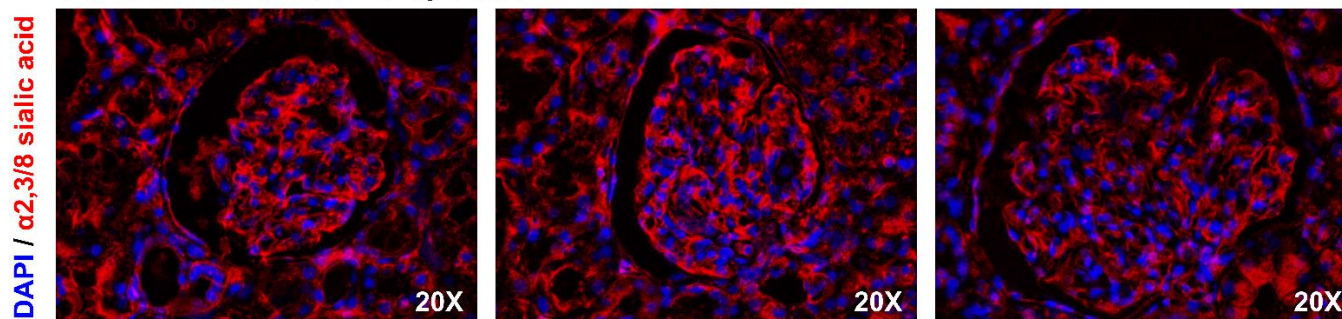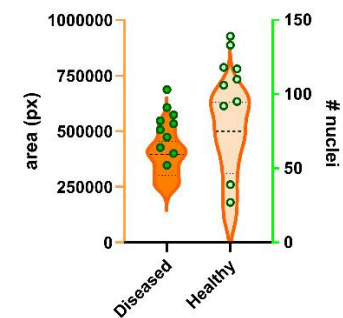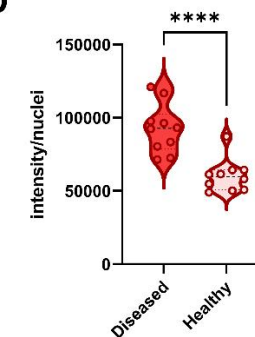
Figure 43. Quantification of SAFER Staining in Healthy and Diseased Glomeruli. α2,3 and α2,8-linked sialic acid (red, Cy5) visualization in a normal kidney tissue compared to a ccRCC tissue. A) 20X optical fluorescence images of 3 (out of 10 total) SAFER-stained glomeruli from a non-diseased kidney tissue sample. B) 20X optical fluorescence images of 3 (out of 10 total) SAFER-stained glomeruli from a ccRCC tissue sample. C) measuring glomerular area and nuclear content. Left axis (orange): glomeruli area (px, pixels) was increased in the healthy sample although not significantly. Right axis (green): # of nuclei per glomeruli was increased in the healthy tissue, although not significantly. D) a significant increase (p = 0.000074) in area and nuclear content-normalized α2,3 and α2,8 sialic acid staining intensity in the diseased glomeruli. Area, nuclei counting and staining intensity measurements performed in ImageJ. **** = p < 0.0001. Nuclei: blue, DAPI.

samples. Specifically, one of these tissues had areas of dense immune cell infiltrate, presumably as a response to infection. This sample was stained by SAFER which revealed intense α2,3 and α2,8-linked sialic acid expression on some, but not all cells in the immune cluster (Figure 44A,B). The structure of this infiltrate was interesting to us, as there were long chain-like groups of cells studding the cluster overall, revealed by both SAFER and H&E staining (Figure 44C,D). We were subsequently driven to investigate the specific cellular compositions of these immune areas to see if we could link α2,3 and α2,8 sialic acid expression to a particular cell type. As part of a larger overall study, our collaborators at the FDA immunohistochemically stained a serial section of this tissue with CD8 and CD11b-targeted antibodies, which are cytotoxic T-cell and pan-leukocyte markers, respectively (Figure 44D,E). Although not definitive, the CD11b^{+} cells surrounding the CD8^{+} cell chains corresponded visually to the α2,3 and α2,8-linked sialic acid-expressing cells stained by SAFER. In the reverse sense, the cells recognized as T-cells by CD8 IHC staining seemed to have lower overall SAFER staining intensity when compared with their cellular neighbors. In future experiments, fluorescent immune cell markers could be used in conjunction with SAFER to specifically reveal the cell types which overexpress α2,3 and α2,8 sialic acid-containing glycoconjugates.

To determine whether SAFER was amenable to other sample formats, we tested our approach on fixed, cultured pancreatic cancer cell lines. The workflow for SAFER staining of cells is similar to that for FFPE tissues, except in that it omits

208
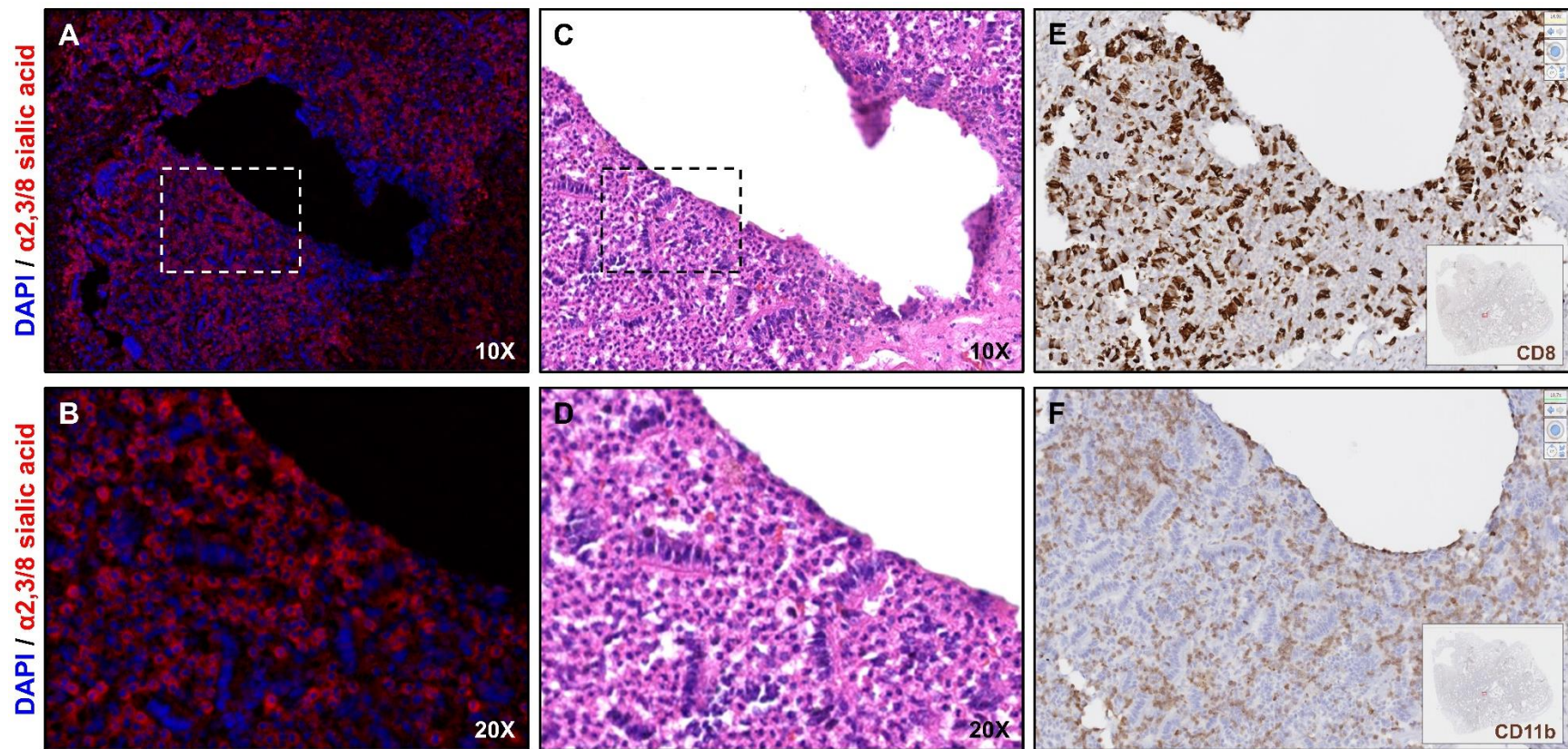
Figure 44. SAFER, H&E and IHC Staining of Immune Cells in SARS-CoV-2-Infected Lungs. Post-mortem COVID-19-infected lung tissue serial sections were treated with SAFER for sialic acid expression, IHC for CD8 and CD11 and were histologically stained. A) 10X and B) 20X optical fluorescence images of immune infiltrate showing variable cell surface expression of α2,3 and α2,8-linked sialic acids (red, Cy5) within the cluster. C) 10X and B) 20X H&E staining revealing differential cellular morphologies within the infiltrate. E) CD8+ and F) CD11b+ positive immunohistochemical staining of different immune cell populations within the area of interest. Nuclei: blue, DAPI.

the antigen retrieval step. Pancreatic cancer cell lines were cultured and fixed for SAFER staining following a published protocol and as previously described during the development of AAXL[203]. SAFER staining images of the ASPC1, HPAC, PANC1 and PL45 pancreatic cancer cell lines used in Chapter 4 are shown in Figure 45. Phenotypic expression differences were observed for each cell type. ASPC1 cells showed intense α2,3 and α2,8 sialic acid staining specific to the cell surface (Figure 45A), as compared to the PANC1 cells where staining was heavy but polarized in a manner suggestive of endoplasmic reticulum or Golgi localization (Figure 45B). SAFER staining was not specific to a particular cellular compartment in the HPAC cell line, rather expression appeared to be ubiquitous across the cell (Figure 45C). PL45 cells stained less intensely than did the others, with very low levels of α2,3 and α2,8 sialic acid expression detected (Figure 45D). In an effort to quantify SAFER staining in the cell lines, we first used the Otsu thresholding function for image binarization in ImageJ to generate masks to control for staining artifacts (Figure 45E). The resulting intensities as outlined within the masks were controlled for the number of nuclei within the field of view, however without a cell membrane marker could not be controlled for differences in cell size. With this caveat in mind, the PANC1 cell line showed the most intense SAFER staining for α2,3 and α2,8-linked sialic acids, with similar staining levels for the ASPC1 and HPAC cells and minimal staining in the PL45 line (Figure 45F). Collectively, these experiments demonstrate the potential of SAFER for both qualitative and quantitative characterization of sialic acid isomer expression in cultured cells.
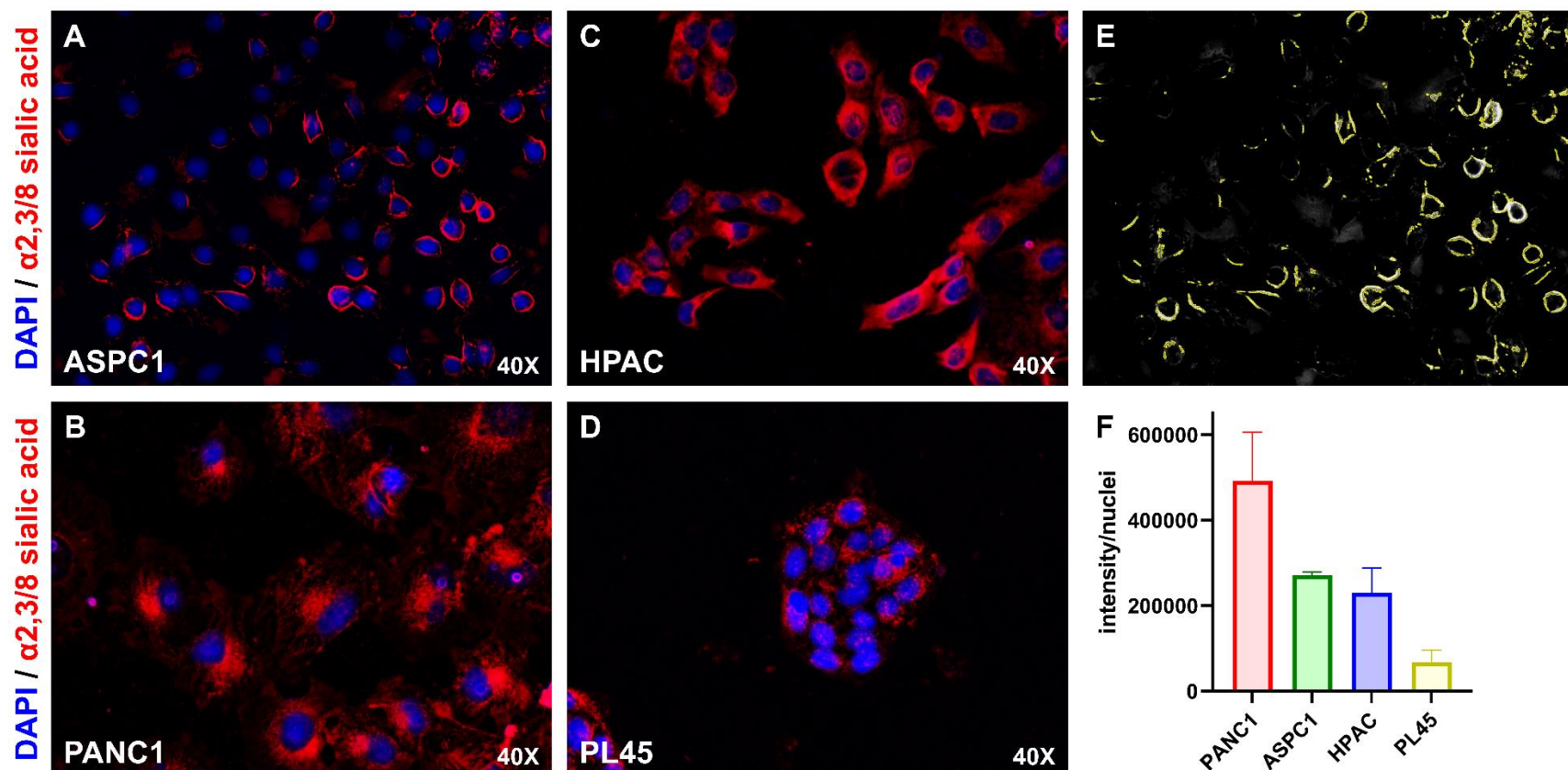
Figure 45. SAFER Staining Reveals Disparate Sialic Acid Expression in Cultured PDAC Cells. 40X optical fluorescence images of SAFER-stained A) ASPC1, B) PANC1, C) HPAC and D) PL45 cell lines. E) Otsu thresholding function defined masks to control for staining artifacts in ImageJ. F) nuclei-normalized intensities of SAFER staining in each cell line. α2,3 and α2,8 sialic acids: red, Cy5; Nuclei: blue, DAPI.

5.3.2 SABER Applied to Prostate Cancer Tissues

Our successful application of AAN$_3$ in SAFER inspired us to explore even more creative approaches for the characterization of sialylated glycoconjugates. A fundamental problem in glycomics is this: the very substantive link between glycans and their protein carriers often needs to be severed in order to release these sugars for analysis. In doing so, these proteins are left behind along with the important biological context which they convey. Intact glycoprotein profiling is able to retain the glycan:protein connection during analysis, however these strategies often hinge on non-specific enrichment techniques to pull glycoproteins from the total protein matrix en bloc. To date, a sialic acid isomer-selective solid phase enrichment strategy has not been demonstrated. To address this technological gap, we developed SABER (sialic acid bead enrichment reaction), where we use the AAN$_3$ and click chemistry-installed biotin handle on α2,3 and α2,8-sialic acids to selectively retain these glycans and their underlying glycoconjugates on an immobilized recombinant streptavidin resin. Captured glycoproteins can then be processed for analysis by LC-MS/MS. The general workflow for SABER is outlined in Figure 46.

We initially tested SABER on the prostate cancer FFPE tissues which were examined in Chapter 4 in an attempt to link the α2,3-sialylated N-glycans revealed by our prior experiments with their glycoprotein carriers. This sample had areas of intense α2,3-sialic acid expression localized to tumor tissue regions, therefore we
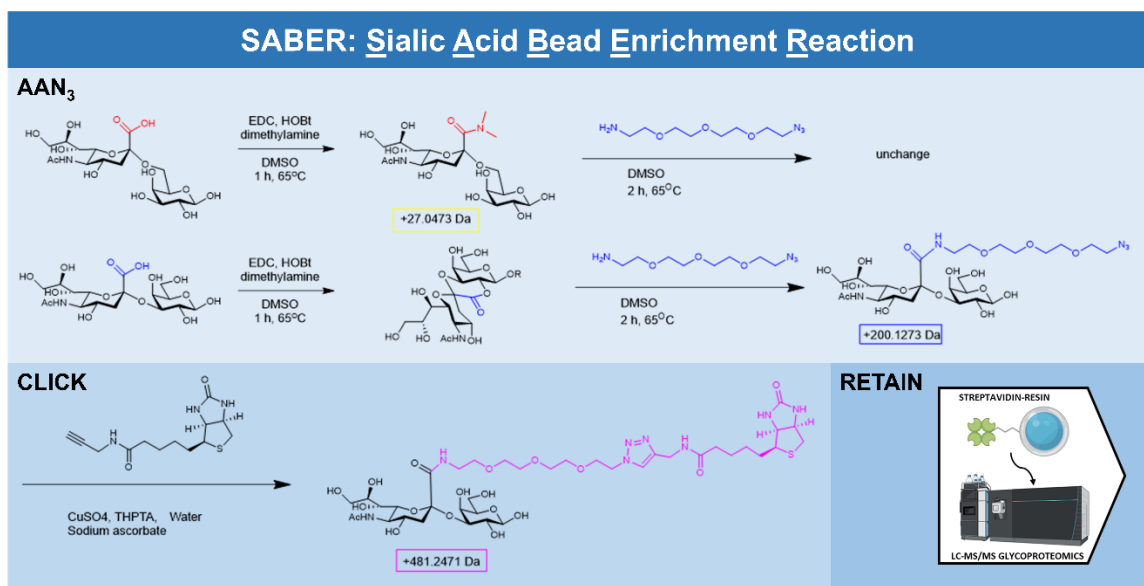
Figure 46. SABER Schematic Workflow. The SABER method entails 1) derivatization of α2,3- and α2,8-linked sialic acids with an amine-azide by AAN$_3$ followed by 2) click biotinylation, 3) biotin-avidin affinity capture on an immobilized streptavidin resin and 4) tryptic digestion and peptide cleanup for LC-MS/MS.

considered it an ideal proving ground for SABER (Figure 35E). As summarized in Figure 46, the SABER workflow begins with AAN$_3$ derivatization and click biotinylation as previously described. Following installation of the biotin handle, the tissue was antigen retrieved then scraped from the slide, homogenized, reduced and alkylated. A protease-resistant streptavidin resin was then used to selectively retain α2,3- and α2,8-linked sialic acid-containing glycoproteins from the tissue homogenate. Captured glycoproteins were digested on-bead and the resulting peptides were cleaned up, desalted and concentrated for subsequent LC-MS/MS analysis. Alongside the derivatized tissue, a non-derivatized serial tissue section was identically prepared as a control for the specificity of SABER for biotinylated sialic acids. Additionally, a third non-derivatized serial tissue section was homogenized, reduced, alkylated, digested with trypsin and cleaned up while omitting SABER enrichment to represent the sample's total proteome for comparison.

Following LC-MS/MS analysis, higher energy collisional dissociation (HCD)-fragmented spectra were annotated by their b and y ion fragmentation patterns to assign a peptide amino acid sequence with high confidence. A protein identification search was then performed where detected peptides were mapped to their full sequences against a human database to confirm protein assignments. Likely contaminants, mostly keratins, were filtered out of the results. 7312 peptides corresponding to 747 proteins were identified in the non-enriched sample while 1844 peptides and 106 proteins were detected in the SABER tissue. The non-derivatized, SABER-enriched sample did not contain a detectable amount of

protein during a quality control check in sample clean up, thus confirming the specificity of SABER for biotinylated targets (data not shown). Of the SABER-enriched proteins, 71 were also identified in the non-enriched sample while 35 were unique to SABER. These 35 proteins, along with their accession numbers, coverage, number of unique peptides and molecular weights are listed in Table 14. Prostate-specific antigen (PSA) and prostatic acid phosphatase (PAP), two well characterized glycoproteins elevated in prostate cancer, were identified in both the enriched and non-enriched samples. Overall, SABER demonstrated a greater than 7-fold enrichment in the number of identified proteins between the non-enriched and SABER-treated sample.

To characterize expression differences between proteins identified in this proof-of-concept experiment, label free quantification (LFQ) was performed in Perseus based on precursor signal intensity (Figure 48A,B). 13 proteins were determined to be enriched in the SABER tissue by LFQ. Of these 13, 8 were extracellular matrix or adhesion junction proteins, which preliminarily suggests a role for α2,3 and α2,8 sialic acids in the interaction between tumor cells and the local microenvironment in prostate cancer (Figure 48C). This is consistent with studies of sialylation in prostate cancer which have shown increased ST3GAL1 expression to be correlated with a more metastatic phenotype[472,475].

To gain more biological context from the identified α2,3 and α2,8-linked sialoproteins in the initial SABER experiment we performed a gene ontology (GO) enrichment analysis using the panther classification system (Table 15). We first

Table 14. Proteins Unique to the SABER Treated Sample.

Accession	Description	Coverage	Unique Peptides	MW [kDa]
P63267	Actin, gamma-enteric smooth muscle	32.98	3	41.850
Q86YZ3	Hornerin	8.84	7	282.228
Q02413	Desmoglein-1	13.06	11	113.676
P81605	Dermcidin	22.73	3	11.277
P29508	Serpin	28.21	9	44.537
P31944	Caspase-14	20.66	7	27.662
Q08554-2	Desmocollin-1 (Isoform 1B)	7.98	5	93.776
Q71UI9-2	Histone H2A.V (Isoform 2)	14.04	2	12.139
P04350	Tubulin beta-4A chain	8.33	4	49.554
Q6NXT2	Histone H3.3C	16.3	3	15.204
Q13835-2	Plakophilin-1 (Isoform 1)	7.85	5	80.445
P02751-12	Fibronectin (Isoform 12)	3.49	5	221.152
P22626-2	Heterogeneous nuclear ribonucleoproteins A2/B1 (Isoform A2)	14.66	3	35.984
Q6UWP8	Suprabasin	12.2	2	60.505
Q5D862	Filaggrin-2	3.35	5	247.928
P31151	Protein S100-A7	12.87	3	11.464
P01040	Cystatin-A	41.84	3	11.000
P02545-3	Prelamin-A/C (Isoform Aδ10)	9.46	4	70.618
Q08188	Protein-glutamine gamma-glutamyltransferase E	3.46	2	76.584
P0DOX5	Immunoglobulin gamma-1 heavy chain	10.69	2	49.298
Q15517	Corneodesmosin	4.35	2	51.490
P05089	Arginase-1	14.29	5	34.713
P02788-2	Lactotransferrin (Isoform δLf)	8.26	5	73.114
Q96P63	Serpin B12	8.15	3	46.247
O75223	Gamma-glutamylcyclotransferase	18.09	3	20.994
P26599-3	Polypyrimidine tract-binding protein 1 (Isoform 3)	19.03	2	59.596
P47929	Galectin-7	16.18	3	15.066
P60174-4	Triosephosphate isomerase (Isoform 3)	14.97	2	17.947
P31025	Lipocalin-1	12.5	2	19.238
P00709	Alpha-lactalbumin	37.32	2	16.214
P09525-2	Annexin A4 (Isoform 2)	8.86	2	27.046
P68363-2	Tubulin alpha-1B chain (Isoform 2)	8.06	2	37.194
P08246	Neutrophil elastase	5.62	2	28.500
P05090	Apolipoprotein D	14.29	3	21.262
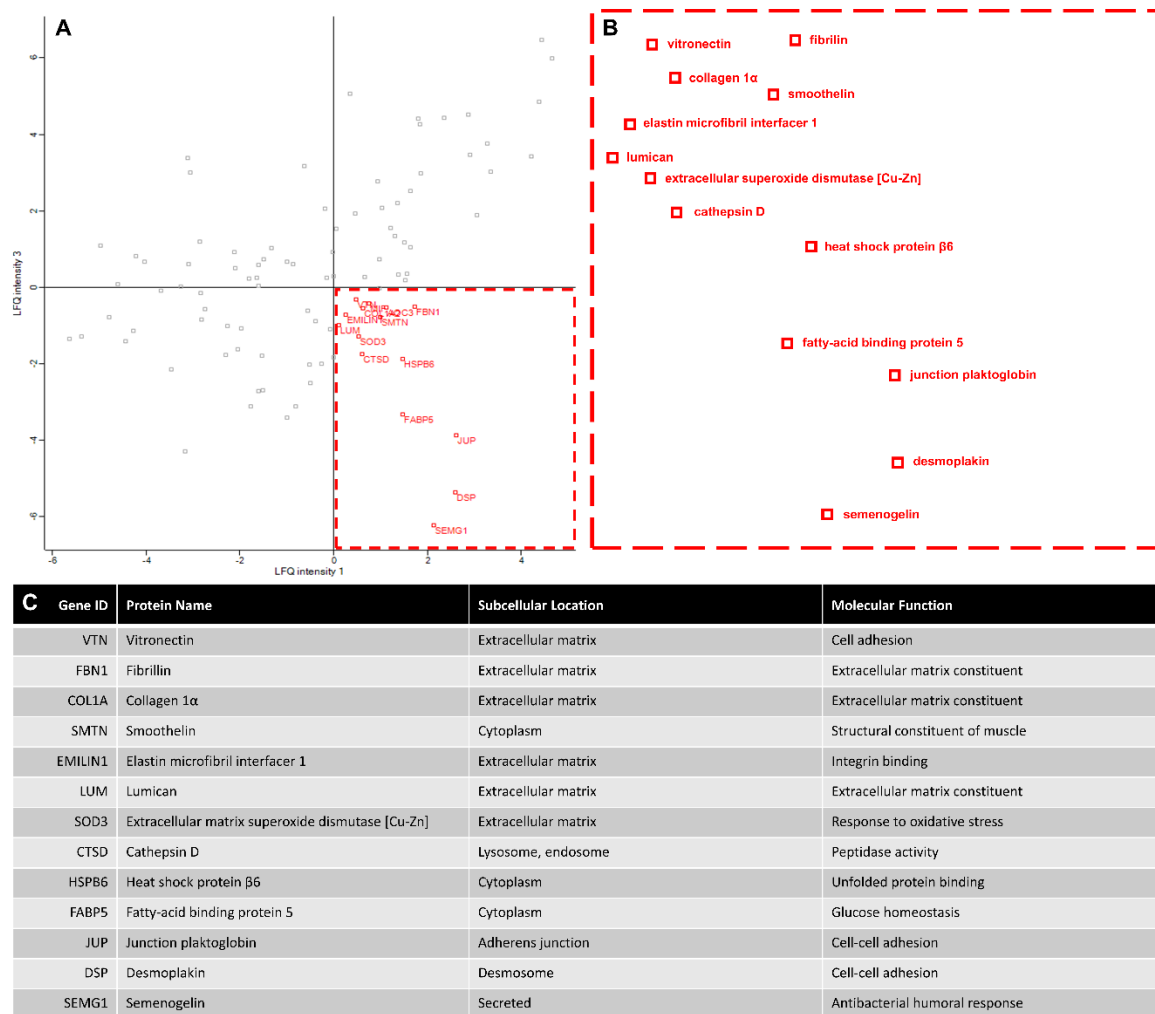
Figure 47. Label Free Quantification of SABER-Enriched Glycoproteins. LFQ intensities for the non-enriched sample (LFQ intensity 3) plotted against the SABER sample (LFQ intensity 1) are shown in A) and enlarged in B) with protein names annotated. C) Table of the 13 enriched proteins in the SABER tissue including gene ID, protein name, subcellular location and molecular function.

Gene ID	Protein Name	Subcellular Location	Molecular Function
VTN	Vitronectin	Extracellular matrix	Cell adhesion
FBN1	Fibrillin	Extracellular matrix	Extracellular matrix constituent
COL1A	Collagen 1α	Extracellular matrix	Extracellular matrix constituent
SMTN	Smoothelin	Cytoplasm	Structural constituent of muscle
EMILIN1	Elastin microfibril interfacer 1	Extracellular matrix	Integrin binding
LUM	Lumican	Extracellular matrix	Extracellular matrix constituent
SOD3	Extracellular matrix superoxide dismutase [Cu-Zn]	Extracellular matrix	Response to oxidative stress
CTSD	Cathepsin D	Lysosome, endosome	Peptidase activity
HSPB6	Heat shock protein β6	Cytoplasm	Unfolded protein binding
FABP5	Fatty-acid binding protein 5	Cytoplasm	Glucose homeostasis
JUP	Junction plaktoglobin	Adherens junction	Cell-cell adhesion
DSP	Desmoplakin	Desmosome	Cell-cell adhesion
SEMG1	Semenogelin	Secreted	Antibacterial humoral response

Table 15. GO Enrichment Analysis of SABER-Identified α2,3 and α2,8 Sialoproteins.

Go Biological Process	IDs mapped to Process	Expected mapped	Fold Enrichment	P value
Cell adhesion	28	4.92	5.7	5.59×10^{-14}
Antimicrobial humoral response	12	0.72	16.57	2.01×10^{-11}
Defense response to bacterium	15	1.86	8.06	8.59×10^{-10}
Cell-cell adhesion	18	2.75	6.54	3.94×10^{-10}
Humoral immune response	15	1.72	8.73	2.99×10^{-10}
Regulation of endopeptidase activity	15	2.14	7.02	5.22×10^{-09}
Peptide cross-linking	7	0.18	38.13	1.96×10^{-09}
Homotypic cell-cell adhesion	8	0.31	26.14	1.93×10^{-09}
Antibacterial humoral response	8	0.3	27.05	1.51×10^{-09}
Defense response to fungus	8	0.28	28.52	1.03×10^{-09}
Tissue development	30	8.6	3.49	1.02×10^{-09}
Epithelial cell differentiation	16	3.09	5.19	9.40×10^{-08}
Regulation of body fluid levels	13	1.91	6.8	8.52×10^{-08}
Response to biotic stimulus	25	7.47	3.35	7.77×10^{-08}
Cellular oxidant detoxification	8	0.47	16.87	4.59×10^{-08}
Response to bacterium	18	3.72	4.83	3.81×10^{-08}
Response to reactive oxygen species	10	0.86	11.67	2.45×10^{-08}
Cell killing	9	0.61	14.71	1.95×10^{-08}
Epithelium development	22	5.38	4.09	1.79×10^{-08}
Response to stress	42	17.34	2.42	1.47×10^{-08}

Reactome Pathway	IDs mapped to Pathway	Expected mapped	Fold Enrichment	P value
Neutrophil degranulation	27	2.43	11.10	2.08×10^{-20}
Innate immune system	35	5.65	6.20	1.15×10^{-18}
Immune system	44	10.48	4.20	1.94×10^{-17}
Extracellular matrix organization	16	1.52	10.49	5.25×10^{-12}
Degradation of the extracellular matrix	12	0.71	16.81	1.73×10^{-11}
ECM proteoglycans	9	0.39	23.22	4.70×10^{-10}
Formation of the cornified envelope	11	0.66	16.72	1.32×10^{-10}
Developmental biology	23	5.56	4.14	6.50×10^{-09}
Integrin cell surface interactions	9	0.43	21.01	1.06×10^{-09}
Collagen degradation	7	0.33	21.45	7.20×10^{-08}
Antimicrobial peptides	8	0.46	17.24	3.92×10^{-08}
Hemostasis	16	3.42	4.68	3.60×10^{-07}
RHO GTPase effectors	11	1.47	7.49	3.56×10^{-07}
Amyloid fiber formation	7	0.41	17.16	2.96×10^{-07}
Apoptotic execution phase	5	0.26	19.22	9.50×10^{-06}
Chaperone-mediated autophagy	4	0.11	35.65	8.58×10^{-06}
Response to elevated platelet cytosolic Ca^{2+}	7	0.67	10.40	6.97×10^{-06}
Platelet degranulation	7	0.65	10.81	5.78×10^{-06}
Cellular response to stimuli	15	3.73	4.02	5.44×10^{-06}
Collagen chain trimerization	5	0.22	22.28	4.88×10^{-06}

Extracellular	Immune	Stress

searched for biological processes enriched in our SABER-identified proteins, which included cell-cell adhesion, peptide crosslinking, bacterial defense response, humoral immune response, response to oxidative stress and oxidant detoxification amongst other functions. Generally, the biological processes could be subdivided into either immune, extracellular or stress response capacities. To gain insight into which signaling pathways these proteins are participating in, we also performed a GO Reactome pathway search which again revealed a host of enriched networks biased towards extracellular, immune and stress functions of the cell. Collectively, these results are in line with the apoptotic, immunosuppressive, and extracellular adhesion properties attributed to sialylated glycoconjugates in cancer. Although these results are preliminary and further developmental work remains to be done, this initial experiment demonstrates the potential for SABER to provide deep biological insights into the roles of α2,3 and α2,8-linked sialic acids in health and disease.

5.4 Discussion

The expanded applications for AAN$_3$ described in this chapter are a promising start for the development of advanced tools to study α2,3 and α2,8 sialylation. The major advantage conveyed by both SAFER and SABER is the ability to be isomer selective. To date, neither fluorescent labeling strategies targeting sialylation nor solid phase enrichment approaches for sialylated glycoconjugates can discriminate between the major sialic acid isomers present in living systems. Our approaches address this technological gap through the preferential incorporation of azide tags directly into α2,3 and α2,8-linked sialic

acids. Critically, our new tools do not require active metabolic machinery to install their click-reactive handles and therefore are applicable clinical tissue and biofluid samples. Another strength of SABER and SAFER is that these techniques rely on the well-characterized specificity of biotin:avidin interactions to generate their expanded functionality[476]. Not only does give us high confidence the selectivity of our probes and enrichment surfaces for their click-chemistry biotinylated targets, but the commercial availability of recombinant streptavidin-conjugated molecules suggests that these are just the first in a line of enhanced approaches potentiated by AAN$_3$.

Although the approach targets many well described tumor carbohydrate antigens that are α2,3-sialylated, a shortcoming of both SAFER and SABER is their inability to recognize α2,6-sialylated molecules. This is especially unfortunate given our understanding of the role α2,6-sialylated glycans play in immune suppression within the tumor microenvironment, amongst other functions. The differential formation of stable α2,6 amides and α2,3 or α2,8 intramolecular lactones under the same reaction conditions during amidation derivatization reactions is strongly dependent on the derivatizing nucleophile used in the 1st reaction step[427,477,478]. It is worth exploring whether an alkyne-containing weak nucleophile could be substituted for the current dimethylamide reagent used in the 1st amidation step of AAN$_3$. Complicating downstream analyses, the protocols we have developed do not allow us to discriminate between α2,3 and α2,8-linked sialic acid isomers, which are identically labeled or selected for by SAFER and SABER. Fortunately, this obstacle can be overcome by the use of α2,3 or α2,8-sialic acid-

targeted sialidases to clear a particular isomer from the tissue prior to derivatization, biotinylation and SABER or SAFER treatment. In a partnership with our academic and industrial collaborators, we are currently evaluating isomer specific sialidases for use in our systems.

Both protocols are still in the developmental stage. For SAFER, use with complementary fluorescent probes still needs to be explored so that this staining technique can be integrated with more traditional immunofluorescence experiments. As SAFER continues to evolve, so too should our methods for staining quantification. While the initial results were promising, SABER requires further refinement. Optimization of capture conditions, reagents and sample cleanup is ongoing and should produce a more robust protocol. We are also interested in increasing the amount of starting material through the use of multiple serial sections to generate a larger number of protein identifications downstream. Collectively, both protocols represent the first steps in a much larger exploration of sialic acid biology by our group. We hope that one day both SAFER and SABER will see routine implementation in our glycobiological workflows and reveal previously unknown mechanisms of disease driven by sialylation.

Chapter 6: Conclusions, Limitations and Future Directions

6.1 Global Overview

The work presented in this dissertation covers three key areas: 1) determining N-glycans and N-glycan structural motifs that are altered in pancreatic ductal adenocarcinoma, then linking these changes with canonical biomarker expression to better discriminate between cancerous and non-transformed tissue; 2) the development of bioorthogonal chemical derivatization strategies to differentiate between sialic acid linkage isomers and their application to FFPE tissues, clinical biofluids and cultured cells; and 3) the translation of this derivatization approach into two novel methods for fluorescent labeling of sialic acid isomers and selective enrichment of sialylated glycoconjugates for glycoproteomic analyses. Each chapter represents a significant step forward in their respective glycobiological fields. The broader implications of each of these research efforts, along with their limitations and potential future directions, are outlined further below.

6.2. N-glycosylation Changes in PDAC

6.2.1 Conclusions

Aim 1, described in Chapter 3 of this dissertation, focused on analyzing the distribution of N-glycans in a pancreatic ductal adenocarcinoma patient cohort by MALDI-IMS to uncover specific N-glycan or glycan structural motifs associated with cancerous tissue regions. Initial investigations into N-glycosylation in normal, healthy pancreas tissues revealed previously undocumented high-mannose N-glycans associated with acinar regions. It is possible that the presence of these glycans, which are heavily associated with protein folding, is a function of the

secretory nature of the pancreas, where digestive enzymes are synthesized, packaged and secreted in large quantities. Accordingly, protein translation and folding – and concomitantly the high-mannose glycans critical to these events – may be elevated at baseline when compared to other organ tissues. Another novel finding was the detection of sulfated, terminally galactosylated N-glycans specific to pancreatic Islets of Langerhans. These unique structures had not been detected in previous N-glycan analyses of pancreatic nor other cancers by our group and warrant further investigation.

Although pancreatic cancer tissues were used during the prior development of N-glycan IMS workflows in our lab, conclusions from those analyses were towards characterization of the method and not the disease itself. Thus, ours represents a first-of-its-kind study to spatially profile the N-glycome in PDAC. The analyses revealed increased N-glycan branching, fucosylation, sialylation and bisecting GlcNAc residues in pancreatic cancer tissue regions as compared to normal adjacent tissue. This data is consistent with the literature, where altered expression of the glycosyltransferases responsible for the above motifs is well characterized in PDAC[239–242]. While some of these findings are not novel for the study of pancreatic cancer in general, they have never before been linked directly to tumor tissue via a comprehensive spatial analysis.

What is novel, however, is the link between N-glycosylation and pancreatic cancer biomarkers explored by this study. Although we could not directly detect the CA19-9 or sTRA epitopes as part of the N-glycans analyzed by IMS, we did conclude that multiply branched N-glycans with both core and outer arm

fucosylation were significantly associated with CA19-9-expressing tumor tissue cores in the tissue microarrays. sTRA-expressing cores tended to have less branched N-glycans which lacked outer arm fucosylation. Whether or not these N-glycans host CA19-9 and sTRA motifs in pancreatic cancer remains an open question. Critically, we were able to translate our findings into a multi-marker panel by combining 11 differentially expressed N-glycan analytes with biomarker immunofluorescence data. Models using this panel as a data source outperformed models using IMS or IF data alone in discriminating between pancreatic cancer tissue cores and adjacent normal cores. This work, along with other projects from out lab, highlights the potential of N-glycan imaging mass spectrometry as a tool for biomarker discovery. Moreover, the novel combination of orthogonal glycan analyses in this study shows the utility of glycans in general as prognosticators of disease in pancreatic cancer.

6.2.2 Limitations

As discussed in Chapter 3, one of the greatest limitations to our study was the enormous structural complexity of the N-glycans present in the pancreatic cancer tissues. Every major feature of N-glycosylation was represented in our dataset, including sialyation, core fucosylation, outer arm fucosylation, branching, bisecting GlcNAc, polylactosamine extensions, terminal HexNAc and sulfation. We addressed fucosylation isomers through the use of EndoF3, which determined that most structures containing one or more fucose were core fucosylated. The precise assignment of outer arm fucose residues to specific termini, however, is not currently possible using traditional N-glycan IMS workflows. The use of ion-mobility

separated mass spectrometers in the future may deconvolute some of this complexity, although more must be understood about the behavior of fucosylated glycans in these instruments. By stabilizing sialic acids with Wuhrer's amidation reactions, we were able to evaluate linkage isomer expression in our tissues. Unfortunately, this workflow reduced overall N-glycan signal in the treated tissues and led to the spectral overlap of analytes, inspiring our later developmental work in Chapters 4 and 5.

An additional challenge was the analysis of high mass N-glycans in this study. Our imaging mass spectrometry methods were designed for optimal signal intensity across the nominal N-glycan mass range (~m/z 700 – 4000), however higher mass glycans ranging above m/z 10000 have been detected in other studies[479]. These ultra-large N-glycans are particularly relevant to the study of cancer, as the overexpression of fucosylation and polylactosamine-creating enzymes in malignant tissues may drive their synthesis. The instrument and method optimization required to reliably detect high mass glycans was beyond the scope of this study, however future investigations should focus on these understudied species. Here, chemical derivatization and secondary laser positronization instrumentation approaches would be useful[205,479].

A final limitation of this study was the lack of clinical information supplied with the sample cohort. Although basic metrics like age, race, biological sex, disease stage and histological characteristics were provided, detailed recurrence and survival data was absent for most patients. Without these features, we could not associate the detection of specific glycans or glycan phenotypes with patient

survival and therefore could not draw many biological conclusions about the impact of glycosylation themes recognized by this study on patient outcomes. Additionally, we would have been eager to incorporate associated clinical data like BMI, comorbidities, socioeconomic background and other factors into our modeling, which in many cases has been shown to improve the sensitivity and specificity of disease detection[480]. Overall, a follow up study in a larger patient cohort with more complete clinical information may be warranted.

6.2.3 Future Directions

There are two main directions in which this research could be furthered to enhance N-glycan-based detection of pancreatic cancer. Firstly, while our comparison between normal pancreatic tissue and cancerous tissue was suitable to highlight cancer-associated N-glycan alterations, a more apt comparison for early detection efforts would include a pancreatitis patient cohort. By studying the progression from normal pancreas to the chronic inflammatory state of pancreatitis through to malignant disease, we could better understand the glycobiological hallmarks and drivers of this transformation. More critically, N-glycan changes associated with the transition from chronic pancreatitis to pancreatic cancer could be used as biomarkers for earlier detection of the disease. Although less than 10% of pancreatic cancers are thought to arise from chronic pancreatitis, this patient population is under constant surveillance for the neoplastic progression of their disease into early stage PDAC[33]. Accordingly, N-glycan changes discovered by future analyses of the CP $\rightarrow$ PDAC evolution could be translated into more

impactful biomarkers in a smaller, more disease prone population which is already being routinely monitored.

The second major research direction that should be pursued in light of this study is the link between N-glycans in PDAC tumors and serum N-glycosylation in pancreatic cancer patients. The relationship between these two N-glycomes is complex. Over 90% of serum proteins are hepatic in origin, meaning that N-glycan motifs detected in the blood of PDAC patients are not likely to have originated in the tumor but rather are a hepatic glycosylation response to the immune system's fight against the tumor. Pancreatic tumors have, however, been shown to leak proteins into the circulation, thus depletion approaches targeted towards the more common serum proteins may reveal low abundance glycoproteins which could be linked directly to the disease. Circulating tumor cells are another attractive target in pancreatic cancer, where glycosylation changes in these cells are immediately representative of tumor glycobiology. Our biofluid N-glycan profiling approach outlined in Chapter 4 and a novel method for slide-based capture and analysis of specific cell types being developed in our labs are directly applicable to these ends and are being pursued. The accessibility and minimal invasiveness of biofluid collection means that N-glycan PDAC markers found in this matrix could be directly translated into a clinical diagnostic application. Whether hepatic or pancreatic in origin, surveilling serum N-glycan changes in pancreatic and other cancers is the ultimate thrust of our long-term clinical research efforts.

6.3 Sialic Acid Derivatization by AAXL and AAN₃

6.3.1 Conclusions

Aim 2 of this dissertation was divided into two main parts: 1) the development of click chemistry-compatible sialic acid derivatization schemes and 2) advanced bioorthogonal applications of these reactions. The development and publication of our azide and alkyne-based labeling techniques was the focus of Chapter 4. These methods, based on a substantial body of knowledge, integrate α2,3-linked sialic acid lactone amidation reactions and bioorthogonal sugar azide labeling to produce a multi-functional set of sialic acid-targeted tools with applications for N-glycan imaging mass spectrometry and histochemical staining. At their most reductive functions, the AAXL and AAN₃ reactions introduce favorable mass shifts in α2,3 and α2,6-linked sialic acids facilitated by the differential stereochemistry between isomers. The small alkyne handle installed through use of a propargylamine reagent by AAXL is ideally suited for imaging mass spectrometry experiments, as its low molecular weight means that labeled glycans remains spectrally close to their original underivatized *m/z*. AAXL was able to distinguish between α2,3 and α2,6-sialylated N-glycans in FFPE tissues, clinical biofluids, and cultured cells in IMS experiments. Because of the robustness of our protocol and its demonstrated performance for labeling *in solution*, we foresee utility for AAXL in liquid chromatography and electrospray ionization mass spectrometry experiments as well.

In terms of bioorthogonal functionality, the short alkyne handle installed by AAXL is unable to penetrate the aqueous click chemistry reagents and showed

inconsistent labeling of α2,3 and α2,8-sialylated glycans by DAB histochemistry. Conversely, in the AAN$_3$ reaction, the PEG$_3$ linker separating the NH$_2$-PEG$_3$-N$_3$ derivatization reagent extends the azide handle well away from the hydrophobic tissue surface, thereby making it much more receptive to click biotinylation. Consequently, AAN$_3$ is much better suited for bioorthogonal conjugation of imaging reporters, as demonstrated by our streptavidin-peroxidase staining experiments.

An advantage of our protocols is that unlike traditional bioorthogonal approaches, they do not rely on the metabolic incorporation of azido sugars by the biological machinery of living systems for their click chemistry functionality[429,432,435]. Thus, our labeling approaches are suitable for formalin fixed clinical tissue specimens meaning there are potentially millions of stockpiled samples which can be analyzed. Additionally, the compatibility of our systems with patient biofluids opens up the possibility that they may one day see clinical implementation. To this end, a final strength of the AAXL and AAN$_3$ reactions is their simplicity. Many chemical labeling approaches targeting sialic acids require lengthy, even overnight, incubations in various expensive reactants and considerable post-reaction clean up[384]. In contrast, our syntheses add only 4 hours of sample preparation time to a traditional N-glycan IMS workflow. Despite the brevity of our reactions, AAXL and AAN$_3$ routinely manage upwards of 90% labeling efficiency in FFPE tissues. Furthermore, the reagents for AAXL and AAN$_3$ are cheap, commercially available and are well-characterized components of more established chemical labeling approaches. These propargylamine and azido-PEG$_3$-amine reaction components are key to the synergism between the two

workflows, which differ only in the secondary derivatization reagent used. The result is an effectively tunable chemistry, where the substitution of one reagent for the other changes the downstream readout or capability. Collectively, these features would allow an unskilled operator to carry out our labeling reactions, potentiating their in-clinic implementation for the analysis of sialic acid isomers in patient samples.

6.3.2 Limitations

In an ideal scenario, the imaging data from AAXL-based IMS and AAN₃-based staining would be co-registered for deeper biological insights. A challenge to their integration, however, is the specificity of the sialylated readouts generated by each approach. AAXL-treated tissues are integrated into our group's N-glycan imaging mass spectrometry workflow, which relies on the use of an N-glycan specific enzyme. Thus, only sialic acids on N-linked glycans are detected and differentiated by IMS in this analysis. In contrast, AAN₃-enabled biotinylation and histochemical staining is indifferent to the glycan carrier of the labeled sialic acid, which occur naturally on N-linked and O-linked glycans as well as on glycolipids[394]. Consequently, AAN₃-HC recognizes more sialylated biomolecules than does AAXL IMS, which detects only the subset attached to N-glycans. In integrating the data through image coregistration, it is currently impossible to distinguish whether the sialylated N-glycans visualized by AAXL-enabled IMS correspond to those molecules visualized by AAN₃-enabled histochemistry. Similar IMS workflows to ours for N-glycans utilizing O-glycan-specific release agents are being developed, which may help resolve some of this complexity.

A related issue arises when trying to determine whether an AAXL or AAN$_3$-labeled sialic acid observed by IMS or histochemistry is in the α2,3 or α2,8 configuration, which are identically labeled by both syntheses. Currently, our reactions – as well as other approaches in the field – are not designed to resolve this population. The stereochemical positions of the carboxylate group in α2,3 and α2,8 linkages both favor internal lactonization during the first amidation step[427,477,481]. In order to distinguish between the two, new chemical reactions which are not based on ring-opening aminolysis must be created. Alternatively, this issue is can be solved by the use of isomer-specific sialidases to clear the tissue of one isomeric linkage or another prior to labeling and staining, leaving only α2,3 or α2,8-linked species for analysis. Nevertheless, the study of α2,8-sialylated molecules remains challenging.

The chemistry upon which our syntheses are based is well characterized, and we have confirmed the specificity of both AAXL and AAN$_3$ derivatization by NMR analysis at multiple steps along the reaction pathway. In addition, we have demonstrated that both methods label their sialylated targets with greater than 90% efficiency, giving us confidence that the data they generate is truly representative of the natural sialylation state of the tissue, cell or biofluid sample. Our confidence notwithstanding, orthogonal confirmation by another sialic acid isomer characterization method would be advisable. Recent experiments in our working group using AAXL are being verified by LC-MS/MS and we expect this data to align with ours.

6.3.3 Future Directions

A goal of ours moving forward is to streamline AAXL and AAN$_3$ into a single synthesis capable of both imaging mass spectrometry visualization and click-enabled biotinylation. As previously described, AAXL uses a propargylamine handle which is small and ionizes well, making it ideal for IMS applications. The proximity of this alkyne handle to the surface of the tissue, unfortunately, limits its use for click chemistry, as it generally fails to enter the aqueous milieu of the click reaction. Concomitantly, AAN$_3$'s azide handle is stereochemically-extended from the tissue surface via a PEG linker and thus is extremely sensitive to click-biotinylation. The high molecular weight of the NH$_2$-PEG$_3$-N$_3$ label in AAN$_3$, however, leads to less-efficient ionization of AAN$_3$-labeled glycans and restricts its utility for IMS experiments. This unresolved dichotomy not only results in a more labor-intensive sample preparation when both IMS and histochemical applications are desired, but also presents a major challenge to the integration of these data. Because AAXL and AAN$_3$ covalently label their target sialic acids, it is not possible to perform both syntheses on the same tissue section. Thus, serial tissue sections must be utilized, which complicates the coregistration of IMS and HC data. We concede that a single, bifunctional synthesis would be more ideal than two with singular functionality. Designing such a system requires exploring alternative click-compatible handles. An ideal label would be of low molecular weight, ionizes efficiently and generates stereochemical distance between the sialic acid and the click-handle. One possible class of molecules that satisfy these requirements are amine-azides (or amine-alkynes) separated by a cleavable linker[452,453]. In theory,

a cleavable linker strategy would work as follows: 1) α2,3 and α2,8 sialic acids would be derivatized with the cleavable azide, biotinylated by click chemistry and histochemically stained then 2) the molecule would be enzymatically or photochemically severed, leaving behind a small mass tag which would label these sialic aids for separation by imaging mass spectrometry. Thus, we could generate multiple datasets from the same tissue which would perfectly co-register, providing deeper biological insight into the sialobiology of our sample. Accordingly, our group is currently pursuing these such reagents as the next generation replacement for the syntheses presented here.

6.4 Advanced Glycomic Studies with SABER and SAFER

6.4.1 Conclusions

Chapter 5 of this dissertation focused on the development of two novel extensions of the AAN_3 azide derivatization approach. Termed SAFER and SABER, these applications allow for the fluorescent labeling and solid phase enrichment, respectively, of α2,3 and α2,8-linked glycoconjugates. The sialic acid fluorescent enhancement reaction (SAFER) uses the AAN_3 and click-installed biotin on α2,3 and α2,8 sialic acid isomers to capture a streptavidin-fluorochrome dye so that these molecules can be visualized by fluorescence microscopy. In FFPE tissues, we showed that SAFER staining could highlight sialylation differences between morphologically separated PDAC tumors, align with other histological images to correlate sialic acid expression to immune cell type and reveal α2,3 and α2,8 sialic acid isomer increases in diseased glomeruli. Further, we demonstrated SAFER staining in cultured pancreatic cell lines which showed

differential sialic acid expression phenotypes as visualized by our system. SAFER is quantifiable in both FFPE tissue and cell culture analyses and with further development, including the use of cell membrane markers, may be able to quantitate sialylation in single cell experiments. The defining feature of SAFER is the ability to generate isomer-specific readouts, making it unique amongst a field of other sialic acid fluorescent detection methods which forgo this selectivity in favor of pan-sialic acid labeling. We expect that with optimization, SAFER can integrate into more traditional immunofluorescence experiments at the point of secondary incubation, allowing the visualization of α2,3 and α2,8-sialylated glycans alongside other markers.

The sialic acid bead enrichment reaction (SABER) we developed relies on biotin affinity capture as does SAFER, where AAN_3-derivitzed, click-biotinylated sialylated glycoconjugates are retained from the total protein matrix through the use of an immobilized streptavidin resin. SABER-enriched α2,3 and α2,8-sialoproteins can then be digested on-bead and the resulting peptides analyzed by LC-MS/MS. Our proof-of-concept experiment using this system was able to identify over 100 proteins, as compared to 700+ in a non-enriched sample. A significant subset of the enriched proteins were also identified in the non-enriched data, however 35 were unique to the SABER. Although preliminary, this result suggests that SABER may be able to enrich low-abundance sialoproteins which are normally lost in the "proteomic noise" when analyzing a non-enriched sample. Label-free quantification of our data showed a number of proteins which were significantly enriched in the SABER sample as compared to the untreated control. Once again,

SABER's most unique strength is its ability to be isomer-selective, which sets it apart from other glycan enrichment approaches that retain sialylated glycoproteins in bulk. As we further refine SABER, we hope to increase the number of identified proteins while streamlining the workflow. A fully developed SABER may deepen our understanding of the protein carriers of α2,3 and α2,8-linked sialic acids and better define their glycobiological functions.

6.4.2 Limitations

As described for AAXL and AAN$_3$, SAFER is limited in its ability to distinguish α2,3 and α2,8-linked sialic acid isomers, which are identically derivatized and biotinylated by the AAN$_3$-click chemistry reactions. This obstacle can be overcome by the use of α2,3 or α2,8-specific sialidases to clear a particular isomer from the tissue prior to imaging, however there may be a cleverer approach that allows both isomers to be imaged and delineated in the same experiment. α2,8 sialic acids occur naturally as part of α2,8 and α2,9-linked polysialic acid chains, with a degree of polymerization ranging from as few as 8 units to over 400[482]. Each α2,8 linkage in this chain serves as a possible installation point for an azide handle, biotin alkyne and streptavidin dye molecule during SAFER staining, meaning each polysialic acid chain could contain tens to hundreds of fluorochromes. Accordingly, a polysialic acid-containing glycan may be substantially brighter during fluorescent excitation than glycans modified with α2,3-linked sialic acids, which are limited by the number of possible attachment points on any given N- or O-linked glycan. With the use of techniques like single-molecule localization super-resolution microscopy[483], it may be feasible to observe individual

α2,3 and α2,8-sialylated glycoconjugates and distinguish them by their fluorescent signal intensity via a thresholding function. Although this approach would require significant optimization of SAFER including the use of new dyes, advanced microscopy systems, sialic acid standards and novel data analysis tools, the specific discrimination between α2,3 and α2,8-sialylation using SAFER as a technological base is theoretically possible.

As it stands today, SABER has two major areas for improvement. Firstly, the number of protein identifications from our samples were low, slightly over 100 in the enriched sample and 700+ in the untreated sample. This is in comparison to other studies which are able to identify thousands of proteins from a single FFPE tissue sections using specialized digestion and separation procedures[484,485]. Currently, we are aiming to increase the number of identifications by increasing the amount of AAN$_3$-derivatized, click-biotinylated starting material. A recent experiment using the pooled material from pancreatic cancer cells grown and derivatized on four glass slides was able to identify over 1000 SABER-enriched proteins. In a similar fashion, combining serial FFPE tissue sections should boost downstream peptide signal intensity leading to a greater number of protein IDs. Another explanation for the low number of identified proteins is that the AAN$_3$ derivatization reaction is expected to amidate carboxylate-containing protein groups as well as α2,6 sialic acids, where the + 27 Da mass shift is likely to confuse the search algorithm. By including static dimethylamide modifications on glutamic acid (Glu), aspartic acid (Asp) and C-terminal amino acids in our search

parameters, we may be able to increase the number of peptides detected and thus protein identifications.

A second limitation of SABER was discovered in our data analysis, where several non-glycoproteins were identified in the enriched dataset. These proteins, including gamma-enteric smooth muscle actin, hornerin, histone family proteins and lipocalin, amongst others, do not contain N- or O-linked glycan sites as currently understood. There are a few explanations as to why these proteins might be enriched by SABER. Firstly, it is likely that these non-glycoproteins may be binding non-specifically to either the immobilized streptavidin or the resin particles themselves. Characterization studies have shown that various commercially available bead materials in combination with different streptavidin formats have disparate binding capacities, where some resins are able to retain non-biotinylated molecules[486]. Experimenting with different resin products and optimization of binding and washing steps may be able to reduce this non-specific binding in further iterations of SABER. Secondly, it is possible that the non-glycosylated proteins in our enriched samples are being retained in complex with the sialylated proteins we enrich for. The binding and wash buffers used for affinity capture are mild, and likely are not astringent enough to disrupt protein-protein interactions. By tailoring buffer strength, we may be able to dissociate these complexes and retain only sialylated glycoproteins, however there is a risk of disrupting biotin-avidin interactions under harsher conditions. Ultimately, if these non-glycosylated proteins are shown to be in complex with our enriched sialoproteins, this feature

of SABER might one day be considered a strength, leading to interaction proteomics applications after further optimization.

6.4.3 Future Directions

Each method has areas for improvement, optimization and application. Both are in their infancy, requiring more development work to characterize their specificity, accuracy, precision, limits of detection and quantification and robustness amongst other factors. The initial experiments with both SABER and SAFER are meant to be the starting point for establishing standardized protocols and the eventual publication of a methods paper to highlight the downstream capabilities of AAN_3. Their recency notwithstanding, the preliminary data generated by both SAFER and SABER suggests exciting new research opportunities ahead.

As previously mentioned, a major developmental milestone for SAFER would be implementation in traditional immunofluorescence workflows alongside other fluorescent markers. Our current data suggests that SAFER staining images can be co-registered with other optical imaging data, however performing SAFER and immunostaining in the same experiment could show direct colocalization between α2,3 and α2,8 linked glycoconjugates and hundreds of potential molecules of interest. This data could lead to discoveries of the protein carriers of these sialic isomers or the molecules with which they interact, amongst other potential insights. The number of molecules identified in a single experiment is typically limited by spectral overlap between fluorophores, however with multi-

round immunofluorescence techniques like the one demonstrated in Chapter 3, tens of markers could be imaged[215,399]. In combination with new machine learning tools for cellular segmentation and identification[487], SAFER could one day be used to gain deep biological context into cell-type specific α2,3 and α2,8 sialic acid isomer expression and the roles which these cells play in their biological neighborhoods.

The initial enrichment strategy for SABER identified only the trypsin-digested peptides for captured glycoproteins, however the sialic-acid modified peptides remained bound to the beads. Thus, critical biological information regarding glycan site occupation and the types of sialylated glycans in our samples was lost. Two future iterations of SABER could be imagined, one which releases the peptide from the glycan and one which releases the biotinylated glycopeptide from the streptavidin resin. The simpler of these two approaches, analytically, would be to chemically or enzymatically cleave the N- or O-linked glycan containing the derivatized sialic acid from the remaining peptide which it modified. In doing so, we could map the released peptides back to their full protein sequences identified from the tryptic digest and determine the exact site at which these proteins were α2,3 or α2,8 sialylated. While more straightforward, this approach would still fail to determine the specific sialic-acid modified glycans in our sample. Alternatively, astringent washes could be used to dissociate the biotin-streptavidin interaction and release the sialylated glycopeptides from the beads. Released glycopeptides could then be analyzed via an intact glycopeptide strategy[488], which may be aided by using derivatization and biotinylation of α2,3

and α2,8 sialic acids as a mass tag to refine downstream searching and ID. These glycan modifications would likely be hyper-variable between peptides and even on the individual glycan site itself, requiring significant computational effort to ensure confident identifications. Nevertheless, SABER has the potential to characterize the specific sialic acid-containing glycan, localized to a specific glycan site on a specific protein, with further development.

6.5 Final Thoughts

Collectively, the work presented in this dissertation was a journey of discovery, where insights from our N-glycan analysis of pancreatic cancer led to the development of novel tools for the separation and characterization of glycan isomers. Each major section of this dissertation offers key advancements in their respective research areas. We demonstrated improved detection of PDAC through the integration of N-glycan IMS and biomarker IF in Chapter 3. In Chapter 4, new sialic-acid specific derivatization reactions were established which showed utility for IMS and histochemical staining of cultured cells, FFPE tissues and clinical biofluids. Finally, advanced bioorthogonal applications for fluorescent labeling and selective enrichment of sialylated glycoconjugates were presented in Chapter 5. Ultimately, the work outlined herein may lead to the discovery of novel carbohydrate biomarkers with therapeutic or early detection potential in pancreatic cancer and other diseases.

REFERENCES

(1)   Bastidas-Ponce, A.; Scheibner, K.; Lickert, H.; Bakhti, M. Cellular and Molecular Mechanisms Coordinating Pancreas Development. *Development (Cambridge)*. Company of Biologists Ltd August 15, 2017, pp 2873–2888. https://doi.org/10.1242/dev.140756.

(2)   Pandol, S. J. Regulation of Whole-Organ Pancreatic Secretion. In *The Exocrine Pancreas*; Morgan & Claypool Life Sciences, 2010. https://doi.org/10.4199/C00026ED1V01Y201102ISP014.

(3)   Reichert, M.; Rustgi, A. K. Pancreatic Ductal Cells in Development, Regeneration, and Neoplasia. *Journal of Clinical Investigation*. American Society for Clinical Investigation December 1, 2011, pp 4572–4578. https://doi.org/10.1172/JCI57131.

(4)   McClean, P.; Weaver, L. T. Ontogeny of Human Pancreatic Exocrine Function. *Arch. Dis. Child.* **1993**, *68* (1 Spec No), 62. https://doi.org/10.1136/ADC.68.1_SPEC_NO.62.

(5)   Yamaoka, T.; Itakura, M. Development of Pancreatic Islets (Review). *Int. J. Mol. Med.* **1999**, *3* (3), 247–261. https://doi.org/10.3892/IJMM.3.3.247/HTML.

(6)   Da Silva Xavier, G. The Cells of the Islets of Langerhans. *J. Clin. Med.* **2018**, *7* (3), 54. https://doi.org/10.3390/jcm7030054.

(7)   Rorsman, P.; Huising, M. O. The Somatostatin-Secreting Pancreatic δ-Cell in Health and Disease. *Nature Reviews Endocrinology*. Nature Publishing Group July 1, 2018, pp 404–414. https://doi.org/10.1038/s41574-018-0020-6.

(8)   Lonovics, J.; Devitt, P.; Watson, L. C.; Rayford, P. L.; Thompson, J. C. Pancreatic Polypeptide: A Review. *Arch. Surg.* **1981**, *116* (10), 1256–1264. https://doi.org/10.1001/ARCHSURG.1981.01380220010002.

(9)   Sato, T.; Nakamura, Y.; Shiimura, Y.; Ohgusu, H.; Kangawa, K.; Kojima, M. Structure, Regulation and Function of Ghrelin. *J. Biochem.* **2012**, *151* (2), 119–128. https://doi.org/10.1093/JB/MVR134.

(10)   Adamska, A.; Domenichini, A.; Falasca, M. Pancreatic Ductal Adenocarcinoma: Current and Evolving Therapies. *International Journal of Molecular Sciences*. MDPI AG July 1, 2017. https://doi.org/10.3390/ijms18071338.

(11)   Siegel, R. L.; Miller, K. D.; Jemal, A. Cancer Statistics, 2020. *CA. Cancer J. Clin.* **2020**, *70* (1), 7–30. https://doi.org/10.3322/caac.21590.

(12)   Sung, H.; Ferlay, J.; Siegel, R. L.; Laversanne, M.; Soerjomataram, I.; Jemal, A.; Bray, F. Global Cancer Statistics 2020: GLOBOCAN Estimates

of Incidence and Mortality Worldwide for 36 Cancers in 185 Countries. *CA. Cancer J. Clin.* **2021**, *71* (3), 209–249. https://doi.org/10.3322/CAAC.21660.

(13) Rawla, P.; Sunkara, T.; Gaduputi, V. Epidemiology of Pancreatic Cancer: Global Trends, Etiology and Risk Factors. *World J. Oncol.* **2019**, *10* (1), 10. https://doi.org/10.14740/WJON1166.

(14) Ma, J.; Siegel, R.; Jemal, A. Pancreatic Cancer Death Rates by Race Among US Men and Women, 1970–2009. *JNCI J. Natl. Cancer Inst.* **2013**, *105* (22), 1694–1700. https://doi.org/10.1093/JNCI/DJT292.

(15) Bosetti, C.; Bertuccio, P.; Negri, E.; La Vecchia, C.; Zeegers, M. P.; Boffetta, P. Pancreatic Cancer: Overview of Descriptive Epidemiology. *Mol. Carcinog.* **2012**, *51* (1), 3–13. https://doi.org/10.1002/MC.20785.

(16) Ushio, J.; Kanno, A.; Ikeda, E.; Ando, K.; Nagai, H.; Miwata, T.; Kawasaki, Y.; Tada, Y.; Yokoyama, K.; Numao, N.; Tamada, K.; Lefor, A. K.; Yamamoto, H. Pancreatic Ductal Adenocarcinoma: Epidemiology and Risk Factors. *Diagnostics 2021, Vol. 11, Page 562* **2021**, *11* (3), 562. https://doi.org/10.3390/DIAGNOSTICS11030562.

(17) Hidalgo, M.; Cascinu, S.; Kleeff, J.; Labianca, R.; Löhr, J. M.; Neoptolemos, J.; Real, F. X.; Van Laethem, J. L.; Heinemann, V. Addressing the Challenges of Pancreatic Cancer: Future Directions for Improving Outcomes. *Pancreatology* **2015**, *15* (1), 8–18. https://doi.org/10.1016/J.PAN.2014.10.001.

(18) Pittman, M. E.; Rao, R.; Hruban, R. H. Classification, Morphology, Molecular Pathogenesis, and Outcome of Premalignant Lesions of the Pancreas. *Arch. Pathol. Lab. Med.* **2017**, *141* (12), 1606–1614. https://doi.org/10.5858/arpa.2016-0426-RA.

(19) Basturk, O.; Hong, S. M.; Wood, L. D.; Adsay, N. V.; Albores-Saavedra, J.; Biankin, A. V.; Brosens, L. A. A.; Fukushima, N.; Goggins, M.; Hruban, R. H.; Kato, Y.; Klimstra, D. S.; Klöppel, G.; Krasinskas, A.; Longnecker, D. S.; Matthaei, H.; Offerhaus, G. J. A.; Shimizu, M.; Takaori, K.; Terris, B.; Yachida, S.; Esposito, I.; Furukawa, T. A Revised Classification System and Recommendations from the Baltimore Consensus Meeting for Neoplastic Precursor Lesions in the Pancreas. In *American Journal of Surgical Pathology*; Lippincott Williams and Wilkins, 2015; Vol. 39, pp 1730–1741. https://doi.org/10.1097/PAS.0000000000000533.

(20) M, D.; D, A.; J, W.; C, P.; R, G. Precursor Lesions for Sporadic Pancreatic Cancer: PanIN, IPMN, and MCN. *Biomed Res. Int.* **2014**, *2014*. https://doi.org/10.1155/2014/474905.

(21) Haeberle, L.; Esposito, I. Pathology of Pancreatic Cancer. *Translational Gastroenterology and Hepatology*. AME Publishing Company 2019. https://doi.org/10.21037/tgh.2019.06.02.

(22)   Allen, P. J.; Kuk, D.; Castillo, C. F. Del; Basturk, O.; Wolfgang, C. L.; Cameron, J. L.; Lillemoe, K. D.; Ferrone, C. R.; Morales-Oyarvide, V.; He, J.; Weiss, M. J.; Hruban, R. H.; Gönen, M.; Klimstra, D. S.; Mino-Kenudson, M. Multi-Institutional Validation Study of the American Joint Commission on Cancer (8th Edition) Changes for Tand N Staging in Patients with Pancreatic Adenocarcinoma. *Ann. Surg.* **2017**, *265* (1), 185–191. https://doi.org/10.1097/SLA.0000000000001763.

(23)   Cong, L.; Liu, Q.; Zhang, R.; Cui, M.; Zhang, X.; Gao, X.; Guo, J.; Dai, M.; Zhang, T.; Liao, Q.; Zhao, Y. Tumor Size Classification of the 8th Edition of TNM Staging System Is Superior to That of the 7th Edition in Predicting the Survival Outcome of Pancreatic Cancer Patients after Radical Resection and Adjuvant Chemotherapy. *Sci. Rep.* **2018**, *8* (1). https://doi.org/10.1038/s41598-018-28193-4.

(24)   Wang, H.; Liu, J.; Xia, G.; Lei, S.; Huang, X.; Huang, X. Survival of Pancreatic Cancer Patients Is Negatively Correlated with Age at Diagnosis: A Population-Based Retrospective Study. *Sci. Rep.* **2020**, *10* (1), 1–9. https://doi.org/10.1038/s41598-020-64068-3.

(25)   Maisonneuve, P.; Lowenfels, A. B. Risk Factors for Pancreatic Cancer: A Summary Review of Meta-Analytical Studies. *Int. J. Epidemiol.* **2015**, *44* (1), 186–198. https://doi.org/10.1093/IJE/DYU240.

(26)   Majumder, S.; Chari, S. T. Chronic Pancreatitis. *Lancet* **2016**, *387* (10031), 1957–1966. https://doi.org/10.1016/S0140-6736(16)00097-0.

(27)   Forsmark, C.; Pham, A. Chronic Pancreatitis: Review and Update of Etiology, Risk Factors, and Management [Version 1; Referees: 2 Approved]. *F1000Research*. F1000 Research Ltd 2018, p 607. https://doi.org/10.12688/f1000research.12852.1.

(28)   Saluja, A.; Dudeja, V.; Dawra, R.; Sah, R. P. Early Intra-Acinar Events in Pathogenesis of Pancreatitis. *Gastroenterology* **2019**, *156* (7), 1979–1993. https://doi.org/10.1053/J.GASTRO.2019.01.268.

(29)   Inman, K. S.; Francis, A. A.; Murray, N. R. Complex Role for the Immune System in Initiation and Progression of Pancreatic Cancer. *World J. Gastroenterol.* **2014**, *20* (32), 11160. https://doi.org/10.3748/WJG.V20.I32.11160.

(30)   Zheng, L.; Xue, J.; Jaffee, E. M.; Habtezion, A. Role of Immune Cells and Immune-Based Therapies in Pancreatitis and Pancreatic Ductal Adenocarcinoma. *Gastroenterology* **2013**, *144* (6), 1230–1240. https://doi.org/10.1053/J.GASTRO.2012.12.042.

(31)   Whitcomb, D. C. Inflammation and Cancer: V. Chronic Pancreatitis and Pancreatic Cancer. *Am. J. Physiol. - Gastrointest. Liver Physiol.* **2004**, *287* (2 50-2). https://doi.org/10.1152/AJPGI.00115.2004/ASSET/IMAGES/LARGE/ZH30

080417510001.JPEG.

(32) Pinho, A. V.; Chantrill, L.; Rooman, I. Chronic Pancreatitis: A Path to Pancreatic Cancer. *Cancer Lett.* **2014**, *345* (2), 203–209. https://doi.org/10.1016/J.CANLET.2013.08.015.

(33) Dhar, P.; Kalghatgi, S.; Saraf, V. Pancreatic Cancer in Chronic Pancreatitis. *Indian J. Surg. Oncol.* **2015**, *6* (1), 57. https://doi.org/10.1007/S13193-014-0373-9.

(34) Everhart, J.; Wright, D. Diabetes Mellitus as a Risk Factor for Pancreatic Cancer: A Meta-Analysis. *JAMA* **1995**, *273* (20), 1605–1609. https://doi.org/10.1001/JAMA.1995.03520440059037.

(35) Kahn, S. E. The Relative Contributions of Insulin Resistance and Beta-Cell Dysfunction to the Pathophysiology of Type 2 Diabetes. *Diabetologia* **2003**, *46* (1), 3–19. https://doi.org/10.1007/S00125-002-1009-0/FIGURES/8.

(36) Dooley, J.; Tian, L.; Schonefeldt, S.; Delghingaro-Augusto, V.; Garcia-Perez, J. E.; Pasciuto, E.; Di Marino, D.; Carr, E. J.; Oskolkov, N.; Lyssenko, V.; Franckaert, D.; Lagou, V.; Overbergh, L.; Vandenbussche, J.; Allemeersch, J.; Chabot-Roy, G.; Dahlstrom, J. E.; Laybutt, D. R.; Petrovsky, N.; Socha, L.; Gevaert, K.; Jetten, A. M.; Lambrechts, D.; Linterman, M. A.; Goodnow, C. C.; Nolan, C. J.; Lesage, S.; Schlenner, S. M.; Liston, A. Genetic Predisposition for Beta Cell Fragility Underlies Type 1 and Type 2 Diabetes. *Nat. Genet. 2016 485* **2016**, *48* (5), 519–527. https://doi.org/10.1038/ng.3531.

(37) Andersen, D. K.; Korc, M.; Petersen, G. M.; Eibl, G.; Li, D.; Rickels, M. R.; Chari, S. T.; Abbruzzese, J. L. Diabetes, Pancreatogenic Diabetes, and Pancreatic Cancer. *Diabetes* **2017**, *66* (5), 1103–1110. https://doi.org/10.2337/DB16-1477.

(38) Momi, N.; Kaur, S.; Krishn, S. R.; Batra, S. K. Discovering the Route from Inflammation to Pancreatic Cancer. *Minerva Gastroenterol. Dietol.* **2012**, *58* (4), 283.

(39) Cui, Y.; Andersen, D. K.; Cui, Y.; Andersen, D. K. Diabetes and Pancreatic Cancer. *Endocr. Relat. Cancer* **2012**, *19* (5), F9–F26. https://doi.org/10.1530/ERC-12-0105.

(40) Pannala, R.; Leirness, J. B.; Bamlet, W. R.; Basu, A.; Petersen, G. M.; Chari, S. T. Prevalence and Clinical Profile of Pancreatic Cancer–Associated Diabetes Mellitus. *Gastroenterology* **2008**, *134* (4), 981–987. https://doi.org/10.1053/J.GASTRO.2008.01.039.

(41) Onitilo, A. A.; Engel, J. M.; Glurich, I.; Stankowski, R. V.; Williams, G. M.; Doi, S. A. Diabetes and Cancer II: Role of Diabetes Medications and Influence of Shared Risk Factors. *Cancer Causes Control 2012 237* **2012**, *23* (7), 991–1008. https://doi.org/10.1007/S10552-012-9971-4.

(42) Pannala, R.; Basu, A.; Petersen, G. M.; Chari, S. T. New-Onset Diabetes: A Potential Clue to the Early Diagnosis of Pancreatic Cancer. *Lancet Oncol.* **2009**, *10* (1), 88–95. https://doi.org/10.1016/S1470-2045(08)70337-1.

(43) Morani, A. C.; Hanafy, A. K.; Ramani, N. S.; Katabathina, V. S.; Yedururi, S.; Dasyam, A. K.; Prasad, S. R. Hereditary and Sporadic Pancreatic Ductal Adenocarcinoma: Current Update on Genetics and Imaging. *Radiol. Imaging Cancer* **2020**, *2* (2). https://doi.org/10.1148/RYCAN.2020190020/ASSET/IMAGES/LARGE/RY CAN.2020190020.TBL2.JPEG.

(44) Luo, J. KRAS Mutation in Pancreatic Cancer. *Semin. Oncol.* **2021**, *48* (1), 10. https://doi.org/10.1053/J.SEMINONCOL.2021.02.003.

(45) Fan, Z.; Fan, K.; Yang, C.; Huang, Q.; Gong, Y.; Cheng, H.; Jin, K.; Liu, C.; Ni, Q.; Yu, X.; Luo, G. Critical Role of KRAS Mutation in Pancreatic Ductal Adenocarcinoma. *Transl. Cancer Res.* **2018**, *7* (6), 1728–1736. https://doi.org/10.21037/25051.

(46) Waters, A. M.; Der, C. J. KRAS: The Critical Driver and Therapeutic Target for Pancreatic Cancer. *Cold Spring Harb. Perspect. Med.* **2018**, *8* (9). https://doi.org/10.1101/cshperspect.a031435.

(47) Liu, P.; Wang, Y.; Li, X. Targeting the Untargetable KRAS in Cancer Therapy. *Acta Pharmaceutica Sinica B*. Chinese Academy of Medical Sciences September 1, 2019, pp 871–879. https://doi.org/10.1016/j.apsb.2019.03.002.

(48) Eser, S.; Schnieke, A.; Schneider, G.; Saur, D. Oncogenic KRAS Signalling in Pancreatic Cancer. *British Journal of Cancer*. Nature Publishing Group 2014, pp 817–822. https://doi.org/10.1038/bjc.2014.215.

(49) Cohen, R.; Neuzillet, C.; Tijeras-Raballand, A.; Faivre, S.; de Gramont, A.; Raymond, E. Targeting Cancer Cell Metabolism in Pancreatic Adenocarcinoma. *Oncotarget* **2015**, *6* (19), 16832–16847. https://doi.org/10.18632/oncotarget.4160.

(50) Gillson, J.; Ramaswamy, Y.; Singh, G.; Gorfe, A. A.; Pavlakis, N.; Samra, J.; Mittal, A.; Sahni, S. Small Molecule KRAS Inhibitors: The Future for Targeted Pancreatic Cancer Therapy? *Cancers (Basel).* **2020**, *12* (5). https://doi.org/10.3390/cancers12051341.

(51) Bar-Sagi, D.; Knelson, E. H.; Sequist, L. V. A Bright Future for KRAS Inhibitors. *Nat. Cancer* **2020**, *1* (1), 25–27. https://doi.org/10.1038/s43018-019-0016-8.

(52) Ren, B.; Liu, X.; Suriawinata, A. A. Pancreatic Ductal Adenocarcinoma and Its Precursor Lesions: Histopathology, Cytopathology, and Molecular Pathology. *American Journal of Pathology*. Elsevier Inc. January 1, 2019, pp 9–21. https://doi.org/10.1016/j.ajpath.2018.10.004.

(53) Hosoda, W.; Chianchiano, P.; Griffin, J. F.; Pittman, M. E.; Brosens, L. A. A.; Noë, M.; Yu, J.; Shindo, K.; Suenaga, M.; Rezaee, N.; Yonescu, R.; Ning, Y.; Albores-Saavedra, J.; Yoshizawa, N.; Harada, K.; Yoshizawa, A.; Hanada, K.; Yonehara, S.; Shimizu, M.; Uehara, T.; Samra, J. S.; Gill, A. J.; Wolfgang, C. L.; Goggins, M. G.; Hruban, R. H.; Wood, L. D. Genetic Analyses of Isolated High-Grade Pancreatic Intraepithelial Neoplasia (HG-PanIN) Reveal Paucity of Alterations in TP53 and SMAD4. *J. Pathol.* **2017**, *242* (1), 16–23. https://doi.org/10.1002/path.4884.

(54) Jonckheere, N.; Skrypek, N.; van Seuningen, I. Mucins and Pancreatic Cancer. *Cancers.* Multidisciplinary Digital Publishing Institute (MDPI) December 2010, pp 1794–1812. https://doi.org/10.3390/cancers2041794.

(55) Petersen, G. M. Familial Pancreatic Cancer. *Semin. Oncol.* **2016**, *43* (5), 548–553. https://doi.org/10.1053/J.SEMINONCOL.2016.09.002.

(56) Klein, A. P.; Brune, K. A.; Petersen, G. M.; Goggins, M.; Tersmette, A. C.; Offerhaus, G. J. A.; Griffin, C.; Cameron, J. L.; Yeo, C. J.; Kern, S.; Hruban, R. H. Prospective Risk of Pancreatic Cancer in Familial Pancreatic Cancer Kindreds. *Cancer Res.* **2004**, *64* (7), 2634–2638. https://doi.org/10.1158/0008-5472.CAN-03-3823.

(57) Schneider, R.; Slater, E. P.; Sina, M.; Habbe, N.; Fendrich, V.; Matthäi, E.; Langer, P.; Bartsch, D. K. German National Case Collection for Familial Pancreatic Cancer (FaPaCa): Ten Years Experience. *Fam. Cancer* **2011**, *10* (2), 323–330. https://doi.org/10.1007/S10689-010-9414-X/FIGURES/2.

(58) Olakowski, M.; Bułdak, Ł. Current Status of Inherited Pancreatic Cancer. *Hered. Cancer Clin. Pract.* **2022**, *20* (1), 1–11. https://doi.org/10.1186/S13053-022-00224-2/TABLES/4.

(59) Raimondi, S.; Lowenfels, A. B.; Morselli-Labate, A. M.; Maisonneuve, P.; Pezzilli, R. Pancreatic Cancer in Chronic Pancreatitis; Aetiology, Incidence, and Early Detection. *Best Pract. Res. Clin. Gastroenterol.* **2010**, *24* (3), 349–358. https://doi.org/10.1016/J.BPG.2010.02.007.

(60) Van Lier, M. G. F.; Wagner, A.; Mathus-Vliegen, E. M. H.; Kuipers, E. J.; Steyerberg, E. W.; Van Leerdam, M. E. High Cancer Risk in Peutz-Jeghers Syndrome: A Systematic Review and Surveillance Recommendations. *Am. J. Gastroenterol.* **2010**, *105* (6), 1258–1264. https://doi.org/10.1038/AJG.2009.725.

(61) Kastrinos, F.; Mukherjee, B.; Tayob, N.; Wang, F.; Sparr, J.; Raymond, V. M.; Bandipalliam, P.; Stoffel, E. M.; Gruber, S. B.; Syngal, S. Risk of Pancreatic Cancer in Families With Lynch Syndrome. *JAMA* **2009**, *302* (16), 1790–1795. https://doi.org/10.1001/JAMA.2009.1529.

(62) Petrucelli, N.; Daly, M. B.; Pal, T. BRCA1- and BRCA2-Associated Hereditary Breast and Ovarian Cancer. *GeneReviews®* **2022**.

(63) Aoude, L. G.; Wadt, K. A. W.; Pritchard, A. L.; Hayward, N. K. Genetics of

Familial Melanoma: 20 Years after CDKN2A. *Pigment Cell Melanoma Res.* **2015**, *28* (2), 148–160. https://doi.org/10.1111/PCMR.12333.

(64) Goggins, M.; Overbeek, K. A.; Brand, R.; Syngal, S.; Del Chiaro, M.; Bartsch, D. K.; Bassi, C.; Carrato, A.; Farrell, J.; Fishman, E. K.; Fockens, P.; Gress, T. M.; Van Hooft, J. E.; Hruban, R. H.; Kastrinos, F.; Klein, A.; Lennon, A. M.; Lucas, A.; Park, W.; Rustgi, A.; Simeone, D.; Stoffel, E.; Vasen, H. F. A.; Cahen, D. L.; Canto, M. I.; Bruno, M. Management of Patients with Increased Risk for Familial Pancreatic Cancer: Updated Recommendations from the International Cancer of the Pancreas Screening (CAPS) Consortium. *Gut* **2020**, *69* (1), 7. https://doi.org/10.1136/GUTJNL-2019-319352.

(65) Mizrahi, J. D.; Surana, R.; Valle, J. W.; Shroff, R. T. Pancreatic Cancer. *Lancet* **2020**, *395* (10242), 2008–2020. https://doi.org/10.1016/S0140-6736(20)30974-0.

(66) Walter, F. M.; Mills, K.; Mendonça, S. C.; Abel, G. A.; Basu, B.; Carroll, N.; Ballard, S.; Lancaster, J.; Hamilton, W.; Rubin, G. P.; Emery, J. D. Symptoms and Patient Factors Associated with Diagnostic Intervals for Pancreatic Cancer (SYMPTOM Pancreatic Study): A Prospective Cohort Study. *Lancet Gastroenterol. Hepatol.* **2016**, *1* (4), 298–306. https://doi.org/10.1016/S2468-1253(16)30079-6.

(67) Schmidt-Hansen, M.; Berendse, S.; Hamilton, W. Symptoms of Pancreatic Cancer in Primary Care: A Systematic Review. *Pancreas* **2016**, *45* (6), 814–818. https://doi.org/10.1097/MPA.0000000000000527.

(68) Strasberg, S. M.; Gao, F.; Sanford, D.; Linehan, D. C.; Hawkins, W. G.; Fields, R.; Carpenter, D. H.; Brunt, E. M.; Phillips, C. Jaundice: An Important, Poorly Recognized Risk Factor for Diminished Survival in Patients with Adenocarcinoma of the Head of the Pancreas. *HPB (Oxford).* **2014**, *16* (2), 150. https://doi.org/10.1111/HPB.12094.

(69) Lohse, I.; Brothers, S. P. Pathogenesis and Treatment of Pancreatic Cancer Related Pain. *Anticancer Res.* **2020**, *40* (4), 1789. https://doi.org/10.21873/ANTICANRES.14133.

(70) Barreto, S. G.; Shukla, P. J.; Shrikhande, S. V. Tumors of the Pancreatic Body and Tail. *World J. Oncol.* **2010**, *1* (2), 52. https://doi.org/10.4021/WJON2010.04.200W.

(71) Zhang, L.; Sanagapalli, S.; Stoita, A. Challenges in Diagnosis of Pancreatic Cancer. *World Journal of Gastroenterology*. Baishideng Publishing Group Co., Limited May 21, 2018, pp 2047–2060. https://doi.org/10.3748/wjg.v24.i19.2047.

(72) Chang, J.; Schomer, D.; Dragovich, T. Anatomical, Physiological, and Molecular Imaging for Pancreatic Cancer: Current Clinical Use and Future Implications. *Biomed Res. Int.* **2015**, *2015*.

https://doi.org/10.1155/2015/269641.

(73) Elbanna, K. Y.; Jang, H. J.; Kim, T. K. Imaging Diagnosis and Staging of Pancreatic Ductal Adenocarcinoma: A Comprehensive Review. *Insights Imaging* **2020**, *11* (1), 1–13. https://doi.org/10.1186/S13244-020-00861-Y/FIGURES/14.

(74) Jani, B. S.; Rzouq, F.; Saligram, S.; Lim, D.; Rastogi, A.; Bonino, J.; Olyaee, M. Endoscopic Ultrasound-Guided Fine-Needle Aspiration of Pancreatic Lesions: A Systematic Review of Technical and Procedural Variables. *North American Journal of Medical Sciences*. North American Journal of Medical Sciences January 1, 2016, pp 1–11. https://doi.org/10.4103/1947-2714.175185.

(75) Lin, E.; Alessio, A. What Are the Basic Concepts of Temporal, Contrast, and Spatial Resolution in Cardiac CT? *J. Cardiovasc. Comput. Tomogr.* **2009**, *3* (6), 403. https://doi.org/10.1016/J.JCCT.2009.07.003.

(76) Van Reeth, E.; Tham, I. W. K.; Tan, C. H.; Poh, C. L. Super-Resolution in Magnetic Resonance Imaging: A Review. *Concepts Magn. Reson. Part A* **2012**, *40A* (6), 306–325. https://doi.org/10.1002/CMR.A.21249.

(77) Kuntner, C.; Stout, D. Quantitative Preclinical PET Imaging: Opportunities and Challenges. *Front. Phys.* **2014**, *2*, 1–12. https://doi.org/10.3389/FPHY.2014.00012/BIBTEX.

(78) Agarwal, B.; Correa, A. M.; Ho, L. Survival in Pancreatic Carcinoma Based on Tumor Size. *Pancreas* **2008**, *36* (1). https://doi.org/10.1097/MPA.0B013E31814DE421.

(79) Ito, H.; Kawaguchi, Y.; Kawashima, Y.; Maruno, A.; Ogawa, M.; Hirabayashi, K.; Mine, T. A Case of Pancreatic Intraepithelial Neoplasia That Was Difficult to Diagnose Preoperatively. *Case Rep. Oncol.* **2015**, *8* (1), 30. https://doi.org/10.1159/000371842.

(80) Lewis, A. R.; Valle, J. W.; McNamara, M. G. Pancreatic Cancer: Are "Liquid Biopsies" Ready for Prime-Time? *World J. Gastroenterol.* **2016**, *22* (32), 7175. https://doi.org/10.3748/WJG.V22.I32.7175.

(81) Yang, J.; Xu, R.; Wang, C.; Qiu, J.; Ren, B.; You, L. Early Screening and Diagnosis Strategies of Pancreatic Cancer: A Comprehensive Review. *Cancer Commun.* **2021**, *41* (12), 1257. https://doi.org/10.1002/CAC2.12204.

(82) Park, W.; Chawla, A.; O'Reilly, E. M. Pancreatic Cancer: A Review. *JAMA* **2021**, *326* (9), 851–862. https://doi.org/10.1001/JAMA.2021.13027.

(83) Yamamoto, T.; Yagi, S.; Kinoshita, H.; Sakamoto, Y.; Okada, K.; Uryuhara, K.; Morimoto, T.; Kaihara, S.; Hosotani, R. Long-Term Survival after Resection of Pancreatic Cancer: A Single-Center Retrospective Analysis. *World J. Gastroenterol.* **2015**, *21* (1), 262.

https://doi.org/10.3748/WJG.V21.I1.262.

(84) Jalanko, H.; Kuusela, P.; Roberts, P.; Sipponen, P.; Haglund, C. A.; Mäkelä, O. Comparison of a New Tumour Marker, CA 19-9(TM), with α-Fetoprotein and Carcinoembryonic Antigen in Patients with Upper Gastrointestinal Diseases. *J. Clin. Pathol.* **1984**, *37* (2), 218–222. https://doi.org/10.1136/jcp.37.2.218.

(85) Hartwig, W.; Strobel, O.; Hinz, U.; Fritz, S.; Hackert, T.; Roth, C.; Büchler, M. W.; Werner, J. CA19-9 in Potentially Resectable Pancreatic Cancer: Perspective to Adjust Surgical and Perioperative Therapy. *Ann. Surg. Oncol.* **2013**, *20* (7), 2188–2196. https://doi.org/10.1245/S10434-012-2809-1/FIGURES/5.

(86) Ballehaninna, U. K.; Chamberlain, R. S. The Clinical Utility of Serum CA 19-9 in the Diagnosis, Prognosis and Management of Pancreatic Adenocarcinoma: An Evidence Based Appraisal. *J. Gastrointest. Oncol.* **2012**, *3* (2), 105–119. https://doi.org/10.3978/j.issn.2078-6891.2011.021.

(87) Uozumi, N.; Gao, C.; Yoshioka, T.; Nakano, M.; Moriwaki, K.; Nakagawa, T.; Masuda, T.; Tanabe, M.; Miyoshi, E. Identification of a Novel Type of CA19-9 Carrier in Human Bile and Sera of Cancer Patients: An Implication of the Involvement in Nonsecretory Exocytosis. *J. Proteome Res.* **2010**, *9* (12), 6345–6353. https://doi.org/10.1021/PR100600U/SUPPL_FILE/PR100600U_SI_006.PDF.

(88) Yue, T.; Partyka, K.; Maupin, K. A.; Hurley, M.; Andrews, P.; Kaul, K.; Moser, A. J.; Zeh, H.; Brand, R. E.; Haab, B. B. Identification of Blood-Protein Carriers of the CA 19-9 Antigen and Characterization of Prevalence in Pancreatic Diseases. *Proteomics* **2011**, *11* (18), 3665–3674. https://doi.org/10.1002/PMIC.201000827.

(89) Sperandio, M.; Gleissner, C. A.; Ley, K. Glycosylation in Immune Cell Trafficking. *Immunol. Rev.* **2009**, *230* (1), 97. https://doi.org/10.1111/J.1600-065X.2009.00795.X.

(90) Stowell, C. P.; Stowell, S. R. Biologic Roles of the ABH and Lewis Histo-Blood Group Antigens Part I: Infection and Immunity. *Vox Sang.* **2019**, *114* (5), 426–442. https://doi.org/10.1111/VOX.12787.

(91) Stowell, S. R.; Stowell, C. P. Biologic Roles of the ABH and Lewis Histo-Blood Group Antigens Part II: Thrombosis, Cardiovascular Disease and Metabolism. *Vox Sang.* **2019**, *114* (6), 535–552. https://doi.org/10.1111/VOX.12786.

(92) Ørntoft, T. F.; Vestergaard, E. M.; Holmes, E.; Jakobsen, J. S.; Grunnet, N.; Mortensen, M.; Johnson, P.; Bross, P.; Gregersen, N.; Skorstengaard, K.; Jensen, U. B.; Bolund, L.; Wolf, H. Influence of Lewis A1-3/4-L-Fucosyltransferase (FUT3) Gene Mutations on Enzyme Activity,

Erythrocyte Phenotyping, and Circulating Tumor Marker Sialyl-Lewis a Levels. *J. Biol. Chem.* **1996**, *271* (50), 32260–32268. https://doi.org/10.1074/JBC.271.50.32260.

(93) Luo, G.; Liu, C.; Guo, M.; Cheng, H.; Lu, Y.; Jin, K.; Liu, L.; Long, J.; Xu, J.; Lu, R.; Ni, Q.; Yu, X. Potential Biomarkers in Lewis Negative Patients with Pancreatic Cancer. *Ann. Surg.* **2017**, *265* (4), 800–805. https://doi.org/10.1097/SLA.0000000000001741.

(94) Kauffmann, F.; Frette, C.; Pham, Q. T.; Nafissi, S.; Bertrand, J. P.; Oriol, R. Associations of Blood Group-Related Antigens to FEV1, Wheezing, and Asthma. *https://doi.org/10.1164/ajrccm.153.1.8542166* **2012**, *153* (1), 76–82. https://doi.org/10.1164/AJRCCM.153.1.8542166.

(95) Djoussé, L.; Karamohamed, S.; Herbert, A. G.; D'Agostino, R. B.; Cupples, L. A.; Ellison, R. C. Fucosyltransferase 3 Polymorphism and Atherothrombotic Disease in the Framingham Offspring Study. *Am. Heart J.* **2007**, *153* (4), 636–639. https://doi.org/10.1016/J.AHJ.2006.12.015.

(96) Engle, D. D.; Tiriac, H.; Rivera, K. D.; Pommier, A.; Whalen, S.; Oni, T. E.; Alagesan, B.; Lee, E. J.; Yao, M. A.; Lucito, M. S.; Spielman, B.; Da Silva, B.; Schoepfer, C.; Wright, K.; Creighton, B.; Afinowicz, L.; Yu, K. H.; Grützmann, R.; Aust, D.; Gimotty, P. A.; Pollard, K. S.; Hruban, R. H.; Goggins, M. G.; Pilarsky, C.; Park, Y.; Pappin, D. J.; Hollingsworth, M. A.; Tuveson, D. A.; Silva, B. Da; Schoepfer, C.; Wright, K.; Creighton, B.; Afinowicz, L.; Yu, K. H.; Grützmann, R.; Aust, D.; Gimotty, P. A.; Pollard, K. S.; Hruban, R. H.; Goggins, M. G.; Pilarsky, C.; Park, Y.; Pappin, D. J.; Hollingsworth, M. A.; Tuveson, D. A. The Glycan CA19-9 Promotes Pancreatitis and Pancreatic Cancer in Mice. *Science* **2019**, *364* (6446), 1156–1162. https://doi.org/10.1126/science.aaw3145.

(97) Ma, Z.; Yang, H.; Peng, L.; Kuhn, C.; Chelariu-Raicu, A.; Mahner, S.; Jeschke, U.; von Schönfeldt, V. Expression of the Carbohydrate Lewis Antigen, Sialyl Lewis A, Sialyl Lewis X, Lewis X, and Lewis Y in the Placental Villi of Patients With Unexplained Miscarriages. *Front. Immunol.* **2021**, *12*, 1978. https://doi.org/10.3389/FIMMU.2021.679424/BIBTEX.

(98) Ardito, C. M.; Grüner, B. M.; Takeuchi, K. K.; Lubeseder-Martellato, C.; Teichmann, N.; Mazur, P. K.; DelGiorno, K. E.; Carpenter, E. S.; Halbrook, C. J.; Hall, J. C.; Pal, D.; Briel, T.; Herner, A.; Trajkovic-Arsic, M.; Sipos, B.; Liou, G. Y.; Storz, P.; Murray, N. R.; Threadgill, D. W.; Sibilia, M.; Washington, M. K.; Wilson, C. L.; Schmid, R. M.; Raines, E. W.; Crawford, H. C.; Siveke, J. T. EGF Receptor Is Required for KRAS-Induced Pancreatic Tumorigenesis. *Cancer Cell* **2012**, *22* (3), 304–317. https://doi.org/10.1016/J.CCR.2012.07.024.

(99) Navas, C.; Hernández-Porras, I.; Schuhmacher, A. J.; Sibilia, M.; Guerra, C.; Barbacid, M. EGF Receptor Signaling Is Essential for K-Ras Oncogene-Driven Pancreatic Ductal Adenocarcinoma. *Cancer Cell* **2012**,

22 (3), 318–330. https://doi.org/10.1016/J.CCR.2012.08.001.

(100) Terraneo, L.; Avagliano, L.; Caretti, A.; Bianciardi, P.; Tosi, D.; Bulfamante, G. Pietro; Samaja, M.; Trinchera, M. Expression of Carbohydrate-Antigen Sialyl-Lewis a on Colon Cancer Cells Promotes Xenograft Growth and Angiogenesis in Nude Mice. *Int. J. Biochem. Cell Biol.* **2013**, *45* (12), 2796–2800. https://doi.org/10.1016/J.BIOCEL.2013.10.003.

(101) Sakuma, K.; Aoki, M.; Kannagi, R. Transcription Factors C-Myc and CDX2 Mediate E-Selectin Ligand Expression in Colon Cancer Cells Undergoing EGF/BFGF-Induced Epithelial-Mesenchymal Transition. *Proc. Natl. Acad. Sci. U. S. A.* **2012**, *109* (20), 7776–7781. https://doi.org/10.1073/PNAS.1111135109/SUPPL_FILE/PNAS.201111135 SI.PDF.

(102) Contribution of Carbohydrate Antigens Sialyl Lewis A and Sialyl Lewis X to Adhesion of Human Cancer Cells to Vascular Endothelium1 | Cancer Research | American Association for Cancer Research https://aacrjournals.org/cancerres/article/53/2/354/499314/Contribution-of-Carbohydrate-Antigens-Sialyl-Lewis (accessed Oct 6, 2022).

(103) Padró, M.; Cobler, L.; Garrido, M.; De Bolós, C. Down-Regulation of FUT3 and FUT5 by ShRNA Alters Lewis Antigens Expression and Reduces the Adhesion Capacities of Gastric Cancer Cells. *Biochim. Biophys. Acta - Gen. Subj.* **2011**, *1810* (12), 1141–1149. https://doi.org/10.1016/J.BBAGEN.2011.09.011.

(104) Poty, S.; Carter, L. M.; Mandleywala, K.; Membreno, R.; Abdel-Atti, D.; Ragupathi, A.; Scholz, W. W.; Zeglis, B. M.; Lewis, J. S. Leveraging Bioorthogonal Click Chemistry to Improve 225 AC-Radioimmunotherapy of Pancreatic Ductal Adenocarcinoma. *Clin. Cancer Res.* **2019**, *25* (2), 868–880. https://doi.org/10.1158/1078-0432.CCR-18-1650/74140/AM/LEVERAGING-BIOORTHOGONAL-CLICK-CHEMISTRY-TO.

(105) Insug, O.; Otvos, L.; Kieber-Emmons, T.; Blaszczyk-Thurin, M. Role of SA–Lea and E-Selectin in Metastasis Assessed with Peptide Antagonist. *Peptides* **2002**, *23* (5), 999–1010. https://doi.org/10.1016/S0196-9781(02)00024-4.

(106) Sawada, R.; Sun, S. M.; Wu, X.; Hong, F.; Ragupathi, G.; Livingston, P. O.; Scholz, W. W. Human Monoclonal Antibodies to Sialyl-Lewisa (CA19.9) with Potent CDC, ADCC, and Antitumor Activity. *Clin. Cancer Res.* **2011**, *17* (5), 1024–1032. https://doi.org/10.1158/1078-0432.CCR-10-2640/289388/P/HUMAN-MONOCLONAL-ANTIBODIES-TO-SIALYL-LEWISA-CA19.

(107) Gupta, S.; McDonald, J. D.; Ayabe, R. I.; Khan, T. M.; Gamble, L. A.; Sinha, S.; Hannah, C.; Blakely, A. M.; Davis, J. L.; Hernandez, J. M. Targeting CA 19-9 with a Humanized Monoclonal Antibody at the Time of

Surgery May Decrease Recurrence Rates for Patients Undergoing Resections for Pancreatic Cancer, Cholangiocarcinoma and Metastatic Colorectal Cancer. *J. Gastrointest. Oncol.* **2020**, *11* (2), 231. https://doi.org/10.21037/JGO.2020.02.01.

(108) Tang, H.; Partyka, K.; Hsueh, P.; Sinha, J. Y.; Kletter, D.; Zeh, H.; Huang, Y.; Brand, R. E.; Haab, B. B. Glycans Related to the CA19-9 Antigen Are Increased in Distinct Subsets of Pancreatic Cancers and Improve Diagnostic Accuracy Over CA19-9. *Cell. Mol. Gastroenterol. Hepatol.* **2016**, *2* (2), 210. https://doi.org/10.1016/J.JCMGH.2015.12.003.

(109) Barnett, D.; Liu, Y.; Partyka, K.; Huang, Y.; Tang, H.; Hostetter, G.; Brand, R. E.; Singhi, A. D.; Drake, R. R.; Haab, B. B. The CA19-9 and Sialyl-TRA Antigens Define Separate Subpopulations of Pancreatic Cancer Cells. *Sci. Rep.* **2017**, *7* (1), 1–13. https://doi.org/10.1038/s41598-017-04164-z.

(110) Staal, B.; Liu, Y.; Barnett, D.; Hsueh, P.; He, Z.; Gao, C. F.; Partyka, K.; Hurd, M. W.; Singhi, A. D.; Drake, R. R.; Huang, Y.; Maitra, A.; Brand, R. E.; Haab, B. B. The Stra Plasma Biomarker: Blinded Validation of Improved Accuracy over CA19-9 in Pancreatic Cancer Diagnosis. *Clin. Cancer Res.* **2019**, *25* (9), 2745–2754. https://doi.org/10.1158/1078-0432.CCR-18-3310.

(111) Haglund, C. Tumour Marker Antigen CA125 in Pancreatic Cancer: A Comparison with CA19-9 and CEA. *Br. J. Cancer* **1986**, *54* (6), 897–901. https://doi.org/10.1038/bjc.1986.259.

(112) Meng, Q.; Shi, S.; Liang, C.; Xiang, J.; Liang, D.; Zhang, B.; Qin, Y.; Ji, S.; Xu, W.; Xu, J.; Ni, Q.; Yu, X. Diagnostic Accuracy of a CA125-Based Biomarker Panel in Patients with Pancreatic Cancer: A Systematic Review and Meta-Analysis. *J. Cancer* **2017**, *8* (17), 3615–3622. https://doi.org/10.7150/jca.18901.

(113) O'Neill, R. S.; Stoita, A. Biomarkers in the Diagnosis of Pancreatic Cancer: Are We Closer to Finding the Golden Ticket? *World J. Gastroenterol.* **2021**, *27* (26), 4045. https://doi.org/10.3748/WJG.V27.I26.4045.

(114) Kim, H.; Kang, K. N.; Shin, Y. S.; Byun, Y.; Han, Y.; Kwon, W.; Kim, C. W.; Jang, J. Y. Biomarker Panel for the Diagnosis of Pancreatic Ductal Adenocarcinoma. *Cancers (Basel).* **2020**, *12* (6). https://doi.org/10.3390/CANCERS12061443.

(115) Dhayat, S. A.; Mirgorod, P.; Lenschow, C.; Senninger, N.; Anthoni, C.; Vowinkel, T. Challenges in Pancreatic Adenocarcinoma Surgery - National Survey and Current Practice Guidelines. *PLoS One* **2017**, *12* (3). https://doi.org/10.1371/journal.pone.0173374.

(116) Badger, S. A.; Brant, J. L.; Jones, C.; McClements, J.; Loughrey, M. B.; Taylor, M. A.; Diamond, T.; Mckie, L. D. The Role of Surgery for Pancreatic Cancer: A 12-Year Review of Patient Outcome. *Ulster Med. J.* **2010**, *79* (2), 70.

(117) Saraee, A.; Vahedian-Ardakani, J.; Saraee, E.; Pakzad, R.; Wadji, M. B. Whipple Procedure: A Review of a 7-Year Clinical Experience in a Referral Center for Hepatobiliary and Pancreas Diseases. *World J. Surg. Oncol.* **2015**, *13* (1). https://doi.org/10.1186/s12957-015-0523-8.

(118) Passeri, M. J.; Baker, E. H.; Siddiqui, I. A.; Templin, M. A.; Martinie, J. B.; Vrochides, D.; Iannitti, D. A. Total Compared with Partial Pancreatectomy for Pancreatic Adenocarcinoma: Assessment of Resection Margin, Readmission Rate, and Survival from the U.S. National Cancer Database. *Curr. Oncol.* **2019**, *26* (3), e346–e356. https://doi.org/10.3747/co.26.4066.

(119) Papavasiliou, P.; Chun, Y. S.; Hoffman, J. P. How to Define and Manage Borderline Resectable Pancreatic Cancer. *Surgical Clinics of North America*. Surg Clin North Am June 2013, pp 663–674. https://doi.org/10.1016/j.suc.2013.02.005.

(120) Gilbert, J. W.; Wolpin, B.; Clancy, T.; Wang, J.; Mamon, H.; Shinagare, A. B.; Jagannathan, J.; Rosenthal, M. Borderline Resectable Pancreatic Cancer: Conceptual Evolution and Current Approach to Image-Based Classification. *Ann. Oncol.* **2017**, *28* (9), 2067–2076. https://doi.org/10.1093/ANNONC/MDX180.

(121) Oba, A.; Ho, F.; Bao, Q. R.; Al-Musawi, M. H.; Schulick, R. D.; Chiaro, M. Del. *Neoadjuvant Treatment in Pancreatic Cancer*; Frontiers Media S.A., 2020; Vol. 10, p 245. https://doi.org/10.3389/fonc.2020.00245.

(122) Hajatdoost, L.; Sedaghat, K.; Walker, E. J.; Thomas, J.; Kosari, S. Chemotherapy in Pancreatic Cancer: A Systematic Review. *Medicina (Lithuania)*. MDPI AG July 1, 2018. https://doi.org/10.3390/medicina54030048.

(123) Abbassi, R.; Algül, H. Palliative Chemotherapy in Pancreatic Cancer-Treatment Sequences. *Translational Gastroenterology and Hepatology*. AME Publishing Company 2019. https://doi.org/10.21037/tgh.2019.06.09.

(124) Conroy, T.; Desseigne, F.; Ychou, M.; Bouché, O.; Guimbaud, R.; Bécouarn, Y.; Adenis, A.; Raoul, J.-L.; Gourgou-Bourgade, S.; de la Fouchardière, C.; Bennouna, J.; Bachet, J.-B.; Khemissa-Akouz, F.; Péré-Vergé, D.; Delbaldo, C.; Assenat, E.; Chauffert, B.; Michel, P.; Montoto-Grillot, C.; Ducreux, M. FOLFIRINOX versus Gemcitabine for Metastatic Pancreatic Cancer. *N. Engl. J. Med.* **2011**, *364* (19), 1817–1825. https://doi.org/10.1056/NEJMoa1011923.

(125) de Jesus, V. H. F.; Camandaroba, M. P. G.; Calsavara, V. F.; Riechelmann, R. P. Systematic Review and Meta-Analysis of Gemcitabine-Based Chemotherapy after FOLFIRINOX in Advanced Pancreatic Cancer. *Ther. Adv. Med. Oncol.* **2020**, *12*. https://doi.org/10.1177/1758835920905408.

(126) Pereira, N. P.; Corrêa, J. R. Pancreatic Cancer: Treatment Approaches

and Trends. *J. Cancer Metastasis Treat.* **2018**, *4* (6), 30. https://doi.org/10.20517/2394-4722.2018.13.

(127) Conroy, T.; Hammel, P.; Hebbar, M.; Ben Abdelghani, M.; Wei, A. C.; Raoul, J.-L.; Choné, L.; Francois, E.; Artru, P.; Biagi, J. J.; Lecomte, T.; Assenat, E.; Faroux, R.; Ychou, M.; Volet, J.; Sauvanet, A.; Breysacher, G.; Di Fiore, F.; Cripps, C.; Kavan, P.; Texereau, P.; Bouhier-Leporrier, K.; Khemissa-Akouz, F.; Legoux, J.-L.; Juzyna, B.; Gourgou, S.; O'Callaghan, C. J.; Jouffroy-Zeller, C.; Rat, P.; Malka, D.; Castan, F.; Bachet, J.-B. FOLFIRINOX or Gemcitabine as Adjuvant Therapy for Pancreatic Cancer. *N. Engl. J. Med.* **2018**, *379* (25), 2395–2406. https://doi.org/10.1056/NEJMOA1809775/SUPPL_FILE/NEJMOA1809775 _DATA-SHARING.PDF.

(128) Paiella, S.; Salvia, R.; Ramera, M.; Girelli, R.; Frigerio, I.; Giardino, A.; Allegrini, V.; Bassi, C. Local Ablative Strategies for Ductal Pancreatic Cancer (Radiofrequency Ablation, Irreversible Electroporation): A Review. *Gastroenterol. Res. Pract.* **2016**, *2016*. https://doi.org/10.1155/2016/4508376.

(129) Berger, A. K.; Haag, G. M.; Ehmann, M.; Byl, A.; Jäger, D.; Springfeld, C. Palliative Chemotherapy for Pancreatic Adenocarcinoma: A Retrospective Cohort Analysis of Efficacy and Toxicity of the FOLFIRINOX Regimen Focusing on the Older Patient. *BMC Gastroenterol.* **2017**, *17* (1), 1–7. https://doi.org/10.1186/S12876-017-0709-3/FIGURES/2.

(130) Cummings, R. D. The Repertoire of Glycan Determinants in the Human Glycome. *Mol. Biosyst.* **2009**, *5* (10), 1087–1104. https://doi.org/10.1039/b907931a.

(131) Gillen, S.; Schuster, T.; Büschenfelde, C. M. Zum; Friess, H.; Kleeff, J. Preoperative/Neoadjuvant Therapy in Pancreatic Cancer: A Systematic Review and Meta-Analysis of Response and Resection Percentages. *PLOS Med.* **2010**, *7* (4), e1000267. https://doi.org/10.1371/JOURNAL.PMED.1000267.

(132) Mikkola, S. Nucleotide Sugars in Chemistry and Biology. *Molecules* **2020**, *25* (23). https://doi.org/10.3390/MOLECULES25235755.

(133) Reitsma, S.; Slaaf, D. W.; Vink, H.; Van Zandvoort, M. A. M. J.; Oude Egbrink, M. G. A. The Endothelial Glycocalyx: Composition, Functions, and Visualization. *Pflugers Archiv European Journal of Physiology*. Springer June 2007, pp 345–359. https://doi.org/10.1007/s00424-007-0212-8.

(134) Martinez-Seara Monne, H.; Danne, R.; Róg, T.; Ilpo, V.; Gurtovenko, A. Structure of Glycocalyx. *Biophys. J.* **2013**, *104* (2), 251a. https://doi.org/10.1016/j.bpj.2012.11.1412.

(135) Alphonsus, C. S.; Rodseth, R. N. The Endothelial Glycocalyx: A Review of the Vascular Barrier. *Anaesthesia*. Blackwell Publishing Ltd July 1, 2014,

pp 777–784. https://doi.org/10.1111/anae.12661.

(136) Liu, H.; Li, J.; Xuan, C.; Ma, H. A Review on the Physiological and Pathophysiological Role of Endothelial Glycocalyx. *J. Biochem. Mol. Toxicol.* **2020**, *34* (11). https://doi.org/10.1002/jbt.22571.

(137) Kuo, J. C. H.; Gandhi, J. G.; Zia, R. N.; Paszek, M. J. Physical Biology of the Cancer Cell Glycocalyx. *Nat. Phys.* **2018**, *14* (7), 658–669. https://doi.org/10.1038/s41567-018-0186-9.

(138) Yilmaz, O.; Afsar, B.; Ortiz, A.; Kanbay, M. The Role of Endothelial Glycocalyx in Health and Disease. *Clinical Kidney Journal.* Oxford University Press February 6, 2019, pp 611–619. https://doi.org/10.1093/ckj/sfz042.

(139) Banerjee, D. K. N-Glycans in Cell Survival and Death: Cross-Talk between Glycosyltransferases. *Biochim. Biophys. Acta - Gen. Subj.* **2012**, *1820* (9), 1338–1346. https://doi.org/10.1016/J.BBAGEN.2012.01.013.

(140) Bieberich, E. *Synthesis, Processing, and Function of N-Glycans in N-Glycoproteins*; NIH Public Access, 2014; Vol. 9. https://doi.org/10.1007/978-1-4939-1154-7_3.

(141) Rush, J. S. Role of Flippases in Protein Glycosylation in the Endoplasmic Reticulum. *Lipid Insights* **2015**, *8* (Suppl 1), 45. https://doi.org/10.4137/LPI.S31784.

(142) Mohorko, E.; Glockshuber, R.; Aebi, M. Oligosaccharyltransferase: The Central Enzyme of N-Linked Protein Glycosylation. *J. Inherit. Metab. Dis.* **2011**, *34* (4), 869–878. https://doi.org/10.1007/S10545-011-9337-1.

(143) Freeze, H. H.; Esko, J. D.; Parodi, A. J. Glycans in Glycoprotein Quality Control. *Essentials Glycobiol.* **2009**.

(144) Leach, M. R.; Williams, D. B. Calnexin and Calreticulin, Molecular Chaperones of the Endoplasmic Reticulum. **2013**.

(145) Tannous, A.; Pisoni, G. B.; Hebert, D. N.; Molinari, M. N-Linked Sugar-Regulated Protein Folding and Quality Control in the ER. *Semin. Cell Dev. Biol.* **2015**, *41*, 79. https://doi.org/10.1016/J.SEMCDB.2014.12.001.

(146) Kizuka, Y.; Taniguchi, N. Enzymes for N-Glycan Branching and Their Genetic and Nongenetic Regulation in Cancer. *Biomolecules* **2016**, *6* (2). https://doi.org/10.3390/BIOM6020025.

(147) Tanichi, N.; Korekane, H. Branched N-Glycans and Their Implications for Cell Adhesion, Signaling and Clinical Applications for Cancer Biomarkers and in Therapeutics. *BMB Rep.* **2011**, *44* (12), 772–781. https://doi.org/10.5483/BMBREP.2011.44.12.772.

(148) Chen, Q.; Tan, Z.; Guan, F.; Ren, Y. The Essential Functions and Detection of Bisecting GlcNAc in Cell Biology. *Front. Chem.* **2020**, *8*, 511.

https://doi.org/10.3389/FCHEM.2020.00511/BIBTEX.

(149) Fisch Der, T.; Laaf, D.; Dey, C.; Elling, L. Enzymatic Synthesis of N-Acetyllactosamine (LacNAc) Type 1 Oligomers and Characterization as Multivalent Galectin Ligands. *Mol. A J. Synth. Chem. Nat. Prod. Chem.* **2017**, *22* (8). https://doi.org/10.3390/MOLECULES22081320.

(150) Wang, X.; Inoue, S.; Gu, J.; Miyoshi, E.; Noda, K.; Li, W.; Mizuno-Horikawa, Y.; Nakano, M.; Asahi, M.; Takahashi, M.; Uozumi, N.; Ihara, S.; Lee, S. H.; Ikeda, Y.; Yamaguchi, Y.; Aze, Y.; Tomiyama, Y.; Fujii, J.; Suzuki, K.; Kondo, A.; Shapiro, S. D.; Lopez-Otin, C.; Kuwaki, T.; Okabe, M.; Honke, K.; Taniguchi, N. Dysregulation of TGF-B1 Receptor Activation Leads to Abnormal Lung Development and Emphysema-like Phenotype in Core Fucose-Deficient Mice. *Proc. Natl. Acad. Sci. U. S. A.* **2005**, *102* (44), 15791–15796. https://doi.org/10.1073/PNAS.0507375102/SUPPL_FILE/07375FIG4.JPG.

(151) De Vries, T.; Knegtel, R. M. A.; Holmes, E. H.; Macher, B. A. Fucosyltransferases: Structure/Function Studies. *Glycobiology* **2001**, *11* (10), 119R-128R. https://doi.org/10.1093/GLYCOB/11.10.119R.

(152) Li, Y.; Chen, X. Sialic Acid Metabolism and Sialyltransferases: Natural Functions and Applications. *Appl. Microbiol. Biotechnol.* **2012**, *94* (4), 887. https://doi.org/10.1007/S00253-012-4040-1.

(153) Suga, A.; Nagae, M.; Yamaguchi, Y. Analysis of Protein Landscapes around N-Glycosylation Sites from the PDB Repository for Understanding the Structural Basis of N-Glycoprotein Processing and Maturation. *Glycobiology* **2018**, *28* (10), 774–785. https://doi.org/10.1093/GLYCOB/CWY059.

(154) Rudd, P. M.; Dwek, R. A. Glycosylation: Heterogeneity and the 3D Structure of Proteins. *http://dx.doi.org/10.3109/10409239709085144* **2008**, *32* (1), 1–100. https://doi.org/10.3109/10409239709085144.

(155) Bause, E. Structural Requirements of N-Glycosylation of Proteins. Studies with Proline Peptides as Conformational Probes. *Biochem. J.* **1983**, *209* (2), 331–336. https://doi.org/10.1042/BJ2090331.

(156) Čaval, T.; Heck, A. J. R.; Reiding, K. R. Meta-Heterogeneity: Evaluating and Describing the Diversity in Glycosylation Between Sites on the Same Glycoprotein. *Mol. Cell. Proteomics* **2021**, *20*, 100010. https://doi.org/10.1074/MCP.R120.002093.

(157) Losfeld, M. E.; Scibona, E.; Lin, C. W.; Villiger, T. K.; Gauss, R.; Morbidelli, M.; Aebi, M. Influence of Protein/Glycan Interaction on Site-Specific Glycan Heterogeneity. *FASEB J.* **2017**, *31* (10), 4623–4635. https://doi.org/10.1096/FJ.201700403R.

(158) Sola, R. J.; Griebenow, K. Effects of Glycosylation on the Stability of Protein Pharmaceuticals. *J. Pharm. Sci.* **2009**, *98* (4), 1223.

https://doi.org/10.1002/JPS.21504.

(159) Shental-Bechor, D.; Levy, Y. Effect of Glycosylation on Protein Folding: A Close Look at Thermodynamic Stabilization. *Proc. Natl. Acad. Sci. U. S. A.* **2008**, *105* (24), 8256–8261. https://doi.org/10.1073/PNAS.0801340105/SUPPL_FILE/0801340105SI.P DF.

(160) Nagae, M.; Yamaguchi, Y. Function and 3D Structure of the N-Glycans on Glycoproteins. *Int. J. Mol. Sci.* **2012**, *13* (7), 8398. https://doi.org/10.3390/IJMS13078398.

(161) Subedi, G. P.; Barb, A. W. The Structural Role of Antibody N-Glycosylation in Receptor Interactions. *Structure* **2015**, *23* (9), 1573. https://doi.org/10.1016/J.STR.2015.06.015.

(162) Shabareesh, P.; Kaur, K. Overview of the Structural and Functional Impact of Protein Glycosylation in Mediating Protein – Protein Interactions. *Trends Carbohydr. Res.* **2015**, *7* (4), 30–40.

(163) Ghazarian, H.; Idoni, B.; Oppenheimer, S. B. A Glycobiology Review: Carbohydrates, Lectins, and Implications in Cancer Therapeutics. *Acta Histochem.* **2011**, *113* (3), 236. https://doi.org/10.1016/J.ACTHIS.2010.02.004.

(164) Fiedler, K.; Simons, K. The Role of N-Glycans in the Secretory Pathway. *Cell* **1995**, *81* (3), 309–312. https://doi.org/10.1016/0092-8674(95)90380-1.

(165) Sun, X.; Tie, H. C.; Chen, B.; Lu, L. Glycans Function as a Golgi Export Signal to Promote the Constitutive Exocytic Trafficking. *J. Biol. Chem.* **2020**, *295* (43), 14750–14762. https://doi.org/10.1074/JBC.RA120.014476.

(166) Caval, T.; Zhu, J.; Tian, W.; Remmelzwaal, S.; Yang, Z.; Clausen, H.; Heck, A. J. R. Targeted Analysis of Lysosomal Directed Proteins and Their Sites of Mannose-6-Phosphate Modification. *Mol. Cell. Proteomics* **2019**, *18* (1), 16. https://doi.org/10.1074/MCP.RA118.000967.

(167) Dahms, N. M.; Lobel, P.; Kornfeld, S. Mannose 6-Phosphate Receptors and Lysosomal Enzyme Targeting. *J. Biol. Chem.* **1989**, *264* (21), 12115–12118. https://doi.org/10.1016/S0021-9258(18)63825-6.

(168) Vagin, O.; Kraut, J. A.; Sachs, G. Role of N-Glycosylation in Trafficking of Apical Membrane Proteins in Epithelia. *Am. J. Physiol. - Ren. Physiol.* **2009**, *296* (3), F459. https://doi.org/10.1152/AJPRENAL.90340.2008.

(169) Jaeken, J.; Matthijs, G. Congenital Disorders of Glycosylation: A Rapidly Expanding Disease Family. *https://doi.org/10.1146/annurev.genom.8.080706.092327* **2007**, *8*, 261–278. https://doi.org/10.1146/ANNUREV.GENOM.8.080706.092327.

(170) Jung, S. Y.; Kim, S. S.; Kim, Y. Il; Chung, H. Y.; Kim, S. H.; Yeo, S. G. Expression, Distribution, and Role of C-Type Lectin Receptors in the

Human and Animal Middle Ear and Eustachian Tube: A Review. *Mol. 2018, Vol. 23, Page 734* **2018**, *23* (4), 734. https://doi.org/10.3390/MOLECULES23040734.

(171) Ferreira, I. G.; Pucci, M.; Venturi, G.; Malagolini, N.; Chiricolo, M.; Dall'Olio, F. Glycosylation as a Main Regulator of Growth and Death Factor Receptors Signaling. *Int. J. Mol. Sci.* **2018**, *19* (2). https://doi.org/10.3390/IJMS19020580.

(172) Matsumoto, K.; Yokote, H.; Arao, T.; Maegawa, M.; Tanaka, K.; Fujita, Y.; Shimizu, C.; Hanafusa, T.; Fujiwara, Y.; Nishio, K. N-Glycan Fucosylation of Epidermal Growth Factor Receptor Modulates Receptor Activity and Sensitivity to Epidermal Growth Factor Receptor Tyrosine Kinase Inhibitor. *Cancer Sci.* **2008**, *99* (8), 1611–1617. https://doi.org/10.1111/J.1349-7006.2008.00847.X.

(173) Zhou, Y.; Fukuda, T.; Hang, Q.; Hou, S.; Isaji, T.; Kameyama, A.; Gu, J. Inhibition of Fucosylation by 2-Fluorofucose Suppresses Human Liver Cancer HepG2 Cell Proliferation and Migration as Well as Tumor Formation. *Sci. Rep.* **2017**, *7* (1). https://doi.org/10.1038/S41598-017-11911-9.

(174) Munkley, J.; Elliott, D. J.; Munkley, J.; Elliott, D. J. Hallmarks of Glycosylation in Cancer. *Oncotarget* **2016**, *7* (23), 35478–35489. https://doi.org/10.18632/oncotarget.8155.

(175) Liberti, M. V.; Locasale, J. W. The Warburg Effect: How Does It Benefit Cancer Cells? *Trends Biochem. Sci.* **2016**, *41* (3), 211. https://doi.org/10.1016/J.TIBS.2015.12.001.

(176) Pucci, M.; Duca, M.; Malagolini, N.; Dall'Olio, F. Glycosyltransferases in Cancer: Prognostic Biomarkers of Survival in Patient Cohorts and Impact on Malignancy in Experimental Models. *Cancers (Basel).* **2022**, *14* (9). https://doi.org/10.3390/CANCERS14092128/S1.

(177) Lau, K. S.; Dennis, J. W. N-Glycans in Cancer Progression. *Glycobiology* **2008**, *18* (10), 750–760. https://doi.org/10.1093/GLYCOB/CWN071.

(178) Granovsky, M.; Fata, J.; Pawling, J.; Muller, W. J.; Khokha, R.; Dennis, J. W. Suppression of Tumor Growth and Metastasis in Mgat5-Deficient Mice. *Nat. Med. 2000 63* **2000**, *6* (3), 306–312. https://doi.org/10.1038/73163.

(179) Dennis, J. W.; Laferté, S.; Waghorne, C.; Breitman, M. L.; Kerbel, R. S. B1-6 Branching of Asn-Linked Oligosaccharides Is Directly Associated with Metastasis. *Science (80-.).* **1987**, *236* (4801), 582–585. https://doi.org/10.1126/SCIENCE.2953071.

(180) Zhao, Y. Y.; Takahashi, M.; Gu, J. G.; Miyoshi, E.; Matsumoto, A.; Kitazume, S.; Taniguchi, N. Functional Roles of N-Glycans in Cell Signaling and Cell Adhesion in Cancer. *Cancer Sci.* **2008**, *99* (7), 1304–1310. https://doi.org/10.1111/J.1349-7006.2008.00839.X.

(181) Scott, D. A.; Casadonte, R.; Cardinali, B.; Spruill, L.; Mehta, A. S.; Carli, F.; Simone, N.; Kriegsmann, M.; Del Mastro, L.; Kriegsmann, J.; Drake, R. R. Increases in Tumor N-Glycan Polylactosamines Associated with Advanced HER2-Positive and Triple-Negative Breast Cancer Tissues. *PROTEOMICS – Clin. Appl.* **2019**, *13* (1), 1800014. https://doi.org/10.1002/prca.201800014.

(182) Taniguchi, N.; Endo, T.; Hart, G. W.; Seeberger, P. H.; Wong, C. H. Glycoscience: Biology and Medicine. *Glycosci. Biol. Med.* **2015**, 1–1569. https://doi.org/10.1007/978-4-431-54841-6/COVER.

(183) Wang, X.; Gu, J.; Ihara, H.; Miyoshi, E.; Honke, K.; Taniguchi, N. Core Fucosylation Regulates Epidermal Growth Factor Receptor-Mediated Intracellular Signaling. *J. Biol. Chem.* **2006**, *281* (5), 2572–2577. https://doi.org/10.1074/jbc.M510893200.

(184) Saldova, R.; Asadi Shehni, A.; Haakensen, V. D.; Steinfeld, I.; Hilliard, M.; Kifer, I.; Helland, Å.; Yakhini, Z.; Børresen-Dale, A. L.; Rudd, P. M. Association of N-Glycosylation with Breast Carcinoma and Systemic Features Using High-Resolution Quantitative UPLC. *J. Proteome Res.* **2014**, *13* (5), 2314–2327. https://doi.org/10.1021/PR401092Y/SUPPL_FILE/PR401092Y_SI_003.XLSX.

(185) Sato, Y.; Takahashi, M.; Shibukawa, Y.; Jain, S. K.; Hamaoka, R.; Miyagawa, J. I.; Yaginuma, Y.; Honke, K.; Ishikawa, M.; Taniguchi, N. Overexpression of N-Acetylglucosaminyltransferase III Enhances the Epidermal Growth Factor-Induced Phosphorylation of ERK in HeLaS3 Cells by up-Regulation of the Internalization Rate of the Receptors. *J. Biol. Chem.* **2001**, *276* (15), 11956–11962. https://doi.org/10.1074/JBC.M008551200.

(186) Miwa, H. E.; Song, Y.; Alvarez, R.; Cummings, R. D.; Stanley, P. The Bisecting GlcNAc in Cell Growth Control and Tumor Progression. *Glycoconj. J.* **2012**, *29* (8–9), 609–618. https://doi.org/10.1007/s10719-012-9373-6.

(187) Cheng, L.; Cao, L.; Wu, Y.; Xie, W.; Li, J.; Guan, F.; Tan, Z. Bisecting N-Acetylglucosamine on EGFR Inhibits Malignant Phenotype of Breast Cancer via Down-Regulation of EGFR/Erk Signaling. *Front. Oncol.* **2020**, *10*, 929. https://doi.org/10.3389/FONC.2020.00929/FULL.

(188) Blomme, B.; Van Steenkiste, C.; Callewaert, N.; Van Vlierberghe, H. Alteration of Protein Glycosylation in Liver Diseases. *J. Hepatol.* **2009**, *50* (3), 592–603. https://doi.org/10.1016/j.jhep.2008.12.010.

(189) Comunale, M. A.; Lowman, M.; Long, R. E.; Krakover, J.; Philip, R.; Seeholzer, S.; Evans, A. A.; Hann, H. W. L.; Block, T. M.; Mehta, A. S. Proteomic Analysis of Serum Associated Fucosylated Glycoproteins in the Development of Primary Hepatocellular Carcinoma. *J. Proteome Res.*

2006, *5* (2), 308–315. https://doi.org/10.1021/pr050328x.

(190) Mehta, A.; Herrera, H.; Block, T. Glycosylation and Liver Cancer. In *Advances in Cancer Research*; Academic Press Inc., 2015; Vol. 126, pp 257–279. https://doi.org/10.1016/bs.acr.2014.11.005.

(191) Aoyagi, Y.; Suzuki, Y.; Isemura, M.; Nomoto, M.; Sekine, C.; Igarashi, K.; Ichida, F. The Fucosylation Index of Alpha-fetoprotein and Its Usefulness in the Early Diagnosis of Hepatocellular Carcinoma. *Cancer* **1988**, *61* (4), 769–774. https://doi.org/10.1002/1097-0142(19880215)61:4<769::AID-CNCR2820610422>3.0.CO;2-M.

(192) Zhao, T.; Jia, L.; Li, J.; Ma, C.; Wu, J.; Shen, J.; Dang, L.; Zhu, B.; Li, P.; Zhi, Y.; Lan, R.; Xu, Y.; Hao, Z.; Chai, Y.; Li, Q.; Hu, L.; Sun, S. Heterogeneities of Site-Specific N-Glycosylation in HCC Tumors With Low and High AFP Concentrations. *Front. Oncol.* **2020**, *10*, 496. https://doi.org/10.3389/fonc.2020.00496.

(193) Drake, R. R.; Schwegler, E. E.; Malik, G.; Diaz, J.; Block, T.; Mehta, A.; Semmes, O. J. Lectin Capture Strategies Combined with Mass Spectrometry for the Discovery of Serum Glycoprotein Biomarkers. *Mol. Cell. Proteomics* **2006**, *5* (10), 1957–1967. https://doi.org/10.1074/MCP.M600176-MCP200.

(194) Marrero, J. A.; Romano, P. R.; Nikolaeva, O.; Steel, L.; Mehta, A.; Fimmel, C. J.; Comunale, M. A.; D'Amelio, A.; Lok, A. S.; Block, T. M. GP73, a Resident Golgi Glycoprotein, Is a Novel Serum Marker for Hepatocellular Carcinoma. *J. Hepatol.* **2005**, *43* (6), 1007–1012. https://doi.org/10.1016/J.JHEP.2005.05.028.

(195) Block, T. M.; Comunale, M. A.; Lowman, M.; Steel, L. F.; Romano, P. R.; Fimmel, C.; Tennant, B. C.; London, W. T.; Evans, A. A.; Blumberg, B. S.; Dwek, R. A.; Mattu, T. S.; Mehta, A. S. Use of Targeted Glycoproteomics to Identify Serum Glycoproteins That Correlate with Liver Cancer in Woodchucks and Humans. *Proc. Natl. Acad. Sci. U. S. A.* **2005**, *102* (3), 779–784. https://doi.org/10.1073/PNAS.0408928102/ASSET/F9662D75-B59A-4BB3-BD16-4FF85C0D689D/ASSETS/GRAPHIC/ZPQ0040570070005.JPEG.

(196) Comunale, M. A.; Rodemich-Betesh, L.; Hafner, J.; Wang, M.; Norton, P.; Di Bisceglie, A. M.; Block, T.; Mehta, A. Linkage Specific Fucosylation of Alpha-1-Antitrypsin in Liver Cirrhosis and Cancer Patients: Implications for a Biomarker of Hepatocellular Carcinoma. *PLoS One* **2010**, *5* (8), e12419. https://doi.org/10.1371/journal.pone.0012419.

(197) Comunale, M. A.; Wang, M.; Rodemich-Betesh, L.; Hafner, J.; Lamontagne, A.; Klein, A.; Marrero, J.; Di Bisceglie, A. M.; Gish, R.; Block, T.; Mehta, A. Novel Changes in Glycosylation of Serum Apo-J in Patients with Hepatocellular Carcinoma. *Cancer Epidemiol. Biomarkers Prev.* **2011**, *20* (6), 1222–1229. https://doi.org/10.1158/1055-9965.EPI-10-1047.

(198) DelaCourt, A. T.; Mehta, A. S. Liver Cancer (Current Therapies). *Ref. Modul. Biomed. Sci.* **2021**. https://doi.org/10.1016/B978-0-12-820472-6.00007-4.

(199) Norton, P. A.; Comunale, M. A.; Krakover, J.; Rodemich, L.; Pirog, N.; D'Amelio, A.; Philip, R.; Mehta, A. S.; Block, T. M. N-Linked Glycosylation of the Liver Cancer Biomarker GP73. *J. Cell. Biochem.* **2008**, *104* (1), 136–149. https://doi.org/10.1002/jcb.21610.

(200) West, C. A.; Wang, M.; Herrera, H.; Liang, H.; Black, A.; Angel, P. M.; Drake, R. R.; Mehta, A. S. N-Linked Glycan Branching and Fucosylation Are Increased Directly in Hcc Tissue As Determined through in Situ Glycan Imaging. *J. Proteome Res.* **2018**, *17* (10), 3454–3462. https://doi.org/10.1021/acs.jproteome.8b00323.

(201) Herrera, H.; Dilday, T.; Uber, A.; Scott, D.; Zambrano, J. N.; Wang, M.; Angel, P. M.; Mehta, A. S.; Drake, R. R.; Hill, E. G.; Yeh, E. S. Core-Fucosylated Tetra-Antennary n-Glycan Containing a Single n-Acetyllactosamine Branch Is Associated with Poor Survival Outcome in Breast Cancer. *Int. J. Mol. Sci.* **2019**, *20* (10), 2528. https://doi.org/10.3390/ijms20102528.

(202) Scott, D. A.; Norris-Caneda, K.; Spruill, L.; Bruner, E.; Kono, Y.; Angel, P. M.; Mehta, A. S.; Drake, R. R. Specific N-Linked Glycosylation Patterns in Areas of Necrosis in Tumor Tissues. *Int. J. Mass Spectrom.* **2019**, *437*, 69–76. https://doi.org/10.1016/j.ijms.2018.01.002.

(203) Angel, P. M.; Saunders, J.; Clift, C. L.; White-Gilbertson, S.; Voelkel-Johnson, C.; Yeh, E.; Mehta, A.; Drake, R. R. A Rapid Array-Based Approach to N-Glycan Profiling of Cultured Cells. *J. Proteome Res.* **2019**, *18* (10), 3630–3639. https://doi.org/10.1021/acs.jproteome.9b00303.

(204) Holst, S.; Heijs, B.; De Haan, N.; Van Zeijl, R. J. M.; Briaire-De Bruijn, I. H.; Van Pelt, G. W.; Mehta, A. S.; Angel, P. M.; Mesker, W. E.; Tollenaar, R. A.; Drake, R. R.; Bovée, J. V. M. G.; McDonnell, L. A.; Wuhrer, M. Linkage-Specific in Situ Sialic Acid Derivatization for N-Glycan Mass Spectrometry Imaging of Formalin-Fixed Paraffin-Embedded Tissues. *Anal. Chem.* **2016**, *88* (11), 5904–5913. https://doi.org/10.1021/acs.analchem.6b00819.

(205) Heijs, B.; Potthoff, A.; Soltwisch, J.; Dreisewerd, K. MALDI-2 for the Enhanced Analysis of N-Linked Glycans by Mass Spectrometry Imaging. *Anal. Chem.* **2020**, *92* (20), 13904–13911. https://doi.org/10.1021/acs.analchem.0c02732.

(206) Boyaval, F.; Van Zeijl, R.; Dalebout, H.; Holst, S.; van Pelt, G. W.; Fariña-Sarasqueta, A.; Mesker, W. E.; Tollenaar, R.; Morreau, H.; Wuhrer, M.; Heijs, B. N-Glycomic Signature of Stage II Colorectal Cancer and Its Association with the Tumor Microenvironment. *Mol. Cell. Proteomics* **2020**, mcp.RA120.002215. https://doi.org/10.1074/mcp.ra120.002215.

(207) Drake, R. R.; Powers, T. W.; Jones, E. E.; Bruner, E.; Mehta, A. S.; Angel, P. M. MALDI Mass Spectrometry Imaging of N-Linked Glycans in Cancer Tissues. In *Advances in Cancer Research*; Academic Press Inc., 2017; Vol. 134, pp 85–116. https://doi.org/10.1016/bs.acr.2016.11.009.

(208) Carter, C. L.; Parker, G. A.; Hankey, K. G.; Farese, A. M.; MacVittie, T. J.; Kane, M. A. MALDI-MSI Spatially Maps N-Glycan Alterations to Histologically Distinct Pulmonary Pathologies Following Irradiation. *Sci. Rep.* **2020**, *10* (1), 11559. https://doi.org/10.1038/s41598-020-68508-y.

(209) Powers, T. W.; Neely, B. A.; Shao, Y.; Tang, H.; Troyer, D. A.; Mehta, A. S.; Haab, B. B.; Drake, R. R. MALDI Imaging Mass Spectrometry Profiling of N-Glycans in Formalin-Fixed Paraffin Embedded Clinical Tissue Blocks and Tissue Microarrays. *PLoS One* **2014**, *9* (9), e106255. https://doi.org/10.1371/journal.pone.0106255.

(210) Powers, T. W.; Holst, S.; Wuhrer, M.; Mehta, A. S.; Drake, R. R.; Powers, T. W.; Holst, S.; Wuhrer, M.; Mehta, A. S.; Drake, R. R. Two-Dimensional N-Glycan Distribution Mapping of Hepatocellular Carcinoma Tissues by MALDI-Imaging Mass Spectrometry. *Biomolecules* **2015**, *5* (4), 2554–2572. https://doi.org/10.3390/biom5042554.

(211) West, C. A.; Liang, H.; Drake, R. R.; Mehta, A. S. New Enzymatic Approach to Distinguish Fucosylation Isomers of N-Linked Glycans in Tissues Using MALDI Imaging Mass Spectrometry. *J. Proteome Res.* **2020**. https://doi.org/10.1021/acs.jproteome.0c00024.

(212) Black, A. P.; Angel, P. M.; Drake, R. R.; Mehta, A. S. Antibody Panel Based N -Glycan Imaging for N -Glycoprotein Biomarker Discovery. *Curr. Protoc. Protein Sci.* **2019**, *98* (1). https://doi.org/10.1002/cpps.99.

(213) Everest-Dass, A. V.; Briggs, M. T.; Kaur, G.; Oehler, M. K.; Hoffmann, P.; Packer, N. H. N-Glycan MALDI Imaging Mass Spectrometry on Formalin-Fixed Paraffin-Embedded Tissue Enables the Delineation of Ovarian Cancer Tissues. *Mol. Cell. Proteomics* **2016**, *15* (9), 3003–3016. https://doi.org/10.1074/mcp.M116.059816.

(214) Briggs, M. T.; Condina, M. R.; Klingler-Hoffmann, M.; Arentz, G.; Everest-Dass, A. V.; Kaur, G.; Oehler, M. K.; Packer, N. H.; Hoffmann, P. Translating *N*- Glycan Analytical Applications into Clinical Strategies for Ovarian Cancer. *PROTEOMICS – Clin. Appl.* **2019**, *13* (3), 1800099. https://doi.org/10.1002/prca.201800099.

(215) McDowell, C. T.; Klamer, Z.; Hall, J.; West, C. A.; Wisniewski, L.; Powers, T. W.; Angel, P. M.; Mehta, A. S.; Lewin, D. N.; Haab, B. B.; Drake, R. R. Imaging Mass Spectrometry and Lectin Analysis of N-Linked Glycans in Carbohydrate Antigen Defined Pancreatic Cancer Tissues. *Mol. Cell. Proteomics* **2020**, *20*, Manuscript submitted for review. https://doi.org/10.1074/mcp.ra120.002256.

(216) Drake, R. R.; McDowell, C.; West, C.; David, F.; Powers, T. W.; Nowling, T.; Bruner, E.; Mehta, A. S.; Angel, P. M.; Marlow, L. A.; Tun, H. W.; Copland, J. A. Defining the Human Kidney N-Glycome in Normal and Cancer Tissues Using MALDI Imaging Mass Spectrometry. *J. Mass Spectrom.* **2020**, *55* (4), e4490. https://doi.org/10.1002/jms.4490.

(217) Scott, D. A.; Drake, R. R. Glycosylation and Its Implications in Breast Cancer. *Expert Review of Proteomics*. Taylor and Francis Ltd 2019, pp 665–680. https://doi.org/10.1080/14789450.2019.1645604.

(218) Seyrek, K.; Richter, M.; Lavrik, I. N. Decoding the Sweet Regulation of Apoptosis: The Role of Glycosylation and Galectins in Apoptotic Signaling Pathways. *Cell Death and Differentiation*. Nature Publishing Group June 1, 2019, pp 981–993. https://doi.org/10.1038/s41418-019-0317-6.

(219) de Leoz, M. L. A.; Young, L. J. T.; An, H. J.; Kronewitter, S. R.; Kim, J.; Miyamoto, S.; Borowsky, A. D.; Chew, H. K.; Lebrilla, C. B. High-Mannose Glycans Are Elevated during Breast Cancer Progression. *Mol. Cell. Proteomics* **2011**, *10* (1), M110.002717. https://doi.org/10.1074/mcp.m110.002717.

(220) Lee, S. B.; Bose, S.; Ahn, S. H.; Son, B. H.; Ko, B. S.; Kim, H. J.; Chung, I. Y.; Kim, J.; Lee, W.; Ko, M.-S.; Lee, K.; Chang, S.; Park, H. S.; Lee, J. W.; Kim, D.-C. Breast Cancer Diagnosis by Analysis of Serum N-Glycans Using MALDI-TOF Mass Spectroscopy. *PLoS One* **2020**, *15* (4), e0231004. https://doi.org/10.1371/journal.pone.0231004.

(221) Lee, J. W.; Lee, K.; Ahn, S. H.; Son, B. H.; Ko, B. S.; Kim, H. J.; Chung, I. Y.; Kim, J.; Lee, W.; Ko, M. S.; Choi, S.; Chang, S.; Ko, C. K.; Lee, S. B.; Kim, D. C. Potential of MALDI-TOF-Based Serum N-Glycan Analysis for the Diagnosis and Surveillance of Breast Cancer. *Sci. Rep.* **2020**, *10* (1), 1–8. https://doi.org/10.1038/s41598-020-76195-y.

(222) De Freitas-Junior, J. C. M.; Morgado-Díaz, J. A. The Role of N-Glycans in Colorectal Cancer Progression: Potential Biomarkers and Therapeutic Applications. *Oncotarget*. Impact Journals LLC April 12, 2016, pp 19395–19413. https://doi.org/10.18632/oncotarget.6283.

(223) Balog, C. I. A.; Stavenhagen, K.; Fung, W. L. J.; Koeleman, C. A.; McDonnell, L. A.; Verhoeven, A.; Mesker, W. E.; Tollenaar, R. A. E. M.; Deelder, A. M.; Wuhrer, M. N-Glycosylation of Colorectal Cancer Tissues: A Liquid Chromatography and Mass Spectrometry-Based Investigation. *Mol. Cell. Proteomics* **2012**, *11* (9), 571–585. https://doi.org/10.1074/mcp.M111.011601.

(224) Holst, S.; Deuss, A. J. M.; Van Pelt, G. W.; Van Vliet, S. J.; Garcia-Vallejo, J. J.; Koeleman, C. A. M.; Deelder, A. M.; Mesker, W. E.; Tollenaar, R. A.; Rombouts, Y.; Wuhrer, M. N-Glycosylation Profiling of Colorectal Cancer Cell Lines Reveals Association of Fucosylation with Differentiation and Caudal Type Homebox 1 (CDX1)/Villin MRNA Expression. *Mol. Cell.*

Proteomics **2016**, *15* (1), 124–140.
https://doi.org/10.1074/mcp.M115.051235.

(225) de Vroome, S. W.; Holst, S.; Girondo, M. R.; van der Burgt, Y. E. M.; Mesker, W. E.; Tollenaar, R. A. E. M.; Wuhrer, M. Serum N-Glycome Alterations in Colorectal Cancer Associate with Survival. *Oncotarget* **2018**, *9* (55), 30610–30623. https://doi.org/10.18632/oncotarget.25753.

(226) Heijs, B.; Holst, S.; Briaire-De Bruijn, I. H.; Van Pelt, G. W.; De Ru, A. H.; Van Veelen, P. A.; Drake, R. R.; Mehta, A. S.; Mesker, W. E.; Tollenaar, R. A.; Bovée, J. V. M. G.; Wuhrer, M.; McDonnell, L. A. Multimodal Mass Spectrometry Imaging of N-Glycans and Proteins from the Same Tissue Section. *Anal. Chem.* **2016**, *88* (15), 7745–7753. https://doi.org/10.1021/acs.analchem.6b01739.

(227) Lemjabbar-Alaoui, H.; McKinney, A.; Yang, Y. W.; Tran, V. M.; Phillips, J. J. Glycosylation Alterations in Lung and Brain Cancer. In *Advances in Cancer Research*; Academic Press Inc., 2015; Vol. 126, pp 305–344. https://doi.org/10.1016/bs.acr.2014.11.007.

(228) Lattová, E.; Skřičková, J.; Hausnerová, J.; Frola, L.; Křen, L.; Ihnatová, I.; Zdráhal, Z.; Bryant, J.; Popovič, M. N-Glycan Profiling of Lung Adenocarcinoma in Patients at Different Stages of Disease. *Mod. Pathol.* **2020**, *33* (6), 1146–1156. https://doi.org/10.1038/s41379-019-0441-3.

(229) Garcia-Bunuel, R.; Monis, B. Histochemical Observations on Mucins in Human Ovarian Neoplasms. *Cancer* **1964**, *17* (9), 1108–1118. https://doi.org/10.1002/1097-0142(196409)17:9<1108::AID-CNCR2820170903>3.0.CO;2-8.

(230) Guo, H.; Abbott, K. L. Functional Impact of Tumor-Specific N-Linked Glycan Changes in Breast and Ovarian Cancers. In *Advances in Cancer Research*; Academic Press Inc., 2015; Vol. 126, pp 281–303. https://doi.org/10.1016/bs.acr.2014.11.006.

(231) Chen, H.; Deng, Z.; Huang, C.; Wu, H.; Zhao, X.; Li, Y. Mass Spectrometric Profiling Reveals Association of N-Glycan Patterns with Epithelial Ovarian Cancer Progression. *Tumor Biol.* **2017**, *39* (7), 101042831771624. https://doi.org/10.1177/1010428317716249.

(232) Briggs, M. T.; Condina, M. R.; Ho, Y. Y.; Everest-Dass, A. V.; Mittal, P.; Kaur, G.; Oehler, M. K.; Packer, N. H.; Hoffmann, P. MALDI Mass Spectrometry Imaging of Early- and Late-Stage Serous Ovarian Cancer Tissue Reveals Stage-Specific *N-* Glycans. *Proteomics* **2019**, *19* (21–22), 1800482. https://doi.org/10.1002/pmic.201800482.

(233) Powers, T. W.; Jones, E. E.; Betesh, L. R.; Romano, P. R.; Gao, P.; Copland, J. A.; Mehta, A. S.; Drake, R. R. Matrix Assisted Laser Desorption Ionization Imaging Mass Spectrometry Workflow for Spatial Profiling Analysis of N-Linked Glycan Expression in Tissues. *Anal. Chem.*

2013, *85* (20), 9799–9806. https://doi.org/10.1021/ac402108x.

(234) Gustafsson, O. J. R.; Briggs, M. T.; Condina, M. R.; Winderbaum, L. J.; Pelzing, M.; McColl, S. R.; Everest-Dass, A. V.; Packer, N. H.; Hoffmann, P. MALDI Imaging Mass Spectrometry of N-Linked Glycans on Formalin-Fixed Paraffin-Embedded Murine Kidney. *Anal. Bioanal. Chem.* **2015**, *407* (8), 2127–2139. https://doi.org/10.1007/s00216-014-8293-7.

(235) von Roemeling, C. A.; Marlow, L. A.; Radisky, D. C.; Rohl, A.; Larsen, H. E.; Wei, J.; Sasinowska, H.; Zhu, H.; Drake, R.; Sasinowski, M.; Tun, H. W.; Copland, J. A. Functional Genomics Identifies Novel Genes Essential for Clear Cell Renal Cell Carcinoma Tumor Cell Proliferation and Migration. *Oncotarget* **2014**, *5* (14), 5320–5334. https://doi.org/10.18632/oncotarget.2097.

(236) Neely, B. A.; Wilkins, C. E.; Marlow, L. A.; Malyarenko, D.; Kim, Y.; Ignatchenko, A.; Sasinowska, H.; Sasinowski, M.; Nyalwidhe, J. O.; Kislinger, T.; Copland, J. A.; Drake, R. R. Proteotranscriptomic Analysis Reveals Stage Specific Changes in the Molecular Landscape of Clear-Cell Renal Cell Carcinoma. *PLoS One* **2016**, *11* (4), e0154074. https://doi.org/10.1371/journal.pone.0154074.

(237) Munkley, J. The Glycosylation Landscape of Pancreatic Cancer. *Oncol. Lett.* **2019**, *17* (3), 2569–2575. https://doi.org/10.3892/ol.2019.9885.

(238) Krishnan, S.; Whitwell, H. J.; Cuenco, J.; Gentry-Maharaj, A.; Menon, U.; Pereira, S. P.; Gaspari, M.; Timms, J. F. Evidence of Altered Glycosylation of Serum Proteins Prior to Pancreatic Cancer Diagnosis. *Int. J. Mol. Sci.* **2017**, *18* (12). https://doi.org/10.3390/ijms18122670.

(239) Pérez-Garay, M.; Arteta, B.; Pagés, L.; de Llorens, R.; de Bolós, C.; Vidal-Vanaclocha, F.; Peracaula, R. A2,3-Sialyltransferase St3gal Iii Modulates Pancreatic Cancer Cell Motility and Adhesion in Vitro and Enhances Its Metastatic Potential in Vivo. *PLoS One* **2010**, *5* (9), 1–11. https://doi.org/10.1371/journal.pone.0012524.

(240) Hsieh, C.-C.; Shyr, Y.-M.; Liao, W.-Y.; Chen, T.-H.; Wang, S.-E.; Lu, P.-C.; Lin, P.-Y.; Chen, Y.-B.; Mao, W.-Y.; Han, H.-Y.; Hsiao, M.; Yang, W.-B.; Li, W.-S.; Sher, Y.-P.; Shen, C.-N. Elevation of β-Galactoside A2,6-Sialyltransferase 1 in a Fructose-Responsive Manner Promotes Pancreatic Cancer Metastasis. *Oncotarget* **2017**, *8* (5), 7691–7709. https://doi.org/10.18632/oncotarget.13845.

(241) Tada, K.; Ohta, M.; Hidano, S.; Watanabe, K.; Hirashita, T.; Oshima, Y.; Fujnaga, A.; Nakanuma, H.; Masuda, T.; Endo, Y.; Takeuchi, Y.; Iwashita, Y.; Kobayashi, T.; Inomata, M. Fucosyltransferase 8 Plays a Crucial Role in the Invasion and Metastasis of Pancreatic Ductal Adenocarcinoma. *Surg. Today* **2020**, *50* (7), 767–777. https://doi.org/10.1007/S00595-019-01953-Z/FIGURES/8.

(242) Gupta, R.; Leon, F.; Thompson, C. M.; Nimmakayala, R.; Karmakar, S.; Nallasamy, P.; Chugh, S.; Prajapati, D. R.; Rachagani, S.; Kumar, S.; Ponnusamy, M. P. Global Analysis of Human Glycosyltransferases Reveals Novel Targets for Pancreatic Cancer Pathogenesis. *Br. J. Cancer 2020 12211* **2020**, *122* (11), 1661–1672. https://doi.org/10.1038/s41416-020-0772-3.

(243) Pan, S.; Tamura, Y.; Chen, R.; May, D.; McIntosh, M. W.; Brentnall, T. A. Large-Scale Quantitative Glycoproteomics Analysis of Site-Specific Glycosylation Occupancy. *Mol. Biosyst.* **2012**, *8* (11), 2850. https://doi.org/10.1039/C2MB25268F.

(244) Pan, S.; Chen, R.; Tamura, Y.; Crispin, D. A.; Lai, L. A.; May, D. H.; McIntosh, M. W.; Goodlett, D. R.; Brentnall, T. A. Quantitative Glycoproteomics Reveals Changesin N-Glycosylation Level Associated with Pancreatic Ductal. *J. Proteome Res.* **2014**, *13* (3), 1293. https://doi.org/10.1021/PR4010184.

(245) Contessa, J. N.; Bhojani, M. S.; Freeze, H. H.; Rehemtulla, A.; Lawrence, T. S. Inhibition of N-Linked Glycosylation Disrupts Receptor Tyrosine Kinase Signaling in Tumor Cells. *Cancer Res.* **2008**, *68* (10), 3803. https://doi.org/10.1158/0008-5472.CAN-07-6389.

(246) Yue, T.; Goldstein, I. J.; Hollingsworth, M. A.; Kaul, K.; Brand, R. E.; Haab, B. B. The Prevalence and Nature of Glycan Alterations on Specific Proteins in Pancreatic Cancer Patients Revealed Using Antibody-Lectin Sandwich Arrays. *Mol. Cell. Proteomics* **2009**, *8* (7), 1697. https://doi.org/10.1074/MCP.M900135-MCP200.

(247) Park, H. M.; Hwang, M. P.; Kim, Y. W.; Kim, K. J.; Jin, J. M.; Kim, Y. H.; Yang, Y. H.; Lee, K. H.; Kim, Y. G. Mass Spectrometry-Based N-Linked Glycomic Profiling as a Means for Tracking Pancreatic Cancer Metastasis. *Carbohydr. Res.* **2015**, *413* (1), 5–11. https://doi.org/10.1016/J.CARRES.2015.04.019.

(248) Zhao, J.; Qiu, W.; Simeone, D. M.; Lubman, D. M. N-Linked Glycosylation Profiling of Pancreatic Cancer Serum Using Capillary Liquid Phase Separation Coupled with Mass Spectrometric Analysis. *J. Proteome Res.* **2007**, *6* (3), 1126–1138. https://doi.org/10.1021/PR0604458/SUPPL_FILE/PR0604458SI20061120_064158.XLS.

(249) Llop, E.; Guerrero, P. E.; Duran, A.; Barrabés, S.; Massaguer, A.; Ferri, M. J.; Albiol-Quer, M.; De Llorens, R.; Peracaula, R.; E Guerrero, P.; Duran, A.; Barrabés, S.; Massaguer, A.; José Ferri, M.; Albiol-Quer, M.; De Llorens, R.; Peracaula, R. Glycoprotein Biomarkers for the Detection of Pancreatic Ductal Adenocarcinoma. *World J. Gastroenterol.* **2018**, *24* (24), 2537–2554. https://doi.org/10.3748/wjg.v24.i24.2537.

(250) Verhelst, X.; Dias, A. M.; Colombel, J. F.; Vermeire, S.; Van Vlierberghe,

H.; Callewaert, N.; Pinho, S. S. Protein Glycosylation as a Diagnostic and Prognostic Marker of Chronic Inflammatory Gastrointestinal and Liver Diseases. *Gastroenterology* **2020**, *158* (1), 95–110. https://doi.org/10.1053/J.GASTRO.2019.08.060.

(251) Chatterjee, B. P.; Mondal, G.; Chatterjee, U. Glycosylation of Acute Phase Proteins: A Promising Disease Biomarker. *Proc. Natl. Acad. Sci. India Sect. B Biol. Sci. 2014 844* **2014**, *84* (4), 865–874. https://doi.org/10.1007/S40011-014-0331-X.

(252) Gornik, O.; Royle, L.; Harvey, D. J.; Radcliffe, C. M.; Saldova, R.; Dwek, R. A.; Rudd, P.; Lauc, G. Changes of Serum Glycans During Sepsis and Acute Pancreatitis. *Glycobiology* **2007**, *17* (12), 1321–1332. https://doi.org/10.1093/GLYCOB/CWM106.

(253) Angata, K.; Fukuda, M. Polysialyltransferases: Major Players in Polysialic Acid Synthesis on the Neural Cell Adhesion Molecule. *Biochimie* **2003**, *85* (1–2), 195–206. https://doi.org/10.1016/S0300-9084(03)00051-8.

(254) Bowles, W. H. D.; Gloster, T. M. Sialidase and Sialyltransferase Inhibitors: Targeting Pathogenicity and Disease. *Front. Mol. Biosci.* **2021**, *8*, 705. https://doi.org/10.3389/FMOLB.2021.705133/BIBTEX.

(255) Kooner, A. S.; Yu, H.; Chen, X. Synthesis of N-Glycolylneuraminic Acid (Neu5Gc) and Its Glycosides. *Front. Immunol.* **2019**, *10* (AUG), 2004. https://doi.org/10.3389/FIMMU.2019.02004/BIBTEX.

(256) Inoue, S.; Sato, C.; Kitajima, K. Extensive Enrichment of N-Glycolylneuraminic Acid in Extracellular Sialoglycoproteins Abundantly Synthesized and Secreted by Human Cancer Cells. *Glycobiology* **2010**, *20* (6), 752–762. https://doi.org/10.1093/GLYCOB/CWQ030.

(257) Bardor, M.; Nguyen, D. H.; Diaz, S.; Varki, A. Mechanism of Uptake and Incorporation of the Non-Human Sialic Acid N-Glycolylneuraminic Acid into Human Cells,. *J. Biol. Chem.* **2005**, *280* (6), 4228–4237. https://doi.org/10.1074/JBC.M412040200.

(258) Ghosh, S. Sialic Acids and Sialoglycoconjugates in the Biology of Life, Health and Disease. *Sialic Acids Sialoglycoconjugates Biol. Life, Heal. Dis.* **2020**, 1–362. https://doi.org/10.1016/C2017-0-03986-1.

(259) D'Addio, M.; Frey, J.; Otto, V. I. The Manifold Roles of Sialic Acid for the Biological Functions of Endothelial Glycoproteins. *Glycobiology* **2020**, *30* (8), 490. https://doi.org/10.1093/GLYCOB/CWAA008.

(260) Nightingale, T. D.; Frayne, M. E. F.; Clasper, S.; Banerji, S.; Jackson, D. G. A Mechanism of Sialylation Functionally Silences the Hyaluronan Receptor LYVE-1 in Lymphatic Endothelium. *J. Biol. Chem.* **2009**, *284* (6), 3935–3945. https://doi.org/10.1074/JBC.M805105200.

(261) Chiodelli, P.; Rezzola, S.; Urbinati, C.; Federici Signori, F.; Monti, E.;

Ronca, R.; Presta, M.; Rusnati, M. Contribution of Vascular Endothelial Growth Factor Receptor-2 Sialylation to the Process of Angiogenesis. *Oncogene 2017 3647* **2017**, *36* (47), 6531–6541. https://doi.org/10.1038/onc.2017.243.

(262) van de Wall, S.; Santegoets, K. C. M.; van Houtum, E. J. H.; Büll, C.; Adema, G. J. Sialoglycans and Siglecs Can Shape the Tumor Immune Microenvironment. *Trends Immunol.* **2020**, *41* (4), 274–285. https://doi.org/10.1016/J.IT.2020.02.001.

(263) Holdbrooks, A. T.; Britain, C. M.; Bellis, S. L. ST6Gal-I Sialyltransferase Promotes Tumor Necrosis Factor (TNF)-Mediated Cancer Cell Survival via Sialylation of the TNF Receptor 1 (TNFR1) Death Receptor. *J. Biol. Chem.* **2018**, *293* (5), 1610–1622. https://doi.org/10.1074/JBC.M117.801480.

(264) Liu, Y.; Pan, D.; Bellis, S. L.; Song, Y. Effect of Altered Glycosylation on the Structure of the I-like Domain of Beta1 Integrin: A Molecular Dynamics Study. *Proteins* **2008**, *73* (4), 989–1000. https://doi.org/10.1002/PROT.22126.

(265) Läubli, H.; Borsig, L. Altered Cell Adhesion and Glycosylation Promote Cancer Immune Suppression and Metastasis. *Front. Immunol.* **2019**, *10*, 2120. https://doi.org/10.3389/FIMMU.2019.02120.

(266) Xu, D.; Newhouse, E. I.; Amaro, R. E.; Pao, H. C.; Cheng, L. S.; Markwick, P. R. L.; McCammon, J. A.; Li, W. W.; Arzberger, P. W. Distinct Glycan Topology for Avian and Human Sialo-Pentasaccharide Receptor Analogues upon Binding Different Hemagglutinins: A Molecular Dynamics Perspective. *J. Mol. Biol.* **2009**, *387* (2), 465. https://doi.org/10.1016/J.JMB.2009.01.040.

(267) Bhagavat, R.; Chandra, N. Common Recognition Principles across Diverse Sequence and Structural Families of Sialic Acid Binding Proteins. *Glycobiology* **2014**, *24* (1), 5–16. https://doi.org/10.1093/GLYCOB/CWT063.

(268) Teppa, R. E.; Petit, D.; Plechakova, O.; Cogez, V.; Harduin-Lepers, A. Phylogenetic-Derived Insights into the Evolution of Sialylation in Eukaryotes: Comprehensive Analysis of Vertebrate β-Galactoside A2,3/6-Sialyltransferases (ST3Gal and ST6Gal). *Int. J. Mol. Sci. 2016, Vol. 17, Page 1286* **2016**, *17* (8), 1286. https://doi.org/10.3390/IJMS17081286.

(269) Liu, Z.; Swindall, A. F.; Kesterson, R. A.; Schoeb, T. R.; Bullard, D. C.; Bellis, S. L. ST6Gal-I Regulates Macrophage Apoptosis via A2-6 Sialylation of the TNFR1 Death Receptor. *J. Biol. Chem.* **2011**, *286* (45), 39654–39662. https://doi.org/10.1074/JBC.M111.276063.

(270) Miyagi, T.; Wada, T.; Yamaguchi, K.; Hata, K. Sialidase and Malignancy: A Minireview. *Glycoconjugate J. 2003 203* **2003**, *20* (3), 189–198. https://doi.org/10.1023/B:GLYC.0000024250.48506.BF.

(271) Stanczak, M. A.; Mantuano, N. R.; Kirchhammer, N.; Sanin, D. E.; Jacob, F.; Coelho, R.; Everest-Dass, A. V.; Wang, J.; Trefny, M. P.; Monaco, G.; Bärenwaldt, A.; Gray, M. A.; Petrone, A.; Kashyap, A. S.; Glatz, K.; Kasenda, B.; Normington, K.; Broderick, J.; Peng, L.; Pearce, O. M. T.; Pearce, E. L.; Bertozzi, C. R.; Zippelius, A.; Läubli, H. Targeting Cancer Glycosylation Repolarizes Tumor-Associated Macrophages Allowing Effective Immune Checkpoint Blockade. *Sci. Transl. Med.* **2022**, *14* (669). https://doi.org/10.1126/SCITRANSLMED.ABJ1270.

(272) Swindall, A. F.; Bellis, S. L. Sialylation of the Fas Death Receptor by ST6Gal-I Provides Protection against Fas-Mediated Apoptosis in Colon Carcinoma Cells. *J. Biol. Chem.* **2011**, *286* (26), 22982–22990. https://doi.org/10.1074/JBC.M110.211375.

(273) Gretschel, S.; Haensch, W.; Schlag, P. M.; Kemmner, W. Clinical Relevance of Sialyltransferases ST6GAL-I and ST3GAL-III in Gastric Cancer. *Oncology* **2003**, *65* (2), 139–145. https://doi.org/10.1159/000072339.

(274) Jin, X. L.; Zheng, S. Sen; Wang, B. S.; Chen, H. L. Correlation of Glycosyltransferases MRNA Expression in Extrahepatic Bile Duct Carcinoma with Clinical Pathological Characteristics. *Hepatobiliary Pancreat. Dis. Int* **2004**, *3* (2), 292–295.

(275) Glavey, S. V.; Manier, S.; Natoni, A.; Sacco, A.; Moschetta, M.; Reagan, M. R.; Murillo, L. S.; Sahin, I.; Wu, P.; Mishima, Y.; Zhang, Y.; Zhang, W.; Zhang, Y.; Morgan, G.; Joshi, L.; Roccaro, A. M.; Ghobrial, I. M.; O'Dwyer, M. E. The Sialyltransferase ST3GAL6 Influences Homing and Survival in Multiple Myeloma. *Blood* **2014**, *124* (11), 1765–1776. https://doi.org/10.1182/BLOOD-2014-03-560862.

(276) Mulloy, B.; Dell, A.; Stanley, P.; Prestegard, J. H. Structural Analysis of Glycans. **2017**. https://doi.org/10.1101/GLYCOBIOLOGY.3E.050.

(277) Varki, A.; Sharon, N. Historical Background and Overview. *Essentials Glycobiol.* **2009**.

(278) Montreuil, J. Chapter 1: The History of Glycoprotein Research, a Personal View. *New Compr. Biochem.* **1995**, *29* (PA), 1–12. https://doi.org/10.1016/S0167-7306(08)60584-0.

(279) Cummings, R. D.; Darvill, A. G.; Etzler, M. E.; Hahn, M. G. Glycan-Recognizing Probes as Tools. **2017**. https://doi.org/10.1101/GLYCOBIOLOGY.3E.048.

(280) Lam, S. K.; Ng, T. B. Lectins: Production and Practical Applications. *Appl. Microbiol. Biotechnol.* **2011**, *89* (1), 45. https://doi.org/10.1007/S00253-010-2892-9.

(281) Bojar, D.; Meche, L.; Meng, G.; Eng, W.; Smith, D. F.; Cummings, R. D.; Mahal, L. K. A Useful Guide to Lectin Binding: Machine-Learning Directed

Annotation of 57 Unique Lectin Specificities. *ACS Chem. Biol.* **2021**. https://doi.org/10.1021/ACSCHEMBIO.1C00689/SUPPL_FILE/CB1C00689 _SI_006.XLSX.

(282) Landry, J. P.; Ke, Y.; Yu, G. L.; Zhu, X. D. Measuring Affinity Constants of 1,450 Monoclonal Antibodies to Peptide Targets with a Microarray-Based Label-Free Assay Platform. *J. Immunol. Methods* **2015**, *417*, 86. https://doi.org/10.1016/J.JIM.2014.12.011.

(283) Cummings, R. D.; Etzler, M. E. *Antibodies and Lectins in Glycan Analysis*; Cold Spring Harbor Laboratory Press, 2009.

(284) Totten, S. M.; Kullolli, M.; Pitteri, S. J. Multi-Lectin Affinity Chromatography for Separation, Identification, and Quantitation of Intact Protein Glycoforms in Complex Biological Mixtures. *Methods Mol. Biol.* **2017**, *1550*, 99–112. https://doi.org/10.1007/978-1-4939-6747-6_9/FIGURES/3.

(285) O'Connor, B.; Monaghan, D.; Cawley, J. Lectin Affinity Chromatography (LAC). *Methods Mol. Biol.* **2017**, *1485*, 411–420. https://doi.org/10.1007/978-1-4939-6412-3_23/FIGURES/2.

(286) Abdu Hussen, A. High-Performance Liquid Chromatography (HPLC): A Review. *Ann. Adv. Chem.* **2022**, *6* (1), 010–020. https://doi.org/10.29328/JOURNAL.AAC.1001026.

(287) Molnarova, K.; Cokrtova, K.; Tomnikova, A.; Krizek, T.; Kozlik, P. Liquid Chromatography and Capillary Electrophoresis in Glycomic and Glycoproteomic Analysis. *Monatshefte für Chemie - Chem. Mon. 2022 1539* **2022**, *153* (9), 659–686. https://doi.org/10.1007/S00706-022-02938-4.

(288) Guile, G. R.; Rudd, P. M.; Wing, D. R.; Prime, S. B.; Dwek, R. A. A Rapid High-Resolution High-Performance Liquid Chromatographic Method for Separating Glycan Mixtures and Analyzing Oligosaccharide Profiles. *Anal. Biochem.* **1996**, *240* (2), 210–226. https://doi.org/10.1006/abio.1996.0351.

(289) Zhou, S.; Veillon, L.; Dong, X.; Huang, Y.; Mechref, Y. Direct Comparison of Derivatization Strategies for LC-MS/MS Analysis of N-Glycans. *Analyst* **2017**, *142* (23), 4446–4455. https://doi.org/10.1039/C7AN01262D.

(290) Zhang, L.; Luo, S.; Zhang, B. Glycan Analysis of Therapeutic Glycoproteins. *MAbs* **2016**, *8* (2), 205. https://doi.org/10.1080/19420862.2015.1117719.

(291) Hanić, M.; Lauc, G.; Trbojević-Akmačić, I. N-Glycan Analysis by Ultra-Performance Liquid Chromatography and Capillary Gel Electrophoresis with Fluorescent Labeling. *Curr. Protoc. Protein Sci.* **2019**, *97* (1), e95. https://doi.org/10.1002/CPPS.95.

(292) Glish, G. L.; Vachet, R. W. The Basics of Mass Spectrometry in the Twenty-First Century. *Nat. Rev. Drug Discov. 2003 22* **2003**, *2* (2), 140–

150. https://doi.org/10.1038/nrd1011.

(293) Awad, H.; Khamis, M. M.; El-Aneed, A. Mass Spectrometry, Review of the Basics: Ionization. *http://dx.doi.org/10.1080/05704928.2014.954046* **2014**, *50* (2), 158–175. https://doi.org/10.1080/05704928.2014.954046.

(294) Haag, A. M. Mass Analyzers and Mass Spectrometers. *Adv. Exp. Med. Biol.* **2016**, *919*, 157–169. https://doi.org/10.1007/978-3-319-41448-5_7/FIGURES/8.

(295) Medhe, S. Mass Spectrometry: Detectors Review. *http://www.sciencepublishinggroup.com* **2018**, *3* (4), 51. https://doi.org/10.11648/J.CBE.20180304.11.

(296) Ho, C. S.; Lam, C. W. K.; Chan, M. H. M.; Cheung, R. C. K.; Law, L. K.; Lit, L. C. W.; Ng, K. F.; Suen, M. W. M.; Tai, H. L. Electrospray Ionisation Mass Spectrometry: Principles and Clinical Applications. *Clin. Biochem. Rev.* **2003**, *24* (1), 3.

(297) Grebe, S. K. G.; Singh, R. J. LC-MS/MS in the Clinical Laboratory – Where to From Here? *Clin. Biochem. Rev.* **2011**, *32* (1), 5.

(298) Banerjee, S.; Mazumdar, S. Electrospray Ionization Mass Spectrometry: A Technique to Access the Information beyond the Molecular Weight of the Analyte. *Int. J. Anal. Chem.* **2012**, *2012*, 1–40. https://doi.org/10.1155/2012/282574.

(299) Harvey, D. J.; Struwe, W. B.; Behrens, A. J.; Vasiljevic, S.; Crispin, M. Formation and Fragmentation of Doubly and Triply Charged Ions in the Negative Ion Spectra of Neutral N-Glycans from Viral and Other Glycoproteins. *Anal. Bioanal. Chem.* **2021**, *413* (29), 7277–7294. https://doi.org/10.1007/S00216-021-03480-8/FIGURES/9.

(300) Suzuki, N. Tissue N-Glycan Analysis Using LC-MS, MS/MS, and MSn. *Curr. Protoc.* **2021**, *1* (7), e200. https://doi.org/10.1002/CPZ1.200.

(301) Pacholski, M. L.; Winograd, N. Imaging with Mass Spectrometry. *Chem. Rev.* **1999**, *99* (10), 2977–3005. https://doi.org/10.1021/cr980137w.

(302) Benninghoven, A. Chemical Analysis of Inorganic and Organic Surfaces and Thin Films by Static Time-of-Flight Secondary Ion Mass Spectrometry (TOF-SIMS). *Angewandte Chemie International Edition in English*. John Wiley & Sons, Ltd June 6, 1994, pp 1023–1043. https://doi.org/10.1002/anie.199410231.

(303) Caprioli, R. M.; Farmer, T. B.; Gile, J. Molecular Imaging of Biological Samples: Localization of Peptides and Proteins Using MALDI-TOF MS. *Anal. Chem.* **1997**, *69* (23), 4751–4760. https://doi.org/10.1021/ac970888i.

(304) Karas, M.; Bahr, U. Laser Desorption Ionization Mass Spectrometry of Large Biomolecules. *Trends in Analytical Chemistry*. Elsevier November 1,

1990, pp 321–325. https://doi.org/10.1016/0165-9936(90)85065-F.

(305) Pineau, C. MALDI Imaging Mass Spectrometry: Applications, Limitations and Potential. In *Farm animal proteomics 2013*; Wageningen Academic Publishers, 2013; pp 34–35. https://doi.org/10.3920/978-90-8686-776-9_9.

(306) Tan, W. C. C.; Nerurkar, S. N.; Cai, H. Y.; Ng, H. H. M.; Wu, D.; Wee, Y. T. F.; Lim, J. C. T.; Yeong, J.; Lim, T. K. H. Overview of Multiplex Immunohistochemistry/Immunofluorescence Techniques in the Era of Cancer Immunotherapy. *Cancer Communications*. John Wiley and Sons Inc. April 1, 2020, pp 135–153. https://doi.org/10.1002/cac2.12023.

(307) Bowman, A. P.; Blakney, G. T.; Hendrickson, C. L.; Ellis, S. R.; Heeren, R. M. A.; Smith, D. F. Ultra-High Mass Resolving Power, Mass Accuracy, and Dynamic Range MALDI Mass Spectrometry Imaging by 21-T FT-ICR MS. *Anal. Chem.* **2020**, *92* (4), 3133–3142. https://doi.org/10.1021/acs.analchem.9b04768.

(308) Prentice, B. M.; Caprioli, R. M. The Need for Speed in Matrix-Assisted Laser Desorption/Ionization Imaging Mass Spectrometry. *Postdoc J.* **2016**, *4* (3), 3. https://doi.org/10.14304/surya.jpr.v4n3.1.

(309) Mainini, V.; Bovo, G.; Chinello, C.; Gianazza, E.; Grasso, M.; Cattoretti, G.; Magni, F. Detection of High Molecular Weight Proteins by MALDI Imaging Mass Spectrometry. *Mol. Biosyst.* **2013**, *9* (6), 1101–1107. https://doi.org/10.1039/c2mb25296a.

(310) Leopold, J.; Popkova, Y.; Engel, K. M.; Schiller, J. Recent Developments of Useful MALDI Matrices for the Mass Spectrometric Characterization of Lipids. *Biomolecules*. MDPI AG December 1, 2018, p 173. https://doi.org/10.3390/biom8040173.

(311) Robinson, K. N.; Steven, R. T.; Bunch, J. Matrix Optical Absorption in UV-MALDI MS. *J. Am. Soc. Mass Spectrom.* **2018**, *29* (3), 501–511. https://doi.org/10.1007/s13361-017-1843-4.

(312) Holle, A.; Haase, A.; Kayser, M.; Höhndorf, J. Optimizing UV Laser Focus Profiles for Improved MALDI Performance. *Journal of Mass Spectrometry*. John Wiley & Sons, Ltd June 1, 2006, pp 705–716. https://doi.org/10.1002/jms.1041.

(313) Chang, W. C.; Huang, L. C. L.; Wang, Y. S.; Peng, W. P.; Chang, H. C.; Hsu, N. Y.; Yang, W. Bin; Chen, C. H. Matrix-Assisted Laser Desorption/Ionization (MALDI) Mechanism Revisited. *Anal. Chim. Acta* **2007**, *582* (1), 1–9. https://doi.org/10.1016/j.aca.2006.08.062.

(314) Drake, R. R.; Powers, T. W.; Norris-Caneda, K.; Mehta, A. S.; Angel, P. M. In Situ Imaging of N-Glycans by MALDI Imaging Mass Spectrometry of Fresh or Formalin-Fixed Paraffin-Embedded Tissue. *Curr. Protoc. Protein Sci.* **2018**, *94* (1), e68. https://doi.org/10.1002/cpps.68.

(315) Holst, S.; Belo, A. I.; Giovannetti, E.; Van Die, I.; Wuhrer, M. Profiling of Different Pancreatic Cancer Cells Used as Models for Metastatic Behaviour Shows Large Variation in Their N-Glycosylation. *Sci. Rep.* **2017**, *7* (1), 1–15. https://doi.org/10.1038/s41598-017-16811-6.

(316) Tarentino, A. L.; Plummer, T. H. Enzymatic Deglycosylation of Asparagine-Linked Glycans: Purification, Properties, and Specificity of Oligosaccharide-Cleaving Enzymes from Flavobacterium Meningosepticum. *Methods Enzymol.* **1994**, *230* (C), 44–57. https://doi.org/10.1016/0076-6879(94)30006-2.

(317) Karas, M.; Bachmann, D.; Hillenkamp, F. Influence of the Wavelength in High-Irradiance Ultraviolet Laser Desorption Mass Spectrometry of Organic Molecules. *Anal. Chem.* **1985**, *57* (14), 2935–2939. https://doi.org/10.1021/ac00291a042.

(318) Karas, M.; Hillenkamp, F. Laser Desorption Ionization of Proteins with Molecular Masses Exceeding 10 000 Daltons. *Analytical Chemistry*. American Chemical Society October 1, 1988, pp 2299–2301. https://doi.org/10.1021/ac00171a028.

(319) Jaskolla, T. W.; Karas, M. Compelling Evidence for Lucky Survivor and Gas Phase Protonation: The Unified MALDI Analyte Protonation Mechanism. *J. Am. Soc. Mass Spectrom.* **2011**, *22* (6), 976–988. https://doi.org/10.1007/s13361-011-0093-0.

(320) Hossain, M.; Limbach, P. A. A Comparison of MALDI Matrices. In *Electrospray and MALDI Mass Spectrometry*; John Wiley & Sons, Inc.: Hoboken, NJ, USA, 2012; pp 215–244. https://doi.org/10.1002/9780470588901.ch7.

(321) Nishikaze, T. Sensitive and Structure-Informative N-Glycosylation Analysis by MALDI-MS; Ionization, Fragmentation, and Derivatization. *Mass Spectrom.* **2017**, *6* (1), A0060–A0060. https://doi.org/10.5702/massspectrometry.a0060.

(322) Gemperline, E.; Rawson, S.; Li, L. Optimization and Comparison of Multiple MALDI Matrix Application Methods for Small Molecule Mass Spectrometric Imaging. *Anal. Chem.* **2014**, *86* (20), 10030–10035. https://doi.org/10.1021/ac5028534.

(323) Yang, J.; Caprioli, R. M. Matrix Sublimation/Recrystallization for Imaging Proteins by Mass Spectrometry at High Spatial Resolution. *Anal. Chem.* **2011**, *83* (14), 5728–5734. https://doi.org/10.1021/ac200998a.

(324) Harvey, D. J. Negative Ion Mass Spectrometry for the Analysis of N-Linked Glycans. *Mass Spectrom. Rev.* **2020**, *39* (5–6), 586–679. https://doi.org/10.1002/mas.21622.

(325) Boesl, U. Time-of-Flight Mass Spectrometry: Introduction to the Basics. *Mass Spectrom. Rev.* **2017**, *36* (1), 86–109.

https://doi.org/10.1002/mas.21520.

(326) Marshall, A. G.; Blakney, G. T.; Chen, T.; Kaiser, N. K.; McKenna, A. M.; Rodgers, R. P.; Ruddy, B. M.; Xian, F. Mass Resolution and Mass Accuracy: How Much Is Enough? *Mass Spectrom.* **2013**, *2* (Spec Iss), S0009–S0009. https://doi.org/10.5702/MASSSPECTROMETRY.S0009.

(327) Ogrinc Potočnik, N.; Porta, T.; Becker, M.; Heeren, R. M. A.; Ellis, S. R. Use of Advantageous, Volatile Matrices Enabled by next-Generation High-Speed Matrix-Assisted Laser Desorption/Ionization Time-of-Flight Imaging Employing a Scanning Laser Beam. *Rapid Commun. Mass Spectrom.* **2015**, *29* (23), 2195–2203. https://doi.org/10.1002/rcm.7379.

(328) Kamata, T.; Shima, N.; Miki, A.; Matsuo, E.; Yamamoto, T.; Tsuchihashi, H.; Sato, T.; Shimma, S.; Katagi, M. High Spatial-Resolution Matrix-Assisted Laser Desorption/Ionization-Ion Trap-Time-of-Flight Tandem Mass Spectrometry Imaging for Depicting Longitudinal and Transverse Distribution of Drugs Incorporated into Hair. *Anal. Chem.* **2020**, *92* (8), 5821–5829. https://doi.org/10.1021/acs.analchem.9b05401.

(329) Lee, J.; Reilly, P. T. A. Limitation of Time-of-Flight Resolution in the Ultra High Mass Range. *Anal. Chem.* **2011**, *83* (15), 5831–5833. https://doi.org/10.1021/ac201537b.

(330) North, S. J.; Huang, H. H.; Sundaram, S.; Jang-Lee, J.; Etienne, A. T.; Trollope, A.; Chalabi, S.; Dell, A.; Stanley, P.; Haslam, S. M. Glycomics Profiling of Chinese Hamster Ovary Cell Glycosylation Mutants Reveals N-Glycans of a Novel Size and Complexity. *J. Biol. Chem.* **2010**, *285* (8), 5759–5775. https://doi.org/10.1074/jbc.M109.068353.

(331) Wang, C. C.; Lai, Y. H.; Ou, Y. M.; Chang, H. T.; Wang, Y. S. Critical Factors Determining the Quantification Capability of Matrix-Assisted Laser Desorption/Ionization-Time-of-Flight Mass Spectrometry. *Philosophical Transactions of the Royal Society A: Mathematical, Physical and Engineering Sciences*. Royal Society of London October 28, 2016. https://doi.org/10.1098/rsta.2015.0371.

(332) Lai, Y.-H.; Wang, Y.-S. Matrix-Assisted Laser Desorption/Ionization Mass Spectrometry: Mechanistic Studies and Methods for Improving the Structural Identification of Carbohydrates. *Mass Spectrom.* **2017**, *6* (3), S0072–S0072. https://doi.org/10.5702/massspectrometry.s0072.

(333) Page, J. S.; Kelly, R. T.; Tang, K.; Smith, R. D. Ionization and Transmission Efficiency in an Electrospray Ionization-Mass Spectrometry Interface. *J. Am. Soc. Mass Spectrom.* **2007**, *18* (9), 1582–1590. https://doi.org/10.1016/j.jasms.2007.05.018.

(334) Barré, F. P. Y.; Paine, M. R. L.; Flinders, B.; Trevitt, A. J.; Kelly, P. D.; Ait-Belkacem, R.; Garcia, J. P.; Creemers, L. B.; Stauber, J.; Vreeken, R. J.; Cillero-Pastor, B.; Ellis, S. R.; Heeren, R. M. A. Enhanced Sensitivity Using

Maldi Imaging Coupled with Laser Postionization (Maldi-2) for Pharmaceutical Research. *Anal. Chem.* **2019**, *91* (16), 10840–10848. https://doi.org/10.1021/acs.analchem.9b02495.

(335) Niehaus, M.; Soltwisch, J.; Belov, M. E.; Dreisewerd, K. Transmission-Mode MALDI-2 Mass Spectrometry Imaging of Cells and Tissues at Subcellular Resolution. *Nat. Methods* **2019**, *16* (9), 925–931. https://doi.org/10.1038/s41592-019-0536-2.

(336) Zavalin, A.; Todd, E. M.; Rawhouser, P. D.; Yang, J.; Norris, J. L.; Caprioli, R. M. Direct Imaging of Single Cells and Tissue at Sub-Cellular Spatial Resolution Using Transmission Geometry MALDI MS. *J. Mass Spectrom.* **2012**, *47* (11), i–i. https://doi.org/10.1002/jms.3132.

(337) Karabacak, N. M.; Easterling, M. L.; Agar, N. Y. R.; Agar, J. N. Transformative Effects of Higher Magnetic Field in Fourier Transform Ion Cyclotron Resonance Mass Spectrometry. *J. Am. Soc. Mass Spectrom.* **2010**, *21* (7), 1218–1222. https://doi.org/10.1016/j.jasms.2010.03.033.

(338) Smith, D. F.; Podgorski, D. C.; Rodgers, R. P.; Blakney, G. T.; Hendrickson, C. L. 21 Tesla FT-ICR Mass Spectrometer for Ultrahigh-Resolution Analysis of Complex Organic Mixtures. *Anal. Chem.* **2018**, *90* (3), 2041–2047. https://doi.org/10.1021/acs.analchem.7b04159.

(339) Marshall, A. G.; Hendrickson, C. L.; Jackson, G. S. Fourier Transform Ion Cyclotron Resonance Mass Spectrometry: A Primer. *Mass Spectrom. Rev.* **1998**, *17* (1), 1–35. https://doi.org/10.1002/(SICI)1098-2787(1998)17:1<1::AID-MAS1>3.0.CO;2-K.

(340) Scigelova, M.; Hornshaw, M.; Giannakopulos, A.; Makarov, A. Fourier Transform Mass Spectrometry. *Molecular and Cellular Proteomics*. American Society for Biochemistry and Molecular Biology July 2011. https://doi.org/10.1074/mcp.M111.009431.

(341) Makarov, A. Electrostatic Axially Harmonic Orbital Trapping: A High-Performance Technique of Mass Analysis. *Anal. Chem.* **2000**, *72* (6), 1156–1162. https://doi.org/10.1021/ac991131p.

(342) Hu, Q.; Noll, R. J.; Li, H.; Makarov, A.; Hardman, M.; Cooks, R. G. The Orbitrap: A New Mass Spectrometer. *Journal of Mass Spectrometry*. John Wiley & Sons, Ltd April 1, 2005, pp 430–443. https://doi.org/10.1002/jms.856.

(343) Zubarev, R. A.; Makarov, A. Orbitrap Mass Spectrometry. *Anal. Chem.* **2013**, *85* (11), 5288–5296. https://doi.org/10.1021/ac4001223.

(344) Denisov, E.; Damoc, E.; Lange, O.; Makarov, A. Orbitrap Mass Spectrometry with Resolving Powers above 1,000,000. *Int. J. Mass Spectrom.* **2012**, *325–327*, 80–85. https://doi.org/10.1016/j.ijms.2012.06.009.

(345) Michalski, A.; Damoc, E.; Lange, O.; Denisov, E.; Nolting, D.; Müller, M.; Viner, R.; Schwartz, J.; Remes, P.; Belford, M.; Dunyach, J. J.; Cox, J.; Horning, S.; Mann, M.; Makarov, A. Ultra High Resolution Linear Ion Trap Orbitrap Mass Spectrometer (Orbitrap Elite) Facilitates Top down LC MS/MS and Versatile Peptide Fragmentation Modes. *Mol. Cell. Proteomics* **2012**, *11* (3), 1–11. https://doi.org/10.1074/mcp.O111.013698.

(346) Kharchenko, A.; Vladimirov, G.; Heeren, R. M. A.; Nikolaev, E. N. Performance of Orbitrap Mass Analyzer at Various Space Charge and Non-Ideal Field Conditions: Simulation Approach. *J. Am. Soc. Mass Spectrom.* **2012**, *23* (5), 977–987. https://doi.org/10.1007/s13361-011-0325-3.

(347) Zhu, H.; Qiu, C.; Gryniewicz-Ruzicka, C. M.; Keire, D. A.; Ye, H. Multiplexed Comparative Analysis of Intact Glycopeptides Using Electron-Transfer Dissociation and Synchronous Precursor Selection Based Triple-Stage Mass Spectrometry. *Anal. Chem.* **2020**, *92* (11), 7547–7555. https://doi.org/10.1021/acs.analchem.0c00014.

(348) Alexandrov, T. MALDI Imaging Mass Spectrometry: Statistical Data Analysis and Current Computational Challenges. *BMC bioinformatics*. BioMed Central 2012, p S11. https://doi.org/10.1186/1471-2105-13-s16-s11.

(349) Chambers, M. C.; MacLean, B.; Burke, R.; Amodei, D.; Ruderman, D. L.; Neumann, S.; Gatto, L.; Fischer, B.; Pratt, B.; Egertson, J.; Hoff, K.; Kessner, D.; Tasman, N.; Shulman, N.; Frewen, B.; Baker, T. A.; Brusniak, M. Y.; Paulse, C.; Creasy, D.; Flashner, L.; Kani, K.; Moulding, C.; Seymour, S. L.; Nuwaysir, L. M.; Lefebvre, B.; Kuhlmann, F.; Roark, J.; Rainer, P.; Detlev, S.; Hemenway, T.; Huhmer, A.; Langridge, J.; Connolly, B.; Chadick, T.; Holly, K.; Eckels, J.; Deutsch, E. W.; Moritz, R. L.; Katz, J. E.; Agus, D. B.; MacCoss, M.; Tabb, D. L.; Mallick, P. A Cross-Platform Toolkit for Mass Spectrometry and Proteomics. *Nature Biotechnology*. NIH Public Access October 2012, pp 918–920. https://doi.org/10.1038/nbt.2377.

(350) Bokhart, M. T.; Nazari, M.; Garrard, K. P.; Muddiman, D. C. MSiReader v1.0: Evolving Open-Source Mass Spectrometry Imaging Software for Targeted and Untargeted Analyses. *J. Am. Soc. Mass Spectrom.* **2018**, *29* (1), 8–16. https://doi.org/10.1007/s13361-017-1809-6.

(351) Bemis, K. D.; Harry, A.; Eberlin, L. S.; Ferreira, C.; Ven, S. M. van de; Mallick, P.; Stolowitz, M.; Vitek, O. Cardinal: An R Package for Statistical Analysis of Mass Spectrometry-Based Imaging Experiments. *Bioinformatics* **2015**, *31* (14), 2418–2420.

(352) Källback, P.; Nilsson, A.; Shariatgorji, M.; Andrén, P. E. MsIQuant - Quantitation Software for Mass Spectrometry Imaging Enabling Fast Access, Visualization, and Analysis of Large Data Sets. *Anal. Chem.* **2016**,

88 (8), 4346–4353. https://doi.org/10.1021/acs.analchem.5b04603.

(353) Römpp, A.; Schramm, T.; Hester, A.; Klinkert, I.; Both, J. P.; Heeren, R. M. A.; Stöckli, M.; Spengler, B. ImzML: Imaging Mass Spectrometry Markup Language: A Common Data Format for Mass Spectrometry Imaging. *Methods Mol. Biol.* **2011**, *696*, 205–224. https://doi.org/10.1007/978-1-60761-987-1_12.

(354) Aichler, M.; Walch, A. MALDI Imaging Mass Spectrometry: Current Frontiers and Perspectives in Pathology Research and Practice. *Lab. Investig.* **2015**, *95* (4), 422–431. https://doi.org/10.1038/labinvest.2014.156.

(355) Alexandrov, T.; Becker, M.; Deininger, S. O.; Ernst, G.; Wehder, L.; Grasmair, M.; Von Eggeling, F.; Thiele, H.; Maass, P. Spatial Segmentation of Imaging Mass Spectrometry Data with Edge-Preserving Image Denoising and Clustering. *J. Proteome Res.* **2010**, *9* (12), 6535–6546. https://doi.org/10.1021/pr100734z.

(356) McCombie, G.; Staab, D.; Stoeckli, M.; Knochenmuss, R. Spatial and Spectral Correlations in MALDI Mass Spectrometry Images by Clustering and Multivariate Analysis. *Anal. Chem.* **2005**, *77* (19), 6118–6124. https://doi.org/10.1021/ac051081q.

(357) Porta Siegel, T.; Hamm, G.; Bunch, J.; Cappell, J.; Fletcher, J. S.; Schwamborn, K. Mass Spectrometry Imaging and Integration with Other Imaging Modalities for Greater Molecular Understanding of Biological Tissues. *Molecular Imaging and Biology*. Springer New York LLC December 1, 2018, pp 888–901. https://doi.org/10.1007/s11307-018-1267-y.

(358) Levenson, R. M.; Borowsky, A. D.; Angelo, M. Immunohistochemistry and Mass Spectrometry for Highly Multiplexed Cellular Molecular Imaging. *Lab. Investig.* **2015**, *95* (4), 397–405. https://doi.org/10.1038/labinvest.2015.2.

(359) Woodin, C. L.; Maxon, M.; Desaire, H. Software for Automated Interpretation of Mass Spectrometry Data from Glycans and Glycopeptides. *Analyst*. Royal Society of Chemistry May 21, 2013, pp 2793–2803. https://doi.org/10.1039/c2an36042j.

(360) Damerell, D.; Ceroni, A.; Maass, K.; Ranzinger, R.; Dell, A.; Haslam, S. M. Annotation of Glycomics MS and MS/MS Spectra Using the Glycoworkbench Software Tool. *Methods Mol. Biol.* **2015**, *1273*, 3–15. https://doi.org/10.1007/978-1-4939-2343-4_1.

(361) Cooper, C. A.; Gasteiger, E.; Packer, N. H. GlycoMod - A Software Tool for Determining Glycosylation Compositions from Mass Spectrometric Data. *Proteomics* **2001**, *1* (2), 340–349. https://doi.org/10.1002/1615-9861(200102)1:2<340::AID-PROT340>3.0.CO;2-B.

(362) Alocci, D.; Mariethoz, J.; Gastaldello, A.; Gasteiger, E.; Karlsson, N. G.; Kolarich, D.; Packer, N. H.; Lisacek, F. GlyConnect: Glycoproteomics Goes

Visual, Interactive, and Analytical. *J. Proteome Res.* **2019**, *18* (2), 664–677. https://doi.org/10.1021/acs.jproteome.8b00766.

(363) Tiemeyer, M.; Aoki, K.; Paulson, J.; Cummings, R. D.; York, W. S.; Karlsson, N. G.; Lisacek, F.; Packer, N. H.; Campbell, M. P.; Aoki, N. P.; Fujita, A.; Matsubara, M.; Shinmachi, D.; Tsuchiya, S.; Yamada, I.; Pierce, M.; Ranzinger, R.; Narimatsu, H.; Aoki-Kinoshita, K. F. GlyTouCan: An Accessible Glycan Structure Repository. *Glycobiology* **2017**, *27* (10), 915–919. https://doi.org/10.1093/glycob/cwx066.

(364) Harvey, D. J. Structural Determination of N-Linked Glycans by Matrix-Assisted Laser Desorption/Ionization and Electrospray Ionization Mass Spectrometry. *Proteomics*. John Wiley & Sons, Ltd May 1, 2005, pp 1774–1786. https://doi.org/10.1002/pmic.200401248.

(365) Ford, K. L.; Zeng, W.; Heazlewood, J. L.; Bacic, A. Characterization of Protein N-Glycosylation by Tandem Mass Spectrometry Using Complementary Fragmentation Techniques. *Front. Plant Sci.* **2015**, *6* (AUG), 674. https://doi.org/10.3389/fpls.2015.00674.

(366) Prentice, B. M.; Chumbley, C. W.; Caprioli, R. M. High-Speed MALDI MS/MS Imaging Mass Spectrometry Using Continuous Raster Sampling. *J. Mass Spectrom.* **2015**, *50* (4), 703–710. https://doi.org/10.1002/jms.3579.

(367) Yang, Y.; Zhang, S.; Howe, K.; Wilson, D. B.; Moser, F.; Irwin, D.; Thannhauser, T. W. A Comparison of NLC-ESI-MS/MS and NLC-MALDI-MS/MS for GeLC-Based Protein Identification and ITRAQ-Based Shotgun Quantitative Proteomics. *J. Biomol. Tech.* **2007**, *18* (4), 226–237.

(368) Mitchell Wells, J.; McLuckey, S. A. Collision-Induced Dissociation (CID) of Peptides and Proteins. *Methods in Enzymology*. Academic Press Inc. January 1, 2005, pp 148–185. https://doi.org/10.1016/S0076-6879(05)02005-7.

(369) Harvey, D. J. Electrospray Mass Spectrometry and Fragmentation of N-Linked Carbohydrates Derivatized at the Reducing Terminus. *J. Am. Soc. Mass Spectrom.* **2000**, *11* (10), 900–915. https://doi.org/10.1016/S1044-0305(00)00156-2.

(370) Harvey, D. J.; Struwe, W. B. Structural Studies of Fucosylated N-Glycans by Ion Mobility Mass Spectrometry and Collision-Induced Fragmentation of Negative Ions. *J. Am. Soc. Mass Spectrom.* **2018**, *29* (6), 1179–1193. https://doi.org/10.1007/s13361-018-1950-x.

(371) Crotti, S.; Menicatti, M.; Pallecchi, M.; Bartolucci, G. Tandem Mass Spectrometry Approaches for Recognition of Isomeric Compounds Mixtures. *Mass Spectrom. Rev.* **2021**, e21757. https://doi.org/10.1002/MAS.21757.

(372) Awad, H.; El-Aneed, A. Enantioselectivity of Mass Spectrometry: Challenges and Promises. *Mass Spectrom. Rev.* **2013**, *32* (6), 466–483.

https://doi.org/10.1002/MAS.21379.

(373) Devakumar, A.; Mechref, Y.; Kang, P.; Novotny, M. V.; Reilly, J. P. Identification of Isomeric N-Glycan Structures by Mass Spectrometry with 157 Nm Laser-Induced Photofragmentation. *J. Am. Soc. Mass Spectrom.* **2008**, *19* (7), 1027–1040. https://doi.org/10.1016/j.jasms.2008.03.005.

(374) Spraggins, J. M.; Djambazova, K. V.; Rivera, E. S.; Migas, L. G.; Neumann, E. K.; Fuetterer, A.; Suetering, J.; Goedecke, N.; Ly, A.; Van De Plas, R.; Caprioli, R. M. High-Performance Molecular Imaging with MALDI Trapped Ion-Mobility Time-of-Flight (TimsTOF) Mass Spectrometry. *Anal. Chem.* **2019**, *91* (22), 14552–14560. https://doi.org/10.1021/acs.analchem.9b03612.

(375) Fernandez-Lima, F. Trapped Ion Mobility Spectrometry: Past, Present and Future Trends. *International Journal for Ion Mobility Spectrometry*. Springer Verlag September 1, 2016, pp 65–67. https://doi.org/10.1007/s12127-016-0206-3.

(376) Kirk, A. T.; Bohnhorst, A.; Raddatz, C. R.; Allers, M.; Zimmermann, S. Ultra-High-Resolution Ion Mobility Spectrometry—Current Instrumentation, Limitations, and Future Developments. *Analytical and Bioanalytical Chemistry*. Springer Verlag September 1, 2019, pp 6229–6246. https://doi.org/10.1007/s00216-019-01807-0.

(377) Pu, Y.; Ridgeway, M. E.; Glaskin, R. S.; Park, M. A.; Costello, C. E.; Lin, C. Separation and Identification of Isomeric Glycans by Selected Accumulation-Trapped Ion Mobility Spectrometry-Electron Activated Dissociation Tandem Mass Spectrometry. *Anal. Chem.* **2016**, *88* (7), 3440–3443. https://doi.org/10.1021/acs.analchem.6b00041.

(378) Ben Faleh, A.; Warnke, S.; Bansal, P.; Pellegrinelli, R. P.; Dyukova, I.; Rizzo, T. R. Identification of Mobility-Resolved N-Glycan Isomers. *Anal. Chem.* **2022**, *94* (28), 10101–10108. https://doi.org/10.1021/ACS.ANALCHEM.2C01181/ASSET/IMAGES/LARGE/AC2C01181_0008.JPEG.

(379) Ollivier, S.; Fanuel, M.; Rogniaux, H.; Ropartz, D. Using a Cyclic Ion Mobility Spectrometer for Tandem Ion Mobility Experiments. *J. Vis. Exp.* **2022**, *2022* (179). https://doi.org/10.3791/63451.

(380) Lane, C. S.; McManus, K.; Widdowson, P.; Flowers, S. A.; Powell, G.; Anderson, I.; Campbell, J. L. Separation of Sialylated Glycan Isomers by Differential Spectrometry. *Anal. Chem.* **2019**, *91* (15), 9916. https://doi.org/10.1021/ACS.ANALCHEM.9B01595.

(381) Barroso, A.; Giménez, E.; Konijnenberg, A.; Sancho, J.; Sanz-Nebot, V.; Sobott, F. Evaluation of Ion Mobility for the Separation of Glycoconjugate Isomers Due to Different Types of Sialic Acid Linkage, at the Intact Glycoprotein, Glycopeptide and Glycan Level. *J. Proteomics* **2018**, *173*,

22–31. https://doi.org/10.1016/J.JPROT.2017.11.020.

(382) Sans, M.; Feider, C. L.; Eberlin, L. S. Advances in Mass Spectrometry Imaging Coupled to Ion Mobility Spectrometry for Enhanced Imaging of Biological Tissues. *Current Opinion in Chemical Biology*. Elsevier Ltd February 1, 2018, pp 138–146. https://doi.org/10.1016/j.cbpa.2017.12.005.

(383) Rivera, E. S.; Djambazova, K. V.; Neumann, E. K.; Caprioli, R. M.; Spraggins, J. M. Integrating Ion Mobility and Imaging Mass Spectrometry for Comprehensive Analysis of Biological Tissues: A Brief Review and Perspective. *J. Mass Spectrom.* **2020**, *55* (12). https://doi.org/10.1002/jms.4614.

(384) Nishikaze, T. Sialic Acid Derivatization for Glycan Analysis by Mass Spectrometry. *Proceedings of the Japan Academy Series B: Physical and Biological Sciences*. Japan Academy 2019, pp 523–537. https://doi.org/10.2183/pjab.95.036.

(385) Wheeler, S. F.; Domann, P.; Harvey, D. J. Derivatization of Sialic Acids for Stabilization in Matrix-Assisted Laser Desorption/Ionization Mass Spectrometry and Concomitant Differentiation of α(2→3)- and α(2→6)-Isomers. *Rapid Commun. Mass Spectrom.* **2009**, *23* (2), 303–312. https://doi.org/10.1002/RCM.3867.

(386) Alley, W. R.; Novotny, M. V. Glycomic Analysis of Sialic Acid Linkages in Glycans Derived from Blood Serum Glycoproteins. *J. Proteome Res.* **2010**, *9* (6), 3062. https://doi.org/10.1021/PR901210R.

(387) Reiding, K. R.; Blank, D.; Kuijper, D. M.; Deelder, A. M.; Wuhrer, M. High-Throughput Profiling of Protein N-Glycosylation by MALDI-TOF-MS Employing Linkage-Specific Sialic Acid Esterification. *Anal. Chem.* **2014**, *86* (12), 5784–5793. https://doi.org/10.1021/ac500335t.

(388) De Haan, N.; Reiding, K. R.; Haberger, M.; Reusch, D.; Falck, D.; Wuhrer, M. Linkage-Specific Sialic Acid Derivatization for MALDI-TOF-MS Profiling of IgG Glycopeptides. *Anal. Chem.* **2015**, *87* (16), 8284–8291. https://doi.org/10.1021/ACS.ANALCHEM.5B02426/SUPPL_FILE/AC5B024 26_SI_003.XLSX.

(389) Li, H.; Gao, W.; Feng, X.; Liu, B. F.; Liu, X. MALDI-MS Analysis of Sialylated N-Glycan Linkage Isomers Using Solid-Phase Two Step Derivatization Method. *Anal. Chim. Acta* **2016**, *924*, 77–85. https://doi.org/10.1016/J.ACA.2016.04.023.

(390) Jiang, K.; Zhu, H.; Li, L.; Guo, Y.; Gashash, E.; Ma, C.; Sun, X.; Li, J.; Zhang, L.; Wang, P. G. Sialic Acid Linkage-Specific Permethylation for Improved Profiling of Protein Glycosylation by MALDI-TOF MS. *Anal. Chim. Acta* **2017**, *981*, 53. https://doi.org/10.1016/J.ACA.2017.05.029.

(391) Hanamatsu, H.; Nishikaze, T.; Miura, N.; Piao, J.; Okada, K.; Sekiya, S.; Iwamoto, S.; Sakamoto, N.; Tanaka, K.; Furukawa, J. I. Sialic Acid Linkage

Specific Derivatization of Glycosphingolipid Glycans by Ring-Opening Aminolysis of Lactones. *Anal. Chem.* **2018**, *90* (22), 13193–13199. https://doi.org/10.1021/ACS.ANALCHEM.8B02775/ASSET/IMAGES/LARGE/AC-2018-027754_0006.JPEG.

(392) Pezer, M.; Rudan, I.; Campbell, H.; Lauc, G.; Pezer, M.; Rudan, I.; Campbell, H. Mechanisms of Disease: The Human N-Glycome. *Biochim. Biophys. Acta - Gen. Subj.* **2016**, *1860* (8), 1574–1582. https://doi.org/10.1016/J.BBAGEN.2015.10.016.

(393) Drake, R. R.; Jones, E. E.; Powers, T. W.; Nyalwidhe, J. O. Altered Glycosylation in Prostate Cancer. In *Advances in Cancer Research*; Academic Press Inc., 2015; Vol. 126, pp 345–382. https://doi.org/10.1016/bs.acr.2014.12.001.

(394) Varki, A. Sialic Acids in Human Health and Disease. *Trends in Molecular Medicine*. NIH Public Access August 2008, pp 351–360. https://doi.org/10.1016/j.molmed.2008.06.002.

(395) Lane, C. S.; McManus, K.; Widdowson, P.; Flowers, S. A.; Powell, G.; Anderson, I.; Campbell, J. L. Separation of Sialylated Glycan Isomers by Differential Mobility Spectrometry. *Anal. Chem.* **2019**, *91* (15), 9916–9924. https://doi.org/10.1021/acs.analchem.9b01595.

(396) Drake, R. R.; West, C. A.; Mehta, A. S.; Angel, P. M. MALDI Mass Spectrometry Imaging of N-Linked Glycans in Tissues. In *Advances in Experimental Medicine and Biology*; Springer New York LLC, 2018; Vol. 1104, pp 59–76. https://doi.org/10.1007/978-981-13-2158-0_4.

(397) Bilimoria, K. Y.; Bentrem, D. J.; Ko, C. Y.; Ritchey, J.; Stewart, A. K.; Winchester, D. P.; Talamonti, M. S. Validation of the 6th Edition AJCC Pancreatic Cancer Staging System: Report from the National Cancer Database. *Cancer* **2007**, *110* (4), 738–744. https://doi.org/10.1002/cncr.22852.

(398) Barnett, D.; Hall, J.; Haab, B. Automated Identification and Quantification of Signals in Multichannel Immunofluorescence Images: The SignalFinder-IF Platform. *Am. J. Pathol.* **2019**, *189* (7), 1402–1412. https://doi.org/10.1016/j.ajpath.2019.03.011.

(399) Ensink, E.; Sinha, J.; Sinha, A.; Tang, H.; Calderone, H. M.; Hostetter, G.; Winter, J.; Cherba, D.; Brand, R. E.; Allen, P. J.; Sempere, L. F.; Haab, B. B. Segment and Fit Thresholding: A New Method for Image Analysis Applied to Microarray and Immunofluorescence Data. *Anal. Chem.* **2015**, *87* (19), 9715–9721. https://doi.org/10.1021/acs.analchem.5b03159.

(400) Miyagawa, S.; Maeda, A.; Kawamura, T.; Ueno, T.; Usui, N.; Kondo, S.; Matsumoto, S.; Okitsu, T.; Goto, M.; Nagashima, H. A Comparison of the Main Structures of N-Glycans of Porcine Islets with Those from Humans. *Glycobiology* **2014**, *24* (2), 125–138.

https://doi.org/10.1093/GLYCOB/CWT088.

(401) Talabnin, K.; Talabnin, C.; Ishihara, M.; Azadi, P. Increased Expression of the High-Mannose M6N2 and NeuAc3H3N3M3N2F Tri-Antennary N-Glycansin Cholangiocarcinoma. *Oncol. Lett.* **2018**, *15* (1), 1030–1036. https://doi.org/10.3892/ol.2017.7384.

(402) Sethi, M. K.; Thaysen-Andersen, M.; Smith, J. T.; Baker, M. S.; Packer, N. H.; Hancock, W. S.; Fanayan, S. Comparative N-Glycan Profiling of Colorectal Cancer Cell Lines Reveals Unique Bisecting GlcNAc and α-2,3-Linked Sialic Acid Determinants Are Associated with Membrane Proteins of the More Metastatic/Aggressive Cell Lines. *J. Proteome Res.* **2014**, *13* (1), 277–288. https://doi.org/10.1021/pr400861m.

(403) Takahashi, T.; Suzuki, T. Role of Sulfatide in Normal and Pathological Cells and Tissues. *Journal of Lipid Research*. American Society for Biochemistry and Molecular Biology August 1, 2012, pp 1437–1450. https://doi.org/10.1194/jlr.R026682.

(404) De Carufel, C. A.; Nguyen, P. T.; Sahnouni, S.; Bourgault, S. New Insights into the Roles of Sulfated Glycosaminoglycans in Islet Amyloid Polypeptide Amyloidogenesis and Cytotoxicity. *Biopolymers* **2013**, *100* (6), 645–655. https://doi.org/10.1002/bip.22243.

(405) Wang, J. R.; Gao, W. N.; Grimm, R.; Jiang, S.; Liang, Y.; Ye, H.; Li, Z. G.; Yau, L. F.; Huang, H.; Liu, J.; Jiang, M.; Meng, Q.; Tong, T. T.; Huang, H. H.; Lee, S.; Zeng, X.; Liu, L.; Jiang, Z. H. A Method to Identify Trace Sulfated IgG N-Glycans as Biomarkers for Rheumatoid Arthritis. *Nat. Commun.* **2017**, *8* (1), 1–14. https://doi.org/10.1038/s41467-017-00662-w.

(406) Mitoma, J.; Bao, X.; Petryanik, B.; Schaerli, P.; Gauguet, J. M.; Yu, S. Y.; Kawashima, H.; Saito, H.; Ohtsubo, K.; Marth, J. D.; Khoo, K. H.; von Andrian, U. H.; Lowe, J. B.; Fukuda, M. Critical Functions of N-Glycans in L-Selectin-Mediated Lymphocyte Homing and Recruitment. *Nat. Immunol.* **2007**, *8* (4), 409–418. https://doi.org/10.1038/ni1442.

(407) Stanley P, C. R. *Stanley P, Cummings RD. Structures Common to Different Glycans*; Cold Spring Harbor Laboratory Press, 2017. https://doi.org/10.1101/glycobiology.3e.014.

(408) Singh, S.; Pal, K.; Yadav, J.; Tang, H.; Partyka, K.; Kletter, D.; Hsueh, P.; Ensink, E.; Kc, B.; Hostetter, G.; Xu, H. E.; Bern, M.; Smith, D. F.; Mehta, A. S.; Brand, R.; Melcher, K.; Haab, B. B. Upregulation of Glycans Containing 3′ Fucose in a Subset of Pancreatic Cancers Uncovered Using Fusion-Tagged Lectins. *J. Proteome Res.* **2015**, *14* (6), 2594–2605. https://doi.org/10.1021/acs.jproteome.5b00142.

(409) Zhan, L.; Chen, L.; Chen, Z. Knockdown of FUT3 Disrupts the Proliferation, Migration, Tumorigenesis and TGF-β Induced EMT in Pancreatic Cancer Cells. *Oncol. Lett.* **2018**, *16* (1), 924–930.

https://doi.org/10.3892/ol.2018.8738.

(410) Yue, T.; Maupin, K. A.; Fallon, B.; Li, L.; Partyka, K.; Anderson, M. A.; Brenner, D. E.; Kaul, K.; Zeh, H.; Moser, A. J.; Simeone, D. M.; Feng, Z.; Brand, R. E.; Haab, B. B. Enhanced Discrimination of Malignant from Benign Pancreatic Disease by Measuring the CA 19-9 Antigen on Specific Protein Carriers. *PLoS One* **2011**, *6* (12), e29180. https://doi.org/10.1371/journal.pone.0029180.

(411) Gupta, R.; Leon, F.; Rauth, S.; Batra, S. K.; Ponnusamy, M. P. A Systematic Review on the Implications of O-Linked Glycan Branching and Truncating Enzymes on Cancer Progression and Metastasis. *Cells* **2020**, *9* (2). https://doi.org/10.3390/CELLS9020446.

(412) Zhang, Z.; Wuhrer, M.; Holst, S. Serum Sialylation Changes in Cancer. *Glycoconj. J.* **2018**, *35* (2), 139. https://doi.org/10.1007/S10719-018-9820-0.

(413) Munkley, J. Aberrant Sialylation in Cancer: Therapeutic Opportunities. *Cancers (Basel).* **2022**, *14* (17). https://doi.org/10.3390/CANCERS14174248.

(414) Thompson, A. J.; Paulson, J. C. Adaptation of Influenza Viruses to Human Airway Receptors. *J. Biol. Chem.* **2021**, *296*. https://doi.org/10.1074/JBC.REV120.013309.

(415) Stencel-Baerenwald, J. E.; Reiss, K.; Reiter, D. M.; Stehle, T.; Dermody, T. S. The Sweet Spot: Defining Virus–Sialic Acid Interactions. *Nat. Rev. Microbiol. 2014 1211* **2014**, *12* (11), 739–749. https://doi.org/10.1038/nrmicro3346.

(416) Liu, M.; Huang, L. Z. X.; Smits, A. A.; Büll, C.; Narimatsu, Y.; van Kuppeveld, F. J. M.; Clausen, H.; de Haan, C. A. M.; de Vries, E. Human-Type Sialic Acid Receptors Contribute to Avian Influenza A Virus Binding and Entry by Hetero-Multivalent Interactions. *Nat. Commun.* **2022**, *13* (1). https://doi.org/10.1038/S41467-022-31840-0.

(417) Angata, T.; Varki, A. Discovery, Classification, Evolution and Diversity of Siglecs. *Mol. Aspects Med.* **2022**, 101117. https://doi.org/10.1016/J.MAM.2022.101117.

(418) Smith, B. A. H.; Bertozzi, C. R. The Clinical Impact of Glycobiology: Targeting Selectins, Siglecs and Mammalian Glycans. *Nat. Rev. Drug Discov. 2021 203* **2021**, *20* (3), 217–243. https://doi.org/10.1038/s41573-020-00093-1.

(419) Duan, S.; Paulson, J. C. Siglecs as Immune Cell Checkpoints in Disease. *https://doi.org/10.1146/annurev-immunol-102419-035900* **2020**, *38*, 365–395. https://doi.org/10.1146/ANNUREV-IMMUNOL-102419-035900.

(420) Angata, T.; Varki, A. Chemical Diversity in the Sialic Acids and Related α-

Keto Acids: An Evolutionary Perspective. *Chem. Rev.* **2002**, *102* (2), 439–469. https://doi.org/10.1021/CR000407M/SUPPL_FILE/CR000407M_SA.PDF.

(421) de Haan, N.; Yang, S.; Cipollo, J.; Wuhrer, M. Glycomics Studies Using Sialic Acid Derivatization and Mass Spectrometry. *Nature Reviews Chemistry*. Nature Research May 1, 2020, pp 229–242. https://doi.org/10.1038/s41570-020-0174-3.

(422) Dall'olio, F.; Pucci, M.; Malagolini, N. The Cancer-Associated Antigens Sialyl Lewisa/x and Sda: Two Opposite Faces of Terminal Glycosylation. *Cancers (Basel).* **2021**, *13* (21). https://doi.org/10.3390/CANCERS13215273.

(423) Garnham, R.; Scott, E.; Livermore, K. E.; Munkley, J. ST6GAL1: A Key Player in Cancer. *Oncol. Lett.* **2019**, *18* (2), 983. https://doi.org/10.3892/OL.2019.10458.

(424) GC, S.; Bellis, S. L.; Hjelmeland, A. B. ST6Gal1: Oncogenic Signaling Pathways and Targets. *Front. Mol. Biosci.* **2022**, *9*, 820. https://doi.org/10.3389/FMOLB.2022.962908/BIBTEX.

(425) Suzuki, Y. Sialobiology of Influenza: Molecular Mechanism of Host Range Variation of Influenza Viruses. *Biol. Pharm. Bull.* **2005**, *28* (3), 399–408. https://doi.org/10.1248/BPB.28.399.

(426) Harvey, D. J.; Royle, L.; Radcliffe, C. M.; Rudd, P. M.; Dwek, R. A. Structural and Quantitative Analysis of N-Linked Glycans by Matrix-Assisted Laser Desorption Ionization and Negative Ion Nanospray Mass Spectrometry. *Anal. Biochem.* **2008**, *376* (1), 44–60. https://doi.org/10.1016/J.AB.2008.01.025.

(427) Pongracz, T.; Verhoeven, A.; Wuhrer, M.; de Haan, N. The Structure and Role of Lactone Intermediates in Linkage-Specific Sialic Acid Derivatization Reactions. *Glycoconj. J.* **2021**, *38* (2), 157–166.

(428) Gervay, J.; Ramamoorthy, P. S.; Mamuya, N. N. Ring Opening of Sialyllactones with Glycine Esters: Synthesis of Selectively Protected Glycinyl-NeuAc Saccharopeptides. *Tetrahedron* **1997**, *53* (32), 11039–11048. https://doi.org/10.1016/S0040-4020(97)00364-5.

(429) Bertozzi, C. R. A Decade of Bioorthogonal Chemistry. *Acc. Chem. Res.* **2011**, *44* (9), 651–653. https://doi.org/10.1021/AR200193F.

(430) Lopez Aguilar, A.; Briard, J. G.; Yang, L.; Ovryn, B.; Macauley, M. S.; Wu, P. Tools for Studying Glycans: Recent Advances in Chemoenzymatic Glycan Labeling. *ACS Chem. Biol.* **2017**, *12* (3), 611–621. https://doi.org/10.1021/ACSCHEMBIO.6B01089/ASSET/IMAGES/LARGE/CB-2016-01089P_0006.JPEG.

(431) Cioce, A.; Malaker, S. A.; Schumann, B. Generating Orthogonal

Glycosyltransferase and Nucleotide Sugar Pairs as Next-Generation Glycobiology Tools. *Curr. Opin. Chem. Biol.* **2021**, *60*, 66–78. https://doi.org/10.1016/J.CBPA.2020.09.001.

(432) Laughlin, S. T.; Agard, N. J.; Baskin, J. M.; Carrico, I. S.; Chang, P. V.; Ganguli, A. S.; Hangauer, M. J.; Lo, A.; Prescher, J. A.; Bertozzi, C. R. Metabolic Labeling of Glycans with Azido Sugars for Visualization and Glycoproteomics. *Methods Enzymol.* **2006**, *415*, 230–250. https://doi.org/10.1016/S0076-6879(06)15015-6.

(433) Hanson, S. R.; Hsu, T. L.; Weerapana, E.; Kishikawa, K.; Simon, G. M.; Cravatt, B. F.; Wong, C. H. Tailored Glycoproteomics and Glycan Site Mapping Using Saccharide-Selective Bioorthogonal Probes. *J. Am. Chem. Soc.* **2007**, *129* (23), 7266–7267. https://doi.org/10.1021/JA0724083/SUPPL_FILE/JA0724083SI20070430_ 054236.PDF.

(434) Slade, P. G.; Hajivandi, M.; Bartel, C. M.; Gorfien, S. F. Identifying the CHO Secretome Using Mucin-Type O-Linked Glycosylation and Click-Chemistry. *J. Proteome Res.* **2012**, *11* (12), 6175–6186. https://doi.org/10.1021/PR300810F/SUPPL_FILE/PR300810F_SI_001.PD F.

(435) Spiciarich, D. R.; Nolley, R.; Maund, S. L.; Purcell, S. C.; Herschel, J.; Iavarone, A. T.; Peehl, D. M.; Bertozzi, C. R. Bioorthogonal Labeling of Human Prostate Cancer Tissue Slice Cultures for Glycoproteomics. *Angew. Chem. Int. Ed. Engl.* **2017**, *56* (31), 8992. https://doi.org/10.1002/ANIE.201701424.

(436) Yang, L.; Nyalwidhe, J. O.; Guo, S.; Drake, R. R.; Semmes, O. J. Targeted Identification of Metastasis-Associated Cell-Surface Sialoglycoproteins in Prostate Cancer. *Mol. Cell. Proteomics* **2011**, *10* (6). https://doi.org/10.1074/MCP.M110.007294.

(437) Roper, S. M.; Zemskova, M.; Neely, B. A.; Martin, A.; Gao, P.; Jones, E. E.; Kraft, A. S.; Drake, R. R. Targeted Glycoprotein Enrichment and Identification in Stromal Cell Secretomes Using Azido Sugar Metabolic Labeling. *Proteomics - Clin. Appl.* **2013**, *7* (5–6), 367–371. https://doi.org/10.1002/prca.201300006.

(438) Calle, B.; Bineva-Todd, G.; Marchesi, A.; Flynn, H.; Ghirardello, M.; Tastan, O. Y.; Roustan, C.; Choi, J.; Galan, M. C.; Schumann, B.; Malaker, S. A. Benefits of Chemical Sugar Modifications Introduced by Click Chemistry for Glycoproteomic Analyses. *J. Am. Soc. Mass Spectrom.* **2021**, *32* (9), 2366–2375. https://doi.org/10.1021/JASMS.1C00084/ASSET/IMAGES/LARGE/JS1C00 084_0005.JPEG.

(439) Li, M.; Huang, J.; Ma, M.; Shi, X.; Li, L. Selective Enrichment of Sialylglycopeptides Enabled by Click Chemistry and Dynamic Covalent

Exchange. No. 18.

(440) McDowell, C. T.; Lu, X.; Mehta, A. S.; Angel, P. M.; Drake, R. R. Applications and Continued Evolution of Glycan Imaging Mass Spectrometry. *Mass Spectrom. Rev.* **2021**. https://doi.org/10.1002/MAS.21725.

(441) Blaschke, C. R. K.; McDowell, C. T.; Black, A. P.; Mehta, A. S.; Angel, P. M.; Drake, R. R. Glycan Imaging Mass Spectrometry. *Clin. Lab. Med.* **2021**, *41* (2). https://doi.org/10.1016/j.cll.2021.03.005.

(442) Chan, L. C.; Cox, B. G. Kinetics of Amide Formation through Carbodiimide/N-Hydroxybenzotriazole (HOBt) Couplings. *J. Org. Chem.* **2007**, *72* (23), 8863–8869. https://doi.org/10.1021/JO701558Y/SUPPL_FILE/JO701558Y-FILE002.PDF.

(443) Hong, V.; Presolski, S. I.; Ma, C.; Finn, M. G. Analysis and Optimization of Copper-Catalyzed Azide–Alkyne Cycloaddition for Bioconjugation. *Angew. Chemie Int. Ed.* **2009**, *48* (52), 9879–9883. https://doi.org/10.1002/ANIE.200905087.

(444) Abel, G. R.; Calabrese, Z. A.; Ayco, J.; Hein, J. E.; Ye, T. Measuring and Suppressing the Oxidative Damage to DNA during Cu(I)-Catalyzed Azide-Alkyne Cycloaddition. *Bioconjug. Chem.* **2016**, *27* (3), 698–704. https://doi.org/10.1021/ACS.BIOCONJCHEM.5B00665.

(445) Blaschke, C.; Black, A.; Mehta, A. S.; Angel, P. M.; Drake, R. R. Rapid N-Glycan Profiling of Serum and Plasma by a Novel Slide Based Imaging Mass Spectrometry Workflow. *J. Am. Soc. Mass Spectrom.* **2020**. https://doi.org/10.1021/jasms.0c00213.

(446) Orlando, R.; Lim, J. M.; Atwood, J. A.; Angel, P. M.; Fang, M.; Aoki, K.; Alvarez-Manilla, G.; Moremen, K. W.; York, W. S.; Tiemeyer, M.; Pierce, M.; Dalton, S.; Wells, L. IDAWG: Metabolic Incorporation of Stable Isotope Labels for Quantitative Glycomics of Cultured Cells. *J. Proteome Res.* **2009**, *8* (8), 3816–3823. https://doi.org/10.1021/pr8010028.

(447) Blaschke, C. R. K.; Hartig, J. P.; Grimsley, G.; Liu, L.; Semmes, O. J.; Wu, J. D.; Ippolito, J. E.; Hughes-Halbert, C.; Nyalwidhe, J. O.; Drake, R. R. Direct N-Glycosylation Profiling of Urine and Prostatic Fluid Glycoproteins and Extracellular Vesicles. *Front. Chem.* **2021**, *9*, 801. https://doi.org/10.3389/FCHEM.2021.734280/BIBTEX.

(448) Liu, R.; Li, Q.; Smith, L. M. Detection of Large Ions in Time-of-Flight Mass Spectrometry: Effects of Ion Mass and Acceleration Voltage on Microchannel Plate Detector Response. *J. Am. Soc. Mass Spectrom.* **2014**, *25* (8), 1374. https://doi.org/10.1007/S13361-014-0903-2.

(449) Huang, Y.; Mechref, Y.; Novotny, M. V. Microscale Nonreductive Release of O-Linked Glycans for Subsequent Analysis through MALDI Mass

Spectrometry and Capillary Electrophoresis. *Anal. Chem.* **2001**, *73* (24), 6063–6069. https://doi.org/10.1021/AC015534C/ASSET/IMAGES/LARGE/AC015534C F00006.JPEG.

(450) Ong, S. E.; Mann, M. A Practical Recipe for Stable Isotope Labeling by Amino Acids in Cell Culture (SILAC). *Nat. Protoc. 2007 16* **2007**, *1* (6), 2650–2660. https://doi.org/10.1038/nprot.2006.427.

(451) Hsu, S. M.; Raine, L.; Fanger, H. Use of Avidin-Biotin-Peroxidase Complex (ABC) in Immunoperoxidase Techniques: A Comparison between ABC and Unlabeled Antibody (PAP) Procedures.: *http://dx.doi.org/10.1177/29.4.6166661* **2017**, *29* (4), 577–580. https://doi.org/10.1177/29.4.6166661.

(452) Leriche, G.; Chisholm, L.; Wagner, A. Cleavable Linkers in Chemical Biology. *Bioorg. Med. Chem.* **2012**, *20* (2), 571–582. https://doi.org/10.1016/J.BMC.2011.07.048.

(453) Bargh, J. D.; Isidro-Llobet, A.; Parker, J. S.; Spring, D. R. Cleavable Linkers in Antibody–Drug Conjugates. *Chem. Soc. Rev.* **2019**, *48* (16), 4361–4374. https://doi.org/10.1039/C8CS00676H.

(454) Sletten, E. M.; Bertozzi, C. R. Bioorthogonal Chemistry: Fishing for Selectivity in a Sea of Functionality. *Angewandte Chemie - International Edition*. NIH Public Access September 7, 2009, pp 6974–6998. https://doi.org/10.1002/anie.200900942.

(455) Prescher, J. A.; Bertozzi, C. R. Chemical Technologies for Probing Glycans. *Cell* **2006**, *126* (5), 851–854. https://doi.org/10.1016/J.CELL.2006.08.017.

(456) Büll, C.; Heise, T.; van Hilten, N.; Pijnenborg, J. F. A.; Bloemendal, V. R. L. J.; Gerrits, L.; Kers-Rebel, E. D.; Ritschel, T.; den Brok, M. H.; Adema, G. J.; Boltje, T. J. Steering Siglec–Sialic Acid Interactions on Living Cells Using Bioorthogonal Chemistry. *Angew. Chemie Int. Ed.* **2017**, *56* (12), 3309–3313. https://doi.org/10.1002/ANIE.201612193.

(457) Parker, C. G.; Pratt, M. R. Click Chemistry in Proteomic Investigations. *Cell* **2020**, *180* (4), 605–632. https://doi.org/10.1016/J.CELL.2020.01.025.

(458) Zhao, X.; Cai, L.; Adogla, E. A.; Guan, H.; Lin, Y.; Wang, Q. Labeling of Enveloped Virus via Metabolic Incorporation of Azido Sugars. *Bioconjug. Chem.* **2015**, *26* (9), 1868–1872. https://doi.org/10.1021/ACS.BIOCONJCHEM.5B00310/ASSET/IMAGES/L ARGE/BC-2015-003105_0004.JPEG.

(459) Zhang, X.; Zhang, Y. *Applications of Azide-Based Bioorthogonal Click Chemistry in Glycobiology*; Multidisciplinary Digital Publishing Institute (MDPI), 2013; Vol. 18, pp 7145–7159. https://doi.org/10.3390/molecules18067145.

(460) Zhang, X.; Nie, H.; Whited, J.; Wang, D.; Li, Y.; Sun, X. L. Recent Approaches for Directly Profiling Cell Surface Sialoform. *Glycobiology* **2018**, *28* (12), 910–924. https://doi.org/10.1093/GLYCOB/CWY046.

(461) Wu, Z. L.; Person, A. D.; Burton, A. J.; Singh, R.; Burroughs, B.; Fryxell, D.; Tatge, T. J.; Manning, T.; Wu, G.; Swift, K. A. D.; Kalabokis, V. Direct Fluorescent Glycan Labeling with Recombinant Sialyltransferases. *Glycobiology* **2019**, *29* (11), 750–754. https://doi.org/10.1093/GLYCOB/CWZ058.

(462) Hart, C.; Chase, L. G.; Hajivandi, M.; Agnew, B. Metabolic Labeling and Click Chemistry Detection of Glycoprotein Markers of Mesenchymal Stem Cell Differentiation. *Methods Mol. Biol.* **2011**, *698*, 459–484. https://doi.org/10.1007/978-1-60761-999-4_33/TABLES/1.

(463) Dehnert, K. W.; Baskin, J. M.; Laughlin, S. T.; Beahm, B. J.; Naidu, N. N.; Amacher, S. L.; Bertozzi, C. R. Imaging the Sialome during Zebrafish Development with Copper-Free Click Chemistry. *ChemBioChem* **2012**, *13* (3), 353–357. https://doi.org/10.1002/CBIC.201100649.

(464) Baskin, J. M.; Prescher, J. A.; Laughlin, S. T.; Agard, N. J.; Chang, P. V.; Miller, I. A.; Lo, A.; Codelli, J. A.; Bertozzi, C. R. Copper-Free Click Chemistry for Dynamic in Vivo Imaging. *Proc. Natl. Acad. Sci. U. S. A.* **2007**, *104* (43), 16793–16797. https://doi.org/10.1073/PNAS.0707090104/SUPPL_FILE/07090SCHEME3. JPG.

(465) Liang, Y.; Jiang, X.; Yuan, R.; Zhou, Y.; Ji, C.; Yang, L.; Chen, H.; Wang, Q. Metabolism-Based Click-Mediated Platform for Specific Imaging and Quantification of Cell Surface Sialic Acids. *Anal. Chem.* **2017**, *89* (1), 538–543. https://doi.org/10.1021/ACS.ANALCHEM.6B04141/ASSET/IMAGES/LARG E/AC-2016-04141W_0004.JPEG.

(466) Sun, N.; Xiong, Y.; Qing, G.; Zhao, Y.; Li, X.; Liang, X. Selective Enrichment of Sialylated Glycopeptides with a d -Allose@SiO 2 Matrix. *RSC Adv.* **2018**, *8* (68), 38780–38786. https://doi.org/10.1039/C8RA07192F.

(467) Palmisano, G.; Lendal, S. E.; Larsen, M. R. Titanium Dioxide Enrichment of Sialic Acid-Containing Glycopeptides. *Methods Mol. Biol.* **2011**, *753*, 309–322. https://doi.org/10.1007/978-1-61779-148-2_21/TABLES/2.

(468) Riley, N. M.; Bertozzi, C. R.; Pitteri, S. J. A Pragmatic Guide to Enrichment Strategies for Mass Spectrometry–Based Glycoproteomics. *Mol. Cell. Proteomics* **2021**, *20*, 100029. https://doi.org/10.1074/MCP.R120.002277.

(469) Nilsson, J.; Rüetschi, U.; Halim, A.; Hesse, C.; Carlsohn, E.; Brinkmalm, G.; Larson, G. Enrichment of Glycopeptides for Glycan Structure and Attachment Site Identification. *Nat. Methods 2009 611* **2009**, *6* (11), 809–

811. https://doi.org/10.1038/nmeth.1392.

(470) Rafiee, M.-R.; Sigismondo, G.; Kalxdorf, M.; Förster, L.; Brügger, B.; Béthune, J.; Krijgsveld, J. Protease-Resistant Streptavidin for Interaction Proteomics. *Mol. Syst. Biol.* **2020**, *16* (5), e9370. https://doi.org/10.15252/MSB.20199370.

(471) Koay, E. J.; Lee, Y.; Cristini, V.; Lowengrub, J. S.; Kang, Y.; Anthony San Lucas, F.; Hobbs, B. P.; Ye, R.; Elganainy, D.; Almahariq, M.; Amer, A. M.; Chatterjee, D.; Yan, H.; Park, P. C.; Rios Perez, M. V.; Li, D.; Garg, N.; Reiss, K. A.; Yu, S.; Chauhan, A.; Zaid, M.; Nikzad, N.; Wolff, R. A.; Javle, M.; Varadhachary, G. R.; Shroff, R. T.; Das, P.; Lee, J. E.; Ferrari, M.; Maitra, A.; Taniguchi, C. M.; Kim, M. P.; Crane, C. H.; Katz, M. H.; Wang, H.; Bhosale, P.; Tamm, E. P.; Fleming, J. B. A Visually Apparent and Quantifiable CT Imaging Feature Identifies Biophysical Subtypes of Pancreatic Ductal Adenocarcinoma. *Clin. Cancer Res.* **2018**, *24* (23), 5883–5894. https://doi.org/10.1158/1078-0432.CCR-17-3668.

(472) Dobie, C.; Skropeta, D. Insights into the Role of Sialylation in Cancer Progression and Metastasis. *Br. J. Cancer* **2021**, *124* (1), 76. https://doi.org/10.1038/S41416-020-01126-7.

(473) Pollak, M. R.; Quaggin, S. E.; Hoenig, M. P.; Dworkin, L. D. The Glomerulus: The Sphere of Influence. *Clin. J. Am. Soc. Nephrol.* **2014**, *9* (8), 1461. https://doi.org/10.2215/CJN.09400913.

(474) Ronny, F. M. H.; Sarungbam, J.; Zhong, X.; Yusuf, Y.; Yang, X.; Zhong, M. Glomerular Sparing Pattern in Primary Kidney Neoplasms: Clinical, Morphological and Immunohistochemical Study. *Am. J. Clin. Exp. Urol.* **2014**, *2* (1), 76.

(475) Pietrobono, S.; Stecca, B. Aberrant Sialylation in Cancer: Biomarker and Potential Target for Therapeutic Intervention? *Cancers (Basel).* **2021**, *13* (9). https://doi.org/10.3390/CANCERS13092014.

(476) Dundas, C. M.; Demonte, D.; Park, S. Streptavidin-Biotin Technology: Improvements and Innovations in Chemical and Biological Applications. *Appl. Microbiol. Biotechnol.* **2013**, *97* (21), 9343–9353. https://doi.org/10.1007/S00253-013-5232-Z/FIGURES/3.

(477) Pongracz, T.; Wuhrer, M.; de Haan, N. Expanding the Reaction Space of Linkage-Specific Sialic Acid Derivatization. *Molecules* **2019**, *24* (19). https://doi.org/10.3390/MOLECULES24193617.

(478) Furukawa, J. I.; Hanamatsu, H.; Nishikaze, T.; Manya, H.; Miura, N.; Yagi, H.; Yokota, I.; Akasaka-Manya, K.; Endo, T.; Kanagawa, M.; Iwasaki, N.; Tanaka, K. Lactone-Driven Ester-to-Amide Derivatization for Sialic Acid Linkage-Specific Alkylamidation. *Anal. Chem.* **2020**, *92* (21), 14383–14392. https://doi.org/10.1021/ACS.ANALCHEM.0C02209/SUPPL_FILE/AC0C022 09_SI_001.PDF.

(479) Bern, M.; Brito, A. E.; Pang, P. C.; Rekhi, A.; Dell, A.; Haslam, S. M. Polylactosaminoglycan Glycomics: Enhancing the Detection of High-Molecular-Weight N-Glycans in Matrix-Assisted Laser Desorption Ionization Time-of-Flight Profiles by Matched Filtering. *Mol. Cell. Proteomics* **2013**, *12* (4), 996–1004. https://doi.org/10.1074/mcp.O112.026377.

(480) Rujchanarong, D.; Scott, D.; Park, Y.; Brown, S.; Mehta, A. S.; Drake, R.; Sandusky, G. E.; Nakshatri, H.; Angel, P. M. Metabolic Links to Socioeconomic Stresses Uniquely Affecting Ancestry in Normal Breast Tissue at Risk for Breast Cancer. *Front. Oncol.* **2022**, *12*, 1. https://doi.org/10.3389/FONC.2022.876651/FULL.

(481) Chen, C. S.; Xu, L.; Lee, W. J. Electrochemical Lactonization of Trisialic Acid. *J. Chinese Chem. Soc.* **2018**, *65* (10), 1245–1250. https://doi.org/10.1002/JCCS.201800080.

(482) Nakata, D.; Troy, F. A. Degree of Polymerization (DP) of Polysialic Acid (PolySia) on Neural Cell Adhesion Molecules (N-CAMs): DEVELOPMENT AND APPLICATION OF A NEW STRATEGY TO ACCURATELY DETERMINE THE DP OF PolySIA CHAINS ON N-CAMS. *J. Biol. Chem.* **2005**, *280* (46), 38305–38316. https://doi.org/10.1074/JBC.M508762200.

(483) Liu, S.; Hoess, P.; Ries, J. Super-Resolution Microscopy for Structural Cell Biology. *https://doi.org/10.1146/annurev-biophys-102521-112912* **2022**, *51*, 301–326. https://doi.org/10.1146/ANNUREV-BIOPHYS-102521-112912.

(484) Wiśniewski, J. R.; Ostasiewicz, P.; Mann, M. High Recovery FASP Applied to the Proteomic Analysis of Microdissected Formalin Fixed Paraffin Embedded Cancer Tissues Retrieves Known Colon Cancer Markers. *J. Proteome Res.* **2011**, *10* (7), 3040–3049. https://doi.org/10.1021/PR200019M/SUPPL_FILE/PR200019M_SI_005.XLS.

(485) Wiśniewski, J. R.; Duś, K.; Mann, M. Proteomic Workflow for Analysis of Archival Formalin-Fixed and Paraffin-Embedded Clinical Samples to a Depth of 10 000 Proteins. *PROTEOMICS – Clin. Appl.* **2013**, *7* (3–4), 225–233. https://doi.org/10.1002/PRCA.201200046.

(486) Berg Luecke, L.; Gundry, R. L. Assessment of Streptavidin Bead Binding Capacity to Improve Quality of Streptavidin-Based Enrichment Studies. *J. Proteome Res.* **2021**, *20* (2), 1153. https://doi.org/10.1021/ACS.JPROTEOME.0C00772.

(487) Greenwald, N. F.; Miller, G.; Moen, E.; Kong, A.; Kagel, A.; Dougherty, T.; Fullaway, C. C.; McIntosh, B. J.; Leow, K. X.; Schwartz, M. S.; Pavelchek, C.; Cui, S.; Camplisson, I.; Bar-Tal, O.; Singh, J.; Fong, M.; Chaudhry, G.; Abraham, Z.; Moseley, J.; Warshawsky, S.; Soon, E.; Greenbaum, S.; Risom, T.; Hollmann, T.; Bendall, S. C.; Keren, L.; Graf, W.; Angelo, M.; Van Valen, D. Whole-Cell Segmentation of Tissue Images with Human-

Level Performance Using Large-Scale Data Annotation and Deep Learning. *Nat. Biotechnol. 2021 404* **2021**, *40* (4), 555–565. https://doi.org/10.1038/s41587-021-01094-0.

(488) Riley, N. M.; Hebert, A. S.; Westphall, M. S.; Coon, J. J. Capturing Site-Specific Heterogeneity with Large-Scale N-Glycoproteome Analysis. *Nat. Commun. 2019 101* **2019**, *10* (1), 1–13. https://doi.org/10.1038/s41467-019-09222-w.